# Molecular Scale Patterning of Photonic Structures via Conformational Control




Alice Marylea Smith

Lincoln College

University of Oxford

A thesis submitted for the degree of

*Doctor of Philosophy*

Trinity 2020

# Acknowledgements

Firstly I would like to thank Prof Donal D. C. Bradley and Dr Paul Stavrinou for giving me this opportunity. Thank you for demanding high standards, giving me the freedom to explore and inspiring me with your endless ideas and vast knowledge in the field.

I'm also extremely grateful to Prof Robert Taylor for supporting me these past 18 months with patience, kindness and expert supervision. Thank you for instinctively knowing when to give me space, for your accessibility and for making no question or issue seem too big or too small.

To my group; Dr Florian Le Roux, Dr Nikki Lambeva, Bingjun Wang and Dr Rick Hamilton, and colleagues; Dr Ross Warren, Dr Hangyang Ye and Dr Tim Puchtler - thank you for providing a friendly and stimulating environment these past years. A special thank you to Dr Claudius Kocher and Dr Florian Le Roux for their company in Room 101, and for giving me so much of their time and attention - I could not have done it without you. Thanks also to Prof Katherine Blundell for her guidance and support.

A huge thank you to everyone at Lincoln College for making these past years so special. Many thanks to Carmella Elan-Gaston and the Rev. Dr Melanie Marshall for their help and kindness during difficult times. To my fellow members of the MCR, particularly Mat Veal, Chris Nicholls, Megan Leaver, Caitlin O'Shaughnessy, Alice Fraser and Shazeaa Ishmael, thank you for all the laughs and for memories I will cherish for years to come. Also a special thank you to Lincoln native Dr Nico Kist for his endless stream of invaluable advice and for being my biggest cheerleader from the beginning to the end.

Thanks also to Dr Olivia Wiles, Dr Helena Kaznowska and Hannah Schneider for their friendship and excellent musical company.

To everyone on the Plastic Electronics CDT, thank you for your fabulous company on the many trips to Switzerland and for the shared knowledge, collaboration and support. In particular thank you to Dr Nathan Cheetham for taking the time to show me the ropes.

To those in the real world, thank you for providing much needed distraction from the lab. To Robert Gorrie, all the Glasgow Girls, Becca Sanders, Daniel Coldridge, Georgia Samwell, Shreya Singhal, Robyn Stapleton, Jessica Evans,

Jessica Steinemann, Chris Clark, Arabella Arcuragi, Daniel Beresford, Jennifer and David Fahy - your humour and friendship were more necessary than you know.

To my parents May and Ian, thank you for your unwavering support, for always having my back and for never doubting me. Thank you also to my sister Phyllis for always being there.

A special thank you to my siblings Lydia and David, who admirably survived being trapped with me as I was writing this thesis. I am hugely grateful for this time spent with you and will always appreciate your hilarious company, tolerance, care and kindness.

Lastly I extend my deepest gratitude to Chris Harrison, for his ubiquitous and immeasurable support that could never be overstated. Thank you for taking on the roles of housekeeper, chef and mentor this past year, and for standing by me throughout the rollercoaster that was this DPhil. Your endless patience and positivity amazes me, and without you this thesis would not have been written.

* * *

I would like to dedicate this thesis to my grandmother Marylea Hollick-Kenyon. As a microbiologist she was ahead of her time, and instilled in our family strong values of education and equality. I will always be inspired by her intelligence, strength of character, sense of humour and innate curiosity.

# Abstract

This thesis comprises a number of studies into controlling the photonic properties of materials by way of controlling their molecular conformation.

The absorption and emission behaviours of fundamental AIE molecules TPE and HPS were probed in solutions with varying degrees of aggregation. It was found, in contrast to the existing RIR hypothesis, that the monomers were able to emit in good solutions with minimal aggregation, and continued to do so upon low levels of aggregation. The monomer emission of TPE was found to be more prevalent than that of HPS due to the difference in conjugation pathways offered by each molecule. These results suggested that the term AIE is misleading, with the assumption that the molecular emission 'switches on' upon aggregation disregarding the fact that the more efficient fluorescence actually results from a quenching process (excimer formation), with RIR causing the increase in efficiency.

A new method for controlling the aggregation in fluorene/fluorenone oligomers was also investigated. Water was found to be highly effective for screening the fluorenone aggregation, with fractions of only 10% sufficient to eliminate the excimer emission. The fluorenone was then successfully reaggregated to varying degrees as the water fraction was increased, due to non-solvent effects. Investigating solutions of thermally oxidised FFF also revealed the method's ability to identify the presence of fluorenone moieties when there was no indication of oxidation in the absorption or PL.

Lastly, dip-pen nanolithography was employed to pattern photonic structures in PFO thin films. $\beta$ phase dots with diameter 548 nm were achieved, demonstrating the potential of DPN in photonic device fabrication, however there were issues with consistency of feature size and damage to the film. An outline of the development of the microscale PL set-up used to analyse the patterns, and the steps taken to maximise its resolution and spectral contrast is also given. The set-up was found to be well suited to highlight the $\beta$ phase of PFO, however there were issues with reproducibility of the PL maps, as well as a trade-off between signal strength and photodegradation of the sample. When compared to patterns imaged on a different set-up, it was clear that the set-up designed here produced too low a signal to accurately compare the new patterns. Further work in sample fabrication, DPN operation and microscale PL optimisation was therefore identified to improve the quality and reproducibility of the patterns.

# Contents

**List of Figures** **ix**

**List of Tables** **xii**

**List of Abbreviations** **xiv**

**1 Introduction** **1**

1.1 Context . . . 2
1.1.1 A Brief History . . . 2
1.1.2 Photonics . . . 2
1.1.3 Organic Semiconductors . . . 4
1.1.4 Motivation . . . 5
1.2 Theory of Organic Semiconductors . . . 6
1.2.1 Conjugation and Semiconductivity . . . 6
1.2.2 Excited States . . . 8
1.2.3 Optical Transitions . . . 10
1.2.4 Molecular Considerations . . . 13
1.2.5 Quenching Mechanisms . . . 14
1.2.6 Excimers . . . 15
1.3 Aggregation Induced Emission . . . 18
1.3.1 AIE Mechanism . . . 18
1.3.2 Polymer Matrix Dispersion . . . 22
1.3.3 AIE Mechanism of TPE and HPS . . . 24
1.3.4 Previous Related Work . . . 27
1.4 Polyfluorenes . . . 28
1.4.1 Background . . . 28
1.4.2 Fluorenone Defects . . . 29
1.4.3 Poly(9,9-dioctylfluorene) Microstructure . . . 31
1.4.4 $\beta$ Phase Characterisation . . . 32
1.4.5 Consequences of $\beta$ Phase . . . 35
1.4.6 Methods for Inducing the $\beta$ Phase . . . 37
1.5 Patterning . . . 40

1.5.1 Micro and Nanoscale Patterning Techniques . . . . . 40
1.5.2 Dip-Pen Nanolithography . . . . . 41
1.5.3 Applications of Patterned PFO or Potential Photonic Structures 44
1.6 In This Thesis . . . . . 48
1.6.1 Monomer Emission and RIR Mechanism of Fundamental AIE Molecules . . . . . 48
1.6.2 Excimer Formation in Fluorene-Fluorenone Oligomers . . . . 49
1.6.3 Dip-Pen Patterning of PFO . . . . . 49
1.6.4 Summary . . . . . 50

**2 Materials and Methods** **51**
2.1 Materials . . . . . 51
2.2 Sample Fabrication . . . . . 51
2.2.1 Solutions . . . . . 54
2.2.2 Thin Films . . . . . 54
2.3 Optical Methods . . . . . 55
2.3.1 UV-Vis Spectroscopy . . . . . 55
2.3.2 Photoluminescence Spectroscopy . . . . . 58
2.3.3 Photoluminescence Quantum Efficiency . . . . . 61

**3 Monomer Emission and RIR Mechanism of Fundamental AIE Molecules** **64**
3.1 Introduction . . . . . 64
3.1.1 Aims . . . . . 65
3.1.2 Order of work . . . . . 66
3.2 Experimental . . . . . 66
3.2.1 Solution Preparation . . . . . 67
3.2.2 Cuvette Preparation . . . . . 68
3.2.3 Optical Measurements . . . . . 68
3.3 Results . . . . . 69
3.3.1 Absorbance . . . . . 73
3.3.2 Photoluminescence . . . . . 74
3.3.3 PLQE . . . . . 77
3.4 Conclusion . . . . . 78

**4 Excimer Formation in Fluorene-Fluorenone Oligomers** **82**
4.1 Introduction . . . . . 82
4.1.1 Aims and Hypothesis . . . . . 84
4.1.2 Order of Work . . . . . 84
4.2 Experimental . . . . . 85

4.2.1 Solution Preparation . . . 85
4.2.2 Cuvette Preparation . . . 87
4.2.3 Optical Measurements . . . 87
4.3 Results . . . 89
4.3.1 Absorbance and Photoluminescence . . . 89
4.3.2 Peak Analysis and PLQE . . . 89
4.3.3 Discussion . . . 89
4.4 Conclusion . . . 99
4.4.1 Summary . . . 99
4.4.2 Tunability and Oxidation . . . 100
4.4.3 Sensitive Oxidation Testing . . . 101

**5 Development of Microscale Photoluminescence 103**
5.1 Introduction . . . 103
5.2 Design . . . 104
5.2.1 Set-up Overview . . . 104
5.2.2 Data Collection & Structuring . . . 107
5.2.3 Key Components & Alignment . . . 109
5.3 Characterisation . . . 115
5.3.1 Resolution . . . 115
5.3.2 Theory of Gaussian Beams . . . 117
5.3.3 Knife Edge Measurements . . . 119
5.3.4 ThorCam Measurements . . . 122
5.3.5 Beam Parameter Calculation . . . 122
5.4 PFO Tests . . . 126
5.4.1 Power Tests . . . 126
5.4.2 Stability . . . 129
5.5 Conclusion . . . 129

**6 Dip-Pen Patterning of PFO 132**
6.1 Introduction . . . 132
6.1.1 Overview and Aims . . . 132
6.1.2 Order of Work . . . 134
6.2 Experimental . . . 135
6.2.1 Sample Preparation . . . 135
6.2.2 DPN Patterning . . . 138
6.3 Results . . . 140
6.3.1 DPN Patterning . . . 140
6.3.2 Micro-PL Maps . . . 142
6.3.3 Dot Analysis . . . 150
6.4 Conclusion . . . 156

**7 Concluding Remarks** **160**
7.1 AIE . . . . . 160
7.2 Fluorene/Fluorenone Oligomers . . . . . 161
7.3 Dip-Pen Patterning of PFO and Micro-scale Photoluminescence . . 162

**Appendices**

**List of Components** **170**

**References** **172**

# List of Figures


1.1 Crystalline Inorganics vs. Amorphous Organics . . . . . 4
1.2 $sp^2$ Hybridisation and $p_z$ Conjugation . . . . . 6
1.3 Conjugation Bands . . . . . 7
1.4 Electron Configuration of Excited Species . . . . . 9
1.5 Jablonski Diagram of Optical Transitions . . . . . 11
1.6 Absorption and Emission of Perylene . . . . . 12
1.7 Excimer Formation and Emission Processes . . . . . 17
1.8 Restriction of Intramolecular Motion (RIM) in AIE . . . . . 19
1.9 Effects of increasing polarity and aggregation in D-A structured molecules . . . . . 20
1.10 Polymer matrix induced RIM . . . . . 21
1.11 Mechanochromism in polymer blends . . . . . 22
1.12 AIE:PMMA blends . . . . . 23
1.13 AIE mechanism of TPE and HPS . . . . . 25
1.14 Conjugation Pathways of TPE and HPS . . . . . 26
1.15 Crystal structures of TPE and HPS . . . . . 26
1.16 Absorption and emission of TPE:PMMA blend films . . . . . 28
1.17 G-band Emission of Polyfluorene . . . . . 29
1.18 Phases and Energy Levels of Poly(9,9-dioctylfluorene) . . . . . 31
1.19 Mean torsion angles of PFO phases . . . . . 32
1.20 Normalised absorption and emission of PFO phases . . . . . 33
1.21 Exciton Migration to the $\beta$ Phase . . . . . 34
1.22 Determination of the $\beta$ Phase Fraction . . . . . 35
1.23 Kramers-Kronig analysis of $\beta$ phase absorption . . . . . 36
1.24 $\beta$ phase induction via spin coating or thermal cycling . . . . . 38
1.25 Dip-Pen Nanolithography . . . . . 42
1.26 Dip-Pen Nanolithography System Overview . . . . . 43
1.27 Potential $\beta$ Phase Waveguide Geometries . . . . . 45
1.28 $\beta$ Phase Microcavity in a PFO OLED . . . . . 46
1.29 Directional Tuning and intensity benefits of microcavities . . . . . 47

2.1 Structures of the materials used in this thesis . . . . . 52

2.2 Structures of the solvents used in this thesis . . . . . 52
2.3 Intensity Attenuation . . . . . 56
2.4 Absorption and Absorbance . . . . . 57
2.5 PL Spectroscopy . . . . . 58
2.6 PL Spectra Correction . . . . . 60
2.7 PLQE measurements . . . . . 61
2.8 Spectral determination of PLQE energy ranges . . . . . 63

3.1 TPE and HPS . . . . . 65
3.2 Absorbance and PL of TPE Solutions . . . . . 70
3.3 Absorbance and PL of HPS Solutions . . . . . 71
3.4 Emission Photographs . . . . . 72
3.5 Solution PLQE . . . . . 73

4.1 Fluorene/Fluorenone Oligomers . . . . . 83
4.2 The Impact of Concentration on Excimer Formation . . . . . 86
4.3 Absorbance and PL of FF, FFF . . . . . 90
4.4 Absorbance and PL of FO, FFF-ox2 . . . . . 91
4.5 Emission Photographs . . . . . 92
4.6 Monomer vs Excimer Intensities of FO and FFF-ox2 . . . . . 93
4.7 Shifts in absorbance and PLQE . . . . . 94

5.1 Micro-PL Set-Up . . . . . 105
5.2 Micro-PL mapping data acquisition and structuring process. . . . . 108
5.3 Condensed PL Signal . . . . . 109
5.4 Improvements in beam quality due to fibre coupling . . . . . 110
5.5 Impact of the objective fill factor on the beam profile . . . . . 111
5.6 Internal spectrometer alignment. . . . . 112
5.7 HeAr spectral lines for CCD alignment. . . . . 113
5.8 Beamsplitter transmission . . . . . 114
5.9 The Abbe diffraction limit for a Gaussian laser beam . . . . . 115
5.10 Demonstration of the diffraction limit of Gaussian beams . . . . . 116
5.11 Diffraction of a Gaussian beam . . . . . 117
5.12 Propagation of a Gaussian beam . . . . . 118
5.13 Deconvolution of 'knife-edge' intensity profile . . . . . 120
5.14 ThorCam image of 'knife-edge' InGaN/Au boundary . . . . . 120
5.15 'Knife-edge' intensity profile . . . . . 121
5.18 FWHM and Area of Gaussian fitted $x, y$ cross-sections . . . . . 122
5.16 $z$-sweep intensity plots of the laser spot . . . . . 123
5.17 $x, y$ cross-sections of $z$-sweep intensity plots . . . . . 124

5.19 Power squares to identify photodegradation of PFO . . . . . 127
5.20 Stability of the piezo stage . . . . . 128

6.1 Selection of suitable sample from PL spectra . . . . . 137
6.2 Absorption and PL of preliminary sample . . . . . 137
6.3 New Pattern layout . . . . . 139
6.4 Preliminary Pattern layout . . . . . 139
6.5 Array of new patterns achieved via DPN . . . . . 140
6.6 Solvent loading onto the tips from inkwells. . . . . 141
6.7 Micro-PL maps of dot patterns with $d = 1\,\mathrm{s}$ . . . . . 144
6.8 Micro-PL maps of dot patterns with $d = 3\,\mathrm{s}$ . . . . . 145
6.9 Micro-PL maps of dot patterns with $d = 5\,\mathrm{s}$ . . . . . 146
6.10 Preliminary micro-PL maps of dot patterns with $d = 5\,\mathrm{s}$ and $20\,\mathrm{s}$ . 147
6.11 Stages of dot patterning . . . . . 149
6.12 Dot PL spectra of new patterns . . . . . 151
6.13 Dot PL spectra of preliminary patterns . . . . . 152
6.14 Measurements of new patterns . . . . . 153
6.15 Measurements of preliminary patterns . . . . . 154

1 Absorption and emission of **A** Benzene, **B** trans-Stilbene and **C** cis-Stilbene. . . . . 165
2 Transmission of solvents and FF, FO, FFF, FFF-ox1, FFF-ox2 solutions. 166
3 PL of solvents and corresponding FF solutions. . . . . 167
4 PL of solvents and corresponding FO solutions. . . . . 168
5 Beam splitter reflection of polarised light [174]. . . . . 169

# List of Tables


1.1 Hildebrand solubility parameters and boiling points of solvents used for processing PFO films and inducing the $\beta$ phase [23][109][113]. . 38
1.2 Examples of techniques to induce the $\beta$ phase in PFO, and the fraction of $\beta$ phase achieved in each. (Non-exhaustive). Adapted from [89][110]. . . . . 40

2.1 Details of the materials used throughout this thesis. . . . . 53
2.2 Details of the solvents used throughout this thesis. . . . . 53
2.3 Spin-coating parameters for PFO thin films. . . . . 55

3.1 Sets of Solutions . . . . . 67
3.2 Details of THF starter solutions for each AIE material, and the final concentration of the material in each set of cuvettes. . . . . 67
3.3 Composition of AIE material and solvent cuvettes. . . . . 68
(a) AIE Cuvettes . . . . . 68
(b) Solvent Background Cuvettes . . . . . 68
3.4 PL and PLQE measurement parameters for each set of AIE cuvettes. 69

4.1 Details of THF starter solutions for each F/O oligomer, and the final concentration of the oligomer in the cuvettes. . . . . 87
4.2 Composition of oligomer and solvent cuvettes. . . . . 88
(a) Oligomer Cuvettes . . . . . 88
(b) Solvent Background Cuvettes . . . . . 88
4.3 PL and PLQE measurement parameters for each set of oligomer cuvettes. . . . . 88

5.1 Theoretical and calculated beam parameters for the $x, y$ cross-sections of $z = 15\,\mu\text{m}$. . . . . 125
5.2 Transmission of laser power through the excitation path. . . . . 127

6.1 Details of the solutions used to fabricate the PFO films used for patterning. $\delta$ is the Hildebrand parameter of solubility [157]. . . . . 135

6.2 Thermal spinning conditions for PFO films spun from toluene (**A**, **A2**, **B**) and THF (**C**, **D**). Various thermal conditions were trialled to minimise the presence of $\beta$ phase. . . . . 136
6.3 Micro-PL mapping parameters of new dot patterns with tip dwell times of 1 s, 3 s and 5 s. Measured using the set-up described in Chapter 5. . . . . 143
6.4 Micro-PL mapping parameters of preliminary dot patterns with tip dwell times of 5 s and 20 s, and a large pitch of 10µm. Maps taken with set-up described in Chapter 5. . . . . 143

# List of Abbreviations

**ACQ** . . . . . Aggregation Caused Quenching

**AEE** . . . . . Aggregation Enhanced Emission

**AFM** . . . . . Atomic force microscopy

**AIE** . . . . . Aggregation Induced Emission

**AN** . . . . . Area Normalisation/Normalised

**BCMDB** . . . 1,4-bis($\alpha$-cyano-4-methoxystyryl)-2,5-dimethoxybenzene

**BzBMN** . . . . 2-benzyloxy-4-diethylaminobenzaldehyde

**CB** . . . . . Covalent Band

**C-C** . . . . . Carbon-Carbon

**D-A** . . . . . Donor-Acceptor

**DCB** . . . . . Dichlorobenzene

**DPN** . . . . . Dip-Pen Nanolithography

**ECL** . . . . . Effective Conjugation Length

**EQE** . . . . . External Quantum Efficiency

**F** . . . . . Fluorene

**FF** . . . . . 2,2'-Bi(9,9-dihexylfluorene)

**FFF** . . . . . 9,9,9',9',9",9"-Hexahexyl-9H,9'H,9"H-2,2':7',2"-terfluorene

**FO** . . . . . 2-(9,9-Dihexyl-9H-fluoren-7-yl)-9H-fluoren-9-one

**F/O** . . . . . Fluorene/Fluorenone

**FRET** . . . . . Förster Resonance Energy Transfer

**FWHM** . . . . Full Width Half Maximum

**G-band** . . . . Green band

**GaAs** . . . . . Gallium Arsenide

**HOMO** . . . . Highest Occupied Molecular Orbital

**HPS** . . . . . Hexaphenylsilole

**IB** . . . . . Ion Beam

**ICS** . . . . . Intersystem Crossing

**ICT** . . . . . Intramolecular Charge Transfer

**IO** . . . . . Integrated Optics

**IPA** . . . . . Isopropyl Alcohol

**LED** . . . . . Light Emitting Diode

**LUMO** . . . . Lowest Occupied Molecular Orbital

**NA** . . . . . Numerical Aperture

**NLP** . . . . . Nano Lithography Platform

**O** . . . . . Fluorenone

**OLED** . . . . . Organic Light Emitting Diode

**PF** . . . . . Polyfluorene

**PFO** . . . . . poly(9,9-dioctylfluorene)

**PL** . . . . . Photoluminescence

**PLQE** . . . . . Photoluminescence Quantum Efficiency

**PMMA** . . . . Poly(methyl methacrylate)

**PN** . . . . . Peak Normalisation/Normalised

**PPV** . . . . . poly(p-phenylene vinylene)

**PS** . . . . . polystyrene

**Rel.** . . . . . Relative Intensity

**RIM** . . . . . Restriction of Intramolecular Movement

**RIR** . . . . . Restriction of Intramolecular Rotation

**RIV** . . . . . Restriction of Intramolecular Vibration

**RT** . . . . . Room Temperature

**THF** . . . . . Tetrahyrdofuran

**TICT** . . . . . Twisted Intramolecular Charge Transfer

**TPE** . . . . . Tetraphenylethylene

**UV-Vis** . . . . Ultraviolet to visible

**VB** . . . . . Valence Band

**XS** . . . . . Cross Section

# 1 Introduction

## Contents


**1.1 Context . . . . . 2**
1.1.1 A Brief History . . . . . 2
1.1.2 Photonics . . . . . 2
1.1.3 Organic Semiconductors . . . . . 4
1.1.4 Motivation . . . . . 5
**1.2 Theory of Organic Semiconductors . . . . . 6**
1.2.1 Conjugation and Semiconductivity . . . . . 6
1.2.2 Excited States . . . . . 8
1.2.3 Optical Transitions . . . . . 10
1.2.4 Molecular Considerations . . . . . 13
1.2.5 Quenching Mechanisms . . . . . 14
1.2.6 Excimers . . . . . 15
**1.3 Aggregation Induced Emission . . . . . 18**
1.3.1 AIE Mechanism . . . . . 18
1.3.2 Polymer Matrix Dispersion . . . . . 22
1.3.3 AIE Mechanism of TPE and HPS . . . . . 24
1.3.4 Previous Related Work . . . . . 27
**1.4 Polyfluorenes . . . . . 28**
1.4.1 Background . . . . . 28
1.4.2 Fluorenone Defects . . . . . 29
1.4.3 Poly(9,9-dioctylfluorene) Microstructure . . . . . 31
1.4.4 $\beta$ Phase Characterisation . . . . . 32
1.4.5 Consequences of $\beta$ Phase . . . . . 35
1.4.6 Methods for Inducing the $\beta$ Phase . . . . . 37
**1.5 Patterning . . . . . 40**
1.5.1 Micro and Nanoscale Patterning Techniques . . . . . 40
1.5.2 Dip-Pen Nanolithography . . . . . 41

1.5.3 Applications of Patterned PFO or Potential Photonic Structures . . . . . 44
**1.6 In This Thesis . . . . . 48**
1.6.1 Monomer Emission and RIR Mechanism of Fundamental AIE Molecules . . . . . 48
1.6.2 Excimer Formation in Fluorene-Fluorenone Oligomers . 49
1.6.3 Dip-Pen Patterning of PFO . . . . . 49
1.6.4 Summary . . . . . 50

---

# 1.1 Context

## 1.1.1 A Brief History

The development of the first metal-oxide-semiconductor transistor in 1959 by John M Atalla at Bell Labs [1] triggered an electronics revolution, resulting in the multitude of electrical devices we are familiar with today. The performance of such devices is ultimately limited by the speed at which their electrical components can communicate, and the density of information they can process. As the modern world continues to demand ever more processing power, it is natural that the focus should shift from electrons to photons as the main carriers of information.

While it goes without saying that light is *fast*, the quantum mechanical properties of photons also offer new properties such as superposition and entanglement. These properties are driving the development of novel technologies such as quantum computers, which are both exponentially more performant than current computers [2], and capable of performing new kinds of computation [3]. As a result, society is on the cusp of a paradigm shift of a scale not seen since the electronics boom of the 1960's. However, this shift is due to developments in photonics rather than electronics, from the mastering of the photon.

## 1.1.2 Photonics

Photonics is the science of the "generation, detection and manipulation" of light [4] and the field was born with the invention of the laser in 1960 by Theodore Maiman [5]. Then in the 1970's came the laser diode, followed by optical fibres and

amplifiers. These formed a suite of photonic devices that paved the way for rapid progress in telecommunications, and enabled the invention of the internet [6][7].

Whilst these devices succeeded in harnessing light as a medium for data transfer, in the past few decades a similar advancement has taken place in controlling the fundamental optical structure of materials. Through patterning refractive index structures *into* materials, photonic structures, known as photonic crystals, can be formed. While a typical semiconductor such as gallium arsenide (GaAs) has an ionic crystal lattice structure with alternating positive and negative charges, a photonic crystal is instead composed of alternating refractive indices with a periodicity of the order of the wavelength of light ($400 - 700\,\mathrm{nm}$).

Akin to the electronic band gap of classical semiconductors, photonic crystals have a photonic band gap that permits the transfer of select wavelengths depending on the crystal periodicity and geometry [8]. The capability to manipulate these features would allow the photonic band gap to be tuned, thus enabling unprecedented control over the material's interaction with light.

The photonic band gap of photonic crystals causes intriguing optical effects that are visible to the naked eye. A common example in nature is opal gemstones, which are formed over tens of millions of years from the deposition of silica dissolved in water. This slow process allows the silica particles to arrange in a highly ordered crystalline structure, with a periodicity of the wavelength of visible light.

Due to their resultant photonic bandgap's directionality and wavelength selectivity, opals exhibit flashes of iridescence as they are observed from different angles. In contrast, amorphous silica (glass) is typically colourless and transmits the full visible spectrum regardless of viewing angle. This difference provides a clear cut example of how the nanostructure can govern the optical properties of a material.

Although the underlying theory of these photonic effects has been understood since the publication of Maxwell's equations in 1856 [9][10], manufacturing nanoscale structures with the required precision involves significant technical challenges that have only been overcome in recent decades. Fabrication of the first photonic crystal tuned to visible light was achieved in 1996 by Krauss *et al.*, using a multi-step

process involving electron-beam lithography, resist patterning and reactive ion etching [11]. These processes require a cleanroom environment, and are both time consuming and costly.

There has been much work in recent decades in the use of organic semiconductors for photonic applications [12][13][14]. Organics are interesting for photonic applications as they are not constrained by a crystalline lattice. Their microstructure, which controls their optical properties, is sensitive to chemical and thermal processing conditions, making them an interesting topic of study for novel photonic structure fabrication techniques.

### 1.1.3 Organic Semiconductors

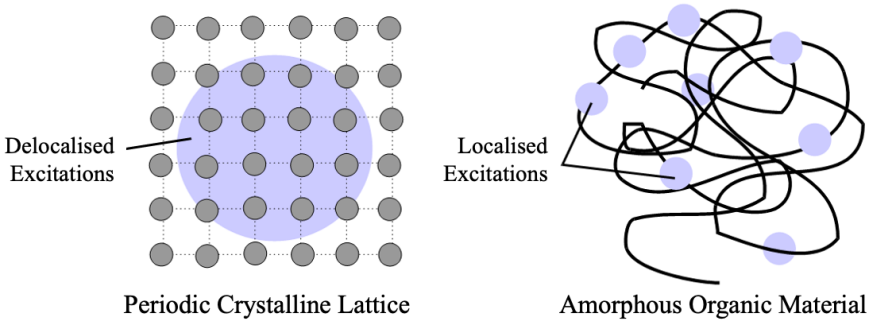



**Figure 1.1:** The periodic crystalline lattice of inorganic semiconductors vs. the amorphous entanglement of conjugated polymers. The electron sea model supports delocalisation of excitations across the lattice, whereas the lack of order in organic materials causes excitations to remain localised to a molecule or polymer chain segment.

Semiconductivity in organic materials was first observed in 1946 [15][16], but it was not until 1987 that C.W.Tang and S.A.Vanslyke produced the first organic light emitting diode (OLED) at Kodak [17]. Following this in 1990, Burroughes *et al.*[18] designed an OLED using the conjugated polymer poly(p-phenylene vinylene) (PPV) as the emitter. This discovery sparked the field of plastic electronics, concerning a new class of semiconducting small molecules and polymers with many properties not achievable with inorganic materials.

Due to their microstructure, organic materials are afforded a range of mechanical properties not typically seen in semiconductor materials. As shown in Figure 1.1,

polymers form an entanglement of chains and are able to adopt a large variety of conformations[1]. Free from a lattice structure, organics are made up of amorphous and crystalline regions, giving them a flexibility and durability not possible in crystalline materials, which in comparison are rigid and brittle.

These properties have inspired polymer devices such as flexible displays and solar cells that can be easily rolled up and transported [20]. Another use case is smart windows and car windscreens, where the integration of transparent organic devices could enable novel functionality [21]. Their softness relative to inorganic semiconductors also makes them adaptable to different optoelectronic circuit requirements, and simplifies their integration with existing systems [22].

Another key property of organic materials is their solubility in organic solvents. This allows them to be solution processable in ambient conditions, giving them a key financial advantage over inorganics which often require a clean room environment. Solution processability offers potential for their fabrication to be upscaled with high volume, low cost production techniques such as roll-to-roll printing.

### 1.1.4 Motivation

The properties detailed above demonstrate the potential benefits offered by organic materials in fabricating the photonic devices of the future. The huge variety of organic materials also offers much scope in terms of photonics research, from carbon based small molecules to oligomers and polymers. The chapters herein will touch on each of these types of molecule in turn.

The first aim is to further develop a technique that has shown great potential for the fabrication of photonic structures. Dip-pen nanolithography (DPN), detailed below in Section 1.5, has previously been used to control the conformation of the polymer poly(9,9-dioctylfluorene) (PFO) at the nanoscale, in order to spatially pattern refractive index structures within the polymer [23]. PFO is of great interest to the photonics community as its blue emission and highly controllable

[1]N.B. Conformation should not be confused with configuration. Configuration is how the molecule arranges relative to other molecules, i.e. its propensity for crystallisation. Conformation is the molecular shape due to rotations about bonds. For example a polymer could, depending on its environment, coil up in a ball or unravel into a straight rod [19].

conformation offer the potential for the generation and manipulation of light to be achieved in a single material.

Additionally, small molecules that display a phenomenon known as Aggregation Induced Emission (AIE), detailed in Section 1.3, and fluorene oligomers, Section 1.4.2, were studied. Both of these groups of materials display interesting optical effects as a result of their aggregation behaviours. These chapters will investigate methods for controlling the optical properties of these materials and discuss their suitability for photonic device applications.

To navigate these properties, it is necessary to understand the various optoelectronic mechanisms of organic semiconductors, starting with how their semiconductivity arises. The fundamental theory underpinning this semiconductivity, followed by the theory of the various concepts studied herein, is presented below.

## 1.2 Theory of Organic Semiconductors

### 1.2.1 Conjugation and Semiconductivity

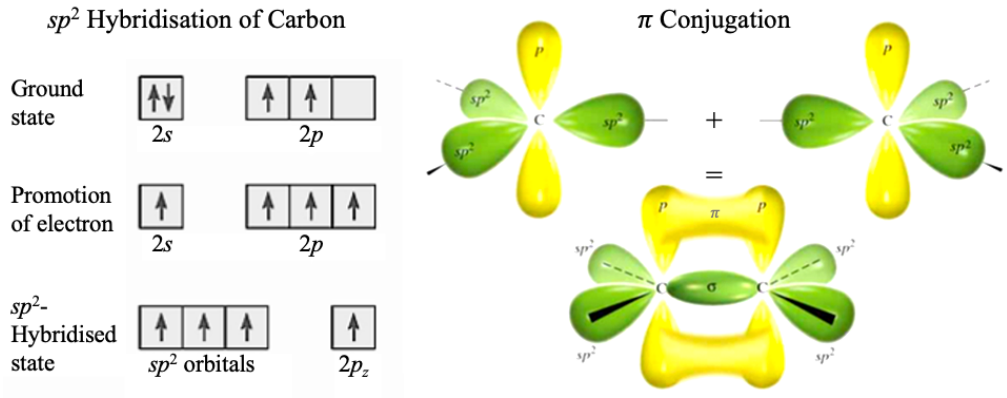



**Figure 1.2:** $sp^2$ Hybridisation and $\pi$ Conjugation. $sp^2$ hybridisation forms 1 $p_z$ and 3 $sp^2$ orbitals. In a C-C double bond, a $\sigma$ bond is formed between 2 such $sp^2$ orbitals, with a $\pi$ bond formed between the 2 lone $p_z$ orbitals, which are delocalised from the molecular plane. Adapted from [24].

As shown in Figure 1.1, the localised excitations of organic molecules can prevent the formation of a continuous band structure. Instead, the semiconducting properties are determined by the material's molecular orbitals, which arise from the nature of the carbon to carbon bonding present in the molecule, described as follows.

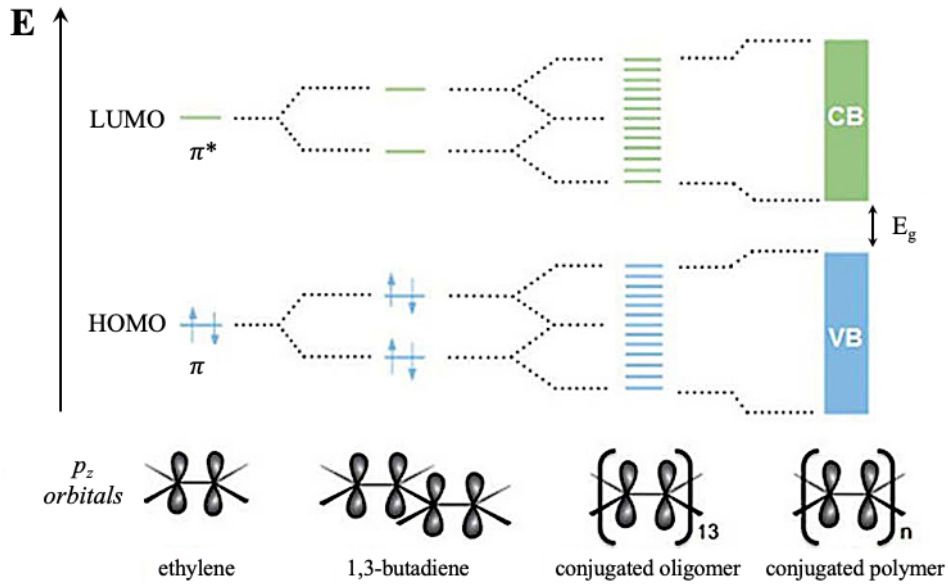



**Figure 1.3:** Conjugation of organic semiconductors. As the density and overlap of $\pi$ orbitals increases across the molecule, more energy levels move into the HOMO-LUMO gap. This reduces $E_{\mathrm{G}}$, such that the semiconductor property of excitation across the gap becomes possible. Adapted from [26].

Carbon to carbon (C-C) sigma bonds are at the heart of all organic molecules. To form C-C double bonds, the carbon $2s$ and $2p$ orbitals undergo $sp^2$ hybridisation as shown in Figure 1.2. This results in 3 $sp^2$ orbitals in one plane, and 1 $p_z$ orbital lying perpendicular to the plane. When a $\sigma$ bond is formed between 2 $sp^2$ orbitals of adjacent hybridised carbons, the proximity of their $p_z$ atomic orbitals enables them to overlap. Thus, $\pi$ bonding and $\pi^*$ antibonding molecular orbitals are formed, containing $\pi$ electrons which are delocalised from the $\sigma$ bond at the core of the molecule. This $\pi$ bonding is termed conjugation, and is the basis for electronic conductivity in organic molecules [24].

As shown in Figure 1.3, as more C-C double bonds are made, a system of conjugation is formed along the chain. As the chain of carbon bonding is extended, this conjugation too is extended, permitting electron and hole transport along the chain. The C-C bonds form a backbone structure, with delocalised $\pi$ electrons free to move along its length. Due to bond resonance, alternating double and single bonds are sufficient to provide a conjugation pathway [25].

The highest (energy) occupied molecular orbital is termed the HOMO and

the lowest unoccupied molecular orbital the LUMO. The number of units across which the conjugation extends is called the effective conjugation length (ECL). As the orbitals overlap, more electronic states are added into the HOMO-LUMO gap, as shown in Figure 1.3, effectively reducing the band or energy gap, $E_{\mathrm{G}}$ of the conjugated system. When this gap becomes small enough for electrons to be optically, thermally or electrically excited from the HOMO to the LUMO, the molecule becomes a semiconductor.

As the conjugation length increases, the density of states increases such that it resembles a continuous band structure, analogous to the conduction (CB) and valence (VB) bands of inorganic semiconductors. However, due to the molecular disorder of organic materials the conjugation length rarely reaches the point of a continuous density of states. For example, if a polymer were entirely rigid and planar, then this conjugation length could extend across the full length of the molecule. However in most cases polymers are flexible, and form entanglements between chains as shown in Figure 1.1. This results in multiple, short conjugation lengths of varying sizes within a polymer chain, with discrete molecular energy levels.

Despite this, a higher degree of conjugation lowers the overall energy of the molecular orbital system. Therefore molecular conformations that favour a high degree of conjugation are more energetically favourable than those which do not promote orbital overlap and electron delocalisation.

Excitations are free to move along the ECL, or hop between conjugated systems of nearby chains. Similarly, a single polymer chain can host many separate excitations, that may move along the ECL and decay without ever interacting. Examples of such excitations are discussed in more detail below.

### 1.2.2 Excited States

The molecular orbital energy level diagram of Figure 1.4 displays the electron configurations of various excited species. The ionisation potential, $I_{\mathrm{p}}$, is the energy required to remove an electron from the HOMO. The electron affinity, $EA$, is the

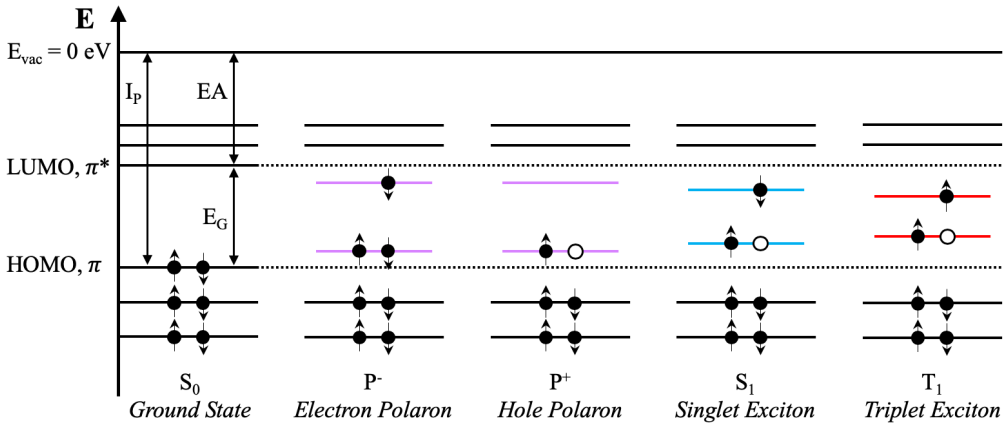



**Figure 1.4:** Electron configuration of excited species. The HOMO and LUMO of the excited states are shifted relative to the ground state due to lattice relaxation, ($P^-$, $P^+$, $S_1$, $T_1$), coulombic forces ($S_1$, $T_1$) and exchange energy ($T_1$). $I_\mathrm{p}$ denotes the ionisation potential, $EA$ the electron affinity, $E_\mathrm{vac}$ the vacuum energy level and $E_\mathrm{G}$ the energy gap.

energy released by adding an electron to the LUMO. $E_\mathrm{vac}$ is the vacuum energy level and $E_\mathrm{G}$ is the energy gap between the HOMO and LUMO energy levels.

When an electron is added or removed from the molecule, there is an accompanying redistribution of charge within the molecule to accommodate the change. This results in changes to bond lengths and angles and is termed lattice distortion. While this distortion can affect the conformation of the molecule, it does not cause dissociation due to the $\sigma$ bonds maintaining the backbone of the molecule remaining undisturbed. This combination of charge and distortion is termed a polaron. The electronic configuration of electron ($P^-$) and hole ($P^+$) polarons is shown in Figure 1.4. This lattice distortion reduces the total energy of the molecule, and so the HOMO and LUMO levels of the polaron excited state move into the ground state energy gap, thus reducing their $E_\mathrm{G}$ [27].

Another type of excited state is an exciton, also detailed in Figure 1.4. An exciton consists of an electron-hole pair bound across $E_\mathrm{G}$. Like polarons their formation causes lattice distortion in response to the movement of charge, but additionally the dipole of the bound pair introduces a coulombic attraction which brings the HOMO and LUMO levels even further into the energy gap than polarons. The exciton can be either a singlet exciton with spin $S = 0$, or a triplet with $S = 1$ [27][28].

Excitons can be formed from the combination of an electron and hole polaron, or from optical excitation of an electron in the ground state. If the exciton is formed from polarons, the exciton will be either singlet or triplet character depending on the spin state of the polarons, with random spin statistics alone providing a distribution of 75% triplet and 25% singlet. If optically excited, a singlet exciton will always be formed due to the electronic selection rules. However, in the presence of heavy atoms, a process termed Intersystem Crossing (ICS) may occur in which the spin state of the excited electron is flipped to form a triplet with S=1, as shown in Figures 1.4 and 1.5. Decay from the triplet state is forbidden due to spin conservation, and so is less efficient than singlet decay. The energy of triplet states is also reduced further than the singlet state by a quantity known as the exchange energy. This accounts for the reduced coulombic repulsion of the triplet electrons due to a smaller overlap in the triplet wavefunction. In conjugated polymers the exchange energy is usually $0.3 - 1\,\mathrm{eV}$ [28].

### 1.2.3 Optical Transitions

When the electrons of an organic molecule are optically excited to form excitons, they are promoted from the ground state ($S_0$) to excited state energy levels ($S_1$, $S_2$ etc.), as shown in Figures 1.4 and 1.5. Within these energy levels also exist vibrational energy levels, which add to the possible transitions and decay pathways of the electron.

Upon optical excitation, a photon of similar energy to $E_G$ is absorbed by an electron in the ground state, resulting in an transition to an excited state such as $S_1$ or $S_2$ depending on the energy of the photon. This ground state absorption is termed a $\pi - \pi^*$ transition as the electron is promoted from the occupied $\pi$ orbital to the unoccupied $\pi^*$. The resultant exciton then rapidly relaxes to the lowest vibrational level of $S_1$ via vibrational relaxation from a higher vibrational state or internal conversion from a higher excited state. The exciton then decays either non-radiatively at rate $\Gamma_{\mathrm{nrad}}$, with the energy lost as heat, or radiatively to a vibrational level in the ground state, where it may undergo further vibrational relaxation. This radiative decay is termed fluorescence, and the photon produced has energy equal

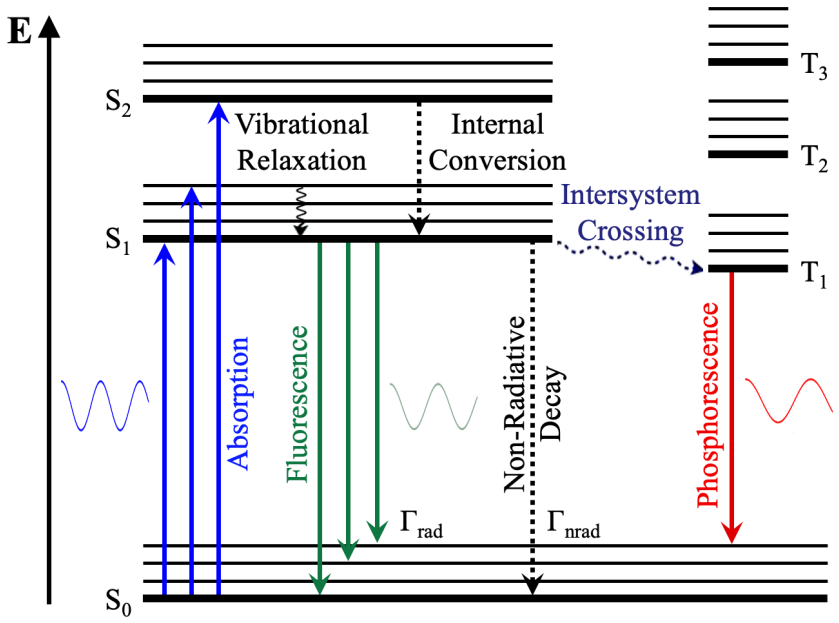



**Figure 1.5:** Jablonski Diagram of Optical Transitions. Absorption can occur from $S_0$ to any vibrational state in $S_1$ or $S_2$ etc. The exciton diffuses to the lowest energy $S_1$ state via vibrational relaxation and/or internal conversion, before undergoing fluorescent decay, with decay rate $\Gamma_{rad}$. Non-radiative decay may also occur at rate $\Gamma_{nrad}$. If able to, the exciton may undergo intersystem crossing to the corresponding triplet state, from which it may exhibit phosphorescent or non-radiative decay to the ground state $S_0$.

to the $S_{1\text{-}0}$ transition. This energy is usually lower than the energy of the absorbed photon due to the various exciton relaxation processes described above, as well as the lattice distortion. This loss of energy is termed the Stokes shift [29], commonly observed as the energy gap between the absorption and emission spectral peaks.

The fluorescence and phosphorescence (emission from triplet decay) together are termed the photoluminescence (PL). Within the PL spectrum, singlet and triplet emission can be distinguished due to their difference in energy. The total fluorescence decay rate is given by Equation 1.1 [30] and the fluorescence quantum yield ($\Phi$), or PL quantum efficiency (PLQE) is given by Equation 1.2 [30][29]. The PLQE describes the ratio of photons emitted to photons absorbed, expressed below as the ratio of radiative to total decay rates. The PLQE can be measured experimentally as described in Chapter 2.

$$\Gamma_T = \Gamma_{rad} + \Gamma_{nrad} \tag{1.1}$$

$$\Phi = \frac{\Gamma_{rad}}{\Gamma_{rad} + \Gamma_{nrad}} \tag{1.2}$$

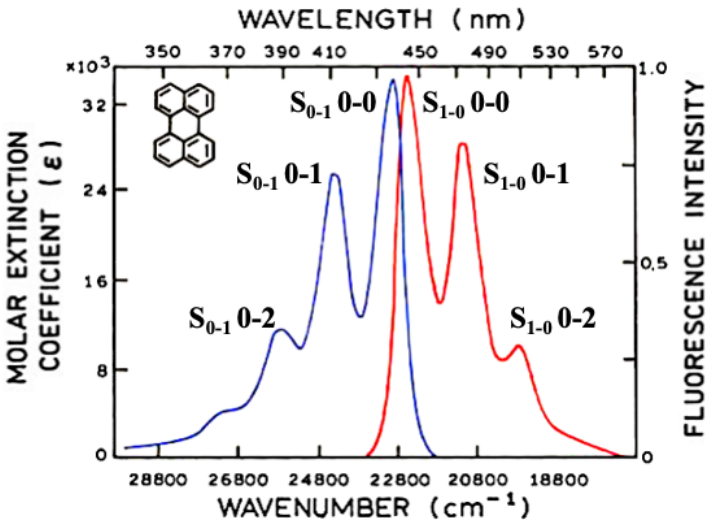



**Figure 1.6:** Absorption and Emission of perylene in benzene. The well defined molecular orbitals of the planar small molecule perylene provide a clear vibronic structure in both the absorption (blue) and emission spectra (red). The labelled molecular orbital transitions display the mirror image rule with very little Stokes shift due to limited disorder in the conjugated system. Adapted from [29].

The absorption and PL spectra can be analysed to understand the various optical transitions taking place in the material. As shown in Figure 1.6, these transitions are named according to the energy levels and vibrational states within each level. For example, $S_{1\text{-}0}$ 0-0 describes the transition between the lowest vibrational levels of $S_1$ and $S_0$, and $S_{1\text{-}0}$ 0-1 the transition between $S_1$ $0^{\text{th}}$ vibrational level to $S_0$ $1^{\text{st}}$ vibrational level. $S_{1\text{-}0}$ 0-0 has a larger $E_G$ than $S_{1\text{-}0}$ 0-1, and so in a structured PL spectrum with a wavelength or wavenumber axis it would correspond to the first PL vibronic peak, and the $S_{1\text{-}0}$ 0-1 transition to the second peak etc.

As shown in Figure 1.1, amorphous organic semiconductors contain a high degree of disorder with many independent, localised excitations, and so there may be a large range of different $E_G$ present across the molecular orbital systems. Therefore, the vibronic character of the absorption and emission spectra provides an indication of the macromolecular structure of the material such as its crystallinity and conformation. For example in a small molecule such as perylene, the energetically favoured planar conformation enables consistent conjugation across the molecule. Therefore, both its absorption and emission spectra have a strong vibronic structure that point clearly to the electronic transitions as shown in Figure 1.6.

On the other hand, a polymer such as PFO in the amorphous glassy phase has a high degree of conformational disorder similar to that of Figure 1.1, and so its absorption spectrum displays a broad, Gaussian distribution of states as shown in Figure 1.20**A**, representing a sum of all exposed states. However even if the absorption is broad, the emission may be well structured due to the exciton diffusion to lower energy states described above. The PL spectrum of polymers such as PFO is therefore indicative of the conformational variety of the polymer chains, which will be discussed in more detail below.

### 1.2.4 Molecular Considerations

While there is a great degree of conformational variety in organic molecules, they can also be conformationally limited by their structure. Steric hindrance between molecular groups can limit their conformational freedom. For example a phenyl group may be forced to rotate about its connecting bond in order to slot in amongst its neighbouring groups. Or, polymers with bulky side chains may experience steric hindrance between adjacent units, which may then be forced to rotate about their connecting bonds resulting in broken conjugation and a reduced ECL [27].

These mechanisms are sensitive to the molecular environment, which may limit a molecule's ability to adapt to its most energetically favourable conformation. The environment of the polymer or molecule can also influence the conjugation. For example, in a good solution a small molecule is free to rotate about its degrees of freedom, causing motion that may break any conjugation across its $\pi$ electron system. Alternatively a polar solvent may encourage a particular conjugation-breaking conformation due to dipole-dipole attraction between the solvent and dipoles inherent in the molecule.

In general, environmental changes which limit movement of the molecules can induce a blueshift in the PL by inhibiting the energy lowering lattice distortion and vibronic relaxtion mechanisms described above. Conversely, changes that allow the molecule to adopt greater conjugation or increase the ECL can induce a redshift due to the greater $\pi$ orbital overlap resulting in a reduced $E_{\mathrm{G}}$. It is

therefore important to consider the molecular environment when analysing any such shifts observed in PL spectra.

The conformation also informs the configuration of the molecules and how it aggregates, such as a planar conformation facilitating stacking or crystallisation. The effect of aggregation on the fluorescence depends on the exposure of the molecule's $\pi$ orbital system, which may be protected by side chains or molecular groups not involved in the conjugation. Aggregation can also impact the intensity of emission, as described in more detail below.

### 1.2.5 Quenching Mechanisms

When analysing a reduction in PL intensity it is important to consider the molecular environment. There are a number of processes that can reduce the fluorescent decay termed quenching processes, referred to in Figure 1.5 as non-radiative decay. These processes cause the excited state energy to be dissipated as heat or as a combination of heat and reduced energy emission. Regardless of whether they are radiative or non-radiative, the total number of fluorescence events from the *absorbing* fluorophore is reduced. For example, ISC mentioned above is a form of quenching, as it reduces the fluorescence decay and the resultant phosphorescence is of lower energy. Here the focus is on the quenching processes that occur when intermolecular distances become very small, or when diffusion enables interaction within excitation lifetimes, collectively termed concentration quenching [31][32][29].

Dynamic concentration quenching involves transfer mechanisms such as Förster resonance energy transfer (FRET) and Dexter (electron exchange), which describe donor-acceptor processes between 2 molecules via coulombic resonance and electron tunnelling respectively. The donor refers to the fluorophore involved in the absorption of energy and the acceptor is the quenching molecule.

In FRET the dipole coupling of the excited electron on the donor creates an oscillating dipole, which then induces a dipole in the acceptor. If these dipoles are in resonance, the acceptor molecule absorbs the energy of the donor dipole to promote an electron, while the donor electron relaxes to the ground state. The

acceptor then fluoresces or loses the energy as heat. This energy transfer does not require contact between the molecules, and occurs at a rate $\propto R^{-6}$, where $R$ is the distance between the donor and acceptor centres. The transfer is 50% efficient at 30 Å, the Förster distance, which is too large a separation for molecular orbital interaction, and so is not sterically limited [29].

Electron exchange quenching on the other hand results from much closer interactions and requires a molecular separation of the order of the van der Waals radii of the materials. In this case when the molecular orbitals of the donor and acceptor make contact, the electron in the LUMO of the donor decays to the HOMO non-radiatively, quenching the fluorescence. The rate of this exchange is $\propto e^{-R}$ and only efficient up to molecular orbital separations of 2 Å, due to the exponential drop in electron density as the distance from the nuclei is increased [29].

In solution both processes require a fairly high concentration, or a low viscosity medium to diffuse through to achieve the molecular separations needed for efficient energy transfer. A concentration of $10^{-2}$ M gives an average separation of 30 Å, and 1 M a separation of 6.5 Å[29].

Another type of concentration quenching involves the formation of complexes, a form of static concentration quenching which can happen when molecules come into close proximity due to a high concentration or when aggregation is induced by environmental factors. Intermolecular $\pi$ stacking can cause the formation of such ground-state complexes, which result in the radiative relaxation pathways of the component molecules becoming forbidden [33]. Excited state complexes such as exciplexes and excimers are described in more detail below.

### 1.2.6 Excimers

An exciplex is the complex of a molecule in the excited state and another molecule in the ground state. An excimer (a portmanteau of excited dimer) is a specific type of exciplex between 2 molecules of the same species,[19].

For excimers to form, the $\pi$ orbital systems of the molecules must be able to overlap with a very small intermolecular separation. Excimers formed from

overlapping phenyl groups commonly have a separation of $\sim$ 3.5 Å [34][35][36], though excimers have also been observed with higher separations of 20 Å [37].

In contrast to energy transfer processes such as Förster and Dexter which describe the passing of an excitation between neighbouring molecular orbital systems, excimers comprise the binding together of an excited state molecule with an molecule in the ground state to form a new, bound excited state. In this quasi-dimer state, the excitation is delocalised across the component molecules, in a state lower in energy than that of the excited monomer [27].

Excimer fluorescence is an important feature in the photophysics of a molecule as it can have a significant impact on the emission profile, intensity and decay rates [19]. This section will focus on the effect of excimers on the energy of emission, which is most relevant to the work of this thesis. The processes of excimer formation and decay processes are described in Equations 1.3 and 1.4 respectively, where the ground and excited state monomer are denoted $M$ and $M^*$. Excimer decay results in fluorescence with energy $\Delta E_{\text{exc}}$, as shown in Figure 1.7**A**.

$$M^* + M \rightarrow (MM)^* \tag{1.3}$$

$$(MM)^* \rightarrow (MM) + \Delta E_{\text{exc}} \rightarrow M + M + \Delta E_{\text{exc}} + \Delta E_{\text{R}} \tag{1.4}$$

Figure 1.7**A** describes the processes governing the formation and fluorescent decay of excimers. As shown in Equation 1.3, following absorption excimers are formed when a ground and excited state monomer, $M + M^*$, associate under close proximity, forming the excited complex $(MM)^*$, with the excitation delocalised over both monomers. This association brings them into even closer contact, and results in a drop in the enthalpy of the system, $\Delta H_{\text{M}}$, which can also be termed the excimer binding energy. From this lower energy state, the excimer undergoes fluorescent decay, after which the 2 bound monomers $(MM)$ rapidly dissociate due to coulombic repulsion, with an energy loss of $\Delta E_{\text{R}}$ (Equation 1.4). As they dissociate their separation increases and they return to the ground state energy of

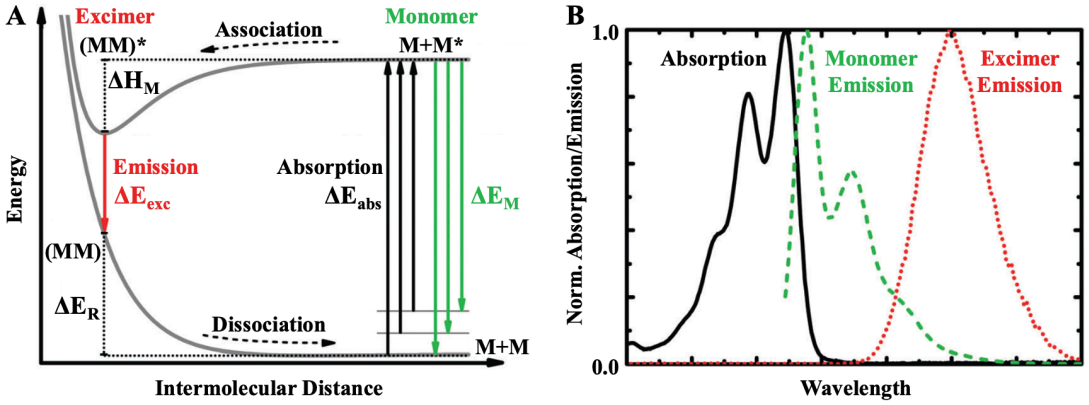



**Figure 1.7:** The formation and emission processes of excimers. **A** shows the energy levels of the transition and association from excited monomer and ground state monomer $M + M^*$ to excimer $(MM)^*$, the subsequent fluorescent decay to $(MM)$ and dissociation to $M + M$. The association causes a change in enthalpy, $\Delta H_{\mathrm{M}}$, and further energy is lost through ground state dissociation due to coulombic repulsion, $\Delta E_{\mathrm{R}}$. **B** shows the emission spectrum of the monomer and excimer. The absorption is the same for both excimer and monomer as excimer formation takes place in the excited state. The excimer has a smaller energy gap, $\Delta E_{\mathrm{exc}}$ than the monomer $\Delta E_{\mathrm{M}}$ due to the processes described in **A**. Adapted from [38].

the monomer. These association and dissociation processes result in a lower energy emission from the excimer than the monomer, as described in Equation 1.5 [27][38].

$$\Delta E_{\mathrm{Shift}} = \Delta H_{\mathrm{M}} + \Delta E_{\mathrm{R}} = \Delta E_{\mathrm{M}} - \Delta E_{\mathrm{exc}} \tag{1.5}$$

This reduced energy results in a shifted PL spectrum relative to the monomer PL, as shown in Figure 1.7**B**, and tends to be broader and more unstructured than the monomer. This is due to $\Delta E_{\mathrm{exc}}$ being dependent on the intermolecular distance between excimer molecules, as opposed to the discrete vibrational transitions of the monomer. This distance is a continuous property that will differ slightly for each excimer that contributes to the spectrum, and so the emission displays a distribution of excimer states. Therefore for excimers, while the emission of the monomer is quenched, the overall emission of the material is in contrast altered (broadened) and reduced in energy.

The larger $\Delta E_{\mathrm{Shift}}$, the more stable the excimers are considered to be. Bulky groups were added to the phenyl rings of polystyrene by Chakraborty *et al.* [19], which limited the ability of the phenyls to overlap and form strong excimers. This

resulted in the excimer emission shifting to the blue, suggesting that the association of the excimers had been less successful, lowering their overall stability.

While high concentration and aggregation is generally considered to cause fluorescence quenching as described above, recent developments have unearthed a class of materials which appear to behave to the contrary.

## 1.3 Aggregation Induced Emission

While many examples of aggregation caused quenching (ACQ) are described above, a class of materials which instead appear to show an increase in PLQE upon aggregation were discovered in 2001 by Luo *et al.* [39]. This effect was termed Aggregation Induced Emission (AIE), and since 2001 its study has become one of the fastest growing fields of the century.

An enormous range of materials tailored to induce AIE in a variety of different scenarios have been developed, resulting in many different applications including high performance OLEDs, [40][41], gas and heavy metal sensing [42][43], forensic science [44][45], morphological studies [46], in vivo bioimaging [47][48], and pH sensing [49][50].

Here the focus shall be on the mechanisms of AIE that could be induced by dispersion in a polymer matrix, and/or through interaction with a solvent. Methods of colour tuning the emission will also be discussed.

### 1.3.1 AIE Mechanism

#### Restriction of Intramolecular Motion

Depending on its structure, a molecule will have a number of degrees of freedom about its bonds. This includes rotational and vibrational freedom, as shown in Figure 1.8**A**, which contributes to the dissipation of energy in non-radiative relaxation. Upon aggregation, these degrees of freedom become limited, constrained by the proximity of their neighbours. The restriction of this intramolecular motion (RIM), is the core mechanism of AIE, and is comprised of the restriction of intramolecular rotation (RIR) and vibration (RIV). An example of RIR is given in Figure 1.8**B**,

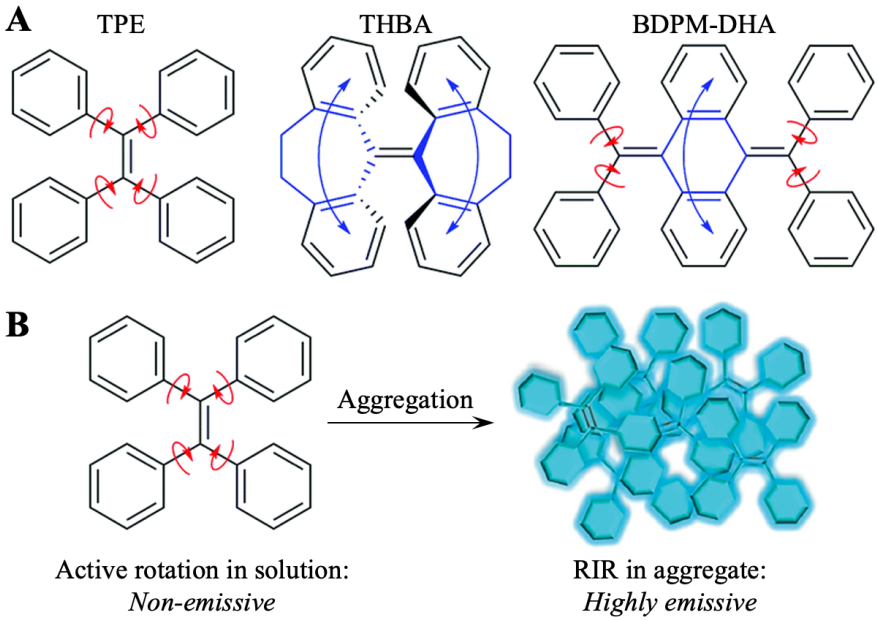



**Figure 1.8:** Restriction of Intramolecular Motion (RIM) in AIE. **A** shows examples of intramolecular rotational and vibrational motion denoted by arrows in red and blue respectively. The TPE molecule exhibits rotational motion, while THBA shows vibrational. Both types of motion can exist in a single molecule as shown in BDPM-DHA (Adapted from [51]). **B** shows the effect of aggregation on the rotational motion of TPE: In solution, TPE is free to rotate about its phenyl groups. After aggregation, the close proximity of adjacent TPE molecules limits this rotation, termed the Restriction of Intramolecular Rotation (RIR), which results in an increase in fluorescence. Adapted from [52].

where the rotation of the phenyl groups in tetraphenylethylene (TPE) is inhibited by aggregation. The molecule is therefore forced to dissipate energy by via alternative, radiative pathways, which consequently increases the PLQE.

RIM can interact with other mechanisms, such as the formation of J-Aggregates and twisted intramolecular charge transfer (TICT).

### J-Aggregate Formation

Named after E. Jelley, who first observed the phenomenon in 1937 [53], J-Aggregates are dye molecules, which when they form aggregates, experience a specific change in their absorption spectra. This change is characterized by a narrowing of the absorption band, a shift to longer wavelengths and a small Stokes shift [54]. The effect of these aggregates is not as straightforward as the RIM mechanism above. This is because molecules that exhibit J-Aggregates may be emissive or non-emissive

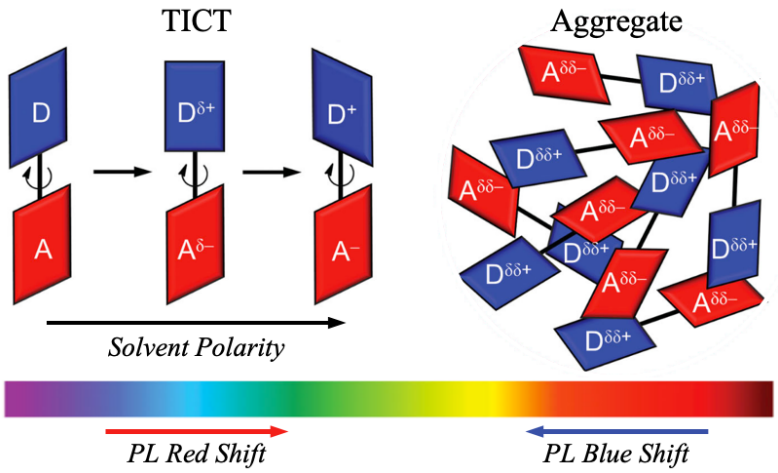



**Figure 1.9:** Effects of increasing polarity and aggregation in D-A structured molecules. In the absence of aggregation, a polar solvent induces TICT in a D-A structured molecule, resulting in an emission redshift and a drop in luminescence efficiency. Upon aggregation, RIM prevents TICT and a blueshift is observed in the PL. Adapted from [57].

prior to aggregation. Also, the formation of J-Aggregates does not always enhance emission, in fact it can also have the effect of reducing it, and in some instances cause ACQ [55]. In other words, J-Aggregates are capable of inducing AIE, but only do so in a subset of cases [56][57].

### Twisted Intramolecular Charge Transfer

AIE can also play a role in enhancing the emission of emissive molecules, sometimes termed aggregation enhanced emission (AEE). If a molecule is of a Donor-acceptor (D-A) structure, then the emission can be disrupted by intramolecular processes. D-A conjugated polymers are particularly desirable in the field of optoelectronics as it is possible to tune their HOMO and LUMO levels through intramolecular charge transfer (ICT) [58], using the dipole-dipole interactions of the donor and acceptor units. Twisted ICT (TICT) however, can have an undesirable effect on the luminescence efficiency as the TICT state is more inclined to decay non-radiatively [59][60][61].

If the D-A structured molecule is in a non-polar environment, high degrees of conjugation are achievable via planar or near planar conformations and the molecule is stable. Polar solvents, however, interact with the donor and acceptor

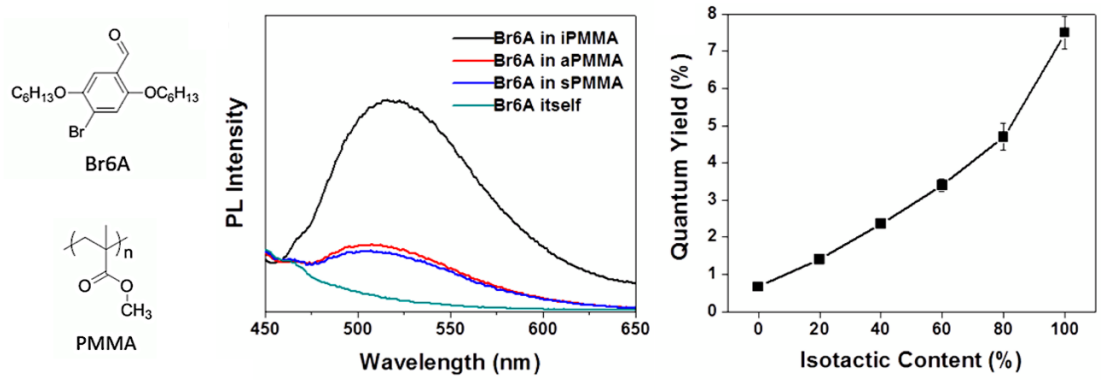



**Figure 1.10:** Polymer matrix induced RIM. The RIM mechanism boosts the PL intensity and quantum yield of p–bromobenzaldehyde when blended in PMMA. Adapted from [62]

dipoles, causing the polymer to twist and enabling TICT. The TICT state causes the HOMO-LUMO gap to decrease, increasing non-radiative decay and redshifting the luminescence as shown in Figure 1.9. This is due to the excited state dipole being further stabilised by the solvent dipole, despite the reduction in conjugation. Therefore, controlling the polarity of the environment provides the opportunity to control both the intensity and colour of emission. This can be achieved by altering the ratios of polar and non-polar solvents in the solution to control the magnitude of the TICT effect.

If aggregation is induced in systems of fluorescent molecules susceptible to TICT, AEE is believed to occur. This is due to the aggregation preventing the transition to the TICT state by invoking RIM and by shielding the D-A system from the solvent dipole. So in this case, rather than triggering emission in an otherwise non-emissive molecule, RIM is instead acting to prevent the TICT quenching process, which in turn increases the PLQE. In the aggregate, colour tuning is dependent on the degree of aggregation, which can be controlled via the solvent ratios or by varying the concentration. A blueshift is observed as the aggregation increases, for reasons described above in Section 1.2.4 [57].

If a molecule is not of the D-A structure, then AIE will occur solely through RIM processes, which remain the core mechanism of AIE [57].

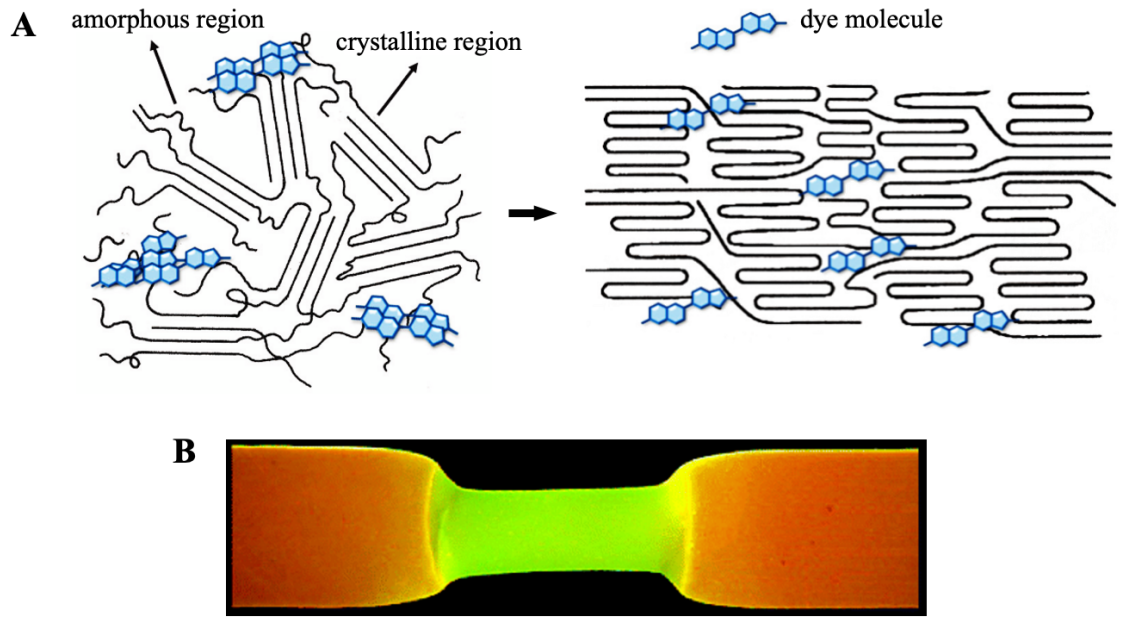



**Figure 1.11:** Mechanochromism in polymer blends. **A** shows the effect of applied mechanical force on the dispersal of dye molecule sin a polymer matrix. The reorganisation causes the aggregated dye molecules to separate. Adapted from [63]. **B** shows a blend of polyethylene and 1,4-bis($\alpha$-cyano-4-methoxystyryl)-2,5-dimethoxybenzene (BCMDB) displaying mechanochromic effects on stretching. Adapted from [64].

### 1.3.2 Polymer Matrix Dispersion

Other than from aggregation, RIM can be achieved from the molecular environment, such as from the rigidity of a polymer matrix, which has been shown to demonstrate RIM capability.

Kim *et al.* blended the phosphor p–bromobenzaldehyde, (whose phosphorescence is normally dependent on the formation of high quality crystals) with PMMA. As shown in Figure 1.10, the blended films exhibited green phosphorescence at room temperature, with the intensity of emission being dependent on the tacticity of the PMMA. Isotactic PMMA in particular provided the highest quantum yield, with solubility matching of the phosphor and polymer found to be critical to ensure good embedding in the film. The results showed a reduction in the vibrational loss of the excited triplet states, which was attributed to the glassy polymer matrix suppressing the vibration in the phosphor through RIM [57][62].

Polymer blends can also display mechanochromism, defined as effects the altering of a molecule's luminescence by way of mechanical force [65]. When a luminescent

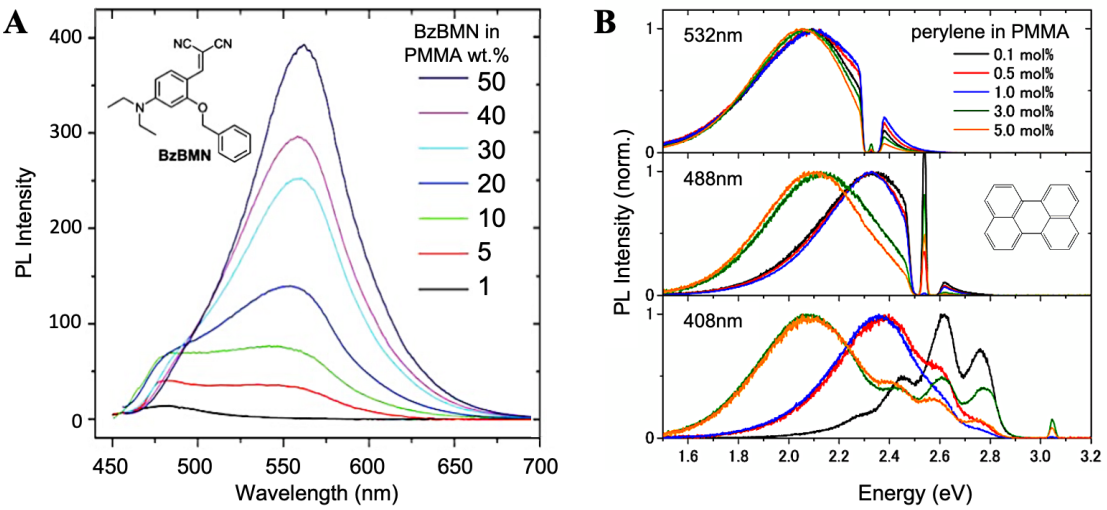



**Figure 1.12:** AIE:PMMA blends. **A** shows relative PL intensity of PMMA films doped with different concentrations of AIE molecule 2-benzyloxy-4-diethylaminobenzaldehyde (BzBMN), adapted from [69]. **B** shows the effect of varying the excitation wavelength on the PL spectra of PMMA films doped with varying concentrations of perylene. Adapted from [70].

dye is dispersed in a polymer matrix, the mechanochromic effects are dependent on the molecular conformation and interphase interactions of the dye and polymer [66]. As shown in Figure 1.11**A**, the application of force can trigger supramolecular reorganisation, which interferes with non-covalent bonds between the dye molecules. This can encourage better mixing with the polymer and change the luminescence [67].

This dispersal behaviour of AIE dye molecules in polymer films has been used by Ciardelli *et al.* to investigate film morphology and phase separation. The emission behaviour of AIE molecules differs in the monomer and aggregate state, and so it is possible to infer regions of phase separation from the PL characteristics [63].

Mechanochromic effects were also demonstrated by Crenshaw, Lowe and Weder, who dispersed the aggregachromic dye molecule 1,4-bis($\alpha$-cyano-4-methoxystyryl)-2,5-dimethoxybenzene (BCMDB) in polyethylene. On stretching the film, the luminescence experienced a blueshift from 650 nm to 500 nm, as shown in Figure 1.11**B**, due to increased dispersion of the monomers [64][68].

Another example of dispersal in PMMA films is work by Q. Dai *et al.*, who blended derivatives of 2-benzyloxy-4-diethylaminobenzaldehyde (BzBMN) into the polymer at various concentrations [69]. The resulting PL is shown in Figure 1.12**A**.

There is a clear increase in emission intensity as concentration is increased, which they attribute to RIR from increased hydrogen bonding. In low concentrations the BzBMN monomer is dominant at 475 nm, whereas at high concentrations the excimer emission at 555 nm begins to dominate.

Monomer/excimer fluorescence can also be seen in the work of K. Kizaki *et al.*, who doped perylene into PMMA films [70]. In the 408 nm excitation of Figure 1.12**B**, vibronic monomer emission is clearly dominant at low molar concentrations but quickly quenched in favour of the excimer as the concentration is increased. The wavelength of excimer emission also depends on this concentration, with higher energy, less stable excimers present in 0.5 and 1 mol%. There is also a dependence on the excitation wavelengths, with only the higher energy 408 nm managing to excite the monomer, with little to no evidence of its existence visible in the 532 nm excitation.

### 1.3.3 AIE Mechanism of TPE and HPS

TPE and hexaphenylsilole (HPS) are exemplary, fundamental AIE molecules. They have a simple molecular structure, and are commonly used as the building blocks of larger AIE macromolecules. The good solubility offered by their phenyl groups, and their potential for incorporation along a polymer backbone makes them an interesting basis for study with a view to incorporating AIE into the field of functional polymers.

Extensive studies of TPE derivatives have demonstrated its suitability as a component of various AIE systems tuned to many applications [72]. The silole core of HPS also provides an interesting electronic structure. The interaction between the silole $\sigma - \pi$ bond and then $\pi^*$ of the remaining butadiene causes the LUMO level to lower, enabling high electron mobility [75]. This electron affinity in combination with its AIE properties makes HPS applicable to many optoelectronic devices [76][77].

Both molecules are structured similarly with their core (ethylene or silole) surrounded by phenyl groups. Conjugation across the molecule may arise due to resonance between the double bonds at the molecular core and the aromatic phenyl rings. Either *trans*- or *cis*-conjugation may occur between opposite or adjacent

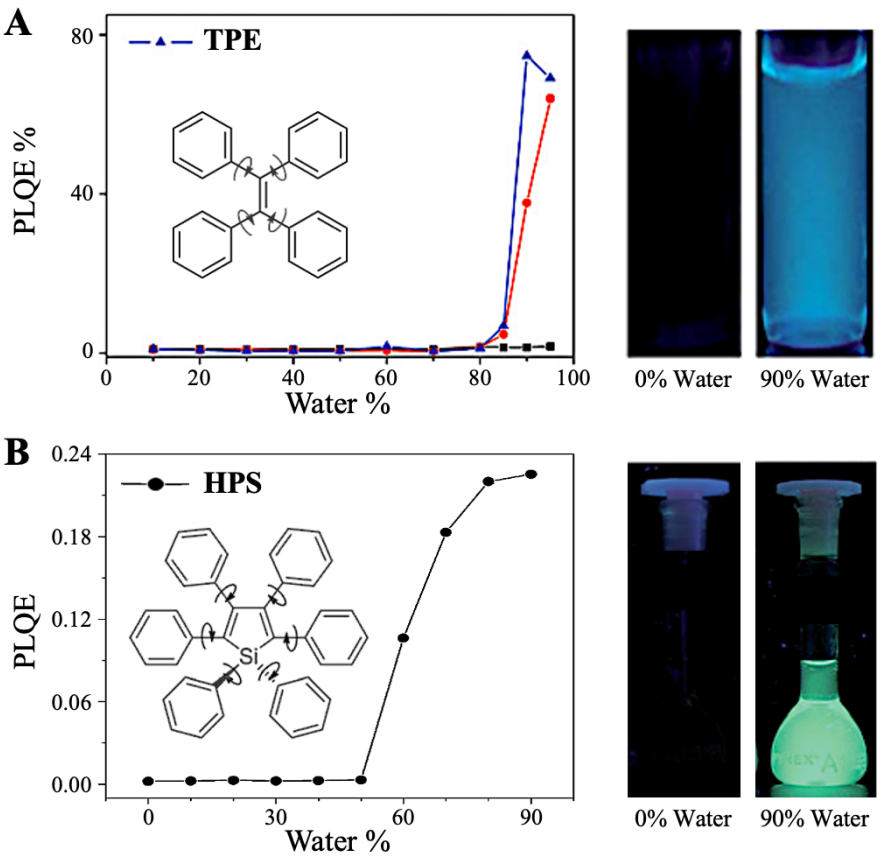



**Figure 1.13:** AIE mechanism of tetraphenylethylene (TPE) and hexaphenylsilole (HPS). Good solutions of TPE and HPS show negligible emission. As the fraction of bad solvent (water) is increased, aggregation is induced via RIR and the PLQE increases. **A** shows the AIE effect of 10 µM TPE in THF:water solutions, adapted from [71][72]. **B** shows the AIE effect of 10 µM HPS in water:acetone solutions adapted from [73][74]. The images of the solutions show the large contrast in emission achievable from RIR.

groups respectively, as shown in Figure 1.14. However the monomer is widely accepted to be non-emissive due to the free rotation of the phenyl groups breaking this conjugation and forming the basis of their AIE effect [74][78].

A common method for quantifying the AIE effect is by varying the ratio of good to bad solvents in solutions of a material [39]. In the good solution little to no aggregation is expected to occur, but as the fraction of bad solvent is increased nanoaggregates begin to form and the PLQE increases. This is shown for TPE and HPS in Figure 1.13, in which both molecules have a large increase in PLQE as the water fraction is increased. In the case of both TPE and HPS, this effect arises from the RIR of their phenyl groups.

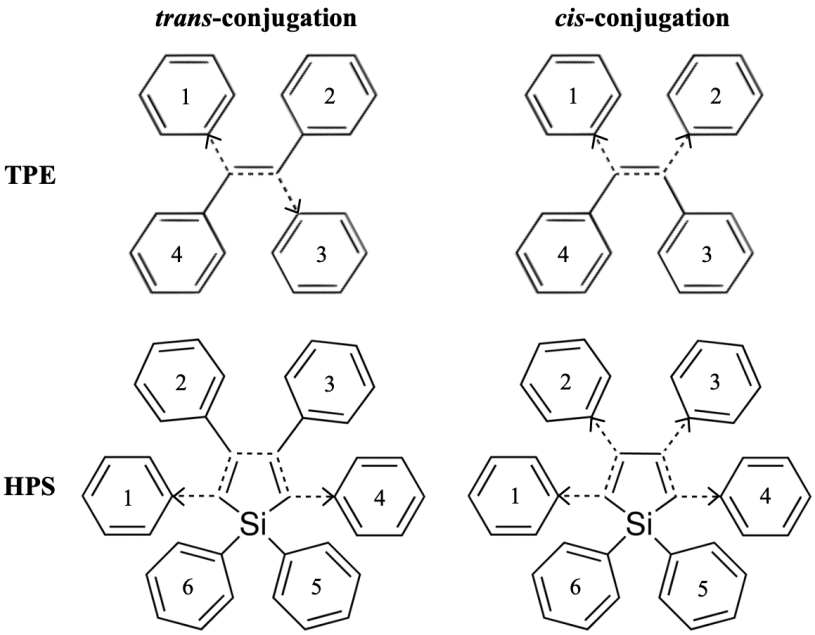



**Figure 1.14:** Potential conjugation pathways of TPE and HPS. TPE has capability for *trans*-conjugation between phenyl groups 1 and 3 or 2 and 4, and HPS between groups 1 and 4. Both have capability for *cis*-conjugation between groups 1 and 2 or 3 and 4.

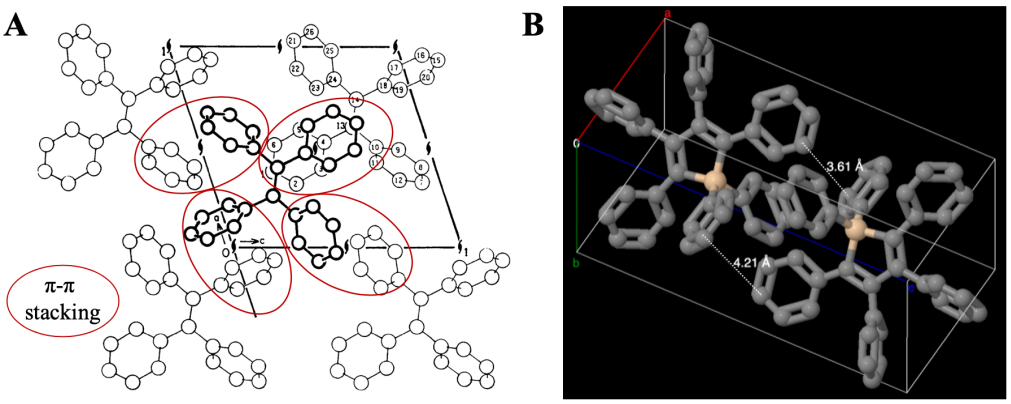



**Figure 1.15:** Crystal structures of TPE and HPS. **A** shows the crystal structure of TPE projected along the (010) plane, adapted from [79]. **B** shows the unit cell of the HPS crystal structure. Adjacent phenyl groups are separated by $3.5 - 4\,\text{Å}$. Adapted from [80].

Their AIE effect extends from solution into crystals or amorphous films. As seen from their crystal structures in Figure 1.15, for both TPE and HPS, under close packing the phenyl groups of adjacent molecules are able to interact. TPE exhibits $\pi - \pi$ stacking between phenyl groups, whereas HPS is slightly less interlocked with a T-shape interaction [81], though still with separations of only $3.5 - 4\,\text{Å}$. In non-crystalline aggregates, the rings may be able to come even closer, and/or become stacked in parallel. Both molecules also have a distinctly non-planar conformation in the aggregate, and there is little room for twisting about their phenyl groups. This suggests that any stacking is likely to be between individual phenyl groups only, and not from the planarisation of the molecule.

### 1.3.4 Previous Related Work

In previous work by the author [82], TPE was dispersed in the polymer PMMA to study the behaviour of this fundamental molecule in a polymer matrix. The aim of this work was to test whether the RIR in TPE could be achieved from interaction with the polymer matrix rather than aggregation, as seen above, and investigate what effect this may have on the emission spectra. The absorption and PL of the blended films are shown in Figure 1.16. A variety of concentrations of TPE were tested.

It was found that the absorption was proportional to the fraction of TPE, and that in addition to the broad excimer emission of the aggregate, the emission displayed a significant contribution from the monomer at low concentrations. This monomer emission, characterised by a strong vibronic structure at $350 - 400\,\text{nm}$ had not been reported in literature, and appeared to contradict the assumption that TPE was non-emissive in the non-aggregated state.

The work also found that PMMA was not the best choice of polymer for mixing with TPE due to its polarity, and that polystyrene may be better due to its matching phenyl groups. It was proposed that this change may improve the blend such that the excimer contribution to the emission may reduce.

However, it was the revelation of the monomer emission that provoked further study of the behaviour of TPE in solution prior to making changes to the blend.

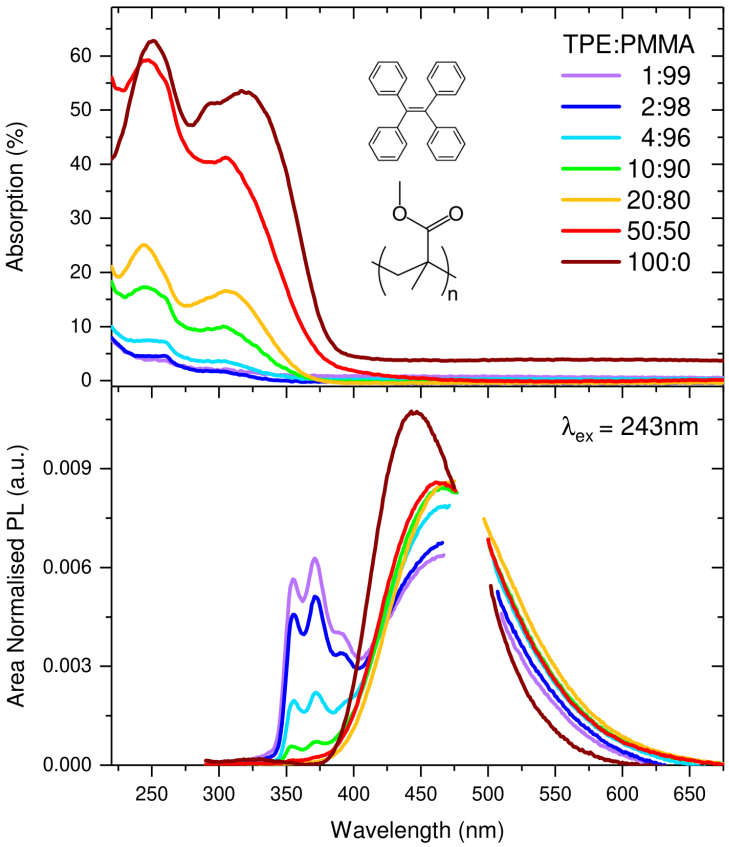



**Figure 1.16:** Absorption and emission of TPE:PMMA blend films. Adapted from [82].

In solution the monomer would be more free to absorb and emit with minimal aggregation or interaction with its solvent environment, which would enable a clearer assessment of its emission potential. This investigation is discussed in more detail below in Section 1.6.

## 1.4 Polyfluorenes

### 1.4.1 Background

Turning from small molecules to conjugated polymers, another topic of this thesis is the photophysics of fluorene polymers and oligomers. Polyfluorene (PF) is a conjugated polymer with a fluorene repeat unit, as shown in Figure 1.17**A**(i), often synthesised with alkyl side chains on the central carbon as shown in Figure 1.17**A**(ii).

There has been much interest in the application of PFs in the field of plastic electronics for a number of reasons. For optical display technologies they are

of particular interest due to their deep blue luminescence [83][84][85], as well as their high mobility [86].

PFs also have interesting morphological properties favourable to the optoelectronics study. When compared to PPV based polymers, PF is able to achieve a higher degree of planarity due to the bridging of its monomer [87][88]. Like many other conjugated polymers, weak van der Waals interaction between chains causes the resultant microstructure to be highly dependent on thermal and chemical processing conditions. This causes a number of different solid state phases to form, as shown in Figure 1.18**B** [89][90], which exhibit several distinct conformations.

### 1.4.2 Fluorenone Defects

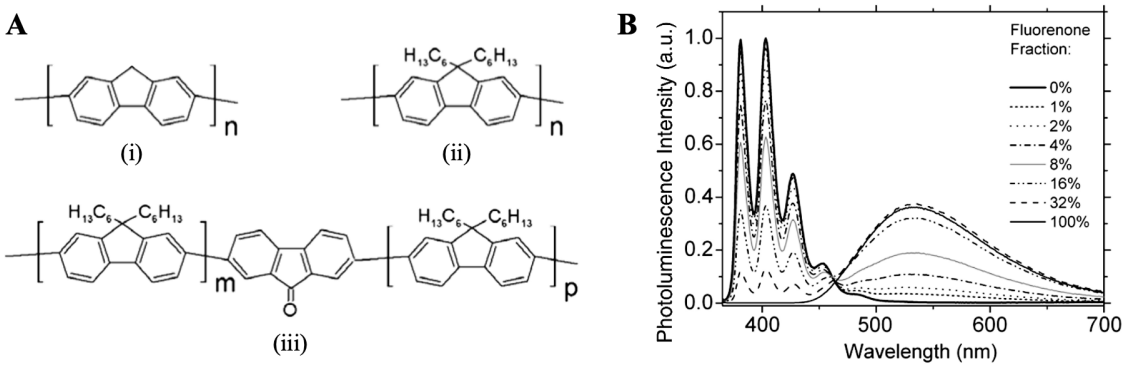



**Figure 1.17:** G-band Emission of Polyfluorene. **A** shows the structure of (i) polyfluorene (PF), (ii) poly(9,9-dihexylfluorene) (F6) and (iii) F6 with single a fluorenone moiety. **B** shows the impact of various fractions of fluorenone on the F6 PL, with the formation of excimers between fluorenone moieties causing a shift from deep blue to broad, green emission. Adapted from [91].

While PF are promising OLED materials, their utility is limited due to their tendency to form oxidation defects. These defects, known as fluorenone moieties, arise when the alkyl side chains are displaced by oxygen, forming a ketone group as shown in Figure 1.17**A**(iii). Fluorenone can form from thermal or UV exposure in air, or from the current passing through an OLED, and is characterised by a broad emission band at 535 nm termed the green or 'G-band' and a reduced PLQE [92].

The fluorenone's ketone dipole induces an attraction between the moieties, and the newly planar structure facilitates excimer formation by enabling $\pi - \pi^*$ stacking.

The formation of fluorenone excimers between polymer chains causes an energy transfer from blue to green emission, as shown in Figure 1.17**B**. The low PLQE results from the MO system of the fluorenone moiety. The $n - \pi^*$ transition from the oxygen's non-bonding lone pair is of lower energy than the $\pi - \pi^*$ of the fluorene and has a low dipole moment relative to the ground state. This can effectively trap the excited state and cause non-radiative decay [93][94][92].

It is clear from this reduced PLQE and the PL of Figure 1.17**B** that the presence of fluorenone can have a significant detrimental effect on the blue emission of polyfluorenes. Therefore much work has been done to understand the mechanism of these defects and their impact on device operation [95].

However, beyond OLED applications, the interplay between fluorenone and fluorene could be used to provide novel methods of controlling the emission. To utilise the fluorenone, much work has been undertaken in the synthesis and study of various oligomers with different proportions of fluorene (F) and fluorenone (O) units, shedding new light on their properties [96][97][98][99][100].

A key feature of F/O oligomers is their proclivity for excimer formation and consequential ACQ. This effect is more pronounced for oligmers in solution than polymers, as the smaller molecules are more free to form aggregates, driven mainly by the dipole-dipole intermolecular attraction between ketones. This aggregation tendency was found to be very strong, with solution concentrations as low as $10^{-12}$ M being required to prevent excimer emission [101]. It provides a stark contrast to oligomers comprising only fluorene units, which were found to show no excimer formation due to steric hinerance of the hexyl side chains, with little evidence of ACQ. Using this contrast to control the emission properties of F/O oligomers is the basis for Chapter 4 of this thesis, as described in Section 1.6. Another aspect of this thesis is controlling the emission of poly(9,9-dioctylfluorene), which is discussed in more detail below.

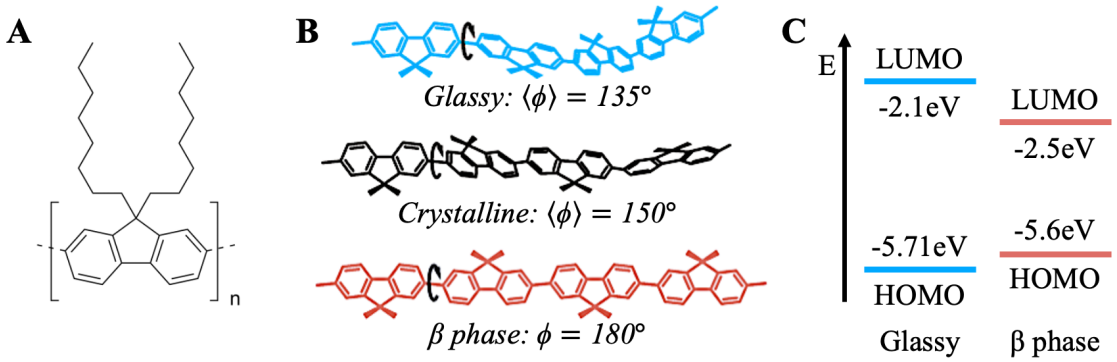



**Figure 1.18:** Phases and Energy Levels of Poly(9,9-dioctylfluorene). **A** shows the structure of the poly(9,9-dioctylfluorene) (PFO). **B** shows the structure and conformation of the glassy, crystalline and $\beta$ phases of PFO, with octyl side chains omitted for clarity (adapted from [89]). **C** shows the difference in HOMO/LUMO levels between the glassy and $\beta$ phases. (Adapted from [102][103])

### 1.4.3 Poly(9,9-dioctylfluorene) Microstructure

Poly(9,9-dioctylfluorene) is a derivative of PF, shown in Figure 1.18**A**. This derivative comprises two octyl side groups at the 9-position of the fluorene unit, and is often termed F8, but for simplicity it shall subsequently be referred to as PFO.

PFO is highly sensitive to thermal and chemical processing conditions, making it possible to study different phases and conformations without changing the chemical properties of the polymer [104]. The chemical structure of the monomer also allows for side chain substitution without affecting the electronic properties of the backbone [105]. These qualities indicate PFO's suitability for studying the effect of conformation and microstructure on photophysical and optoelectronic properties.

As shown in Figure 1.18**B**, the glassy conformation of PFO is an amorphous, spaghetti-like entanglement of chains with a large range of intermonomer torsion angles, averaging at 135 °. In the crystalline phase, torsion angles increase to an average of 150 °, increasing the planarity and conjugation of the chains. The monomers also twist to arrange the side chains on alternating sides of the backbone.

The $\beta$ phase however is the most planar, and henceforth most conjugated conformation with an intermonomer torsion angle of 180 °. Although the $\beta$ phase displays the planar conformation often favourable to crystal formation, it does not imply crystallinity. This is because the $\beta$ phase demonstrates *intra*molecular as

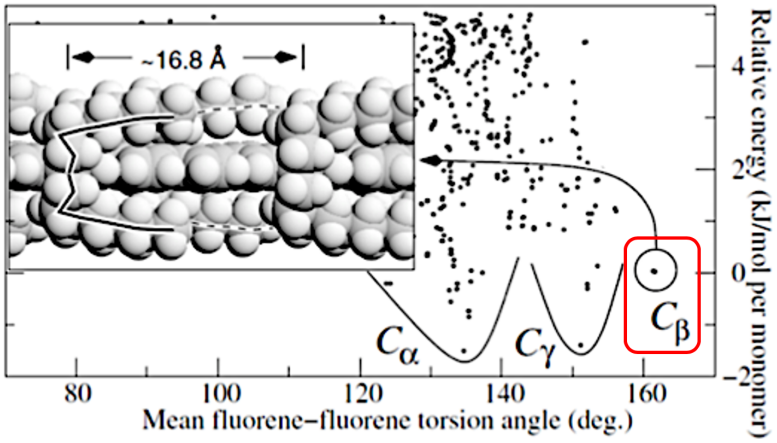



**Figure 1.19:** Mean torsion angles of PFO phases. The glassy ($C_\alpha$) and crystalline ($C_\gamma$) phases contain many possible conformations, while the $\beta$ phase is isolated at a single conformation, with an intermonomer torsion angle of $160 - 180\,°$. Adapted from [106].

opposed to *inter*molecular order. For example, the overall phase of the material may be glassy, but regions of the $\beta$ phase may exist within some chains.

From structural modelling of various conformations of PFO, carried out by Chunwaschirasiri *et al.* [106], it can be seen that the $\beta$-phase conformation stands out as an isolated state. As shown in Figure 1.19, energy was plotted against intermonomer torsion angle for the glassy ($C_\alpha$), crystalline ($C_\gamma$) and $\beta$ ($C_\beta$) phases. The glassy and crystalline conformations adopt a large range of torsion angles, whereas the $\beta$ phase conforms to a single value [106]. This highlights the $\beta$ phase as a distinct species displaying a high degree of order, making it an intriguing area of study for optoelectronic applications. Various methods to induce the $\beta$ phase and its characteristics are described below.

### 1.4.4 $\beta$ Phase Characterisation

The photophysics of the $\beta$ phase conformation is studied through analysing changes in the absorption and PL spectra.

#### Absorption

The absorption spectra of the glassy, crystalline and $\beta$ phases of PFO are shown in Figure 1.20**A**. As the polymer chains begin to adopt the $\beta$ phase, the broad

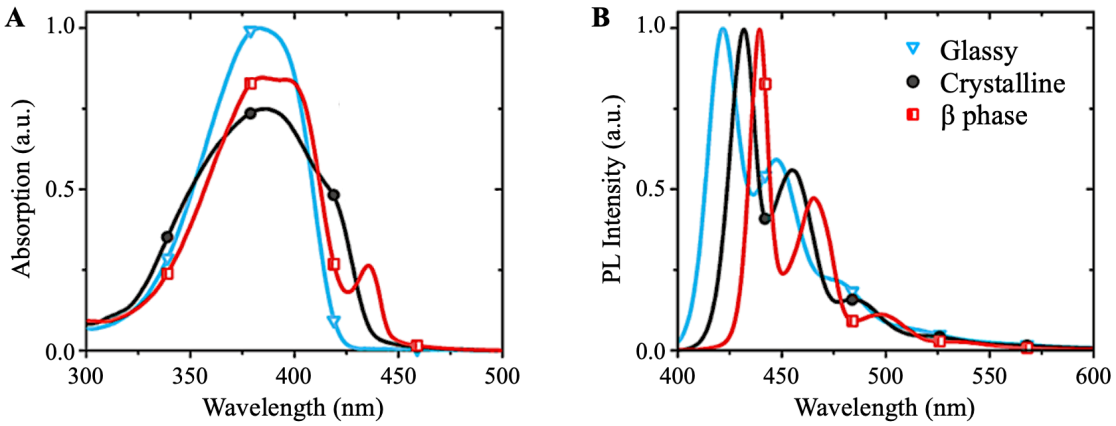



**Figure 1.20:** Normalised absorption (**A**) and emission (**B**) of PFO phases. The absorption and PL shift to the red and gain vibronic structure as the molecular disorder is reduced, with the highly conjugated $\beta$ phase displaying the lowest energy optical transitions. Adapted from [89].

glassy absorption is narrowed and redshifted, reflecting the increased order of the conformation. The $\beta$ phase absorption is characterised by a new peak at 435 nm, representing the distinct contribution from the highly conjugated $\beta$ phase chain segments. While the crystalline absorption also displays a small shoulder, the solitary nature of the $\beta$ phase peak reinforces the $\beta$ phase as a new and separate absorbing species in the film [107].

### Emission

The glassy phase displays a vibronic emission, with the $S_{1\text{-}0}$ 0-0 transition at $423-425$ nm and $S_{1\text{-}0}$ 0-1 at 450 nm. The $\beta$ phase emission is redshifted with $S_{1\text{-}0}$ 0-0 at $438-440$ nm and $S_{1\text{-}0}$ 0-1 at 466 nm. The highly resolved vibronic structure continues with small features at 499 nm and 532 nm.

If the $\beta$ phase fraction of the film is high the $S_{1\text{-}0}$ 0-0 peak may be reduced by $\beta$ phase reabsorption at 435 nm. Therefore, while a quantitative method is detailed below, the relative heights of the $S_{1\text{-}0}$ peaks can provide a rough, qualitative indication of the $\beta$ phase fraction.

While the PL of polymers is typically more structured than the absorption due to the migration of excitons to energetically favourable positions before recombination and emission [23][108], the $\beta$ phase PL is even more so due to its highly ordered and

consistent energy levels. As shown in Figure 1.18**C**, the increased conjugation along the $\beta$ phase segments causes their energy levels to move into the HOMO-LUMO gap. As a consequence of this reduction in $E_G$, the $\beta$ phase becomes a trap-like state, which further establishes its narrow vibronic structure.

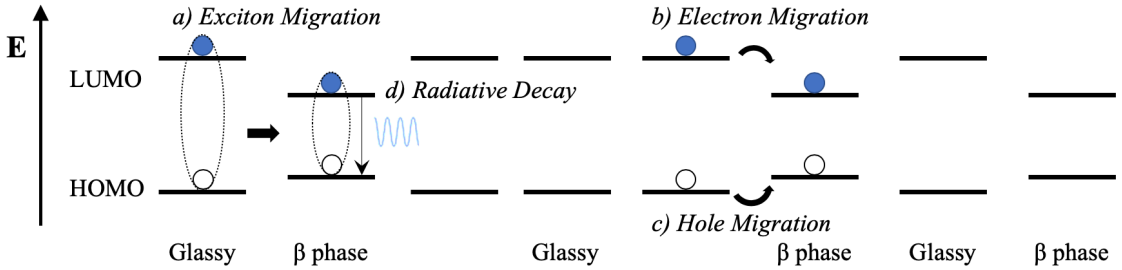



**Figure 1.21:** Exciton migration to the $\beta$ phase chain segments from adjacent glassy chains. The $\beta$ phase acts as a trap state due to its reduced HOMO-LUMO gap. This encourages exciton migration as shown in *(a)* or the migration of free charge carriers electrons and holes as shown in *(b)* and *(c)* respectively. Once in localised on the $\beta$ phase, there is an energy barrier to dissociation, and so the higher instance of radiative decay *(d)* results in a higher PLQE in the $\beta$ than glassy phase [109][110].

The migration of electrons, holes and excitons through a PFO film with some $\beta$ fraction is shown in Figure 1.21. As described above, the excitons travel to the lowest energy state before decaying. Once they reach the low energy $\beta$ phase, there is an energy barrier to leaving. This results in an increase in PLQE due to the energy barrier causing a reduction in exciton diffusion and dissociation [109][111]. Thus, even if the $\beta$ fraction is low, the $\beta$ phase segments attract and trap the excitons.

Therefore the emission from $\beta$ phase segments tends to be over representative of their true proportion in the film. This causes the $\beta$ phase to dominate the emission spectrum even at low fractions, and makes it difficult to estimate the $\beta$ fraction from the PL. Instead, decomposition of the glassy and $\beta$ absorption spectra is used to calculated the $\beta$ fraction, as detailed below.

### $\beta$ Phase Fraction

The $\beta$ phase fraction can be determined from the decomposition of the normalised absorption spectra. It can also be estimated from the PL spectra, however this is more challenging due to reasons described above. As shown in Figure 1.22,

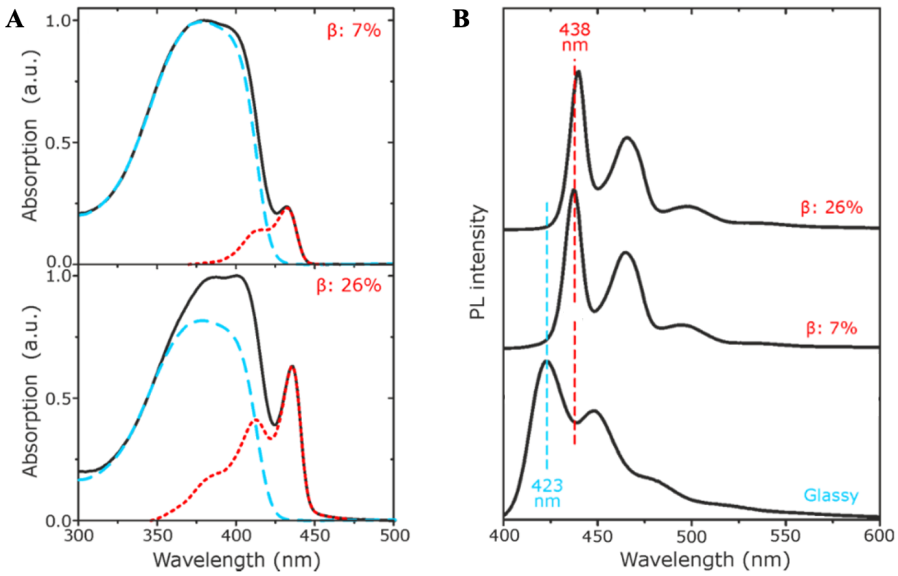



**Figure 1.22:** Determining the $\beta$ phase fraction. **A** shows the deconvolution of the glassy (blue dashed line) and $\beta$ phase (red dotted line) components of the absorption spectrum for PFO films with 7% and 26% $\beta$ phase. **B** shows the corresponding PL spectra of the films compared to the glassy PL. While the contrast in absorption between the 7% and 26% films is clear, they display little discernible difference in the PL other than a small redshift in the $S_{1\text{-}0}$ 0-0 peak. Adapted from [89].

by subtracting the absorption spectra of a neat glassy sample, the $\beta$ phase's contribution to the absorption is revealed. The fraction can then be determined from the integrals of the $\beta$ contribution ($A_\beta$), and the total spectrum ($A_{\text{total}}$), where $A_{\text{total}} = A_{\text{glassy}} + A_\beta$, as shown in Equation 1.6.

$$\%\beta = \frac{A_\beta}{A_{\text{total}}} \times 100 = \frac{A_\beta}{A_\beta + [(A_{\text{total}} - A_\beta) \times 1.08]} \times 100 \tag{1.6}$$

The 1.08 factor is required to acknowledge the difference in oscillator strength between the phases, according to Huang *et al.*, who found that $f_{\text{osc}}^{\beta} = 1.08 \times f_{\text{osc}}^{\text{glassy}}$ [89][111].

### 1.4.5 Consequences of $\beta$ Phase

The distinctly different absorption of the $\beta$ phase in PFO, shown in Figure 1.23**A**, affects the optical properties of the material, namely the refractive index, $n$. The impact of the $\beta$ phase on $n$ was studied by Stavrinou *et al.* [107], and their results are summarised below. PFO is dispersive, and so both its $n$ and attenuation

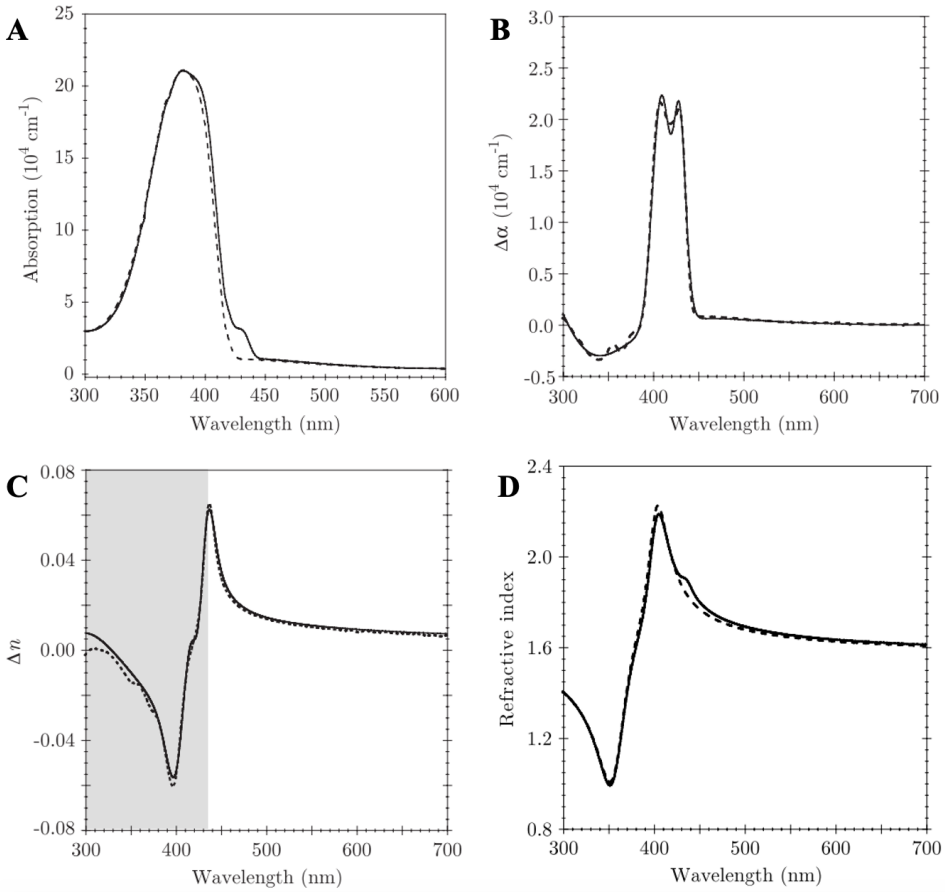



**Figure 1.23:** Kramers-Kronig analysis of PFO absorption to quantify the change in refractive index between the glassy and $\beta$ phases. **A** shows the absorption spectrum of the glassy (dashed line) and $\beta$ (solid line) phases. The dashed line of **B** shows the difference in absorption ($\Delta\alpha$) between the phases, fit to the solid line. **C** shows the difference in $\Delta n$ between the phases evaluated from Equation 1.11 using $\Delta\alpha$ of plot **B** (dashed line) and obtained analytically (solid line). **D** shows the refractive index of each phase where $n_g$ (dashed line) was measured using ellipsometry and the $n_\beta$ (solid line) was evaluated from Equation 1.10. Adapted from [107].

coefficient ($\alpha$) are wavelength dependent. $n$ and $\alpha$ are given by,

$$\alpha = 4\pi\kappa\lambda_0 \tag{1.7}$$

$$n(\omega) = ck/\omega \tag{1.8}$$

where $\kappa$ is the extinction coefficient, $k$ the wavenumber, $\lambda_0$ the vacuum wavelength, $\omega$ the angular frequency and $c$ the speed of light. The relationship of $\alpha$ and $n$ can also be expressed via the Kramers-Kronigs relations [112],

$$n(\omega) = 1 + \frac{c}{\pi} P \int_0^\infty \frac{\alpha(\omega')}{(\omega')^2 - \omega^2} d\omega' \tag{1.9}$$

where $P$ is the principal value. For a PFO sample with some $\beta$ phase fraction, the effect of the $\beta$ phase can be considered a perturbation in the glassy refractive index, $n_{\mathrm{g}}$,

$$n_{\beta} = n_{\mathrm{g}} + \Delta n \tag{1.10}$$

This assumption holds as the $\beta$ phase comprises the minority fraction of the film, and will therefore not dominate its optical properties. It is also assumed that $\Delta n$ is largest in the absorption range of PFO. Therefore, Equation 1.9 can be rewritten as,

$$\Delta n(\omega) = \frac{c}{\pi} P \int_{\omega_a}^{\omega_b} \frac{\Delta\alpha(\omega')}{(\omega')^2 - \omega^2} d\omega' \tag{1.11}$$

From Equation 1.11, $\Delta n$ was calculated using an experimentally obtained $\Delta\alpha$, as shown in Figure 1.23**B** and **C**, with $\Delta n \approx 0.065$ at the 435 nm absorption peak. At this wavelength $n \approx 1.9$, giving roughly a 3% increase in the local refractive index due to the induction of the $\beta$ phase.

The fact that $n_{\mathrm{PFO}}$ is locally controllable indicates its suitability as a material for fabricating photonic structures. This is discussed in more detail below, and a variety of potential applications which utilise this property are described.

While the change in $n$ shown above was small, it was calculated using a very slight $\beta$ phase fraction of $< 5\%$. Therefore if more substantial fractions are achieved there is scope for higher increases in $n$. Various methods to induce the $\beta$ phase, and an indication of the possible fractions achievable in each, are discussed below.

### 1.4.6 Methods for Inducing the $\beta$ Phase

The $\beta$ phase is induced through various solvent interaction methods. This interaction can occur during film processing or through the treatment of glassy films post deposition. The suitability of a solvent to induce $\beta$ is determined by PFO's solubility in the solvent.

As PFO is non-polar, the Hildebrand solubility parameter ($\delta$) can be used to identify suitable solvents for processing glassy or $\beta$ phase films. For reference, the $\delta$ and boiling point of solvents commonly used to process PFO films and induce the $\beta$ phase are shown in Table 1.1, ordered by the similarity of their $\delta$ to $\delta_{\mathrm{PFO}}$.

| Solvent/Polymer | $\delta$ $(cal^{1/2}cm^{-3/2})$ | b.p. (°C) |
|---|---|---|
| PFO | 9.1 - 9.3 | - |
| Tetrahydrofuran (THF) | 9.1 | 66 |
| Toluene | 8.9 | 110 |
| Decalin | 8.7 | 190 |
| Cyclohexane | 8.2 | 81 |
| Methanol | 7.4 | 65 |

**Table 1.1:** Hildebrand solubility parameters and boiling points of solvents used for processing PFO films and inducing the $\beta$ phase [23][109][113].

In this section, a solvent with $\delta$ different to $\delta_{\text{PFO}}$ is considered a poor solvent, whereas one where $\delta_{\text{solvent}} \approx \delta_{\text{PFO}}$ is termed a good solvent. If the difference in $\delta$ is large it is considered a non-solvent, and will not meaningfully interact with PFO.

### Spin-Coating and Thermal Cycling

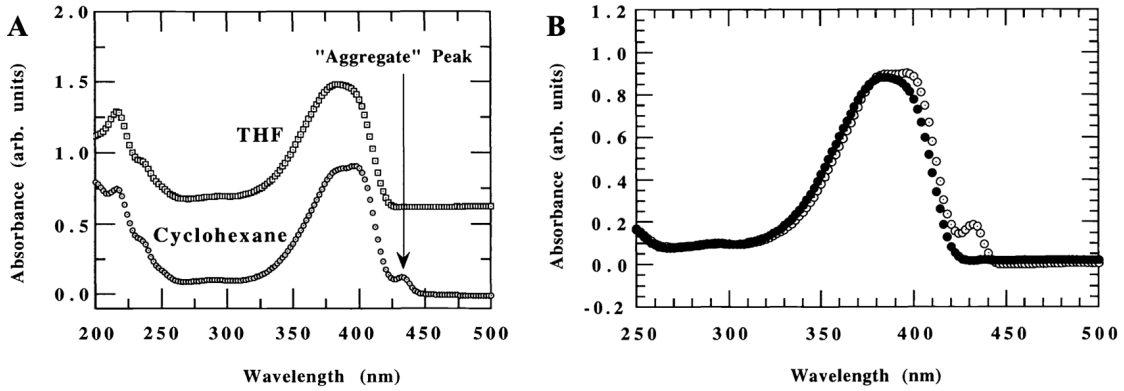



**Figure 1.24:** $\beta$ phase induction via spin-coating or thermal cycling. **A** shows the absorbance of a PFO film spun from solutions of THF and cyclohexane. The $\beta$ phase "aggregate" peak is shown in the film spun from a poor solvent for PFO ($\delta_{cyclohexane} = 8.2\,cal^{1/2}cm^{-3/2}$, $\delta_{\text{solvent}} = 9.1 - 9.3\,cal^{1/2}cm^{-3/2}$) at the characteristic 435 nm. **B** shows the result of thermal cycling a PFO film that did not initially display $\beta$ phase characteristics and was spun from a good solvent, ($\delta_{THF} = 9.1\,cal^{1/2}cm^{-3/2}$). Dark circles show the absorbance of the glassy film pre thermal cycling with no feature at 437/435 **nm**, while post thermal cycling dot-centered circles show a $\beta$ phase peak at 437/435 **nm**. Adapted from [113].

The $\beta$ phase was first identified in PFO films spun from solutions with poor solvent matching [113]. As shown in Figure 1.24**A**, spinning a film of PFO from cyclohexane solution induced $\beta$ phase in the film. Initially termed "aggregates",

$\beta$ phase regions were found to form via this method due to the poor solubility of the PFO in cyclohexane preventing good interaction between the polymer chains and solvent, thus causing the formation of aggregates. Consequently, the close packing of the PFO within aggregated regions forced the chains to adopt the $\beta$ phase conformation.

It was also found that if spun from a good solvent, $\beta$ phase can be induced in the film via thermal cycling. This involves cooling the film in liquid nitrogen and leaving it to slowly return to room temperature. As shown in Figure 1.24**B** this technique induced the $\beta$ phase in an initially glassy film, producing a $\beta$ phase fraction of $\sim$ 25% [113].

**Solvent Vapour Annealing**

Another method to induce the $\beta$ phase is by solvent vapour annealing. This involves thermally annealing a glassy PFO film in the vapour of a poor solvent. Here the PFO chains are thought to adopt the $\beta$ phase conformation in response to the swelling stress induced by this process [105][109]. As shown in Table 1.2, a variety of thermal conditions and solvent exposure times have been utilised to induce the $\beta$ phase via this method, each producing a different $\beta$ fraction.

A benefit of this technique is the opportunity to control exposure to the solvent vapour exposure, and hence the local $\beta$ phase content. This enabled Ryu *et al.*, through the use of masks, to pattern $\beta$ phase regions into glassy PFO [114]. This work demonstrated the ability to spatially control the structural properties of PFO at the molecular scale, and in doing so, highlighted PFO's potential as a functional metamaterial.

**Contact Swelling**

More direct than solvent vapour annealing is the contact swelling or 'dipping' method. As detailed in Table 1.2, Lu *et al.* found that submerging glassy PFO in a solvent mixture for a few seconds produced a $\beta$ fraction of $\sim$ 1.32% [109][110]. The mechanism behind this method is the same as for solvent vapour annealing, however the contact with liquid solvent rather than vapour solvent induces the change

| Technique | Method | Solvent(s) | Approx. $\beta$% |
|---|---|---|---|
| Thermal Cycling [113] | Cool glassy film to −196℃, slowly warm to RT | THF | ∼ 25 |
| Solvent Vapour Annealing [114][89][105][109][85] | Expose to solvent vapour for 2-12 hrs at 50 ℃ | Toluene | ∼ 23 |
| | Expose to solvent vapour for 24 hrs at 35 ℃ | Toluene | ∼ 9 |
| Contact Swelling [89][110] | Dipped in solvent/non-solvent mix | THF/Toluene and Methanol | 1.32-2.31 |
| | Solvent temporarily deposited on film | Decalin | ∼ 7 |

**Table 1.2:** Examples of techniques to induce the $\beta$ phase in PFO, and the fraction of $\beta$ phase achieved in each. (Non-exhaustive). Adapted from [89][110].

more rapidly. Additionally, as liquid constitutes a surface, this method enables the patterning of $\beta$ regions with a higher degree of contrast than solvent vapour.

Various examples of the above techniques are described in Table 1.2. It is the contact swelling method however which provides the basis for the work in this thesis. Direct solvent contact provides the opportunity to pattern regions of the $\beta$ phase into glassy PFO with a higher degree of control than the masking of solvent vapours described above. In doing so there is scope for the fabrication of photonic structures in the PFO by using the larger $n_\beta$ to produce refractive index patterns.

Such photonic structures can be formed by patterning *physical* structures onto or into a material, or patterning *optical* structures by periodically modulating a material's refractive index or its emission properties. For structures to interact with visible light, the periodicity of the pattern must be of the same order as its wavelength: $400 - 700$ nm. As described below, there are many established methods of patterning at this scale.

## 1.5 Patterning

### 1.5.1 Micro and Nanoscale Patterning Techniques

Electron-beam lithography is a nanopatterning technique that has been used to fabricate distributed feedback (DFB) lasers [115][116], however the substrate is not patterned directly. A photoresistive layer on the substrate surface is patterned by the e-beam and then etched or washed leaving the patterned elements behind. The resolution is limited only by the diffraction limit of electrons, but multiple

materials and steps are required resulting in a slow and expensive process with limited scalability [114].

Ion beam (IB) implantation is commonly used for the doping of semiconductors [117], but has also been used to pattern nanostructures [118][119][120]. An accelerated IB implants ions into a substrate, resulting in altered physical and/or chemical properties [121]. The beam can also pattern additively, depositing material on the surface of the substrate [122] or subtractively by using the beam to etch or "mill" the substrate, altering its topography [118]. IB lithography can achieve resolution of the order of tens of nanometres, however it requires large, expensive equipment including a vacuum chamber.

Beam-Pen lithography [123] is a recently developed technique, wherein an array of pyramidal, gold coated polymer tips are used to channel light to the substrate. The beam aperture is determined by how much gold is removed from the apex of the pyramid through contact with an adhesive layer. Although the technique has succeeded in achieving resolution of 400 nm and the tip array enables scalability, as with e-beam it is dependent on the substrate being coated with a photoresist to interact with the beam of light.

While these techniques describe patterning of a substrate surface, structures can also be formed within a material. The photo induced isomerisation of polymers causes the molecular configuration to flip between the cis- and trans- isomers, and has been used to pattern photoisomer gratings [124][125]. The exposure to patterns of UV light periodically altered the polymer refractive index, forming a Bragg grating.

This conformational change is similar to the contrast between glassy and $\beta$ phase PFO. To pattern the $\beta$ phase at the sub-micron scale, dip-pen nanolithography was used, as detailed below.

### 1.5.2 Dip-Pen Nanolithography

Dip-pen nanolithography (DPN) is an additive nanoscale patterning technique which utilises tips designed for atomic force microscopy (AFM) to deposit very small volumes of an ink onto a substrate [126][127], as shown in Figure 1.25. A key benefit

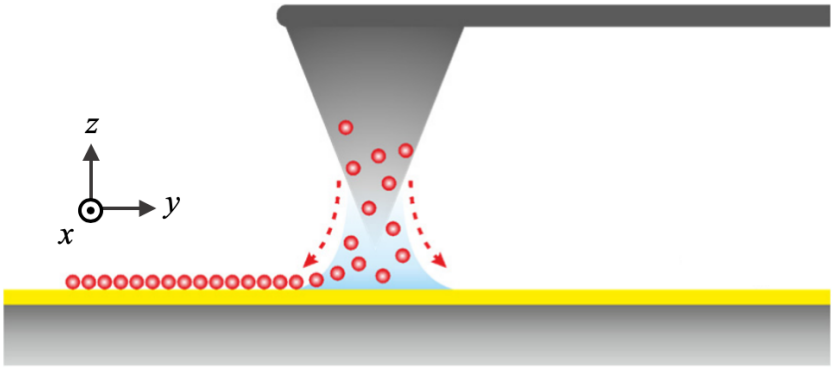



**Figure 1.25:** Dip-Pen Nanolithography: AFM tips are used to deposit small volumes of inks. At ambient conditions a water meniscus forms at the tip-substrate interface, through which the ink molecules are transported. Adapted from [89]

of DPN is the direct writing of inks onto a substrate. No masks, photoresists or intermediate steps are required, nor a vacuum or special environmental conditions. It comprises a simple, single step process akin to writing with pen and paper. Desired patterns can be imported as bitmaps, or automated in the software. The patterning can also be performed manually for testing purposes.

DPN printing of features at the micro and nano scale has led to its application in many fields such as molecular electronics and biology, where its ability to deposit single molecules has been used to construct macromolecules and further the understanding of biological processes [128][129]. The ambient conditions also lend the technique to polymers, with feature sizes of $\sim 600\,\text{nm}$ achieved when patterning conductive inks onto polymer substrates [130][131].

Although the precision of the process may slow the patterning throughput, it is also readily scalable with capacity for multi-tip printing [132][133][134].

### DPN Patterning of PFO

In a recent proof of concept study [23] Perevedentsev *et al.* demonstrated the capability of DPN for nanopatterning photonic elements in PFO, with the patterning of a $\beta$ phase dots and lines using solvent deposition to induce $\beta$ phase. Dot elements of diameter $\sim 500\,\text{nm}$, and line elements of width $\sim 400\,\text{nm}$ were achieved.

In this case, the DPN was used as a form of structural patterning in the PFO rather than additive, as the solvent evaporated following deposition. This

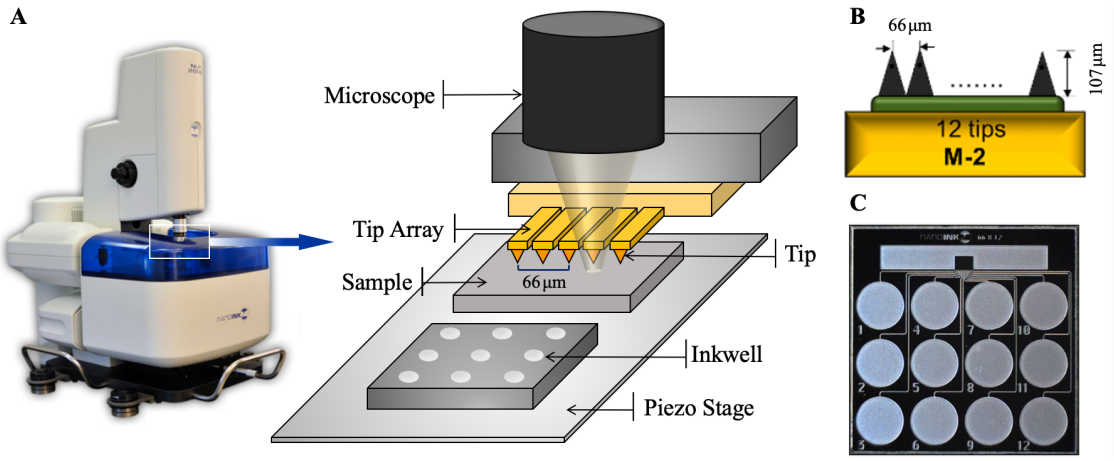



**Figure 1.26:** Dip-pen nanolithography system overview. **A** shows the desktop dip-pen Nano Lithography Platform system (NLP 2000) used to pattern the films. The sample is placed behind an inkwell chip on a piezo stage, which moves in $x$, $y$, $z$ relative to an array of tips. The patterning process is imaged through the microscope. **B** details the M-2 tips and **C** shows the inkwells and channels leading to the loading point. Adapted from [135] and [136].

study demonstrated that patterning at this length scale, when combined with the resultant change in refractive index, offers a novel route for the patterning of various optoelectronic components.

In the study presented herein, the desktop dip-pen Nano Lithography Platform system (NLP 2000) by Nanoink was used to pattern the films. As shown in Figure 1.26**A**, the sample and inkwell chip are placed on a piezo stage. The stage is capable of moving in $x$, $y$ and $z$, as well as tilting about $x$ and $y$. The tips are secured at a fixed point beneath the microscope, and brought into contact with the sample by raising the piezo stage. The tips were monitored through the microscope camera. As shown in Figure 1.26**C**, the solvent travels through the inkwell channels to the loading point, where the channels align with the the tip array. Ink was loaded onto the tips by dipping them into the inkwell, and deposited by bringing the sample into close contact with the tips, such that they are deflected by a small amount. Decalin was selected as the solvent due to its high boiling point of 190 ℃, which was found to produce a higher $\beta$ phase fraction than more volatile alternatives [23]. In this thesis the work of Perevedentsev *et al.* will be developed to utilise the multi-tip capability of DPN.

As the $\beta$ phase is induced via the contact swelling method, the feature resolution depends on the swelling of the film, the dwell time of the solvent and the surface tension of the solvent. The dwell time must be long enough to deposit sufficient solvent to induce the $\beta$ phase. A high dwell time will cause more ink to flow onto the surface, resulting in a larger feature size. A high surface tension will limit the solvent spreading, but may increase the drying time due to a higher boiling point. Understanding the interplay of these parameters to pattern nanoscale $\beta$ phase features is therefore a key part of the work presented here.

### 1.5.3 Applications of Patterned PFO or Potential Photonic Structures

Nano patterning the $\beta$ phase has shown potential for fabricating a variety of photonic devices such as 1D photonic crystals and DFB Lasers [23][82]. Here, some of the potential photonic structures possible to pattern with DPN are discussed.

#### Waveguides

$\beta$ phase nanopatterns could be used for optical confinement and waveguiding, an application for which there is much prior work to show that a small $\Delta n$ can be effective [137][138].

A $\beta$ phase line could be patterned into glassy PFO to produce a strip waveguide with a $\beta$ phase core and glassy cladding so that $n_{1(\text{core})} > n_{2(\text{cladding})}$, giving propagation along the $\beta$ phase strip, as shown in Figure 1.27**A**. Such a line was patterned by Perevedentsev *et al.* as shown in Figure 1.27**B** [23], with a width of $\sim 1\,\mu\text{m}$. A waveguide of this design would be a hybrid of the channel and ridged geometries detailed in Figure 1.27**C** due to the swelling of the PFO surface on interaction with the solvent interaction, and the depth profile of the $\beta$ fraction not being strictly determined. If the waveguide was desired to be closed to air, a second glassy film could be deposited on top, however this may be difficult to achieve as the solvents used would likely erase the $\beta$ phase patterns.

This demonstrates the potential use of $\beta$ phase waveguides in integrated optics (IO), which commonly use these waveguide geometries [139]. The DPN fabrication

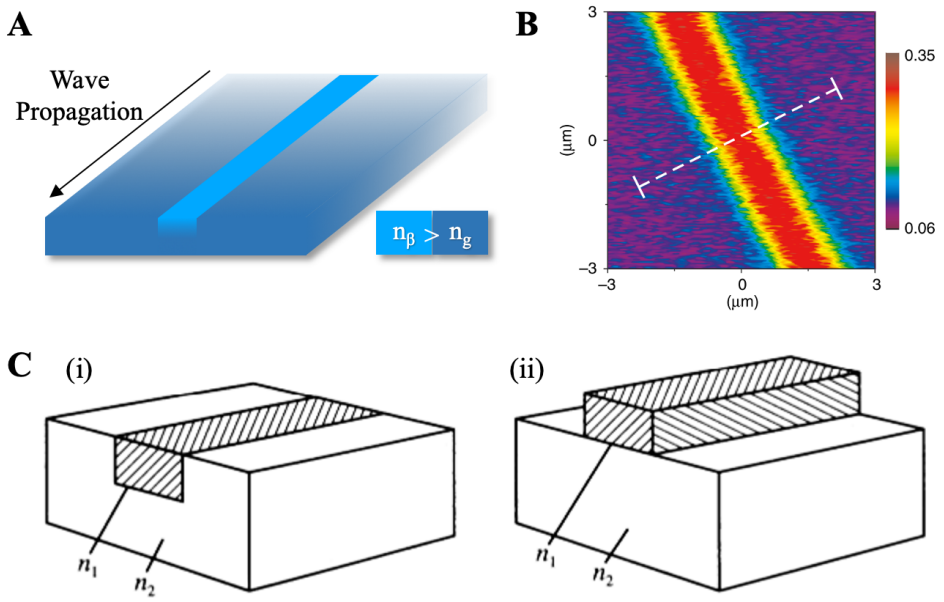



**Figure 1.27:** Potential $\beta$ phase waveguide geometries. **A** shows a possible design of strip waveguide comprising a $\beta$ phase line patterned on PFO, with the $\beta$ phase section acting as the waveguide core and the glassy phase the cladding. **B** shows a micro-PL plot of a $\beta$ phase line patterned via DPN. Adapted from [23]. **C** shows the channel (i) and ridged (ii) strip waveguide geometries. Adapted from [139].

method also lends itself well to IO as multiple waveguides could be easily drawn alongside each other on a single PFO film.

For confinement in $x$ and $y$, a single mode waveguide requires a strip width and thickness of a few times the propagating wavelength, in this case $\sim 460\,\text{nm}$ to prevent reabsorptions. To produce such a waveguide would therefore require a much thicker PFO film than the normal spin-coated thickness of ($\sim 100\,\text{nm}$). Drop casting could be a more effective fabrication method in this case, however this would likely affect the film uniformity and consequently the performance of the waveguide. Also in order to design the waveguide, the gradient of $\beta$ penetration into the film would need to be determined.

This gradient is also present at the edge of $\beta$ phase features, and so the sharp contrast between $\beta$ and glassy shown in Figure 1.27**A** is somewhat inaccurate, and the boundary would instead be gradual reduction in $\beta$% as is shown in the film cross section and the intensity gradient of 1.27**B**. This would result in a graded rather than step index waveguide, with the refractive index changing smoothly

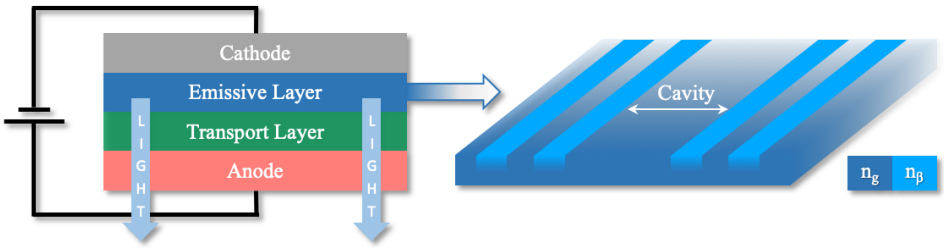



**Figure 1.28:** $\beta$ phase microcavity in a PFO OLED. Possible design of microcavity patterned within the emissive layer of an OLED. Using the $\beta$ phase to pattern a periodic refractive index structure could increase the intensity of the emission out of the device by directionally tuning the emission.

rather than sharply over the boundary [140].

DPN provides the ability to tune both the structural geometry and $\Delta n$ of the waveguide. The dimensions of the $\beta$ phase features may be controlled by controlling the spread and dwell time of the solvent, while $\Delta n$ may be tuned from controlling the $\beta$ phase fraction. DPN can also help to improve optoelectronic device performance, as detailed below.

### Microcavities

It is common for OLEDs to achieve very high internal quantum efficiencies, but internal reflection at the electrode-air interface can drastically reduce the external quantum efficiency (EQE). Optical structures have been integrated into the device architecture to help control their emission profile [141], but another option would be to pattern the optical structures directly into the emitting later. One potential optical structure is a microcavity, as shown in Figure 1.28, comprising a modulating refractive index structure with a gap in its periodicity, which forms a cavity. Depending on the cavity width and periodicity of the index modulation, wavelengths can be selected for transmission or reflection.

Microcavities are used to directionally tune the emission of a material, as shown Figure 1.29**A**, as well as as redistribute the emission to give a narrower, more intense spectral peak (Figure 1.29**B**). If incorporated into the emissive layer of a device, they could increase the EQE and reduce lateral waveguiding within the multiple layers by tuning the material to emit normally to the device surface, as shown in Figure 1.28.

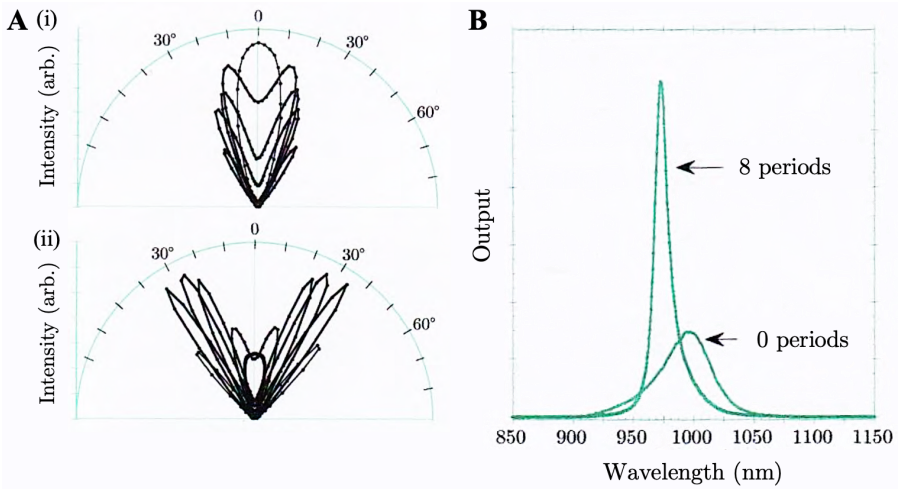



**Figure 1.29:** **A** shows the angle resolved intensity of a (i) tuned microcavity vs. (ii) detuned. **B** shows the narrowing redistribution of the emission, thus increasing the intensity about the desired wavelength as a result of increasing the number of periods bounding the cavity. Adapted from [142].

### DPN and $\beta$ Phase Considerations

There are a number of optical considerations to be taken into account when assessing the suitability of this approach to photonic structure design. The optical confinement achievable within $\beta$ phase regions must be considered, as it may be may be compromised by the gradual change in refractive index between phases. Optical confinement is a result of contrast at the $n_1$, $n_2$ boundary and so a graded index waveguide gives a grading in confinement, though can still provide effective waveguiding [143][144]. In some sense it is also desirable, as it can result in lower scattering loss than a step index, as the index profile is more similar to that of the guided wave [114]. Therefore although it is beyond the scope of this thesis, work to measure $n$ profile of the boundary would be highly beneficial to feature design.

Again outside the scope of this thesis, work to quantify the scattering loss would also be beneficial. Perevedentsev *et al.* found that DPN caused minimal roughening of the surface [23], however AFM and reflectance spectroscopy could help to ensure this going forward.

While much of the above section is beyond the scope of this thesis, its inclusion is necessary to understand the context of the work presented herein, and provide a view of the long term goals of this research.

Before further device design can take place, the DPN patterning process must be honed such that the size, periodicity and $\beta$ fraction of DPN dot arrays can be consistently reproduced, without the need to analyse each dot individually. As described above, DPN offers highly versatile tuning capabilities. Gaining full control over the patterning parameters and understanding more how they impact the $\beta$ phase fraction would result in a uniquely flexible method for fabricating photonic structures.

## 1.6 In This Thesis

This thesis comprises studies corresponding to the themes of the previous sections: AIE, fluorenes and patterning. To deconstruct the thesis title, the photonic structure aspect refers to the patterning of $\beta$ phase refractive index patterns detailed above. While the AIE and fluorenone materials are not subject to patterning, exploratory studies in new methods to control their emission properties at the molecular scale are presented.

### 1.6.1 Monomer Emission and RIR Mechanism of Fundamental AIE Molecules

In the following chapter, the emission properties of fundamental AIE molecules are investigated. Previous work showed a significant contribution from the TPE monomer when it was dispersed in PMMA. Here, this monomer emission and the RIR hypothesis described above shall be probed further by studying the materials in solution, where they are free to move and their aggregation state can be actively controlled. To do so, good solutions (where monomers are likely found in abundance) of TPE and a second fundamental AIE molecule HPS are studied, and compared to solutions with varying degrees of aggregation. To achieve a spectrum of aggregation states, the solvent composition of the solutions is varied, with the proportion of a non-solvent being increased to trigger aggregation.

This study aims to understand more about the AIE process through the lens of the emission spectrum, rather than just the contrast in PLQE. In particular,

the origin of the AIE effect and how the balance of monomer vs. aggregated emission can be controlled is discussed.

### 1.6.2 Excimer Formation in Fluorene-Fluorenone Oligomers

The method for controlling aggregation in the AIE solutions is then applied to solutions of F/O oligomers. In this case, the non-solvent used to induce aggregation also serves to increase the polarity of the solution. This study therefore aims to screen the ketone dipole responsible for the prolific excimer formation observed in good solutions of the oligomers, effectively switching it off without reducing the solution concentration. In conjunction, as the proportion of the polar non-solvent is increased further, the study investigates whether it is possible to reactivate the excimer formation through controlled aggregation (as opposed to dipole-dipole attraction).

Oligomers containing O units are compared to those with only F as a control, as oligomers comprised of F alone were not expected to form excimers due to their conjugated systems being shielded by bulky side groups. In doing so, this study aims to test whether by controlling the formation of fluorenone excimers, a new method for tuning the emission spectrum and PLQE can be determined.

### 1.6.3 Dip-Pen Patterning of PFO

From oligofluorenes the focus then shifts to polyfluorenes, specifically patterning the $\beta$ phase in PFO at a length scale suitable for photonic device fabrication. As described above, DPN is utilised to induce the $\beta$ phase at the nanoscale via the contact swelling method. Leading on from the work of Perevedentsev *et al.*, DPN with multiple tips is trialled, with a view to creating $\beta$ phase dot arrays in glassy PFO. This study aims to discuss the scalability reliability of this technique with a multi-tip array and discusses key considerations for upscaling the process.

Although lines comprise the majority of the structural elements shown above, the DPN study was conducted with dot patterning. This was due to the relative ease of such pattern types being considered a good place to start, and their lower dimensionality being more straightforward for controlling the printing parameters.

To support this study, a micro-PL system was developed for analysing the DPN patterns. The design and optimisation of this set-up is detailed prior to the patterning study, in Chapter 5.

### 1.6.4 Summary

To summarise, while the materials differ between the studies, consistent throughout is the concept of controlling the conformation or aggregation state to regulate the emission properties of organic semiconductors. Whether this be in solution or thin films, each study aims to map out the parameter space of such control, and identify the potential of the methods for use in organic electronic device applications.

# 2 Materials and Methods

## Contents


**2.1 Materials . . . . . 51**
**2.2 Sample Fabrication . . . . . 51**
2.2.1 Solutions . . . . . 54
2.2.2 Thin Films . . . . . 54
**2.3 Optical Methods . . . . . 55**
2.3.1 UV-Vis Spectroscopy . . . . . 55
2.3.2 Photoluminescence Spectroscopy . . . . . 58
2.3.3 Photoluminescence Quantum Efficiency . . . . . 61


## 2.1 Materials

The materials used throughout this thesis are detailed in Table 2.1, and their structures shown in Figure 2.1. Similarly the solvents used are shown in Table 2.2 and Figure 2.2.

## 2.2 Sample Fabrication

Processes specific to a chapter such as solution composition and any thermal treatments applied to the films are detailed in the relevant chapter. Common processes such as cleaning routines and spin-coating parameters are detailed below.

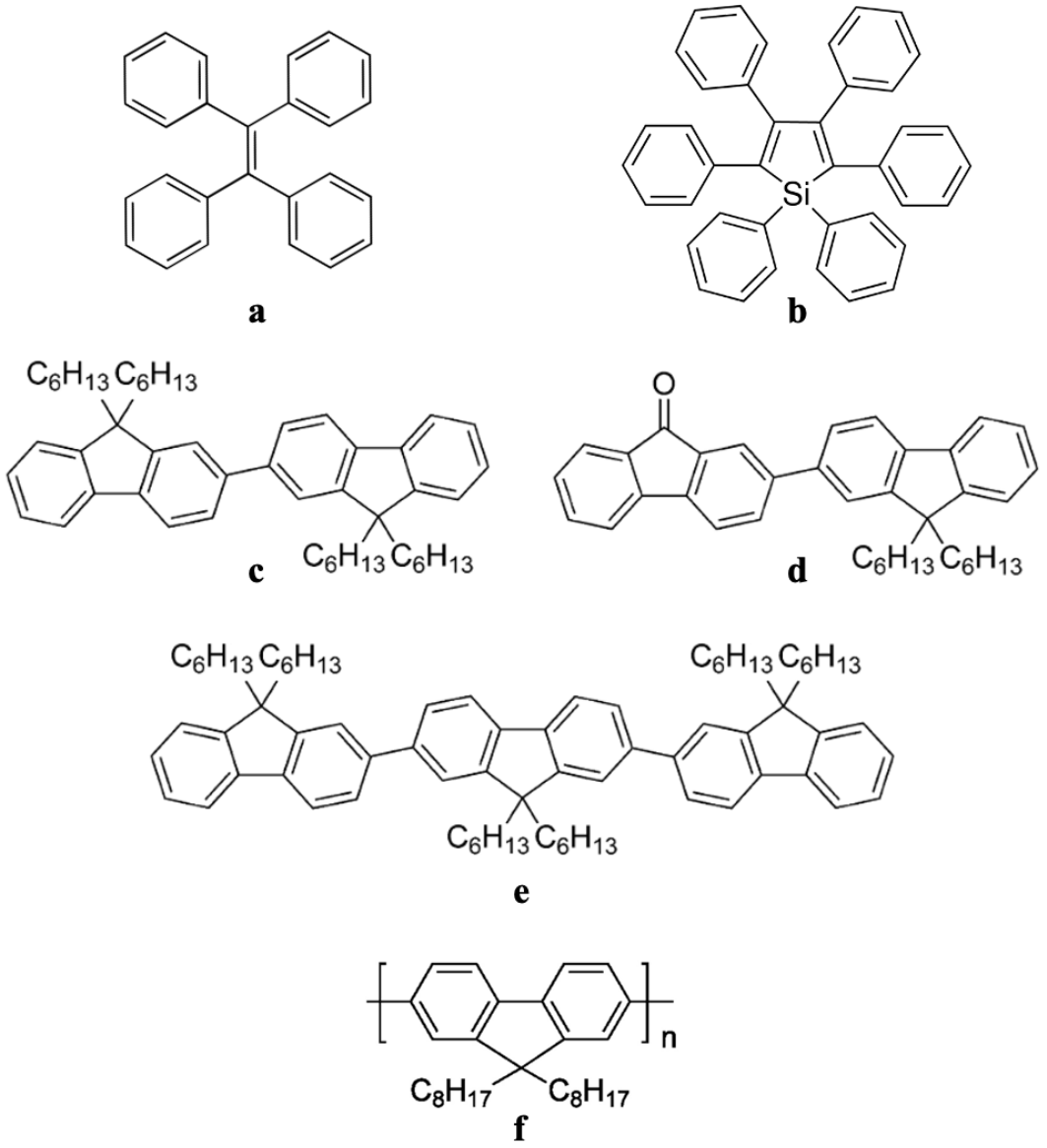



**Figure 2.1:** The chemical structures of the materials used in this thesis. **a** is TPE, **b** HPS, **c** FF, **d** FO, **e** FFF, and **f** PFO.

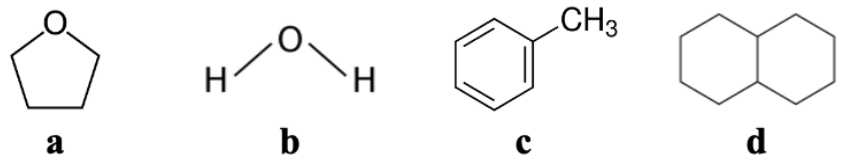



**Figure 2.2:** The chemical structures of the solvents used in this thesis. **a** is THF, **b** water, **c** Toluene, **d** Decalin

| Chapter | Name | Full Name | Source | Structure (Figure 2.1) |
|---|---|---|---|---|
| 3 | TPE | 1,1,2,2- Tetraphenylethylene | Sigma-Aldrich: T26204 | **a** |
| | HPS | 1,1,2,3,4,5-Hexaphenyl-1H-silole | Sigma-Aldrich: 797294 | **b** |
| 4 | FF | 2,2'-Bi(9,9-dihexylfluorene) | Dr Khai-Leok Chan, Prof Andrew Holmes | **c** |
| | FO | 2-(9,9-Dihexyl-9H-fluoren-7-yl)-9H-fluoren-9-one | „ | **d** |
| | FFF | 9,9,9',9',9",9"-Hexahexyl-9H,9'H,9"H-2,2':7',2"-terfluorene | „ | **e** |
| 6 | PFO | poly(9,9-dioctylfluorene) | 1-Material Inc. PFO/PL0388 CAS: 123864-00-6 | **f** |

**Table 2.1:** Details of the materials used throughout this thesis.

| Chapter(s) | Name | Full Name | Source | Structure (Figure 2.2) |
|---|---|---|---|---|
| 3 and 4 | THF | Tetrahyrdofuran | Sigma-Aldrich: 401757 Anhydrous 99.9% | **a** |
| | water | Deionised | Sigma-Aldrich: 38796 | **b** |
| 6 | Toluene | - | Sigma-Aldrich: 244511 Anhydrous 99.8% | **c** |
| | Decalin | Decahydronaphthalene, mixture of *cis* + *trans* | Sigma-Aldrich: 294772 Anhydrous 99% | **d** |

**Table 2.2:** Details of the solvents used throughout this thesis.

### 2.2.1 Solutions

Each sample solution was made up of various starter solutions which were then combined into Hellma absorption cuvettes, made of Suprasil quartz - a high purity synthetic fused silica (Sigma-Aldrich: Z800015). The cuvettes had a spectral range of $200-2500$ nm, volume of 350 µl and optical path length of 1 mm. For each sample cuvette, a second cuvette was made with the matching ratios of pure solvent.

Due to their small volume, the cuvettes required a very thorough cleaning process: (To prevent scratches no needles were used.)

1. All cuvettes filled with THF and submerged with their caps in a large beaker of THF.
2. Beaker sonicated for 20 mins.
3. Beaker drained and solvent gently removed from the cuvettes by tapping down into paper.
4. Repeat steps 1-3 with toluene.
5. Repeat steps 1-3 with 1,2-DCB.
6. Caps and cuvettes left pointing up in a clean beaker to dry overnight
7. Outside of cuvettes polished with IPA

### 2.2.2 Thin Films

To produce the glassy PFO thin films studied in Chapter 6, solutions of PFO were spin-coated onto Spectrosil fused silica substrates with dimensions $12 \times 12 \times 2$ mm. The substrates were cleaned and spin-coated according to the following routine:

1. Substrates submerged in a solution of detergent in deioinised water at a ratio of 1:3.
2. Beaker sonicated for 40 mins.

| Vol. (µl) | Acceleration | rpm | Duration (min) |
|---|---|---|---|
| 120 | 500 | 2000 | 1 |

**Table 2.3:** Spin-coating parameters for PFO thin films.

3. Beaker drained and substrates rinsed in fresh deionised water and dried using blasts of nitrogen gas

4. When dry, substrates subjected to oxygen plasma treatment at 100 W for 3 mins to increase their surface energy.

5. Substrates spin-coated with PFO solution according to Table 2.3 within 15 mins of plasma treatment

6. Uncoated side of each substrate carefully dragged along a wipe soaked in toluene to remove any solution on the underside of the quartz

7. Films left to dry in the fume hood for 15 mins

## 2.3 Optical Methods

### 2.3.1 UV-Vis Spectroscopy

#### Overview and Theory

UV-Vis spectroscopy was used to determine the absorption of the materials in the UV and visible range. As shown in Figure 2.3, the spectrophotometer records the change in intensity of light as it passes through the sample. Using Equation 2.1, where $I_0$ is the intensity of light from the source and $I$ the intensity transmitted through the sample, the transmission ($T$) of the sample is determined across the spectral range. From $T$, the absorbance ($A$) or absorption ($A_{\%}$) can be calculated. The relationship between $T$ and $A$ is also shown in Equation 2.1.

$$T = \frac{I}{I_0} = 10^{-A} \tag{2.1}$$

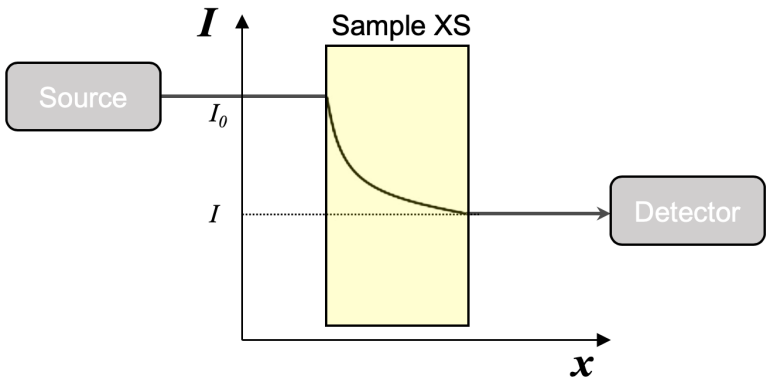



**Figure 2.3:** Intensity Attenuation. As light passes through the absorbing sample, its initial intensity, $I_0$ is attenuated to intensity $I$, due to absorption. The transmission is determined by Equation 2.1.

To calculate the absorbance, the Beer-Lambert-Bouguer Law [145][146][147] states that the attenuation through a material is proportional to the concentration of the material, and defines absorbance of a sample relative to air as,

$$A = -\log_{10}\left(\frac{T_{\text{sample}}\%}{100}\right) \tag{2.2}$$

However as described above, the material of interest is either spin-coated onto a fused silica substrate, or dissolved in solvent and encapsulated within a fused silica cuvette. Both the fused silica and solvent may contribute to the attenuation, therefore the absorbance of the *material* is given by,

$$A = -\log_{10}\left(\frac{T_{\text{sample}}}{T_{\text{ref}}}\right) = \varepsilon \times c \times l \tag{2.3}$$

Where $T_{\text{sample}}$ is the transmission of the sample, $T_{\text{ref}}$ is the transmission of the blank substrate or cuvette containing only solvent, $\varepsilon$ is the molar attenuation coefficient with units (L mol$^{-1}$ cm$^{-1}$), $c$ is the molar concentration (mol L$^{-1}$), and $l$ is the pathlength of the beam through the sample (cm). Compared to Equation 2.2, Equation 2.3 gives the absorbance due to the material of interest, rather than the sample as a whole.

Although commonly used, Equation 2.3 does not account for the effects of reflection or scattering, which may incorrectly be attributed to absorption. Therefore

if possible to do so, it is desirable to measure the reflection ($R$) in addition to $T$ and instead calculate the absorption ($A_{\%}$) according to Equation 2.4.

$$A_{\%} = 100 - T_{\%} - R_{\%} \tag{2.4}$$

Where $R_{\%}$ is the total proportion of light reflected comprising specular and diffuse reflection ($R_{S\%} + R_{D\%}$). $A_{\%}$ is thus defined as the proportion of light that is neither transmitted nor reflected nor scattered.

An example of both $A$ and $A_{\%}$ for a thin film of PFO is shown in Figure 2.4.

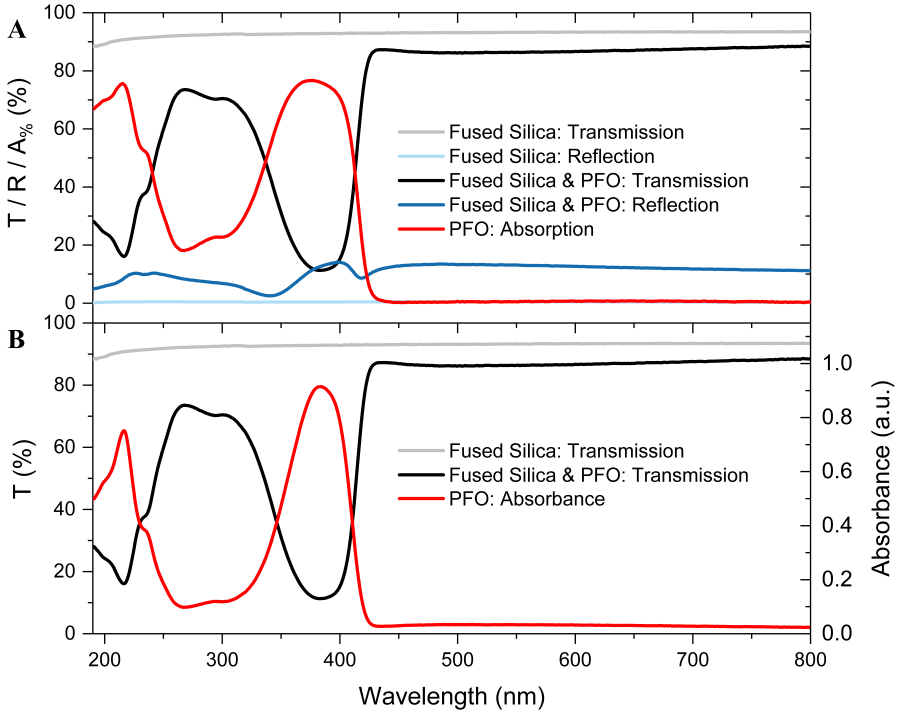



**Figure 2.4:** Absorption and Absorbance of PFO. **A** shows the transmission ($T_{\%}$) and specular reflection ($R_{S\%}$) of the fused silica substrate with and without the PFO film, and the absorption ($A_{\%}$) of PFO calculated from Equation 2.5. **B** shows the ($T_{\%}$) of the fused silica with and without the PFO film and the absorbance ($A$) calculated from Equation 2.3.

### Experimental Set-Up

The absorption spectra were recorded with a Perkin-Elmer Lambda 1050 UV/Vis spectrophotometer. For each sample $T$ was measured from $800 - 190\,\text{nm}$ at increments of $1\,\text{nm}$.

The reflection was not recorded for cuvettes, and so $A$ is shown for solution samples. For thin films, $R_{S\%}$ was measured at an incident angle of 6°. However, the integrating sphere attachment required to measure $R_{D\%}$ was not available at the time of measurement and so Equation 2.4 was adapted and $A_{\%}$ calculated as shown in Equation 2.5.

$$A_{\%} = 100 - T_{\%} - R_{S\%} \tag{2.5}$$

### Normalisation

The absorption and absorbance spectra are shown raw and peak normalised (PN). Depending on the material, they were either normalised at the maximum absorption peak, or at the wavelength chosen for excitation.

## 2.3.2 Photoluminescence Spectroscopy

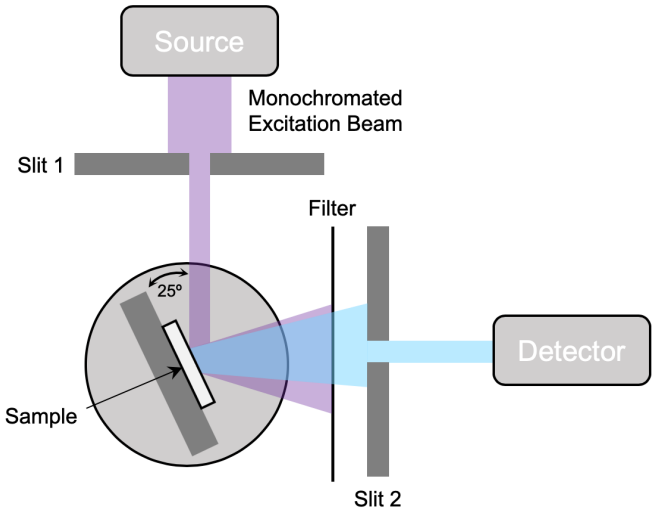



**Figure 2.5:** PL Spectroscopy. The sample was arranged so the excitation beam hit the sample at 65 ° to the normal. For some excitation wavelengths a filter was placed in the collection path to prevent disruption of the emission spectrum.

### Overview

The emission of the materials was analysed using photoluminescence (PL) spectroscopy. As shown in Figure 2.5, PL spectroscopy involves exciting samples at

their peak absorption wavelength, determined from their UV-Vis spectrum, and collecting the resultant emission. The emission is directed to a diffraction grating which disperses the beam, enabling the spectrometer to output counts-per-second of photons for each wavelength.

**Experimental Set-Up**

The PL spectra were recorded with a Horiba Scientific Fluoromax-4 Spectrophotometer (Fluoromax). As shown in Figure 2.5, the incident angle of excitation was fixed at 65 ° to the sample normal, which had previously been found to minimise re-absorption of the emission [148]. The excitation and collection beams were controlled with slits 1 and 2 respectively and the spectra recorded with an increment of 1 nm. Slit widths were chosen such that the count rate of the emission did not exceed $2 \times 10^6$ to prevent saturation of the detector. A single slit width was chosen for both the excitation and collection beams. The slit width, excitation wavelength and wavelength range are detailed within the relevant chapters.

**Correction and Normalisation**

The recorded PL signal S1 must be corrected and tempered with the signal of the corrected reference beam $R1_C$ (recorded at the same time as S1), resulting in a corrected PL spectrum of the form $S1_C/R1_C$.

As detailed in Figure 2.6, to find $S1_C$, the S1 signal was first baselined by subtracting a value found by averaging over a 5 nm range in a flat region of the spectrum. Then, the wavelength response correction factor of the detector was applied, as determined from the internal Fluoromax correction. The excitation peaks and higher order resonances were also removed.

The PL was then plotted as $S1_C/R1_C$. In the context of comparing multiple PL spectra, they are referred to as the *Rel. PL*. This terminology signals that the spectra have all been recorded at the same slit width, therefore providing a rough indication of how the PL intensity varies between the samples.

Due to the breadth and changing nature of the PL spectra shown within, area normalisation (AN) rather than PN was employed. This was chosen due to

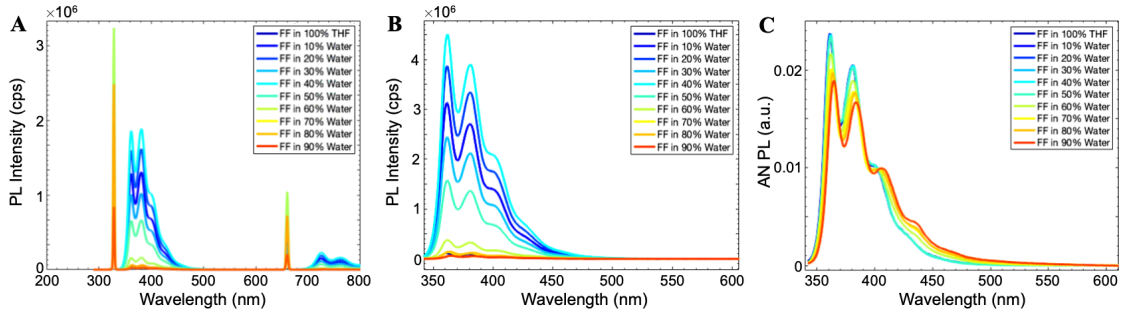



**Figure 2.6:** Example of PL correction for a set of samples. **A** shows the raw spectra S1 with excitation and emission resonances visible at long wavelengths. **B** shows the spectra baselined and corrected for the detector wavelength response, then divided by the reference signal $R1_C$ and the resonances removed. This $S1_C/R1_C$ signal constitutes the Rel. PL as all spectra were recorded at the same slit width. **C** shows the spectra following area normalisation, allowing for clear comparison of each spectral profile. This normalisation was carried out using spectra recorded with the largest non-saturating slit width for each sample to maximise the signal to noise ratio.

the ability of AN to clearly display shifts in the emission distribution between various emitting species.

To area normalise, the spectra were scaled by the integral of their emission range, allowing the comparison of PL profiles without pinning the spectra at a particular peak or inflection point. To ensure a strong signal and good spectral resolution, the slit widths for spectra intended for AN were chosen such that the S1 signal approached the $2 \times 10^6$ saturation limit.

Therefore for each set of samples, spectra were recorded at the maximum non-saturating slit width of each sample, and also at a slit width equal across the set for the Rel. PL. This Rel. slit width was chosen from the smallest 'maximum' slit width in the set. The Rel. and AN PL spectra are shown for each sample.

### Filters

In the case of an excitation wavelength being sufficiently low such that its resonance might interrupt the emission spectra, a filter was placed in the collection path to remove the excitation contribution. 370 nm or 400 nm longpass filters were used depending on the excitation wavelength. The filters were cleaned with IPA, acetone and ethanol to remove any absorbing or scattering matter.

For instances in which the filtered range may include a wavelength region of interest, the PL was recorded both with and without the filter. Then, following correction, the unfiltered *low* wavelength range was extracted and combined with the filtered *high* wavelength range to produce a full, uninterrupted spectrum.

### 2.3.3 Photoluminescence Quantum Efficiency

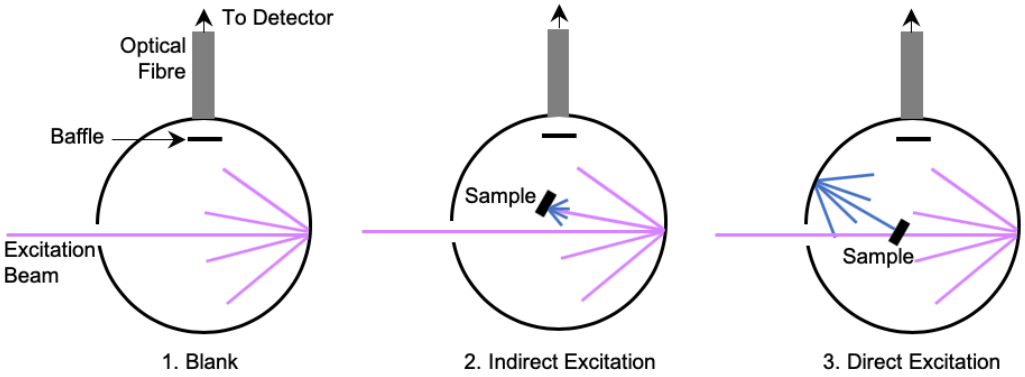



**Figure 2.7:** PLQE measurements. The 3 integrating sphere spectra required to calculate the PLQE using the De Mello method.

#### Overview

While the Rel. PL gives a rough comparison of the emission between samples, to gain a true understanding of emission efficiency the PLQE ($\Phi$) must be determined. This is because the PL measurement fails to capture all of the emission due to scattering and Lambert's cosine law [149]. The solution PLQE was determined via the de Mello method [150]. As shown in Figure 2.7, the de Mello method requires three spectra to be recorded to calculate $\Phi$:

1. **Blank:** Solvent background cuvette placed in sphere and excitation beam arranged in indirect position.

2. **Indirect Excitation:** Sample placed in sphere away from the first pass of the excitation beam. Any emission is due to absorption of the reflected excitation beam.

3. **Direct Excitation:** Sample placed in sphere directly in the path of the excitation beam. Emission is due to absorption from this direct excitation as well as any absorption from reflections.

The absorption, $A$, and $\Phi$, are then calculated from Equations 2.6 and 2.7, where $L$ is the area under the excitation peak and $P$ is the area under the emission curve of the denoted spectra. As the integrated sphere enables multiple reflections of the laser beam to be absorbed, (compared to single pass transmission of the UV-Vis), $A_{\%}$ calculated from Equation 2.6 is likely to be higher than the UV-Vis $A_{\%}$. For accurate results, the de Mello method requires $A_{\%} > 30\%$ [P.N. Stavrinou, personal communication].

$$A = 1 - \frac{L_3}{L_1} \tag{2.6}$$

$$\Phi = \frac{P_3 - (1 - A)P_2}{L_1 A} \tag{2.7}$$

**Experimental Set-Up**

The Fluoromax was connected to a Quantum-$\phi$ Integrating Sphere, also from Horiba Scientific, via an optical fibre. Each spectrum was recorded with an increment of 0.25 nm to ensure the narrow excitation peak was well resolved, and with the same slit width and range for each sample. Slit widths and ranges are detailed in the relevant chapters.

To ensure accuracy, the PLQE set-up was calibrated against literature values of the fluorescence standards Quinine Sulfate (emission range: $375 - 650$ nm) and Fluorescin 27 (emission range: $500 - 700$ nm) [151][152].

**Correction**

To determine $L$ and $P$, the spectra were baselined and converted from nm to eV using the Jacobian correction [153], to take into account the non-linear relationship between photon energy and wavelength ($E = \frac{hc}{\lambda}$). The correction is derived in Equation 2.8.

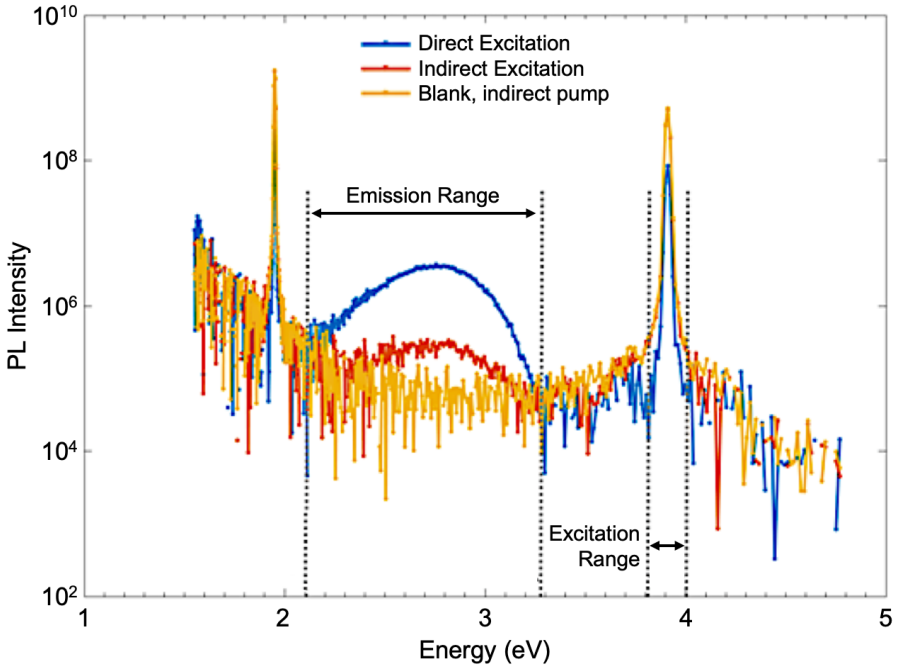



**Figure 2.8:** Spectral determination of PLQE energy ranges. An example of the visual inspection of spectra obtained from the measurements of Figure 2.7 required to determine the emission and excitation ranges for integration.

$$f(E) = f(\lambda)\frac{\mathrm{d}\lambda}{\mathrm{d}E} = f(\lambda)\frac{\mathrm{d}}{\mathrm{d}E}\left(\frac{hc}{E}\right) = -f(\lambda)\frac{hc}{E^2} \tag{2.8}$$

The spectra were then integrated over the emission and excitation ranges, which were determined by visual inspection of the spectra as shown in Figure 2.8.

# 3

# Monomer Emission and RIR Mechanism of Fundamental AIE Molecules

## Contents


**3.1 Introduction . . . . . 64**
3.1.1 Aims . . . . . 65
3.1.2 Order of work . . . . . 66
**3.2 Experimental . . . . . 66**
3.2.1 Solution Preparation . . . . . 67
3.2.2 Cuvette Preparation . . . . . 68
3.2.3 Optical Measurements . . . . . 68
**3.3 Results . . . . . 69**
3.3.1 Absorbance . . . . . 73
3.3.2 Photoluminescence . . . . . 74
3.3.3 PLQE . . . . . 77
**3.4 Conclusion . . . . . 78**


## 3.1 Introduction

As described in Section 1.3.3, TPE and HPS are exemplary AIE molecules. In solution, they display negligible emission, and then experience a large increase in PLQE once aggregation is induced.

Previous work dispersing TPE in polymer films identified emission from both the TPE monomer and excimer, with the excimer proportion increasing with the

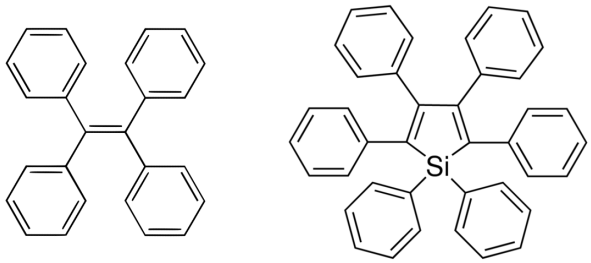



**Figure 3.1:** The AIE molecules used in this study: tetraphenylethylene (TPE) and hexaphenylsilole (HPS).

concentration of TPE [82]. Such clear, vibronic monomer emission had not yet been reported in the literature, and appeared to be evidence of the polymer matrix enacting RIR on the TPE. The decision was therefore taken to further investigate the monomer emission of TPE, and simple AIE molecules in general.

HPS, shown in Figure 3.1, was selected for investigation alongside TPE as they both exhibit an RIR-driven AIE mechanism and have similar solubility. However, due to its silole core and more numerous phenyl groups, HPS has a lower HOMO-LUMO gap and is more limited in its conformational capability. It was therefore expected to provide an interesting comparison to TPE.

Prior to developing the film dispersal of the previous work, this work focuses on the study of TPE and HPS in solution. In this environment the molecules are free to rotate and move outwith the confines of a polymer matrix or aggregate, enabling the behaviour of the monomers to be studied in isolation.

### 3.1.1 Aims

The aims of this chapter are therefore as follows:

1. To probe the monomer emission of AIE molecules by studying TPE and HPS in solution, and to identify whether emission can be detected in the absence of aggregation.

2. To induce aggregation in the solutions, and study its impact on the PL and PLQE.

3. To further the understanding of RIR within the context of monomer vs. aggregate emission.

### 3.1.2 Order of work

Good solutions of TPE and HPS were made in THF, and compared to solutions with varying degrees of induced aggregation. To induce aggregation, a second solvent was introduced into the solutions, in which TPE and HPS were not soluble, causing the molecules to aggregate within the THF regions of the solution. Water was chosen as this second, bad solvent, as it is highly miscible with THF but does not dissolve TPE nor HPS. Henceforth, any mention of a good or bad solvents refers to THF and water respectively.

The degree of aggregation was assumed to be monotonically dependent on the water fraction of the solution, and so to achieve different levels of aggregation, the proportion of good and bad solvent was varied within each solution. For each molecule, sets of solutions with 2 different concentrations were fabricated, to additionally study the effect of concentration on the aggregation property.

To measure the emission behaviour of each solution, the UV-Vis absorbance and PL spectra were recorded and the PLQE calculated using the de Mello method.

## 3.2 Experimental

In the literature, the AIE effect commonly triggered the greatest changes in PLQE with water fractions over 80%. Therefore the focus was placed on high water fractions, and the chosen THF:water ratios were as follows: 100:0, 50:50, 20:80, 10:90 and 5:95. Each ratio is hereafter referred to by its water fraction.

The composition of the solutions was also designed to ensure that the concentration of AIE material in each solution was equal, despite containing different solvent mixes. This was decided to allow a true comparison between the solutions, and guaranteed any observed aggregation effect was purely due to changes in the solvent environment, not changes in concentration. Additionally, for the optical

| AIE Molecule | $C_{\text{Final}}$ (µM) | Water Fractions (%) |
|---|---|---|
| TPE | 10 | [0, 50, 80, 90, 95] |
| TPE | 50 | [0, 50, 80, 90, 95] |
| HPS | 10 | [0, 50, 80, 90, 95] |
| HPS | 50 | [0, 50, 80, 90, 95] |

**Table 3.1:** Sets of Solutions

| Material | $m_{\text{W}}$ ($gmol^{-1}$) | $m$ (mg) | $V_{\text{THF}}$ (ml) | $C_{\text{Starter}}$ ($mg\,ml^{-1}$) | $C_{\text{Starter}}$ (mM) | $C_{\text{Final}}$ (µM) |
|---|---|---|---|---|---|---|
| TPE | 332.44 | 1.40 | 20 | 0.07 | 0.2 | 10 |
| TPE | 332.44 | 1.32 | 4.0 | 0.33 | 1.0 | 50 |
| HPS | 538.75 | 1.08 | 10 | 0.11 | 0.2 | 10 |
| HPS | 538.75 | 2.16 | 4.0 | 0.54 | 1.0 | 50 |

**Table 3.2:** Details of THF starter solutions for each AIE material, and the final concentration of the material in each set of cuvettes.

analyses it was a way of ensuring that the density of AIE molecules within the path length would be roughly equal across the solutions.

### 3.2.1 Solution Preparation

As shown in Table 3.1, 4 sets of solutions were made. Each set originated from a single starter solution, a small volume of which was added to each cuvette and then diluted with THF and water. The concentrations of the starter solutions were back-calculated from the desired final concentrations of the solutions - 10 µM and 50 µM, as detailed in Table 3.2.

The concentration of the solutions was required to be be low enough to ensure the materials stayed in solution with a water fraction of 95%, but high enough to absorb sufficient light for optical measurements within the 1 mm pathlength of the cuvette.

The starter solutions were made in advance of cuvette preparation with newly opened THF anhydrous to 99.9% (Sigma-Aldrich #401757) and left mixing overnight to ensure good solvation. The water was deioinised (Sigma-Aldrich #38796), and both solvents were filtered before use.

### 3.2.2 Cuvette Preparation

The solutions were made directly in quartz cuvettes, which were first cleaned according to Section 2.2.1. The cuvettes were filled first with the starter solution, then THF, and lastly water according to Table 3.3(a). Each cuvette was sealed with parafilm and inspected for precipitation. All remained optically clear after the water was added, indicating the chosen concentrations were sufficiently low. A corresponding set of solvent cuvettes containing THF and water with the same ratios, as detailed in in Table 3.3(b), were made alongside the AIE cuvettes to provide a background reference for the absorption measurements. The optical properties of each cuvette were then measured within 24 hrs as described below.

| $\%_{\text{water}}$ | $\%_{\text{THF}}$ | $V_{\text{water}}$ (µl) | $V_{\text{THF}}$ (µl) | $V_{\text{Starter}}$ (µl) |
|---|---|---|---|---|
| 0 | 100 | 0 | 332.5 | 17.5 |
| 50 | 50 | 175 | 157.5 | 17.5 |
| 80 | 20 | 280 | 52.5 | 17.5 |
| 90 | 10 | 315 | 17.5 | 17.5 |
| 95 | 5 | 332.5 | 0 | 17.5 |

**(a)** Ratios and Volumes of THF, water and the AIE material starter solutions used to make up each cuvette.

| $\%_{\text{water}}$ | $\%_{\text{THF}}$ | $V_{\text{water}}$ (µl) | $V_{\text{THF}}$ (µl) |
|---|---|---|---|
| 0 | 100 | 0 | 350 |
| 50 | 50 | 175 | 175 |
| 80 | 20 | 280 | 70 |
| 90 | 10 | 315 | 35 |
| 95 | 5 | 332.5 | 17.5 |

**(b)** Ratios and Volumes of THF and water used to make up each solvent background cuvette.

**Table 3.3:** Composition of AIE material and solvent cuvettes.

### 3.2.3 Optical Measurements

The UV-Vis transmission of all cuvettes was measured from 800 nm to 190 nm as described in Section 2.3.1. The absorbance of the AIE cuvettes was then calculated with respect to the solvent cuvettes, and suitable wavelengths were identified for excitation: 318 nm for TPE, and 364 nm for HPS. Large absorbance peaks were seen below 300 nm, however any emission between 300 nm and 364 nm would likely be reabsorbed by the solution.

The PL and PLQE were measured as described in Sections 2.3.2 and 2.3.3, according to the parameters detailed in Table 3.4. Due to the shape of the cuvettes,

| Material | $C$ (µM) | $\lambda_{exc}$ (nm) | PL | | PLQE | | | |
|---|---|---|---|---|---|---|---|---|
| | | | Slit (nm) | Range (nm) | Slit (nm) | Range (nm) | Excitation (eV) | Emission (eV) |
| TPE | 10 | 318 | 5 | 290 - 800 | - | - | - | - |
| TPE | 50 | 318 | 4.6 | 290 - 800 | 1.35 | 290 - 800 | 3.658 - 4.066 | 2.098 - 3.425 |
| HPS | 10 | 364 | 3.1 | 290 - 800 | - | - | - | - |
| HPS | 50 | 364 | 2.7 | 290 - 800 | 0.94 | 290 - 800 | 3.293 - 3.503 | 1.968 - 3.293 |

**Table 3.4:** PL and PLQE measurement parameters for each set of AIE cuvettes.

the cubic cuvette holder was not appropriate as it could not hold them securely. Instead the normal sample holder was used to hold them at an angle of 15 ° to the excitation beam.

To prevent disruption of the PL spectrum by excitation resonances, a 370 nm filter was inserted in the collection path of the Fluoromax. Of the 2 concentrations, only the 50 µM solutions were measured both with and without the filter. In this instance to provide a complete spectrum, the filtered and unfiltered spectra were scaled and cut together, as described in Section 2.3.2.

Due to low absorption of solutions, it was not possible to measure the PLQE of the 10 µM solutions. Therefore an indication of the PLQE trend was sought by integrating the PL spectra taken at the same slit width. Due to only a fraction of the emission being collected and scattering not being taken into account, this approach cannot provide real PLQE values. However, it can still give a rough indication of the PLQE trend in the absence of other data.

Following the PL measurement, the cuvette emission was photographed with an iPhone 6 camera. To achieve the clearest photo, the cuvettes were positioned normal to the excitation beam, and the slit was opened to its maximum width of 14 nm.

## 3.3 Results

The absorbance and PL of TPE and HPS solutions are shown in Figures 3.2 and 3.3 respectively. Photos of the emission and PLQE then follow in Figures 3.4 and 3.5.

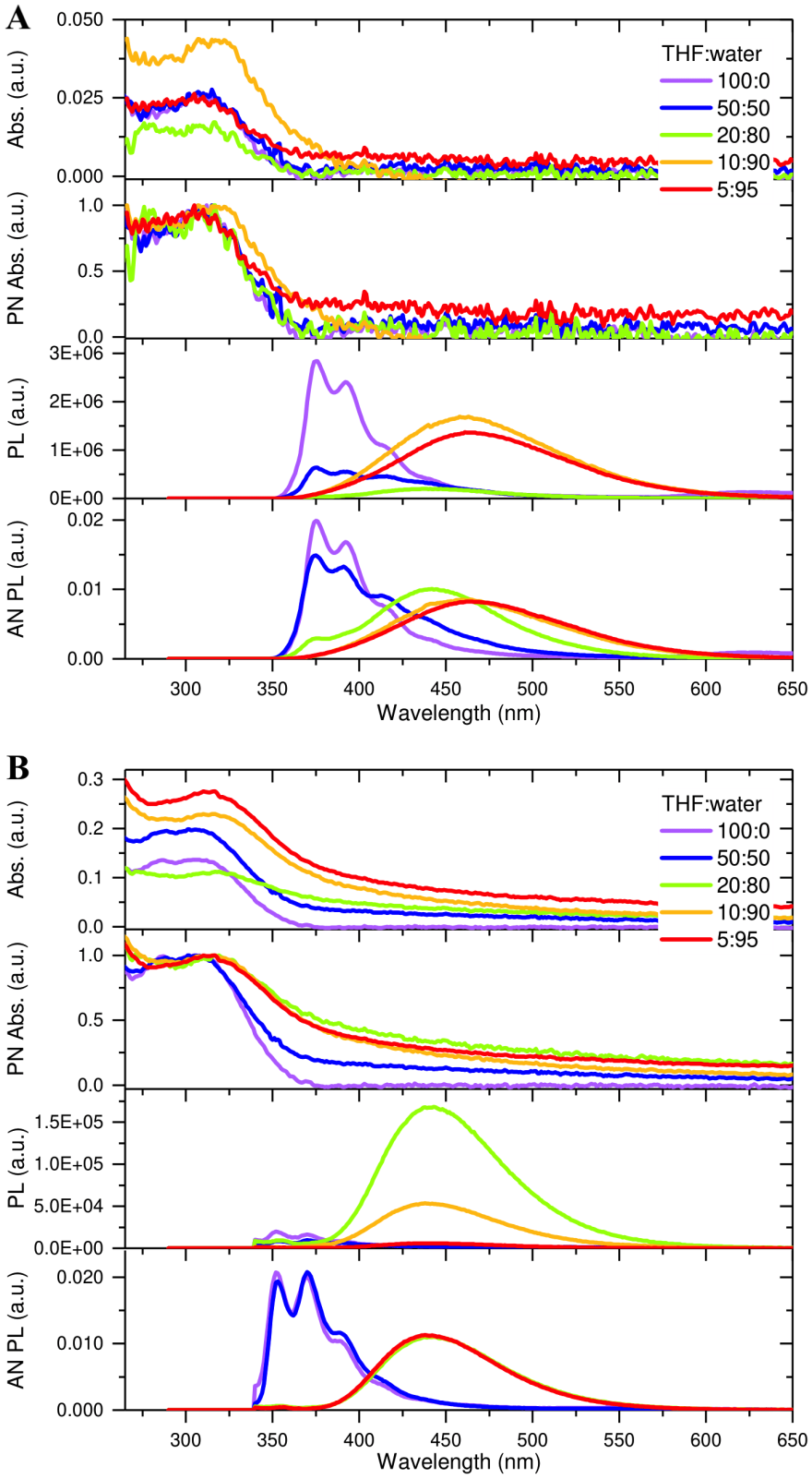



**Figure 3.2:** Absorbance, PN Absorbance, PL and AN PL of 10 µM (**A**) and 50 µM (**B**) TPE solutions. Vibronic monomer emission dominates the solutions with low water fractions. Beyond 50% water excimer emission can be seen. PL of 10 µM solutions was recorded with a filter at 370 nm.

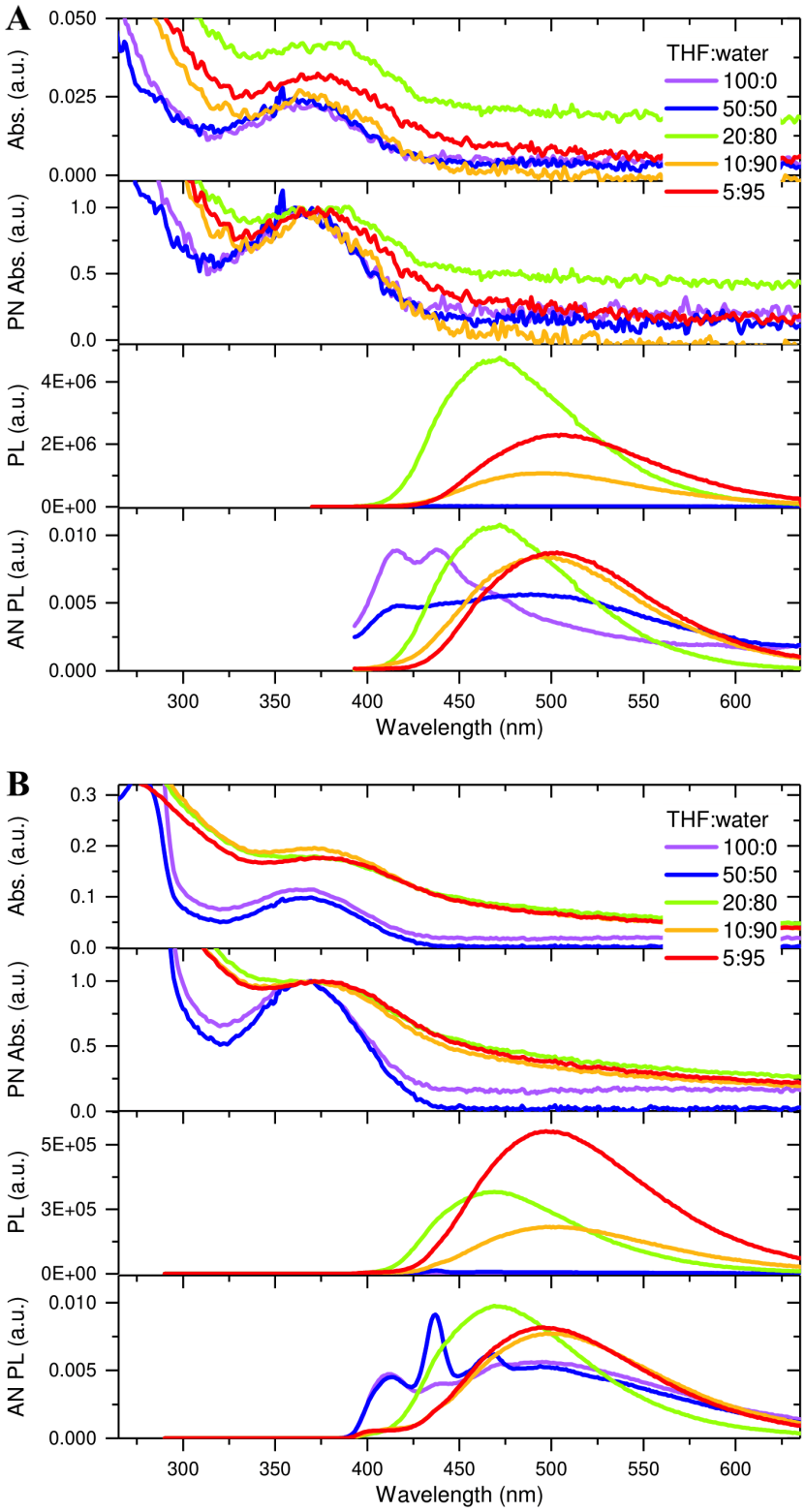



**Figure 3.3:** Absorbance, PN Absorbance, PL and AN PL of 10 µM (**A**) and 50 µM (**B**) HPS solutions. Some monomer emission is seen in the good solutions, but excimer emission is present throughout.

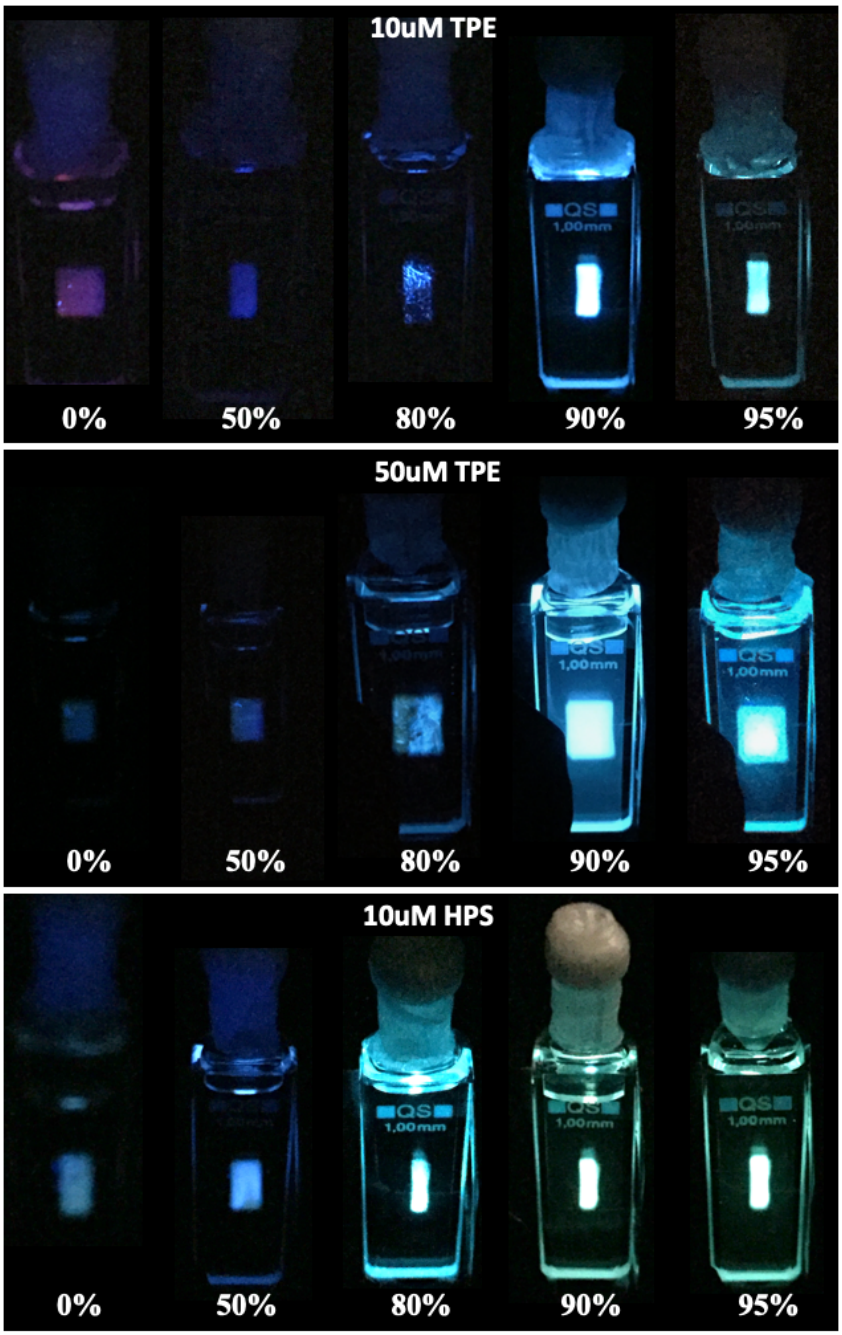



**Figure 3.4:** Photographs of solution emission at various water fractions. The 50 µM TPE photos were taken with a slit width of 14 nm. The 10 µM TPE and HPS photos were taken at the maximum non-saturating slit of each sample.

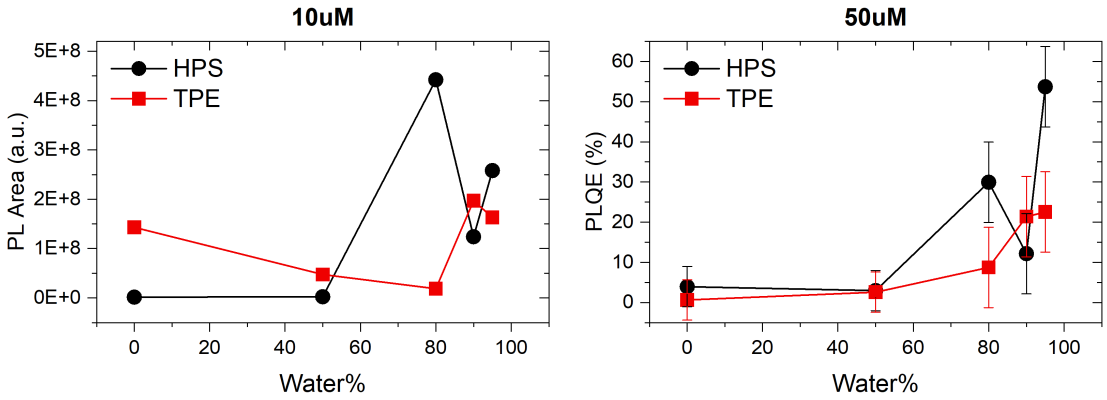



**Figure 3.5:** The PLQE of the 10 µM could not be calculated due to low absorbance, so **A** shows the integrals of their PL spectra. The 50 µM solution PLQE is shown in **B**. There is a clear increase in PLQE as the aggregation is increased.

### 3.3.1 Absorbance

The first spectrum of Figures 3.2 and 3.3 shows the absorbance of the TPE and HPS solutions. The PN absorbance is shown beneath the absorbance.

The 50 µM TPE in THF solution (the good solution) shows some vibronic structure at 285 nm and 306 nm similar to that seen in trans-stilbene (Appendix Figure 1). This trans-stilbene character in TPE suggests that in free solution the molecule was able to adopt a planar conformation across opposite phenyl groups. This character is retained at 50% water. Beyond 50% the absorption broadens with a small redshift to peak at 318 nm, due to the increase in solvent polarity. In HPS, there is no vibronic structure, instead a Gaussian absorption profile at 369 nm, but similar to TPE there is a redshift after 50% water to 376 nm. Despite their similar conjugation options described in Figure 1.14, the absorption of HPS is at a lower energy to TPE due to the effect of the silole core on the LUMO level, as described in Section 1.3.3.

The absorption of the 10 µM solutions is very low with a lot of noise in the signal. The 10 µM TPE solutions also appear to show less scattering than the 10 µM HPS, suggesting that smaller aggregates were formed by TPE. In the 50 µM solutions, the scattering tail increases with the water fraction, with the good THF and 50% water solutions showing distinctly less scattering than the higher water fractions,

which appear to show a roughly equal degree of scattering. This suggests that the degree of aggregation was roughly consistent for 80%-95% water.

### 3.3.2 Photoluminescence

In good solutions, 100% THF and 50% water, the AN PL of Figures 3.2 and 3.3 shows a dominance of monomer emission, characterised by narrow, vibronic structure towards the blue end of the spectrum. In contrast to the TPE films of Figure 1.16 of Section 1.3.4, these solutions show emission solely from the monomer, indicating negligible aggregation took place in THF.

As the water fraction is increased, there is an emergence of excimers characterised by broad, redshifted emission, and a quenching of the monomer, indicating that the molecules have formed aggregates. Upon aggregation the molecules twist about their cores and break the conjugation between the phenyl groups, leaving intermolecular interactions, i.e. excimers, the sole contributors to the emission.

The TPE monomer is characterised by vibronic peaks at 352 nm, 369 nm, 389 nm and 412 nm. The 10 µM TPE is missing the first of these peaks due to the filter at 370 nm, which was not used for the 50 µM solutions. The TPE excimers then settle at 464 nm in 10 µM, and 438 nm for 50 µM at 95% water. In HPS the monomer is less distinct, but some vibronic character is seen at 412 nm, 441 nm and 472 nm. In contrast to TPE, the HPS excimers are seen at all water fractions except the good solution of 10 µM. They settle at 95% water at 503 nm in 10 µM, and 496 nm for 50 µM. This pervasiveness of the HPS excimers may be due to HPS being slightly larger than TPE, and/or its more numerous phenyl rings providing more opportunities for excimers to form.

In TPE the monomer emission is quenched gradually, with it dominating both the THF and 50% water solutions, and a trace also visible in the 80% water. However between 10 µM and 50 µM TPE, there is a difference at 80% water. At the lower concentration, this fraction appears to be in a transition phase between the monomer and excimer emission, whereas at the higher concentration, it is firmly aligned with the excimer component. It can be seen in the 10 µM PL that the

emission strength of this solution is also lower than those either side of it. This suggests that the lower concentration was insufficient to enable stable excimer formation at this water fraction, and required either more TPE or more aggregation to reach the settled excimers seen 90% and 95% water.

A similar pattern is seen in HPS, however even in the 50 µM solutions with 80% water the excimer lies at an intermediate wavelength. This suggests that in general, HPS requires a higher degree of aggregation to form stable excimers. This could be due to the nature of HPS packing, as mentioned in Figure 1.15 of Section 1.3.3. As the phenyl groups of HPS approach each other with a non-parallel, T-shape geometry, their excimers are less stable. This reduces the energy drop of excimer association ($\Delta H_M$), and results in a bluer excimer emission. At higher degrees of aggregation in 90% and 95% water, it may be that the HPS molecules are being forced together such that the excimer geometry becomes more parallel, increasing $\Delta H_M$ and giving a redder emission.

This could also be the reason behind the contrast in $\Delta E_{\text{Shift}}$ between TPE and HPS. As seen in the PL spectra and emission photos of Figure 3.4, the TPE displays a large colour shift between its monomer and excimer emission, ranging from violet in THF solution to cyan in 95% water. In comparison the HPS excimer overlaps with the monomer, resulting in a small colour change from blue/cyan to green. This could be due to the difference in the nature of excimer formation in TPE and HPS.

The more planar and parallel interaction between the phenyl groups of TPE could provide the TPE excimers with a consistently larger $\Delta H_M$ than the HPS excimers, leading to a larger $\Delta E_{\text{Shift}}$ in their emission [81].

**Monomer Emission of TPE vs. HPS**

In the PL of solutions with low water fractions, the vibronic monomer emission of TPE is consistently more prevalent than that of HPS, regardless of concentration. To understand why the TPE monomer may be a stronger emitter than HPS we refer to the various conjugation pathways within each molecule detailed in Figure 1.14 of Section 1.3.3.

The difference could be due to either the number of pathways available, as well as the ability of the molecule to adopt the conformation required to permit each conjugation pathway. As shown in Figure 1.14, HPS has only 1 trans-conjugation pathway whereas TPE has 2, and both molecules have 2 cis-conjugation pathways. For strong conjugation, planarity along these pathways is required to allow $\pi$ orbital overlap.

Steric interactions between adjacent phenyl groups mean the phenyl rings with potential cis-conjugation are unlikely to lie on the same plane. Therefore, it is unlikely that cis-conjugation in either molecule is contributing significantly to the emission. Steric hindrance across the TPE molecule is minimized if phenyl rings 1 and 3 rotate 90 ° about the double bond, resulting in two pairs of planar phenyl rings lying perpendicular to each other. This conformation would the enable the trans-conjugation from rings 2 to 4 or 1 to 3 to contribute to the emission. The crowded HPS molecule has no such symmetry, and the increased steric hindrance of two extra phenyl rings renders it even less likely that the conformation would favour its single trans-conjugation pathway.

This idea is supported by the emission of stilbene, of which the trans- and cis-isomers serve as an analogue to the conjugation pathways of TPE. As shown in the Appendix Figure 1, the trans-stilbene displays a moderately vibronic absorption and emission, similar in profile to the TPE monomer, suggesting the trans-conjugation of TPE is favoured over the cis. The cis-stilbene instead shows a broad absorption and emission, at a wavelength closer to the excimers seen above.

The cis-stilbene emission is also much weaker than trans-stilbene ($\Phi_{\text{trans}} = 0.027 - 0.055, \Phi_{\text{cis}} = 1.4 \times 10^{-4}$ [154], and so unlikely to contribute in aggregated solutions, where the monomer emission is already weak in comparison to the excimer. In addition, the cis conjugation is highly unlikely in the aggregate due to the packing/crystal formation shown in Figure 1.15 showing a lack of planarity between adjacent phenyl groups.

Therefore the small amount of monomer emission seen in HPS is most likely from the rare trans-conjugation pathway. This pathway is also slightly longer

than the trans pathway of TPE, resulting in a redder emission, (which perhaps also contributes to the small monomer-excimer energy gap in addition to the reasons described above). The stronger, more resolved monomer emission in TPE is therefore due to the both more numerous, and more sterically favourable trans-conjugation enabling conformations.

### 3.3.3 PLQE

The PLQE of TPE and HPS shows a similar trend to the literature, with low values in good solutions and a dramatic increase at high water fractions.

For 50 µM TPE, the good 0% water solution of TPE is nearly negligible, starting at just 0.63% before rising to 2.58% and 8.73% in 50% and 80% water respectively. Then there is a jump to 21.37% and 22.55% at the highest water fractions.

The 50 µM HPS solutions start a little higher at 3.93% and remain steady at the 50% water at 2.97%. There is then a large jump to 29.94% at 80% water, which falls to 12.18% at 90% water before rising sharply to 53.71% at 95% water. The same trend is seen in the PL intensity of the solutions, and it is hard to say whether the 80% is unexpectedly too high or the 90% too low. It may be that the less stable excimers at 80% water for some reason are more emissive than the stable ones of the higher water fractions, however this has not been reported in the literature.

The PLQE estimate of the 10 µM solutions follows a similar trend, but with perhaps an artificially high value for TPE 0% water compared to the 50 µM version.

The 50% water TPE solution is interesting, as in the PL there is no hint of the excimer formation, but the PLQE, while still low, is much higher than the 0% water solution. This suggests that even prior to aggregation, the water may be inducing enough RIR to impact the molecule to a small degree. However this is not seen in the HPS solutions, and so may be only a feature of this particular measurement.

In general, the HPS aggregates achieve higher PLQE than the TPE. This could be due to HPS having 2 more phenyl groups than TPE, giving 50% more opportunities to form excimers. Its larger molecular size may also be contributing to the stronger AIE effect.

As detailed in Section 1.3, this AIE effect is defined as the PLQE increasing in the aggregate. But what makes the aggregate so much more efficient than the monomer in these AIE molecules? Although the PL spectra clearly captured monomer emission, in good solution the TPE and HPS molecules remain free to rotate about their phenyl groups - an energy loss mechanism causing non-radiative decay. In addition to dissipating energy, this rotation disrupts the conjugation pathways discussed above that are required for monomer emission. Therefore when free to rotate, the PLQE of TPE and HPS is likely to be low, as shown above, while excimers are not subject to these decay mechanisms. As such, it may not be a case of the excimers being *more* efficient, but that the monomers are in a particularly poor environment for radiative decay.

The formation of excimers also puts the notion of RIR being the driving force of the AIE effect into doubt. These results show that the increase in PLQE is driven by the emergence of excimers, not from any increase in the capability of the monomer to emit due to RIR. If this were the case then the monomer emission would have been retained in the emission spectra. Instead, upon aggregation the monomer is quenched, and excimers dominate the PL. Therefore while RIR may still be a mechanism by which to increase the emission of the *monomer*, it is not necessarily relevant in the aggregate. It is true that rotation is limited in the aggregate, however excimers form prior to energy dissipation via rotation, and therefore the aggregate itself has no direct impact on the rotation.

A true test of RIR as an AIE mechanism would instead involve the monomers in an environment that could induce RIR *without* aggregation, which may then show an increase of monomer PLQE rather than excimer formation. Ideas for such a test are discussed in more detail below.

## 3.4 Conclusion

To summarise, a more detailed understanding of the behaviour of fundamental AIE molecules in solution has been achieved. The absorption has given some

indication as to the conformation of the molecules, with the similarities to trans-stilbene enabling the deduction that the trans-conjugation pathways were the largest contributors to the monomer emission. The PL offered an insight to the behaviour of the molecules at varying degrees of aggregation, from freely rotating monomers to the formation of excimers.

By comparing TPE and HPS, we have seen the difference in excimer formation due to different packing geometries such as T-shape (HPS) and parallel (TPE), and how the geometry contributes to the stability of the excimers and their emission wavelength. We have also observed a concentration dependence due to geometry and molecular size, with TPE requiring a higher concentration to form stable excimers.

The capability of this solution based technique to carefully tune the molecular environment via controlling the solvent ratio has also been demonstrated. By studying the molecular interaction in detail for the first time, we have shown it is possible to balance the monomer and excimer emission of these fundamental AIE molecules.

Previous studies into AIE molecules have focussed on the excimer behaviour, often writing off or excluding the monomer emission entirely, but here it is shown that the monomer does indeed emit, and in stark contrast to the excimer. These new insights into the monomer emission demonstrate the potential for AIE to be considered not just an on/off change in the emission, but instead a spectrum of change that could be utilised to enhance the sensing capability of AIE systems beyond their current sensitivity.

The literature shows an increase in PLQE with aggregation, but from the PL it is clear that this trend is due to excimer formation and not the result of RIR in the monomer. If RIR were behind the increase in emission, then the monomer emission would be retained in the PL spectra. Instead we see only excimer emission in solutions with high PLQE. Therefore, while it may have been helped along by RIR, the formation of excimers and consequential rise in PLQE was driven by aggregation.

These results also show that there is reason to question the nomenclature of AIE. While it is true the overall PLQE increases with aggregation, the emission of the

originally absorbing fluorophore actually decreases. The results show a quenching of the monomer emission, and a rising of the excimer. As described above in Section 1.2.6, excimer formation is one of many ACQ processes. Therefore even though the overall emission efficiency is going up, we are still observing a quenching process. In that sense, rather than a new phenomenon behaving "oppositely" to ACQ as described in [155], AIE should instead be considered a subset of ACQ wherein the quenching provides a more efficient emission process than the original fluorescence. It is therefore true that this is different to typical ACQ in that the emission of the original fluorophore is usually stronger than the quenched form, however the notion that fluorophore emission is somehow enabled by aggregation remains incorrect.

The current terminology contributes to confusion and misunderstanding around ACQ. For example, in [156] the authors describe the AIE effect as entirely due to RIR in HPS. They say that excimer formation due to $\pi - \pi$ stacking is a quenching mechanism, and the reason siloles are emissive in aggregates is because their structure inhibits such stacking. If this were true, then the emission would be predominantly monomeric in the aggregate state, but the present results show strong excimer emission from the HPS aggregate. While the silole structure indeed prevents planar stacking, excimers are still able to form between the phenyl rings. They also say that any $\pi$ stacking of the AIE molecule is small and weak relative to the RIR, and so AIE is still possible despite some stacking. Therefore they acknowledge that excimers do contribute to the aggregate emission, but are weak relative to the RIR of the monomer. This does not reconcile with the spectra measured here, in which the excimer emission clearly dominates at high water fractions and it is the monomer emission that is quenched.

As mentioned above, it would be interesting to study how TPE and HPS might behave when subjected to RIR in the absence of aggregation. Not only would this be a true test of the RIR hypothesis as described in the literature, but also potentially a means to control both the efficiency and range of emission. For example, if RIR could be achieved in the monomer, it may increase the efficiency of the monomer emission seen in the good solutions above, without relying on excimer formation.

The PLQE of all solutions measured here was non-zero, and so the monomer may be capable of much higher PLQE given the right environment. If possible, this would allow tuning of the emission colour from the blue monomer to the lower energy red excimer, whilst maintaining across the full spectrum the high efficiency currently only seen in the excimer emission.

We saw in Figure 1.16 that TPE monomer emission was achievable when dispersed in PMMA films [82]. This work could be developed to increase the RIR effect of the polymer matrix on TPE. In the previous work, excimer emission was present at all concentrations, and so the next steps would be to reduce the excimer formation while increasing the PLQE of the monomer. If successful, the increased PLQE could then be attributed to the RIR of TPE.

It was shown that a ratio of 1:99 TPE:PMMA emitted with roughly equal monomer and excimer contributions. This shows that excimers were able to form even at low concentrations, and so a much thinner dispersal would be required to eliminate the excimer contribution. To do so, the blend might be improved by trialling polystyrene (PS) in place of PMMA, as the phenyl side groups of PS are similar to those of TPE. Lower concentrations of TPE could also be trialled, however this would likely cause a trade-off with absorption which may then inhibit accurate investigations into the PLQE.

Inducing efficient monomer emission in this way would enable efficient tuning of the TPE emission across its spectrum. Aggregation could then be induced into the film, either by via solvent interaction as seen in the $\beta$ phase of PFO, or by patterning the surface by depositing additional TPE solution. Achieving an excimer-free emitting film could therefore be considered a baseline for future patterning applications. Furthermore, extending the technique to larger molecules might broaden the tunable range of emission.

To conclude, these results have provided clarification around the behaviour of AIE molecules in solution and as they aggregate. While this has triggered new criticism of the fundamental AIE theory, it has also opened up new opportunities in controlling the emission of AIE materials, and sparked ideas in photonic patterning applications.

# 4

# Excimer Formation in Fluorene-Fluorenone Oligomers

## Contents


**4.1 Introduction . . . . . 82**
4.1.1 Aims and Hypothesis . . . . . 84
4.1.2 Order of Work . . . . . 84
**4.2 Experimental . . . . . 85**
4.2.1 Solution Preparation . . . . . 85
4.2.2 Cuvette Preparation . . . . . 87
4.2.3 Optical Measurements . . . . . 87
**4.3 Results . . . . . 89**
4.3.1 Absorbance and Photoluminescence . . . . . 89
4.3.2 Peak Analysis and PLQE . . . . . 89
4.3.3 Discussion . . . . . 89
**4.4 Conclusion . . . . . 99**
4.4.1 Summary . . . . . 99
4.4.2 Tunability and Oxidation . . . . . 100
4.4.3 Sensitive Oxidation Testing . . . . . 101


## 4.1 Introduction

As discussed in Chapter 1, the formation of fluorenone in fluorenes has been studied extensively due to their detrimental impact on the deep blue emission and PLQE of polyfluorenes, which are highly prized in LED applications. However,

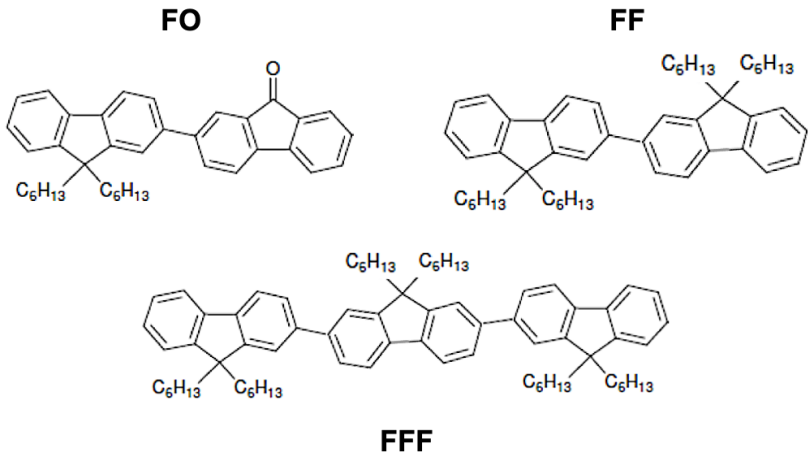



**Figure 4.1:** The oligomers of fluorene (F) and fluorenone (O) used in this study.

beyond their reputation as defects, oligomers of fluorene and fluorenone have many interesting properties which make them worthy of study as functional materials in their own right.

Of these properties, their strong tendency to aggregate and form excimers is reminiscent of the AIE materials studied in Chapter 3, and provides a large contrast in both the oligomer emission spectra and PLQE. This lends them to the style of analysis used in Chapter 3, wherein a solution-based method for controlling the aggregation of small molecules was utilised to probe their fundamental AIE properties. Here we use this method to create a system in which we can control the formation of excimers in solution, in a bid to 'turn off' and 'turn on' the fluorenone emission.

As described in Chapter 1, preventing the formation of excimers was attempted previously by reducing the concentration, but was not successful until it was reduced to $10^{-12}$M [101]. Here we will investigate whether this can instead be achieved by screening the fluorenone ketone dipole with a polar solvent. If the polar solvent also happens to be a poor solvent for the fluorene units (which is likely as fluorene has low polarity), as its proportion is increased the oligomers will be forced to aggregate within regions of the good solvent, thereby reactivating the excimer formation seen in the good solution. Therefore in this work, the 'bad' solvent of the AIE method is utilised to both screen the dipole and induce aggregation.

### 4.1.1 Aims and Hypothesis

The aims of this work are therefore:

1. To screen the formation of fluorenone excimers with a polar solvent.

2. To control the reintroduction of excimers by inducing aggregation via the addition of a non-solvent.

3. To investigate the emission properties of FO, FF, FFF and oxidised FFF as the solvent fraction is varied.

By varying the proportion of fluorenone within the solutions, we aim to understand how its aggregation can best be controlled. The 3 fluorene/fluorenone (F/O) oligomers shown in Figure 4.1 were supplied by Dr Khai-Leok Chan and Professor Andrew Holmes: FO, FF and FFF. A thermally oxidised form of the FFF oligomer was also tested, in order to probe the behaviour of oligomers with small fluorenone concentrations.

In a good solution of FO, excimer emission is expected to dominate. As polar solvent is added the excimer emission is expected to reduce, allowing the monomer emission to dominate. As more polar solvent is added, the molecules are expected to aggregate, which in turn may reintroduce the excimer emission, and quench the monomer. For FF and FFF, no screening effect or excimer formation is expected, only monomer emission with ACQ at high fractions of the polar solvent.

### 4.1.2 Order of Work

As mentioned above, the same technique employed in Chapter 3 to encourage varying degrees of aggregation is employed here. The optical properties of good solutions of the fluorene/fluorenone oligomers are compared to those with varying ratios of good and bad solvents, with an equal volume of material present throughout. The absorbance, PL and PLQE of solutions of FF, FFF, FO and 2 types of thermally oxidised FFF were measured.

## 4.2 Experimental

The solvents selected were THF and water, as THF is a good solvent for PFO ($\delta_{\text{THF}} = 9.1\,\text{cal}^{1/2}\text{cm}^{-3/2}$, $\delta_{\text{PFO}} = 9.1 - 9.3\,\text{cal}^{1/2}\text{cm}^{-3/2}$) and so should also be a very good solvent for fluorene. Water is highly polar (Polarity Index = 9), a non-solvent for fluorene ($\delta_{\text{water}} = 23.5\,\text{cal}^{1/2}\text{cm}^{-3/2}$), and mixes very well with THF [157], and so satisfies aims 1 and 2 listed above. To investigate the screening properties of water, cuvettes with varying ratios of THF:water were made, ranging from 100% THF to 10% THF, 90% water by volume in increments of 10%. Due to a limited number of cuvettes, low water ratios in FFF solutions and 40% water in oxidised FFF were omitted. The results below will show that no critical change happened across these ratios and so no information was lost. The composition of the solutions was designed such that the final concentration of each oligomer was equal across all cuvettes for that oligomer, i.e. each FFF cuvette would contain 23 µM of FFF (see Table 4.1), despite comprising different solvent mixes. This was decided to allow a true comparison of optical effects between the cuvettes, providing insight into how the oligomers behave under different conditions.

### 4.2.1 Solution Preparation

As described in Figure 4.2, the concentration ($C$) of the solutions was important to get right. If $C$ were too high, the volume of water added may be insufficient to have the desired screening effect and its addition may cause the oligomer to fall out of solution. If too low, there may not be sufficient density of oligomers to form excimers in THF solution. The concentration 'sweet spot' must enable excimer formation in 100% THF solution, whilst still being susceptible to the dipole screening effect of the water. Due to findings from previous work, the former is unlikely to be an issue, as solutions of FFOFF and FOF needed to be diluted to $10^{-12}$ M to quench the excimer emission [101]. Therefore the potential issue lies in starting so high that the effect of the water is negligible. The decision was therefore taken to make cuvettes with concentrations in the region of $10^{-6}$ M, with the option to further dilute if the screening effect was not observed.

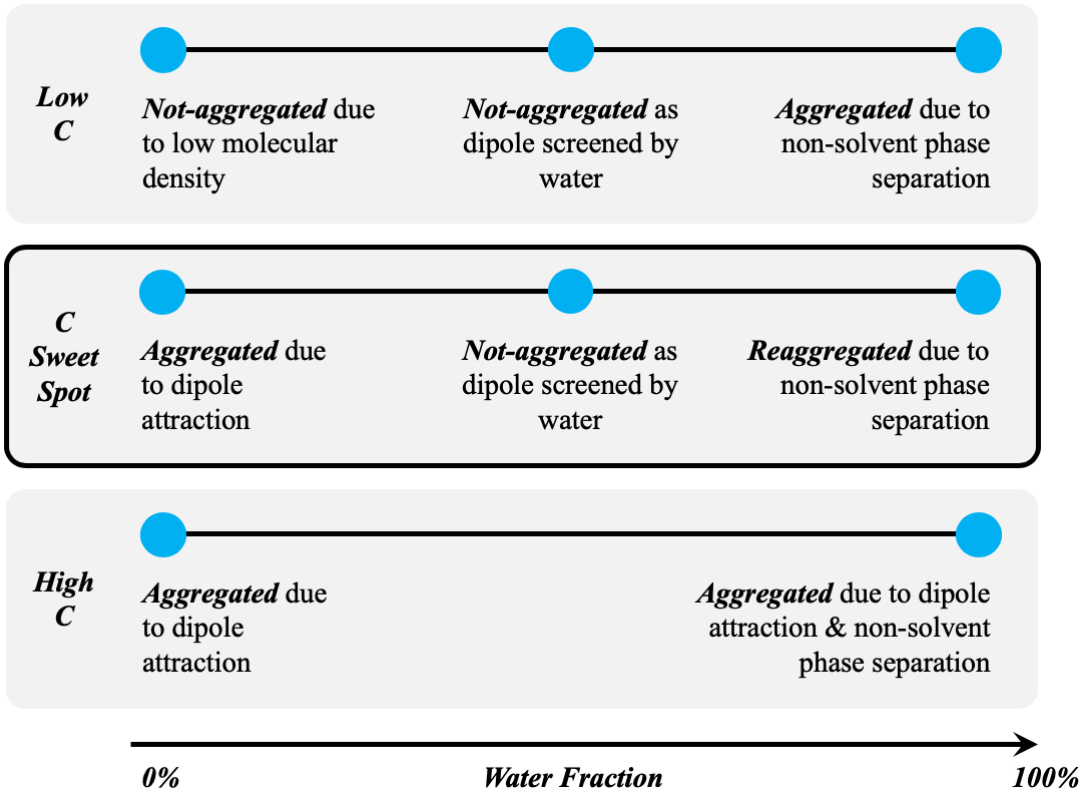



**Figure 4.2:** The impact of concentration on excimer formation. If $C$ is too low, the excimers may fail to form at in good solution (0% water), and so any screening would not be observed. If $C$ is too high, the screening may not take place at all. An appropriate concentration would enable excimer formation in good solution, exhibit screening at low water fractions, and then allow the resurgence of aggregation at high water fractions due to the high volumes of the non-solvent in the solution.

The solvents used were deionised water (Sigma-Aldrich 38796) and newly opened THF anhydrous to 99.9% (Sigma-Aldrich 401757). Both were filtered before use. Starter solutions with a higher concentration ($C_{\text{Starter}}$) than the final cuvette concentration ($C_{\text{Final}}$) were made as detailed in Table 4.1. By using equal volumes of the starter solution across the set of cuvettes, which would then each be diluted with a unique mix of THF and water according to Table 4.2(a), an equal concentration of oligomer could be preserved across the set.

### Thermal Oxidation

To create a second set of solutions containing fluorenone, the process for making the FFF solutions was duplicated, however before adding the solvent the vial containing

| Oligomer | $M_W$ (g/mol) | $m$ (mg) | $V_{\text{THF}}$ (ml) | $C_{\text{Starter}}$ (mg/ml) | $C_{\text{Starter}}$ (mM) | $C_{\text{Final}}$ (µM) |
|---|---|---|---|---|---|---|
| FO | 512.715 | 3.8 | 15 | 0.253 | 0.49 | 25 |
| FF | 667.066 | 4.5 | 15 | 0.3 | 0.45 | 22.5 |
| FFF | 999.589 | 2.5 | 5.44 | 0.46 | 0.46 | 23 |

**Table 4.1:** Details of THF starter solutions for each F/O oligomer, and the final concentration of the oligomer in the cuvettes.

the FFF was heated in air. 2 thermal oxidation methods were tested: 150 ℃ for 1 hr (FFF-ox1) and 300 ℃ for 24 hrs (FFF-ox2).

### 4.2.2 Cuvette Preparation

The solutions were made directly in quartz cuvettes, which were first cleaned according to Section 2.2.1. The oligomer cuvettes were filled according to Table 4.2(a): first with the starter solution, then THF, and lastly water, before being sealed with parafilm. Each cuvette was inspected for precipitation and all remained optically clear after the water was added, indicating the chosen concentration was not too high. For each set of oligomer cuvettes, a matching set was made at the same time containing only the solvents in the same ratios, as detailed in Table 4.2(b). These solvent cuvettes were measured alongside the oligomer solutions to provide a background reference for the absorption measurements and also to distinguish which features of the absorbance and PL could be attributed to the oligomers.

### 4.2.3 Optical Measurements

To analyse the solutions, all measurements were carried out within 24 hrs of each cuvette being filled due to the volatility of THF. This ensured minimal evaporation had occurred and the solvent ratios were preserved. Before each measurement the cuvettes were again polished with IPA to remove any dirt picked up from their boxes, and handled with gloves. The UV-Vis transmission of the oligomer and solvent cuvettes was measured from 800 nm to 190 nm as described in Section 2.3.1. The absorbance of the oligomers was then calculated with respect to the solvent, from which suitable wavelengths were identified for excitation.

| $\%_{water}$ | $\%_{THF}$ | $V_{water}$ (µl) | $V_{THF}$ (µl) | $V_{Starter}$ (µl) |
|---|---|---|---|---|
| 0 | 100 | 0 | 332.5 | 17.5 |
| 10 | 90 | 35 | 297.5 | 17.5 |
| 20 | 80 | 70 | 262.5 | 17.5 |
| 30 | 70 | 105 | 227.5 | 17.5 |
| 40 | 60 | 140 | 192.5 | 17.5 |
| 50 | 50 | 175 | 157.5 | 17.5 |
| 60 | 40 | 210 | 122.5 | 17.5 |
| 70 | 30 | 245 | 87.5 | 17.5 |
| 80 | 20 | 280 | 52.5 | 17.5 |
| 90 | 10 | 315 | 17.5 | 17.5 |

**(a)** Ratios and Volumes of THF, water and the oligomer starter solutions used to make up each oligomer cuvette.

| $\%_{water}$ | $\%_{THF}$ | $V_{water}$ (µl) | $V_{THF}$ (µl) |
|---|---|---|---|
| 0 | 100 | 0 | 350 |
| 10 | 90 | 35 | 315 |
| 20 | 80 | 70 | 280 |
| 30 | 70 | 105 | 245 |
| 40 | 60 | 140 | 210 |
| 50 | 50 | 175 | 175 |
| 60 | 40 | 210 | 140 |
| 70 | 30 | 245 | 105 |
| 80 | 20 | 280 | 70 |
| 90 | 10 | 315 | 35 |

**(b)** Ratios and Volumes of THF and water used to make up each solvent background cuvette.

**Table 4.2:** Composition of oligomer and solvent cuvettes.

| Oligomer | $\lambda_{exc}$ (nm) | PL | | PLQE | | | |
|---|---|---|---|---|---|---|---|
| | | Slit (nm) | Range (nm) | Slit (nm) | Range (nm) | Excitation (eV) | Emission (eV) |
| FO | 300 | 3.2 | 320 - 800 | 1.70 | 290 - 800 | 4.000 - 4.276 | 1.812 - 3.721 |
| FF | 330 | 1.65 | 290 - 800 | 1.20 | 290 - 800 | 3.647 - 3.863 | 2.299 - 3.639 |
| FFF | 353 | 1.2 | 290 - 800 | 1.05 | 290 - 800 | 3.397 - 3.666 | 2.220 - 3.347 |
| FFF-ox1 | 353 | 1.02 | 290 - 800 | 1.05 | 290 - 800 | 3.397 - 3.666 | 2.220 - 3.347 |
| FFF-ox2 | 353 | 2.00 | 290 - 800 | 1.05 | 290 - 800 | 3.397 - 3.666 | 2.220 - 3.347 |

**Table 4.3:** PL and PLQE measurement parameters for each set of oligomer cuvettes.

The PL and PLQE were measured as described in Sections 2.3.2 and 2.3.3, according to the parameters detailed in Table 4.3. Due to the planarity of the cuvettes, the cubic cuvette holder was not appropriate as it could not hold them securely. Instead the normal sample holder was used to hold them at an angle of 15° to the excitation beam. Following measurement of the PL, the cuvette emission was photographed with an iPhone 6 camera. To achieve the clearest photo, the cuvettes were positioned normal to the excitation beam, and the slit was opened to its maximum width of 14 nm.

## 4.3 Results

### 4.3.1 Absorbance and Photoluminescence

The absorbance (Abs.), PN Abs., Rel. PL and AN PL of the fluorene oligomers (FF, FFF) and fluorenone oligomers (FO and FFF-ox2) are shown in Figures 4.3 and 4.4 respectively. The transmission data of all solutions are shown in the Appendix Figure 2, along with the PL of the solvent-only cuvettes (Figures 3 and 4). The FFF-ox1 data was omitted as it showed near identical absorbance and emission to the FFF solutions, indicating that the first thermal oxidation method failed to have a significant effect. Data omitted from absorbance spectra is the removal of a spike caused by a common fault in the detector.

### 4.3.2 Peak Analysis and PLQE

Further plots analysing the monomer vs. excimer intensities, shifts in the absorption and PL, and the PLQE, are shown in Figures 4.6 and 4.7 respectively.

### 4.3.3 Discussion

In THF solution, the fluorene oligomers FF and FFF have peak absorbance at 330 nm, and 353 nm respectively, the longer wavelength for FFF due to greater conjugation across the 3 fluorene units. The FFF-ox2 absorbance peaks close to FFF at 352 nm. The absorbance of FO has 2 peaks at 295 nm and 335 nm, representing a shift from the delocalised $\pi$-$\pi^*$ to the localised phenyl $\pi$-$\pi^*$ transitions as described in [92] and following the values and profile for oligomers with fluorenone units in [158][159]. The weak $n$-$\pi^*$ absorption of the fluorenone unit can also be seen at 430 nm in the 100% THF solution. The strongest absorbance is seen for FFF in THF at 0.43, likely due to FFF being the largest molecule in a well distributed solution.

All oligomers undergo a distinct broadening of the absorbance as water is added, indicating an increase in the range of molecular conformation as they aggregate. Additionally, as the water fraction is raised there is a small redshift for all oligomer solutions, detailed in Figure 4.7**A**. Previous solution studies of fluorenone/fluorene oligomers have showed the impact of solvent polarity on the excited state dipole,

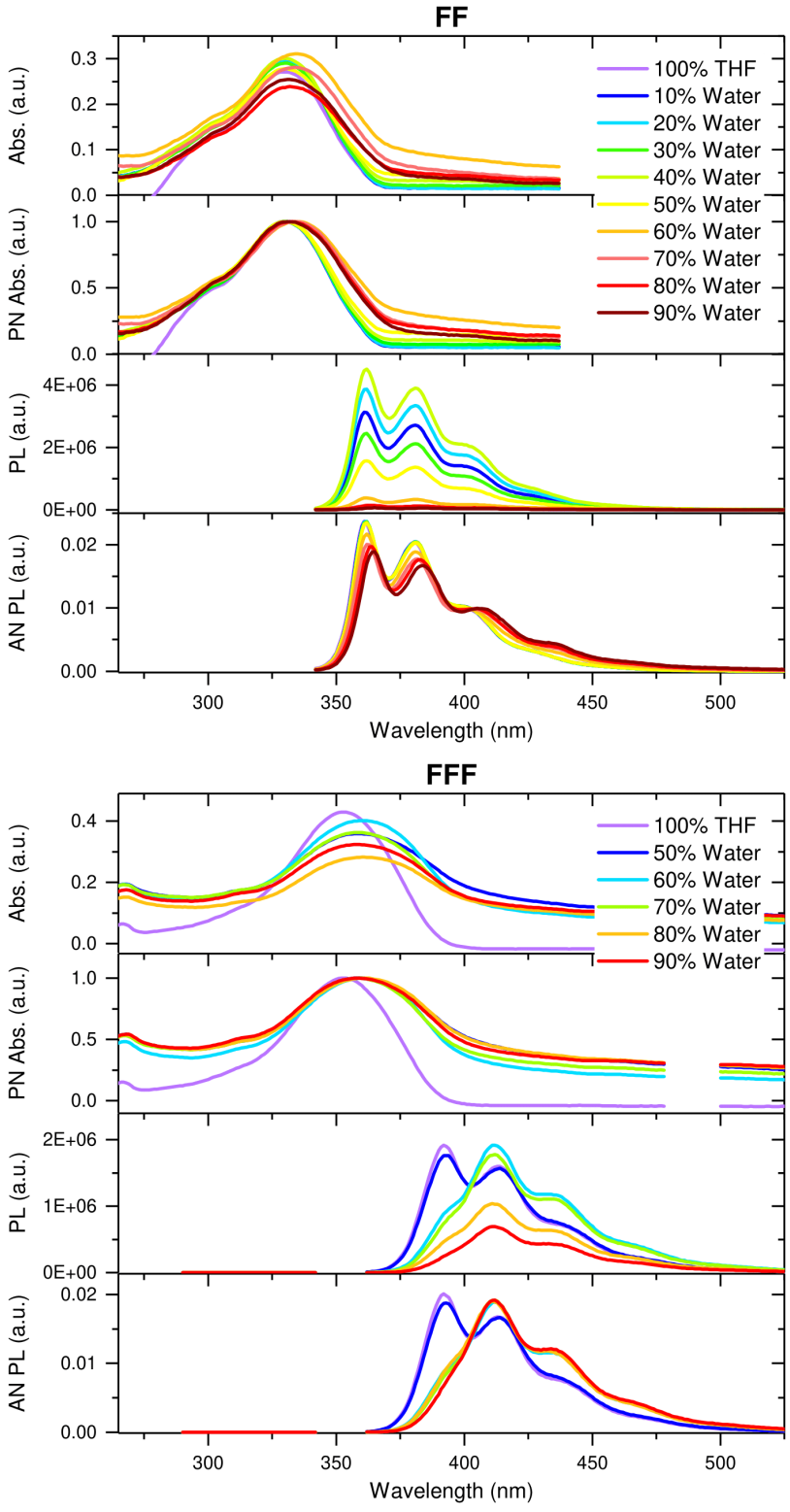



**Figure 4.3:** Abs., PN Abs., PL and AN PL of FF and FFF. Both FF and FFF exhibit little change in emission profile upon the addition of water, with persistent vibronic monomer emission and no indication of excimer formation. ACQ is prevalent at high water fractions.

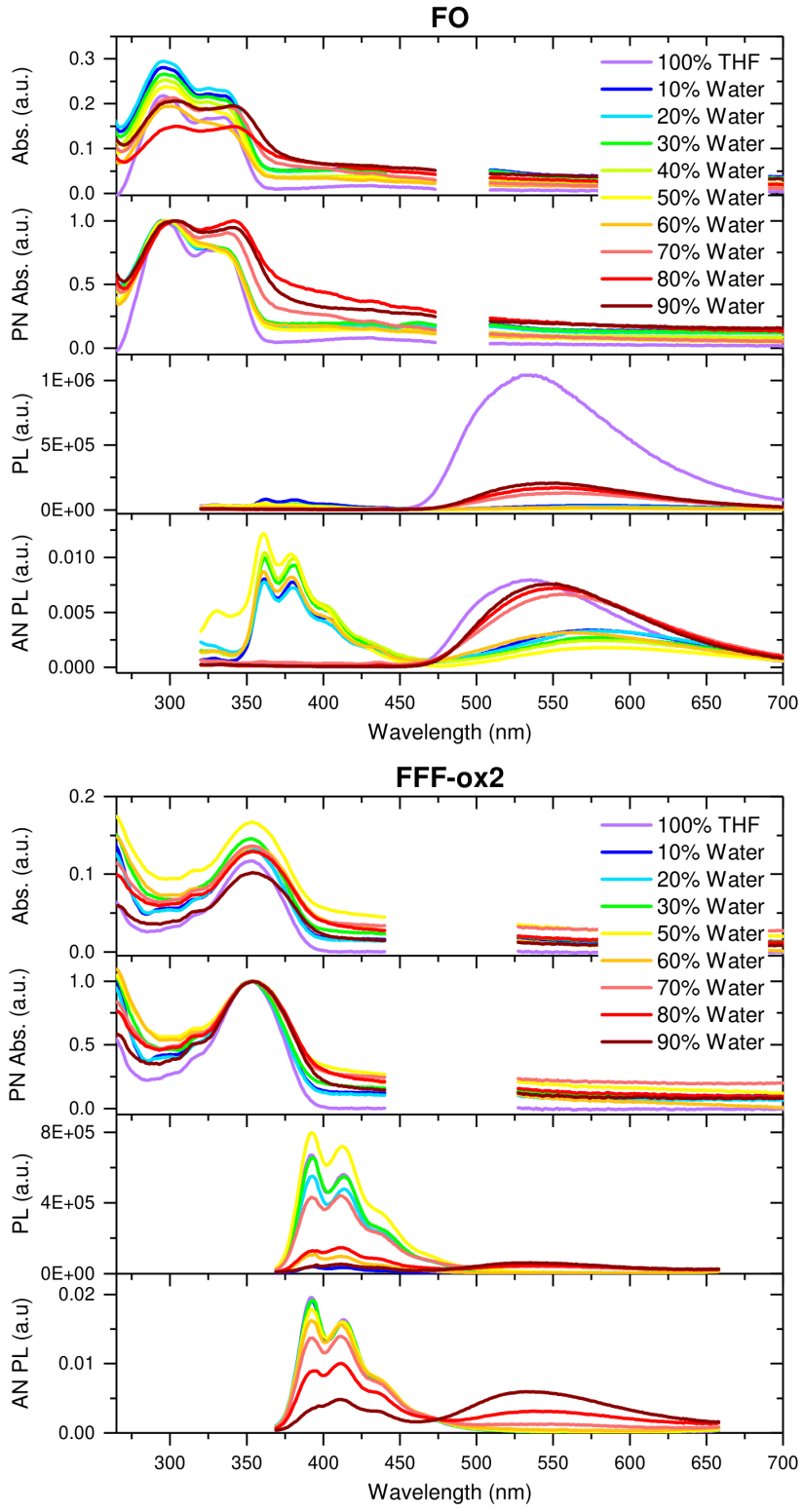



**Figure 4.4:** Abs., PN Abs., PL and AN PL of FO and FFF-ox2. The FO PL shows a rapid change from excimer dominated emission at 0% water, to monomer dominated when screened by water and then back to excimer at high water fractions. FFF-ox2 shows a resistance to aggregation until 90% water when excimers begin to form, indicating a low degree of oxidation.

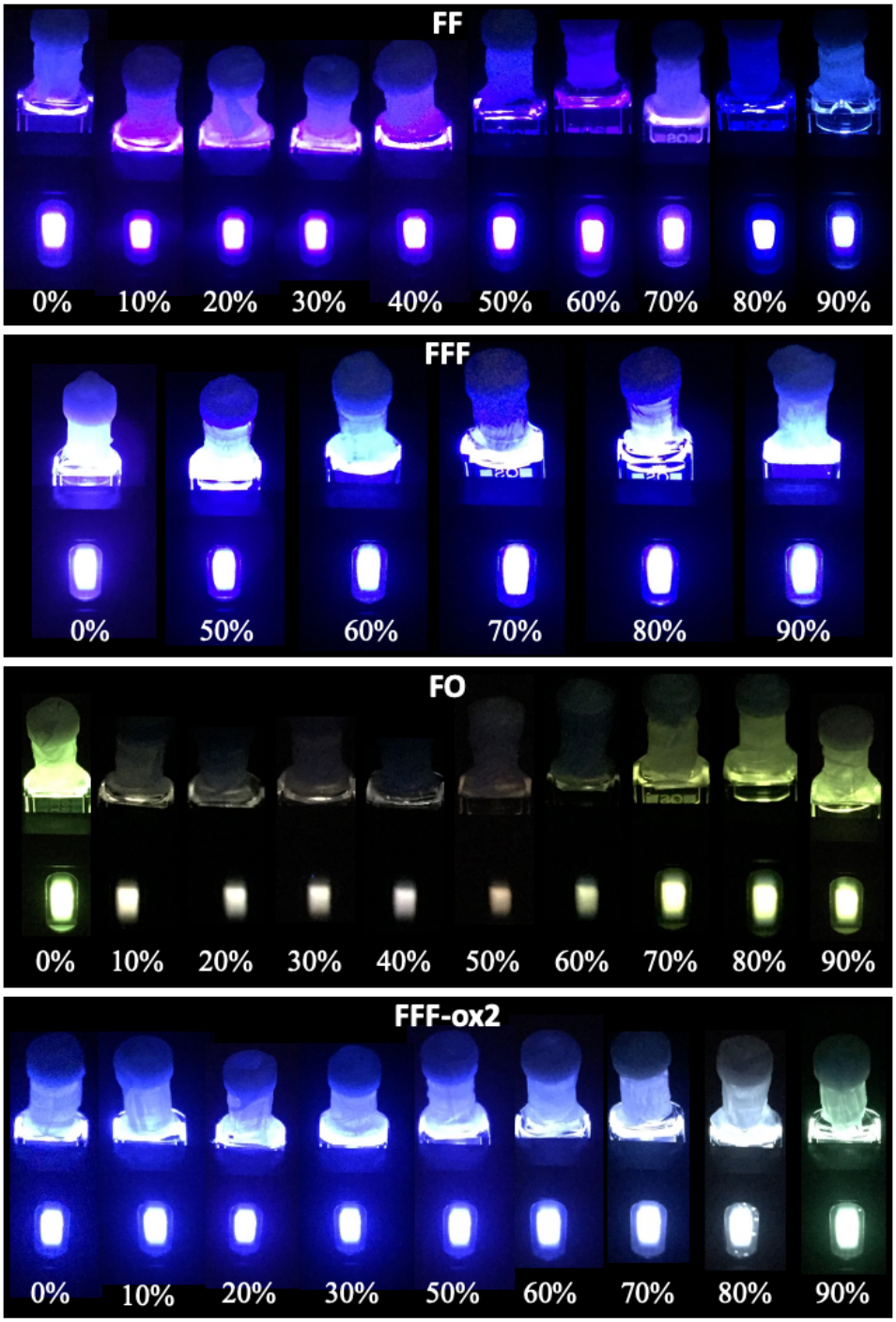



**Figure 4.5:** Photos of the PL taken with an iPhone 6 camera, normal to the Fluoromax excitation beam at a slit width of 14 nm. For FF and FFF there is little change in the emission colour, with a subtle shift from violet to deep blue.The drop in PLQE of FO as the water is added is obvious, with the new balance in monomer/excimer formation resulting in a shift from yellow-green to white emission. The FFF-ox2 maintains blue emission before shifting to a light green via a bright white, demonstrating the tuning capabilities of the solvent ratios.

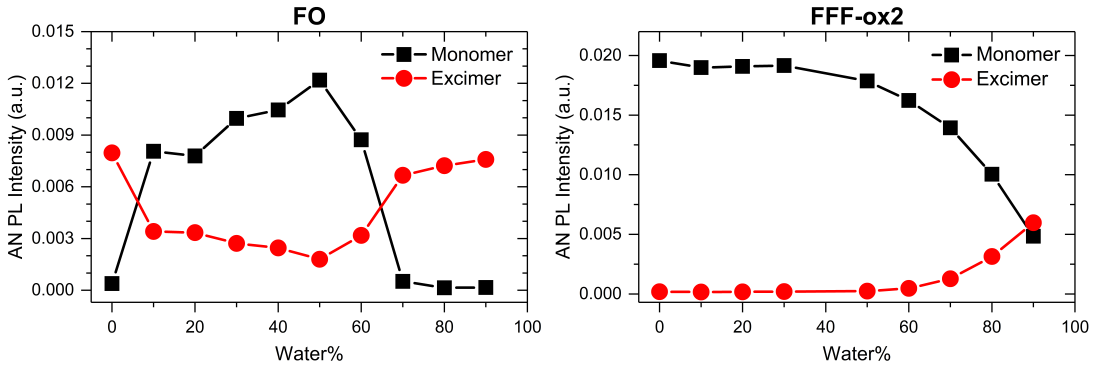



**Figure 4.6:** Monomer vs Excimer Intensities of FO and FFF-ox2 taken from the AN PL. The excimer emission quenching seen in FO and consequent increase in the monomer demonstrates the screening effect of the water. The return of excimers at high water fractions signals the controlled reaggregation caused by the FO's insolubility in water. Conversely for FFF-ox2, the monomer emission dominates until high water fractions, when the low concentration of oligomers containing fluorenone are able to form excimers due to controlled aggregation.

causing a redshift in the absorption [158], as increasing $\varepsilon$ can reduce the energy of the $\pi^*$ orbital. This redshift contributes to the broadening of the absorbance spectrum, due to the $\pi^*$ energies being distributed by water stabilisation. The solvent polarity strongly affects FFF as it has the most delocalised $\pi^*$ orbital, as well as FO due to its fluorenone unit allowing better mixing with water, which further exposes the fluorene-localised $\pi^*$ orbitals. The impact of the shift in the FFF solutions is clearly seen in their PL with a reduction in the $S_{1\text{-}0}$ 0-0 vibronic emission for solutions with over 50% water. For FO, the solutions with the largest redshift correspond to PL spectra with minimal monomer emission and so the impact of the shift is less visible. However, as shown in Figure 4.7**A**, the redshifts are non-linear with the water fraction. This could mean the polarity effect is being countered or shielded in some way by the aggregation of the oligomers.

Turning to the PL in Figure 4.3, as expected no excimer emission is seen in the FF and FFF solutions, with well structured vibronic emission from the monomers at 361 nm, 381 nm, 400 nm, 435 nm and 392 nm, 413 nm, 436 nm, 467 nm respectively, with ACQ introduced at high volumes of water. Both FF and FFF experience a very small Stokes shift due to their molecular rigidity allowing minimal lattice distortion. The FF AN PL experiences a small redshift starting at 60% water and

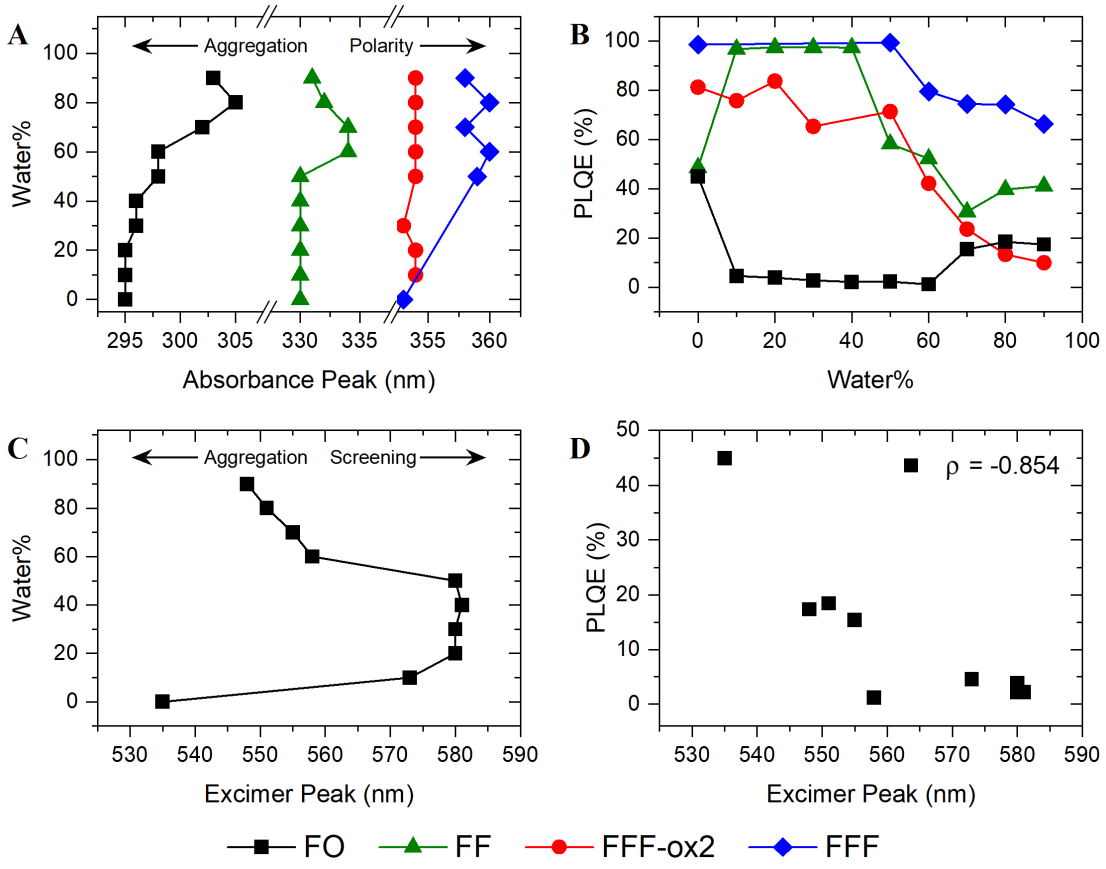



**Figure 4.7:** **A** shows the shifts in peak absorbance as the water fraction is increased. A redshift due to the increased polarity of the solvent mix occurs in low water fractions, until high fractions of water cause aggregation. For oligomers with 2 units, this results in a blueshift, as aggregation limits the impact of the water screening. For those with 3 units this blueshift is not seen, perhaps due to the larger volume of aggregated clusters enabling the screening effect to persist. **B** shows the PLQE profile of each oligomer solution as the water fraction increases. **C** shows the wavelength shifts in the excimer peaks of FO, with the large redshift again due to the screening of the fluorenone dipole by the water. The blueshift after 50% indicates the reduced impact of the water screening due to aggregation of the oligomers. **D** shows the correlation between PLQE and the excimer peak wavelength for FO, with a strong negative correlation of $-0.85$ indicating that the screening-induced redshifts have a direct impact on the PLQE.

continuing as the water volume is increased, due to the shift seen in the absorbance at the same values. This can be seen in Figure 4.5 FF images as a subtle change from blue-violet to deep blue at 80% water. Therefore it is deduced that FF is able to maintain separation until this water fraction.

The FFF AN PL experiences less of a redshift, but a distinct redistribution between 50% and 60% to the $S_{1\text{-}0}$ 0-1 and $S_{1\text{-}0}$ 0-2 vibronics at 413 nm and 436 nm as the absorbance shifts into the range of the $S_{1\text{-}0}$ 0-0 vibronic at 392 nm. This shift is more distinct than continuous, as the FFF absorbance broadens more than the FF from low water fractions. In Figure 4.5 FFF images, the blue-violet changes to deep blue from 60% water.

In the Rel. PL, the FF has a very low signal in THF solution, which increases with the addition of water, until ACQ causes it to drop again. This could be due to the low concentration of FF, with adding small quantities of water effectively causing a small local increase in concentration, as it reduces the volume of good FF solvent in the cuvette. This is not seen in FFF, which maintains a high Rel. PL signal from 0-70% water before ACQ starts. Despite their similar molar concentrations (Table 4.1), the larger volume of the FFF molecule could mean its threshold concentration for efficient emission is lower than for FF. Therefore if both of their concentrations were slightly higher, the signal of FF in THF solution may be higher, but ACQ may also begin at lower water fractions for FFF.

This effect is mirrored in the PLQE, shown in Figure 4.7**B**. In THF solution, the FF PLQE is roughly 50% before rising to near 100% for 10-40% water. From 50% water, the effect of ACQ is clear with the PLQE dropping to a low of roughly 30%. The FFF on the other hand maintains a near 100% PLQE from 0-50% water before dropping to to a low of roughly 65% due to ACQ. Interestingly the FFF appears to be more robust to ACQ than FF despite its larger volume. This could be due to its more numerous side chains effectively shielding the conjugated system from adjacent molecules, preventing the formation of non-radiative complexes until overcome with high water fractions.

For FO in Figure 4.4, the AN PL clearly shows the dominance of excimer emission in the THF solution, with the desired screening effect of water immediately evident as 10% water is added. The excimer emission is heavily reduced for 10%-60% water and the spectra are dominated instead by vibronic monomer emission at 361 nm, 380 nm and 402 nm. The intensities of monomer vs excimer were extracted in Figure 4.6. The FO starts with negligible monomer and strong excimer emission in THF solution, but a ratio of only 10% water is required to reduce the excimer and allow the monomer to dominate. This continues to an excimer low (and monomer high) at 50% water. From 60% water the monomer begins to drop and the excimer grow. For 70-90% water the excimer is once again dominant and the monomer emission quenched. This resurgence of the excimer, indicates that as more water was added, its screening effect was overtaken by the aggregation of FO within the small volumes of THF.

The AN PL of FFF-ox2 in Figure 4.4 is similar to that of FFF for low water volumes, with vibronic monomer emission at 392 nm, 413 nm and 436 nm, suggesting the concentration of fluorenone is minimal. However as detailed in Figure 4.6, from 70% water the excimer contribution grows, becoming more dominant than the monomer at 90% water, (though still considerably lower than in FO). This indicates that the second thermal oxidation method was somewhat successful in oxidising the FFF. The degree of oxidation must be small, as there was no evidence of excimer formation in THF solution, when the oxidised molecules would have been most free to form excimers. Similarly, the monomer emission survived even at 90%, amidst the aggregation that triggered the most excimer formation in FO (though we saw above that the FFF was more robust to ACQ which could have helped the monomer survive in this instance). As there was no evidence of excimers at 90% water in FFF or FF, the FFF-ox2 therefore behaved similarly to the FO with aggregation induced excimer formation at high water fractions, but without the presence of excimers in the good THF solution, (nor the total quenching of the monomer emission). This indicates that this solution based approach has potential for identifying very low levels of oxidation, which evade both the absorbance and PL in a good solution.

It can be seen in Figure 4.7**B** that the FO PLQE follows a profile similar to its excimer intensity of Figure 4.6, whereas the FFF-ox2 PLQE profile follows its monomer intensity profile. This agrees with the literature, in which the PLQE of fluorenone excimers was found to be higher than fluorenone monomers [158]. Although FFF-ox2 does not see an upturn in the PLQE as excimers form, it does see a slowing of the decline, suggesting a balance was forming between the onset of the excimers and ACQ.

However, although the intensity of the FO excimer emission recovers to the original level in Figure 4.6, its PLQE tells a different story. Figure 4.7**B** shows the PLQE of excimers formed at 70-90% water due to aggregation only reaches 17.35%, compared to 44.95% for those in good THF solution. To understand this we must delve further into the behaviour of the excimers at different water ratios. It can be seen in Figure 4.7**C** that the excimer emission of FO is not only switched on and off by the water screening and aggregation, but also appears to shift in energy depending on the water fraction. As soon as water is added there is a large redshift from 535 nm to 573 nm. This shifts further to 581 nm for 20-50% water. When excimers begin to form again at 60% there is a blueshift back to 558 nm, which gets steadily bluer before settling at 548 nm for 90% water. This trend may suggest that while excimers are indeed forming at high water fractions, they are not forming in the same environment as they did in good THF solution.

As described in Chapter 1, excimer formation is dependent on the density of monomers. In THF these monomers are free to move about the solution, and are attracted to each other due to the fluorenone dipole. In mixed THF-water solutions, both this movement and the dipole attraction are limited - the former by the monomer not being soluble in the the water, and the latter by the screening of the fluorenone dipole with the dipole moment of water. Therefore, although the aggregation of the monomer induces the formation of excimers, some of the fluorenone units will continue to be screened by the water, which by this point is the majority solvent. At the same time, some phase separation may start to occur between the water and oligomers aggregated in the THF, limiting the ability

of the water to access the fluorenone unit and screen the dipole. These results therefore present a balance between excimer formation and dipole screening, the former constricting the latter.

This concept is supported by the peak wavelength of FO excimers *continuing* to blueshift between 50% and 90% water. This continuation suggests that the impact of the water screening is reduced as the oligomers aggregate, gradually reducing the screening-induced redshift. On the other hand the PLQE increases from nearly 0% at 50% water to a plateau of 17% from 70%-90% water, suggesting that while the reduction in dipole screening is continuous, the formation of excimers is not, due to the limitations of solubility mentioned above. The redshift is therefore not indicative of a different type of excimer, but a measure of the screening function of the water. As aggregation kicks in, the excimer formation limits the ability for water to screen the dipole, and so the redshift is decreased.

The FFF-ox2 PLQE in THF solution is high at $\sim 80\%$, but lower than the near 100% of FFF indicating the presence of fluorenone units. As water is added it declines steadily, experiencing ACQ amongst its highly efficient FFF monomers, beginning at 60% water. The onset of excimer formation at 70% corresponds with a slight upturn in this decline, suggesting a new balance between the ACQ and excimer.

Figure 4.7**D** shows a correlation plot describing the relationship between PLQE and excimer peak wavelength for FO. While there is inherent error in this approach, with the small sample size of the solutions and the breadth of the excimer emission spectra, the correlation appears to support the above analysis. A strong negative correlation of $-0.85$ between the PLQE and peak wavelength can be seen for FO. This reinforces that the redshift of the excimer signals a higher prevalence of water screening, as the lower PLQE is a result of the reduced fluorenone-fluorenone attraction and subsequent reduction in excimer formation.

## 4.4 Conclusion

### 4.4.1 Summary

The results presented above support the hypothesis described in Section 4.1.1 in its entirety, and succeeded in the aims to screen the excimer emission with water, and control the excimer formation with aggregation. The screening effect was clear, with a large drop in FO's PLQE and PL excimer contribution when water was added, with an accompanying rise in monomer emission. The aggregation was also well controlled with a gradual drop in monomer contribution corresponding to a rise in the excimer, the former fully quenched at high water fractions with a resurgence in the PLQE.

As expected, the PL intensities of FFF and FF were unaffected by the water polarity, but displayed ACQ as the aggregation was increased. FFF-ox2 behaved similarly to FFF and FF at low water fractions, but similar to FO as the water fraction was increased, with evidence of excimer formation at the highest water fractions. This indicated that small amounts of fluorenone had been formed during the thermal oxidation process. These low levels of oxidation meant the emission was dominated by highly efficient FFF molecules, giving a strong blue emission from the monomer not seen in the FO solutions.

As expected there was a large contrast between the PLQE of FO and the fluorene oligomers, with the former always remaining lower than the latter. Between FF and FFF there was some evidence of concentration dependence on the PLQE, with the smaller molecules having a lower PLQE in good solution than in 10% water solution due to a reduction in their solution volume and an effective increase in concentration. The fluorene oligomers however succumbed to ACQ due to their inability to form excimers, providing a contrast to the FFF-ox2 PLQE, the decline of which was slowed by the excimer formation at high water fractions.

Figure 4.5 demonstrates the large range of emission intensities and colours achievable through varying the oxidation level. If low, the highly efficient blue fluorene emission dominates, and when high, the yellow-green fluorenone excimer takes hold, though at a lower emission strength. When the contributions of the

fluorene monomer and fluorenone excimer are balanced, as seen for FFF-ox2 80% water, a bright white emission can be achieved. This demonstrates the capability for broad tuning of emission with high PLQE offered by fluorene oligomers, that could be controlled solely by the degree of oxidation.

From the FO emission in Figure 4.5 it can be seen that during the screening phase of 10%-40% water, the emission appears white as the monomer and excimer emission becomes balanced. This indicates the excimers were not fully screened by the water, and so further work could focus on fully quenching their emission. As the excimer contribution of 10-40% water is roughly constant, this quenching would likely require a lower concentration of starter solution. However reducing the water fraction below 10% at the current concentration would still be interesting to find the lower-bound water fraction for the onset of the screening, and also the point at which the monomer and excimer are balanced.

Similarly, increasing the water beyond 90% to test whether the excimers are able to return to the strongest, bluest form seen in THF solution, before reaching a water fraction at which they fall out of solution, would be useful to understand the limits of the technique, as well as the upper-bound of the water screening. Though, due to the solubility limitations described above it seems unlikely that the screening would not impact the excimer formation above 90% water.

### 4.4.2 Tunability and Oxidation

Further work to enable full control over the balance of monomer and excimer emission would also allow for careful tuning of the PLQE and emission colour, and enable the emission to be tuned across a large range of the optical spectrum from blue through white to yellow-green to green, all from a single fluorene material. As well as investigating different concentrations, controlling the degree of oxidation would be key to this tuning, as seen when comparing FO and FFF-ox2.

Oxidation is also central to controlling the PLQE, as the results above showed the PLQE was directly linked to the oxidation level. Indeed, as the PLQE profile matched that of the monomer and excimer intensity for FFF-ox2 and FO respectively,

there is likely a level of oxidation for which the PLQE is consistent across the screening and aggregation phases. We saw that for slightly oxidised FFF (FFF-ox2) the PLQE never reached the 100% achieved by FFF, and so it follows that there may be a point of oxidation for which the PLQE is reduced to the level that could be matched by the fluorenone excimers.

Therefore it would be interesting to investigate the emission and PLQE of different oxidation levels, and identify a method for reliably quantifying and reproducing the fluorenone concentration. Future work in controlling the oxidation, perhaps using UV photo-oxidation instead of thermal could help achieve this level of control, and may be able to identify a solution and fluorenone concentration for which the full range of emission colours were possible at a consistent PLQE. Alternatively it may be possible to achieve only a small colour range but a large contrast in PLQE. This work should be conducted on both FF and FFF, as from the results seen above, the smaller molecular size of FF may lend itself to more readily forming excimers than FFF at a low oxidation level.

Future studies could then investigate the effect of water screening as the fluorenone content ranges from 0% in FF to 50% in FO, with various degrees of oxidation studied in between. Alternative methods of oxidation may be so successful as to achieve an OO molecule, for which the excimer formation may be very difficult to screen due to its very strong tendency to stack. Regardless, achieving a high level of control in the solution and fluorenone concentration could lend this technique to a variety of sensing applications, for which a large colour range, PLQE contrast, or both may be desired.

### 4.4.3 Sensitive Oxidation Testing

As well as identifying potential sensing capabilities, this work has discovered a novel technique for identifying very low levels of oxidation. In THF solution the FFF-ox2 looked indistinguishable from FFF. It was only at high water fractions that the fluorenone became apparent via the formation of excimers. This test is

therefore more sensitive than typical spectroscopy methods, and apparently capable of identifying extremely small concentrations of fluorenone.

Further work could identify whether the technique could be applied to other oligomers with excimer forming defects. Alternatively the current version of the technique could be adapted to polymers, to identify low levels of the fluorenone defect commonly seen in PFO [92]. This adaptation would require considerable testing, as polymers behave differently to oligomers in solution due to their ability to form a variety of molecular conformations. Additionally, entanglements within or between polymer chains could result in more numerous meeting points for fluorenones, or the chains could coil in such a way as to screen the oxidised units from other chains. At high water fractions, the fluorenones may also be drawn to the outside of the coils, behaving like micelles [160], which may hinder their ability to come together. Each of these scenarios could either enable or hinder excimer formation.

Solubility and concentration would also need to be considered as the large $M_W$ of polymers would require more THF molecules to remain in solution. Therefore the first step would be identifying a cuvette concentration suitably low to prevent precipitation at high water fractions, but high enough to enable sufficient excimer formation.

The polymer PL may also be less structurally defined than the oligomer monomer emission, with its breadth potentially making it more challenging to distinguish and interpret the screening and aggregation effects of the technique. In short, a rigorous study of all of these parameters would be required before the technique could be applied to quantifying oxidation in polymers.

To conclude, the results described above demonstrate a proven method for switching off the stubborn excimer emission of fluorenone, and discusses further methods for achieving better control of oxidation and aggregation in fluorene. The high tunability enabled by this control illustrates the wealth of opportunities for further study of the technique, which holds a lot of potential in a variety of sensing applications. The technique is also very promising as a novel sensitive identification method for fluorenone and other excimer-forming defects.

# 5

# Development of Microscale Photoluminescence

## Contents


**5.1 Introduction . . . . . 103**
**5.2 Design . . . . . 104**
5.2.1 Set-up Overview . . . . . 104
5.2.2 Data Collection & Structuring . . . . . 107
5.2.3 Key Components & Alignment . . . . . 109
**5.3 Characterisation . . . . . 115**
5.3.1 Resolution . . . . . 115
5.3.2 Theory of Gaussian Beams . . . . . 117
5.3.3 Knife Edge Measurements . . . . . 119
5.3.4 ThorCam Measurements . . . . . 122
5.3.5 Beam Parameter Calculation . . . . . 122
**5.4 PFO Tests . . . . . 126**
5.4.1 Power Tests . . . . . 126
5.4.2 Stability . . . . . 129
**5.5 Conclusion . . . . . 129**


## 5.1 Introduction

To analyse the phase change achieved following Dip-Pen Patterning of PFO, the local PL about the patterned region must be studied. To achieve this, a microscale photoluminescence set-up was designed, to map an image of the emission across

the patterned regions. The set-up was designed with the following aims:

1. **High Resolution:** The aim of this work is to pattern structures at the order of the excitation wavelength, 440 nm. Although many of the patterns will exceed this size, the set up must be have sufficiently high resolution to identify such feature sizes.

2. **Sensitivity:** The PL is to be measured in an oxygen environment. As is common with blue emitters, photo-oxidation by overpowered UV excitation degrades the material, and distorts the luminescence. As described in Chapter 1, G-band emission can arise from photo-oxidation in PFO. Therefore the set-up must be sensitive enough to enable the material to be excited delicately, yet provide sufficient signal.

3. **Contrast:** The set-up is required to identify a change in phase. As this is not a sharp phase change, (in both patterned and non-patterned material the PL will comprise a convolution of phases) there must be enough contrast in the right regions of the spectra to sufficiently image the change.

This chapter will focus on these aims, and discuss the suitability of the set-up for analysing PFO. The question of if this set-up can supply enough quality data to analyse the patterns, and whether PL data can provide the information needed to fine-tune the Dip-Pen process will be answered in the following chapter.

The set-up design is described below. The components used are listed in the Appendix. They are referred to here as they are shown in Figure 5.1.

## 5.2 Design

### 5.2.1 Set-up Overview

The beampath starts on the RHS of Figure 5.1 with a pulsed laser producing a 400 nm beam at 77.9 MHz. The beam, shown in violet, was focussed into an optical fibre with a 20× 0.4 NA objective. The fibre transmitted the beam with a high quality Gaussian profile, which was essential to achieve a spot-like excitation at the required resolution.

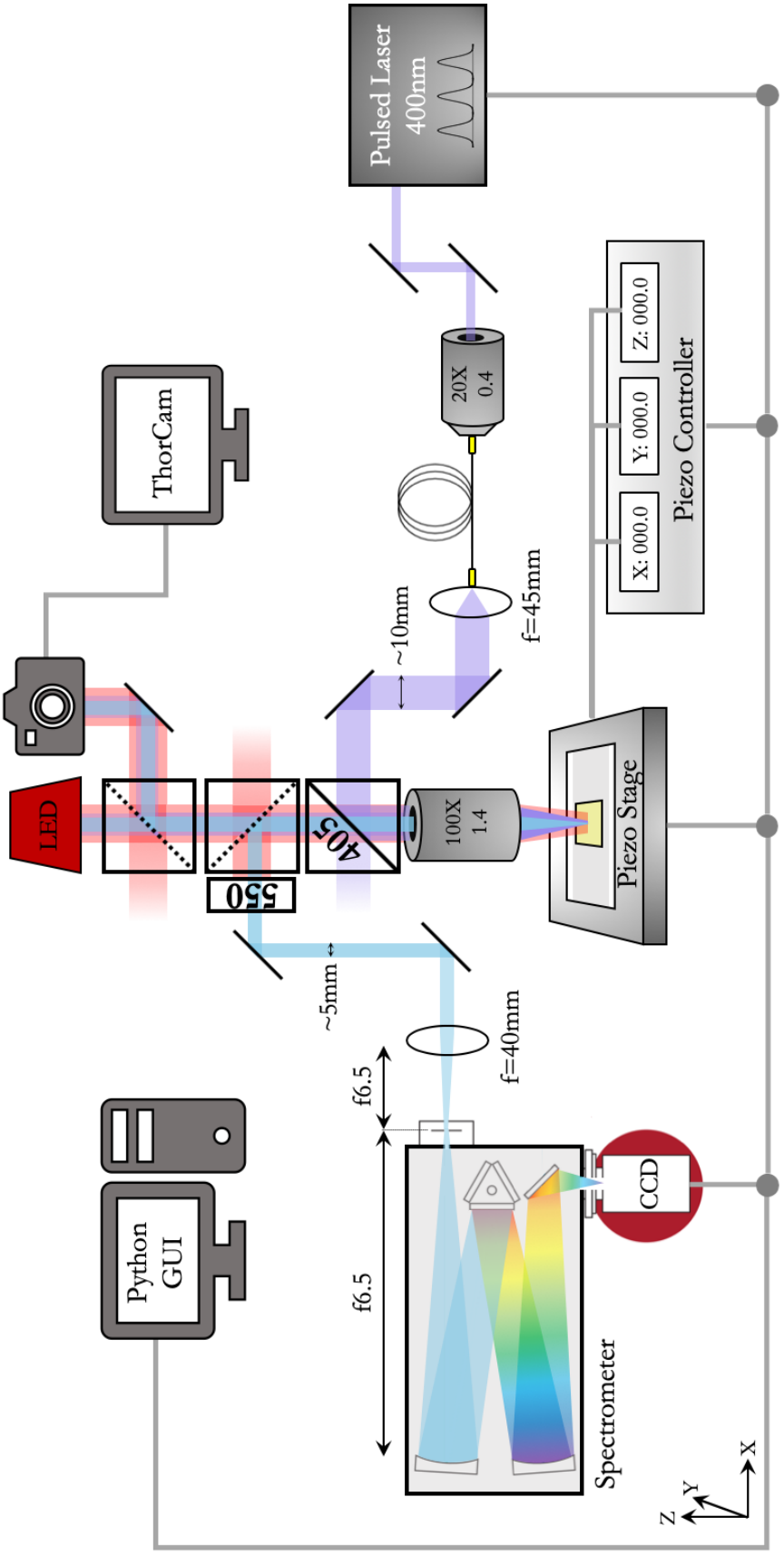



**Figure 5.1:** Design of the micro-PL set-up described in this chapter. For clarity, the distance between the 1.4 NA objective and sample has been increased, and the oil connecting the two has been omitted.

After exiting the fibre the beam was expanded to a cross section of around 10 mm by a 45 mm focal length lens. The reason for this expansion is described further in Section 5.2.3. The beam was then directed vertically upwards with 2 mirrors and then downwards into the 100× 1.4 NA oil objective by a 405 nm dichroic mirror. This arrangement was necessary to allow the piezo stage to rest horizontally on the optical table for stability.

The 405 nm dichroic was required to both direct the laser, and allow the emission from the sample to pass through into the collection path. A dichroic was decided to be a better option than a beam splitter to ensure minimal loss of both the laser and the emission.

A high NA objective was used to increase resolution. Oil was required to connect the objective aperture to the sample to match the high refractive index of the objective and collect the full cone of light from the sample, ($n_{\text{oil}} = 1.518 > n_{\text{air}} = 1$). This was omitted from the diagram for clarity.

The laser was then focussed to a small spot by the objective, exciting a small area of the sample which then emits into the collection path, shown in light blue. This emission passes through the 405 nm dichroic to meet a beam splitter. A splitter was used here to allow the emission to be directed down to the spectrometer, but also for the small amount of the laser spot transmitted through the 405 nm dichroic to remain visible to the monitoring camera. The monitoring system comprised a red LED, CCD camera and ThorCam software, and was operated continuously to monitor the laser focus. It was also essential for navigating about the sample, utilising the LED to illuminate the surface.

The red LED light was removed from the collection path with a 550 nm filter, leaving only the emission and a small signal from the laser (not shown for clarity). The emission was then focussed into the spectrometer, where it was mapped onto a CCD and the spectrum recorded. After each spectrum was taken, the piezo stage moved to a new map position where the next spectrum was taken etc.

The CCD, spectrometer, piezo stage, piezo controller and the laser were all controlled centrally by a python GUI. This allowed manual intervention to be

limited to finding initial feature positions and lowering the oil objective to a rough focus. The sensitivity of the set-up meant that further manual tweaking would have moved the sample out of range and/or altered the focus to an unknown position.

### 5.2.2 Data Collection & Structuring

The mapping data collection process is described in Figure 5.2, in which an example $3 \times 3$ gridpoint map is constructed.

Following definition of mapping parameters step-$x$, step-$y$, length-$x$, and length-$y$, the piezo stage moves to the start position (0, 0). It then proceeds to move in increments of the step size to the final position (2, 2) in a snaking manner. This was implemented to limit large jumps in the piezo movements, which could upset the focus and increase the position error.

At each position the spectrum is recorded and saved in a new file. The first step of the analysis was to combine these into a single file, as shown in Figure 5.2:**2**. If separate files were not created, the 'snaking' nature of the data collection would make it more challenging to construct the map array, as the order would have to be flipped for every evenly numbered row. However, this was avoided by combining the files based on their filename instead of file creation time. By adding files in order of their $x$-coordinate it was possible to construct the map array by simply specifying a new row every 'length-$x$' of columns, resulting in the correct map configuration. The order of data *collected* is shown in Equation 5.1, where the square brackets contain the map rows. The order of data *combined*, is shown in Equation 5.2. The order difference is highlighted in bold in the spectra columns "**S6 S5 S4**" of Figure 5.2.

As the wavelength range of the spectrum was projected across the CCD's 2048 pixels, the wavelength column were non-integers, meaning multiple rows of data were attributed to a particular wavelength. The file was therefore condensed and averaged to integer wavelength values to simplify the phase-selective plotting and reduce noise, as shown in Figure 5.2:**3.a**. An example output of this process normalised about the laser wavelength can be seen in Figure 5.3.

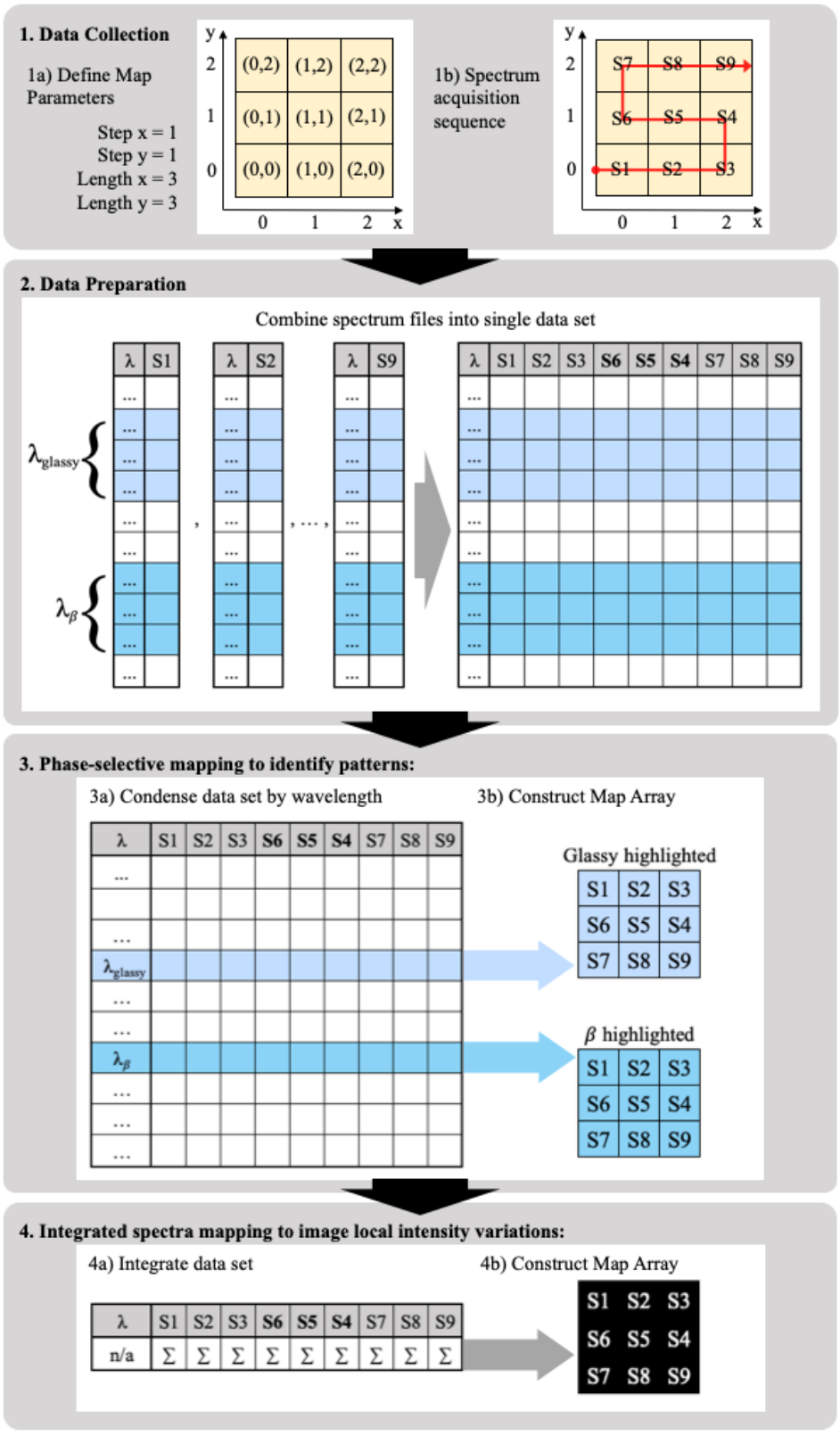



**Figure 5.2:** Micro-PL mapping data acquisition and structuring process.

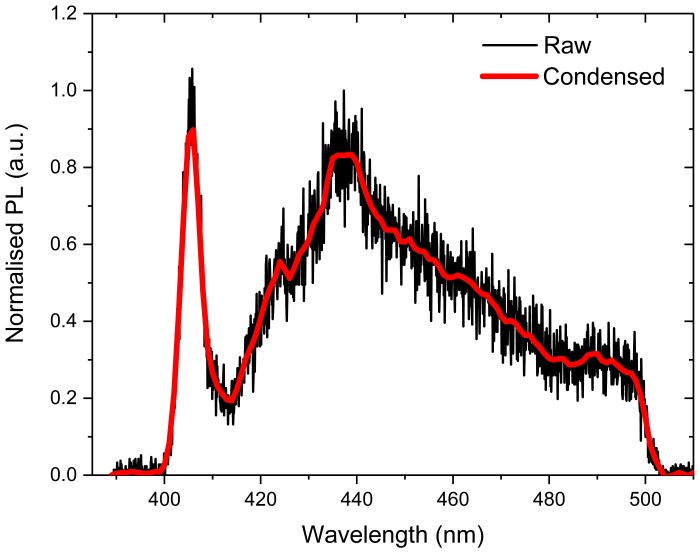



**Figure 5.3:** Condensed PL signal. Example showing the result of condensing the data to integer wavelengths.

$$[(0,0)(1,0)(2,0)],[(2,1)(1,1)(0,1)],[(0,2)(1,2)(2,2)] \tag{5.1}$$

$$[(0,0)(1,0)(2,0)],[(\mathbf{0},\mathbf{1})(\mathbf{1},\mathbf{1})(\mathbf{2},\mathbf{1})],[(0,2)(1,2)(2,2)] \tag{5.2}$$

Once combined and condensed, a wavelength of interest was defined (such as $\lambda_\beta$), and the row containing this wavelength was extracted (Figure 5.2:**3.a**), and reordered into a 2D map array (Figure 5.2:**3.b**). From these arrays, surface plots show the phase-selective PL map, highlighting the areas with strong signal from the chosen phase. An integrated map could also be constructed, by integrating each spectrum in place of selecting a wavelength (Figure 5.2:**4**). These maps were plotted when local intensity variations across the map area were of interest.

### 5.2.3 Key Components & Alignment

#### Optical Fibre

Figure 5.4**A** shows a ThorCam image from an earlier version of the set-up without fibre coupling the laser beam. The beam was large, poorly aligned and shapeless. To improve the beam quality the laser was coupled into a single mode fibre. As the

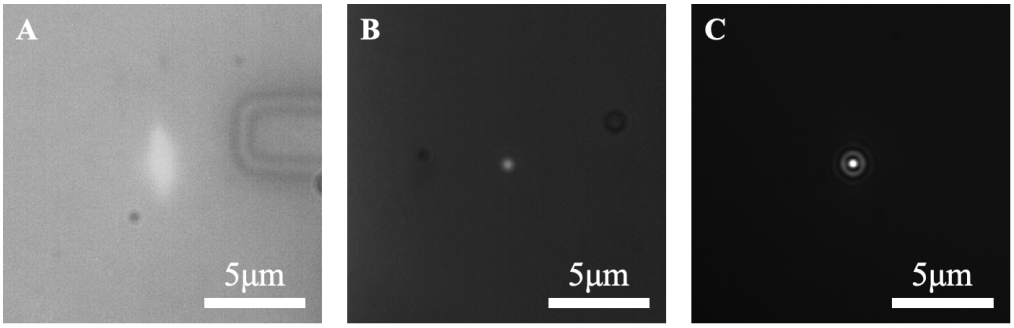



**Figure 5.4:** Improvements in beam quality due to fibre coupling. **A** shows the raw laser spot, **B** shows the fibre-coupled laser spot and **C** shows the fibre-coupled laser spot with the addition of the 45 mm focal length lens to overfill the objective. The samples were PFO for **A** and InGaN for **B** & **C**.

fibre was single mode, it only transmitted the $TEM_{00}$ mode of the beam, producing a high quality Gaussian profile. To fibre couple the laser, a 20× objective with NA = 0.4 was used to focus the beam. Aligning the beam into the fibre was achieved by cycling through microscale alterations of the $xyz$ axes of the fibre coupler, and adjusting the two oval mirrors to maximise the power output of the fibre. The result can be seen in Figure 5.4**B**, where the fibre coupled laser is immediately smaller, Gaussian and more spot-like.

### Objective Filling

$$f_0 = \frac{\omega_0}{f \sin \theta_{\max}} \tag{5.3}$$

To fully utilise the oil objective, it was necessary to have a sufficiently high fill factor ($f_0$). Figure 5.5 shows modelled outputs of an NA = 1.4 objective with various $f_0$. It is clear that an underfilled objective produces a broad beam profile, with little Gaussian character. When $f_0 = 1$, despite matching the objective aperture, the beam profile is still broader and less intense than $f_0 = 2$. Therefore to achieve the best resolution, it was necessary to overfill the objective. The 45 mm focal length lens was placed at the fibre output for this purpose, expanding and collimating the beam to a diameter of $\sim 10$ mm. The objective aperture was 8 mm, and so a beam profile between $f_0 = 1$ and $f_0 = 2$ was achieved. The resultant beam can be seen in Figure 5.4**C**, clearly showing a more intense and defined Gaussian.

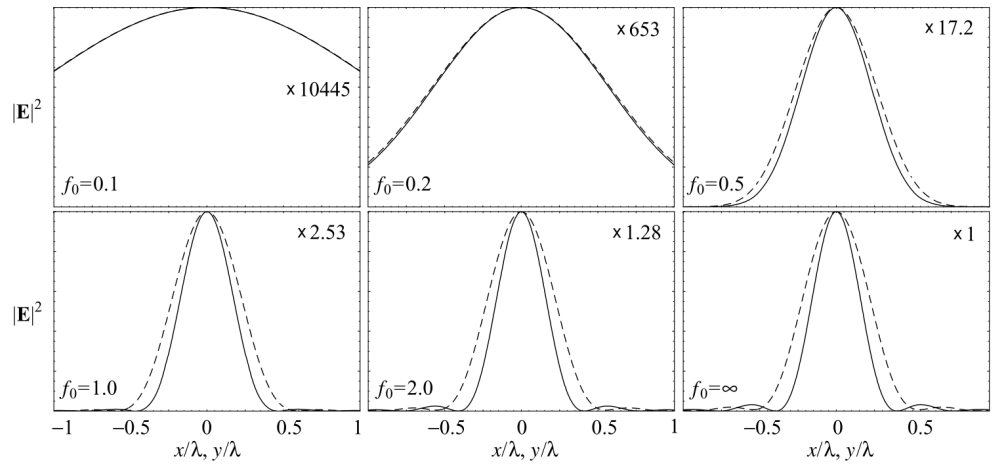



**Figure 5.5:** Impact of the objective fill factor on the beam profile. Normalised intensity plots of the focal plane of an objective similar to the one used here (NA = 1.4, n = 1.518) with different fill factors. The dotted and solid lines show the $x, y$ cross-sections respectively. In this set-up, the beam profile is not expected to differ in $x$ and $y$. From [161].

After the 45 mm focal length lens, repeated manual adjustment of the vertical pair of circular mirrors was used to align the laser beam through the centre of the objective to produce the circularly symmetric Gaussian shown in Figure 5.4**C**.

### Spectrometer & CCD

For the collection path, the vertical oval mirrors following the 550 nm filter were adjusted to centre the beam on the 40 mm focal length lens. The purpose of this lens was to achieve good spectral resolution by optimising the collection of light at the spectrometer entrance port. As well as minimising loss by focussing the collection beam into the slit, it was necessary to choose the $f-$number of the focussing lens to match that of the spectrometer. This ensured the full width of the 1st directing mirror was used, which in turn maximised the spread of the beam hitting the grating, improving the spectral resolution. The $f-$number, $N$, is given by,

$$N = f/D \tag{5.4}$$

where $f$ is the focal length of the lens, and $D$ is the aperture of the source [149]. Within the spectrometer, $f$ is analogous to the distance between the slit and first curved mirror (along which the beam diverges), and $D$ is equivalent to the width

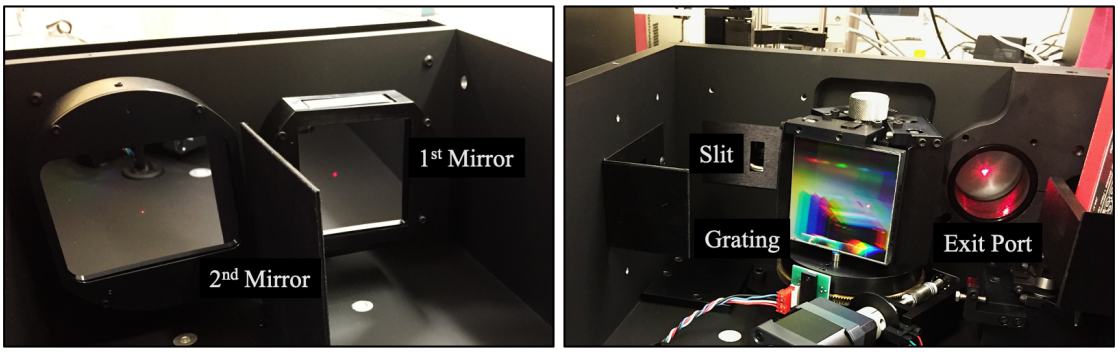



**Figure 5.6:** Internal spectrometer alignment. The HeNe laser can be seen hitting the 1st mirror, grating, 2nd mirror and finally the exit port.

of the mirror. On the side of the lens focussing the beam into the spectrometer, $D$ is the collection beam diameter. Due to its passage through the filters and beamsplitter, the collection beam was much less intense than the excitation beam, and very dim to the eye. Therefore the diameter was challenging to measure and was estimated at 5 mm. As this was a rough measurement, the following calculation was only done to give an indicator of the required focal length of the lens, not a precise value. The appropriate focal length was then determined by,

$$f = ND = 6.5 \times 5 = 32.5\,\text{mm}.$$

During optimisation, a 40 mm focal length lens was found to give the largest signal, suggesting that the 5 mm diameter measurement was not far off of the back-calculated value of 6.2 mm.

A bright HeNe laser was used to check the internal alignment of the spectrometer. The laser was attached to follow the collection path, entering the spectrometer via the slit. The spectrometer was positioned so the beam was centred on the exit port, ensuring it would be fully collected when deflected to the CCD. Due to the spectrometer design this required the beam to meet the 1st mirror and grating *off* centre, resulting in the beam meeting the 2nd mirror and exit port *on* centre, as shown in Figure 5.6. From this, the position of the spectrometer relative to the caged set up was considered well-aligned, and the spectrometer was fixed in position.

To align the CCD, a IntelliCal HeAr lamp from Princeton Instruments was used. The 2D output of the CCD translates the lamp spectra to spectral lines,

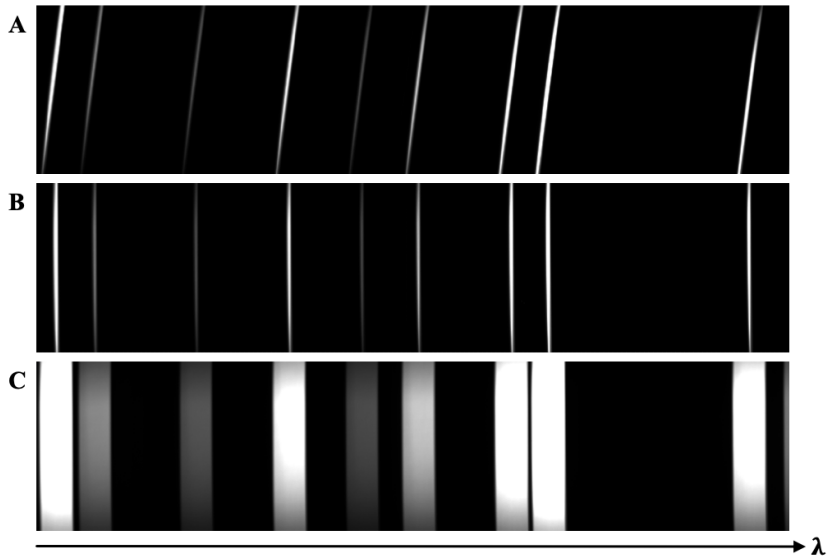



**Figure 5.7:** HeAr spectral lines for CCD alignment. **A** shows a misaligned CCD with slit 25 µm, **B** is aligned with slit 25 µm and **C** is aligned with slit 1000 µm.

thus allowing the correct orientation of the CCD relative to the output port to be identified. Figure 5.7**A** shows a poorly aligned CCD, with the lines clearly skewed, whereas **B** and **C** show the final CCD alignment for slits 25 µm and 1000 µm respectively. The 25 µm lines show slight vertical bowing, but are overall vertically orientated and symmetrical. This bowing is not an issue for spectrometry, as the emission will be recorded only within the central rows of the $512 \times 2048$ area, so there will be little change in calibrated intensity.

### Beamsplitter Suitability

As described above, a beamsplitter was used to allow continuous monitoring the sample surface during measurement. To understand what impact this could have on the PL data, the transmission of the beam splitter was measured at the angle it meets the beam in the set-up: 45°. Apparatus to measure the reflection was only available at an angle of 6°, so the reflection at 45° was assumed to be reciprocal to the transmission. However, this is not precise due to inevitable scattering and absorption of the reflective layer, and so the data only be considered a rough guide for assessing the impact on the PL.

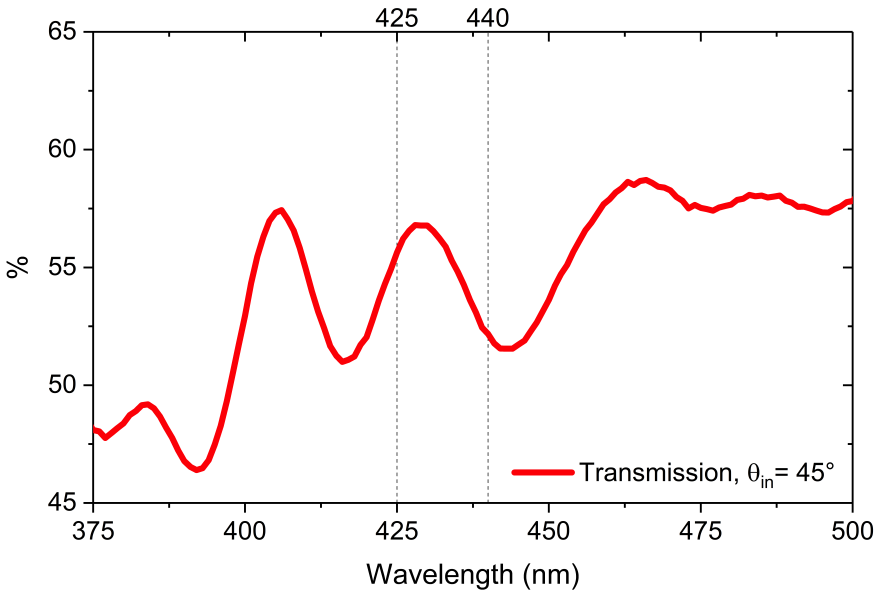



**Figure 5.8:** Beamsplitter transmission across the wavelength range of interest measured at 45°, matching the angle of incidence present in the set-up.

In Figure 5.8, it can be seen that within the PL range of PFO, $400 - 500\,\text{nm}$, there is some fluctuation in transmission. At $\lambda_{\text{glassy}}$ (425 nm) T=56% and at $\lambda_\beta$ (440 nm) T=52%. Therefore it is expected that $R_{\lambda\text{glassy}} < R_{\lambda\beta}$, and the $\beta$ phase emission will be preferentially reflected along the collection path. If the $\beta$ phase also had spectral features about 425 nm this would have been an issue, as it could have altered the PL distribution collected for each phase. However the $\beta$ phase has no emission in this range, so this contrast in reflection only serves to increase the contrast between the phases by effectively filtering some of the glassy signal. This was advantageous, as measuring contrast between the phases - not their relative efficiency - was a key aim of the set-up.

Another consideration of the beamsplitter was polarisation of the emission, as the reflectivity change across polarisations is larger for beamsplitters than other mirrors and dichroics (see Appendix Figure 5). The $\beta$ phase has been shown to be more readily polarised [108], however the alternative polarisations still exhibit the same spectral features. Therefore even if one polarisation were to be preferentially reflected, it would only alter the resultant intensity of the emission, and not distort the spectral profile. Any remaining discrepancy could potentially be corrected,

however the polarisation of the beam hitting the splitter is not known nor possible to measure in this set-up, and the integrity of the data could be affected.

## 5.3 Characterisation

### 5.3.1 Resolution

Maximising resolution is a key aim of the set-up. Here, we attempt to characterise the beam at its smallest possible spot size. Due to the wave nature of light, it cannot be focussed to a point, rather at the focal length it converges to a spot. This spot size is determined by the numerical aperture (NA) of the objective used to focus the beam. The NA is given by $n \sin\theta$ [161], so a high NA will produce a wider cone of light, and as such a smaller spot. The theoretical minimum spot size of an objective can be determined by the Abbe limit, shown in Figure 5.9, and calculated from Equation 5.5 [162], which describes the closest proximity with which 2 adjacent beams can appear distinct.

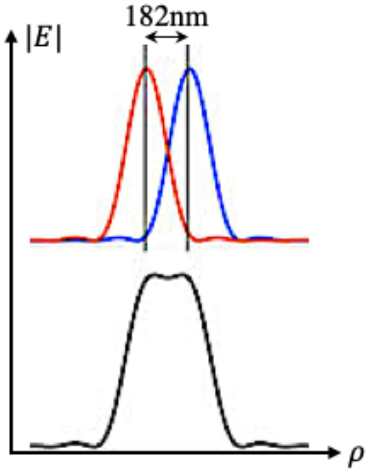



**Figure 5.9:** The Abbe diffraction limit for a Gaussian laser beam with $\lambda = 510\,\text{nm}$, NA = 1.4. Adapted from [163].

$$d = \frac{\lambda}{2n \sin\theta} = \frac{\lambda}{2\text{NA}} \tag{5.5}$$

Figure 5.9 demonstrates the Abbe limit of diffraction to be 182 nm for a laser beam with $\lambda = 510\,\text{nm}$ at NA = 1.4. This is the closest proximity that these

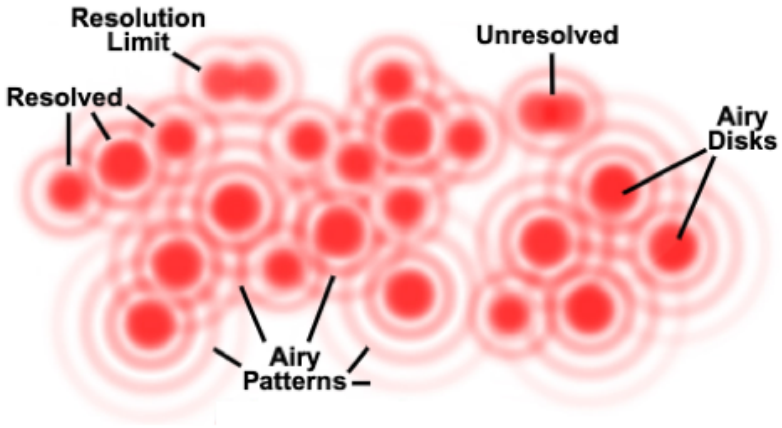



**Figure 5.10:** Demonstration of the diffraction limit of Gaussian beams. The diameter of the central airy disc determines the resolution. The limit of the resolution is characterised by a small overlap in the discs, but greater overlap will make them unresolvable. Adapted from [164].

adjacent beams, shown in red and blue, can have to maintain resolvability. The total signal shown in black shows the subtle difference in the intensity that remains to distinguish the peaks.

The laser propagates with a profile characterised by an intense central Gaussian peak known as the Airy disc. As shown in Figure 5.9, some overlap of Airy discs is permitted by the Abbe limit. When imaging features such as Dip-Pen patterns, the ability of the set-up to resolve details of the patterns depends on the step size used during mapping, and the consequent Airy disc overlap. As shown in Figure 5.10, overlap which exceeds the diffraction limit is unresolved.

The chosen step size of the PL mapping must not be smaller than the resolution, as this would make the adjacent map points indistinguishable, returning blurred PL spectra and rendering the data useless for imaging patterns. The step size must also not be so large that it fails to map the PL of the region between map points. Therefore understanding the size of the Airy discs is of great importance to our experiment, as it will inform the appropriate step size for mapping the patterns.

In this set-up the objective lens has NA = 1.4, $\lambda_{ex} = 400\,\text{nm}$ and $n = 1.518$, where $n$ is the refractive index of the medium the light travels through, in this case Nikon Immersion Oil Type F. This gives $\theta = 67.3\,^\circ$ and a potential resolution

of 143 nm. However to achieve this theoretical limit, very precise alignment and stability is required. The path of a Gaussian beam through a convex lens is shown in green in Figure 5.11. This beam has a non-zero divergence, and so to achieve the theoretical minimum, the laser must enter the lens at the minimum waist of the beam prior to focussing ($\omega_0$ of Equation 5.3 - to be discussed in more detail below). Alternatively, the alignment prior to this point must guarantee zero divergence of the laser beam. The tools and techniques to determine the position of $\omega_0$ were beyond the scope of the project, as was the ability to maintain the stability required for such a configuration if it were to be achieved. Therefore to obtain the actual resolution of the set-up (likely to be considerably larger than 143 nm), the profile of the laser beam needed to be captured and characterised. The theory of Gaussian beams is described in more detail below.

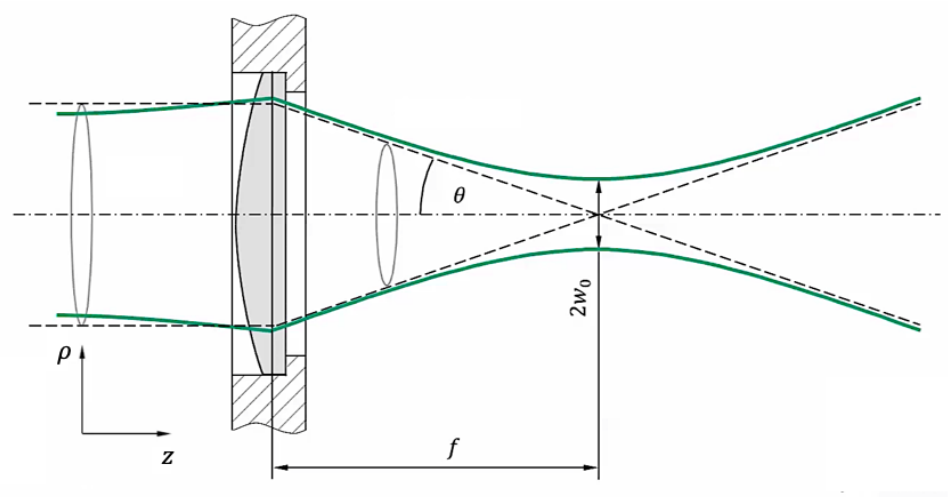



**Figure 5.11:** Diffraction of a Gaussian beam. The green line shows the path of a Gaussian beam through a convex lens, compared to the classical example of a plane wave, the dotted line. The beam converges to a spot with diameter $2\omega_0$. This diameter is increased by the non-zero divergence. Adapted from [165].

### 5.3.2 Theory of Gaussian Beams

Gaussian beams are characterised by several parameters [161][166]. The beam waist, $\omega$, is the radial distance from the centre of the beam to the point the intensity drops to $1/e^2$, or $\sim 13.5\%$ of its maximum value. From Figure 5.12 it can be seen

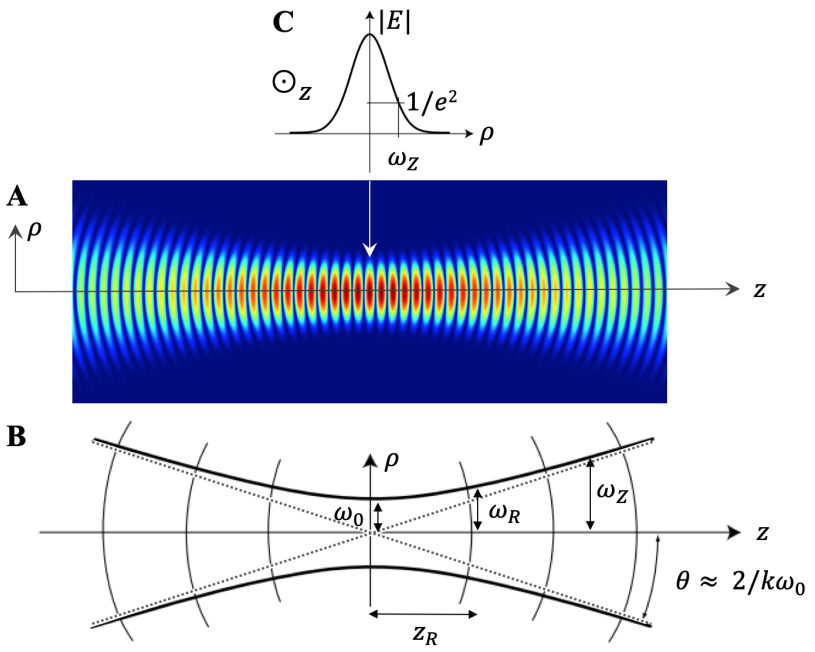



**Figure 5.12:** Propagation of a Gaussian beam focussed by an objective. **A** shows the radially-symmetric Gaussian intensity profiles of the beam propagating along $z$, becoming more intense in the narrowest point of the beam and broadening as it diverges. **B** illustrates the variance of the beam waist with $z$ and the characterising parameters of the beam: minimum beam waist ($\omega_0$), Rayleigh range ($z_\mathrm{R}$), and divergence ($\theta$). **C** shows the transverse intensity profile of the Gaussian beam, where $\omega_z$ is measured from the centre to $1/e^2$ of the peak intensity.

that the divergence $\theta$ is related to the minimum beam waist $\omega_0$ by,

$$\tan\theta = \frac{\omega_0}{z_\mathrm{R}}. \tag{5.6}$$

Consequently, in the small angle approximation,

$$\theta \approx \frac{\omega_0}{z_\mathrm{R}}. \tag{5.7}$$

The Rayleigh range, $z_R$, along which the beam is approximately collimated, is given by,

$$z_\mathrm{R} = \frac{\pi\omega_0^2}{\lambda}. \tag{5.8}$$

The beam waist at this point, the Rayleigh half-diameter, is given by,

$$\omega_\mathrm{R} = \sqrt{2}\omega_0. \tag{5.9}$$

Combining equations 5.7 and 5.8, gives

$$\theta = \frac{2}{k\omega_0} = \frac{\lambda}{\pi\omega_0}. \tag{5.10}$$

By considering the variation in the beam waist, the waist at any point along $z$ can be determined by,

$$\omega_z = \omega_0\sqrt{1 + \left(\frac{z}{z_\mathrm{R}}\right)^2}. \tag{5.11}$$

Therefore, given $\omega_0$ and $\lambda$, it is possible to calculate $z_\mathrm{R}$, $\omega_z$ and $\theta$ of the beam.

To determine $\omega_z$, the beam profile can be fitted to a Gaussian distribution, shown in Equation 5.12, where the expected value $\mu$ is the wavelength of excitation, and the full width at half maximum (FHWM) can be determined from the standard deviation $\sigma$ using Equation 5.13 [167].

$$P(x) = \frac{1}{\sigma\sqrt{2\pi}} e^{-(x-\mu)^2/2\sigma^2} \tag{5.12}$$

$$\mathrm{FWHM} = 2\sqrt{2\ln 2}\sigma \approx 2.355\sigma \tag{5.13}$$

Once the FWHM is obtained, $\omega_z$ can be determined by,

$$\omega_z = \frac{\mathrm{FWHM}(z)}{\sqrt{2\ln 2}} \tag{5.14}$$

It can be seen from Figure 5.9 that the proximity of the beams permitted by the Abbe limit is approximately equal to the FWHM of the beam. Therefore the resolution of the set-up was taken to be the FWHM.

### 5.3.3 Knife Edge Measurements

A typical method to obtain the profile of a laser beam profile is a 'knife-edge' measurement [168]. This method is so named as it involves the insertion of a sharp, opaque object into the path of the beam, interrupting its path to the detector. The drop in intensity recorded at the detector as the object is moved incrementally across the beam profile is not linear, due to the Gaussian shape of the beam. Thus the intensity profile can be fitted to a Sigmoid function, as shown in Figure 5.13,

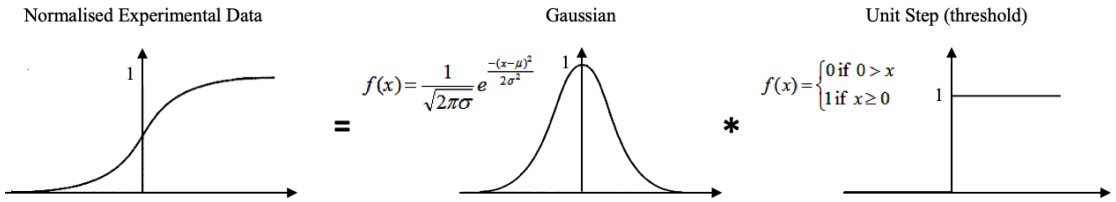



**Figure 5.13:** Deconvolution of 'knife-edge' intensity profile into Gaussian and unit step components.

which is a convolution of a unit step function with a Gaussian. It is therefore possible to obtain the Gaussian by deconvolving the Sigmoid fit.

The set-up here, however, does not have the capability to conduct such a measurement in transmission, due to the non-linear beam path about the objective and piezo stage. Therefore an adapted version was designed in reflection, using a sample containing a sharp boundary of two materials of different reflectivities. The scanning capability of the piezo stage across this boundary could then simulate the movement of an opaque object across the beam, whereby the contrast in reflectivity is analogous to the transmission contrast of the opaque object.

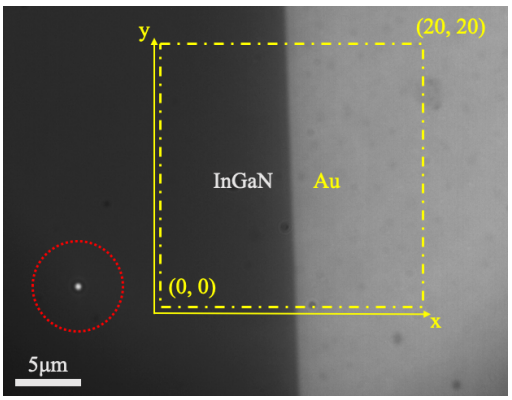



**Figure 5.14:** ThorCam image of the laser focussed on the InGaN/Au sample used for the adapted knife-edge experiment. The laser was positioned at the centre of the red dotted circle and the $20 \times 20\,\mu m$ scanned region is shown by the yellow dash dotted box.

The chosen sample comprised InGaN with regions of evaporated gold. It can be seen in Figure 5.14 that the boundary between the InGaN and gold provided a sharp contrast in reflectivity. The sample was overlaid with a coverslip to utilise the high NA oil objective, and the laser scanned across a $20 \times 20\,\mu m$ region outlined in yellow, moving in steps of 500 nm. A 2D map was scanned, (as opposed to a

1D trace as shown in Figure 5.13) to provide a good view of the boundary and enable potential averaging of the Sigmoid profile during analysis. The prolonged duration of such a map, ($>$ 1 hr) would additionally allow the stability of the piezo stage and laser power to be assessed.

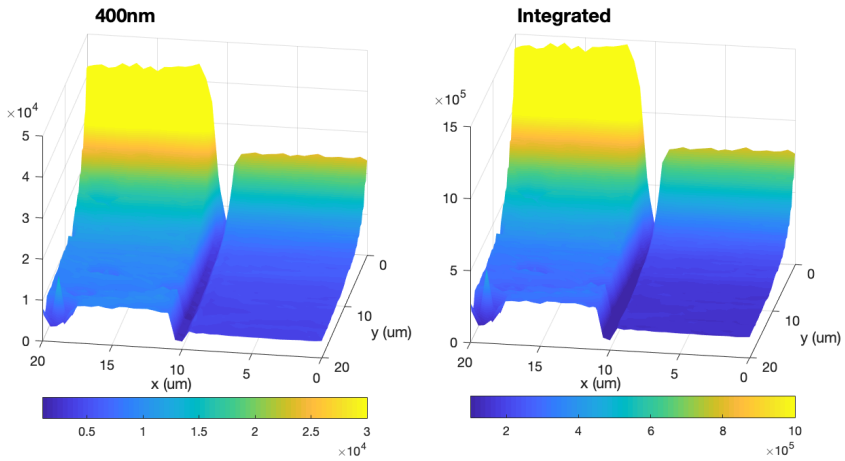



**Figure 5.15:** Results of the first adapted knife-edge experiment.

Figure 5.15 shows the 2 maps produced (with the method described in Figure 5.2): the first phase-selected to the laser wavelength; the second showing the total reflected spectrum at each point. As no emission was collected, the 2 plots show a similar profile. There was a step change in reflectivity as the laser moved from the InGaN (dark blue) to the gold (lighter blue). The profile also showed a deep trench across the length of the boundary. This was hypothesised to be due to scattering losses caused by some roughness at the edge of the gold being exaggerated by wave-guiding along the cover slip.

To test this and reduce losses through guiding, a quick scan was repeated using a lower NA objective that did not require oil or a coverslip. The trough persisted, suggesting the loss of signal was predominantly from scattering due to the boundary being rougher than expected. In the absence of a more suitable sample, the decision was taken to abandon this approach and instead try to profile the beam directly by imaging it with the ThorCam CCD.

### 5.3.4 ThorCam Measurements

To obtain the laser profile, a film was recorded of the laser sweeping through $z$ positions, with the power adjusted to ensure the laser spot did not saturate the camera. To minimise scattering the laser was positioned on the InGaN, as it can be seen in Figure 5.15 that it offered a smoother surface than the gold. The position of the piezo stage was started below the focus of the objective, then moved up in increments of 0.5 µm to a point well beyond the focus where many interference rings could be observed. This continuation ensured the focus would be passed through, and allowed assessment of the alignment quality.

At each $z$, an image of the laser was extracted from the film and plotted in a MATLAB surface plot. Figure 5.16 shows each plot in blue alongside the image it represents. The interference patterns appear circular and even, indicating good alignment of the laser. The minimum spot appears to be in the range $14 - 15.5$ µm. To measure the beam parameters, the $x$ and $y$ cross-sections of the beams were extracted, as shown in Figure 5.17.

### 5.3.5 Beam Parameter Calculation

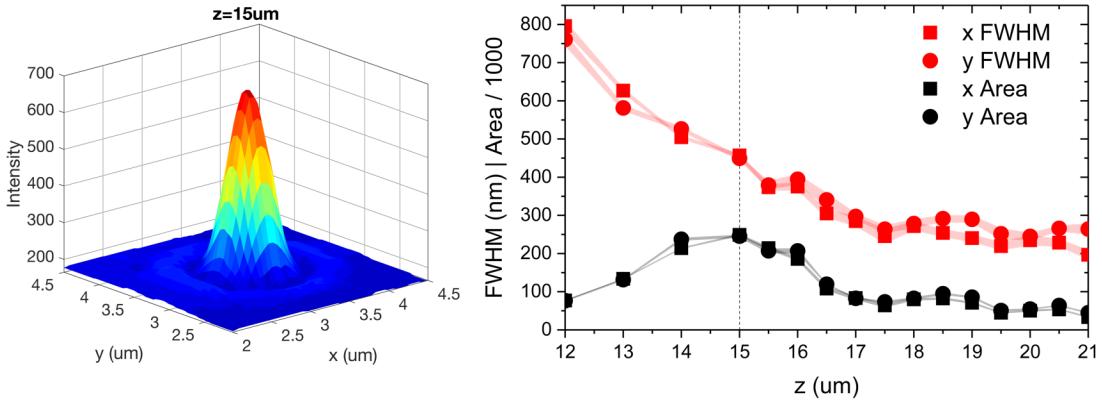



**Figure 5.18:** FWHM and Area of Gaussian fitted $x, y$ cross-sections. The FWHM and Area of the central Gaussian at each $z$ position, obtained from Gaussian fitting the cross-sections shown in Figure 5.17. Peak focus occurred at $z = 15$ µm, shown on the left. Area is scaled by 1/1000. The fit outputs are roughly equal for $x$ and $y$ confirming the beam was well aligned in both dimensions. The fit error is shown as the linewidth.

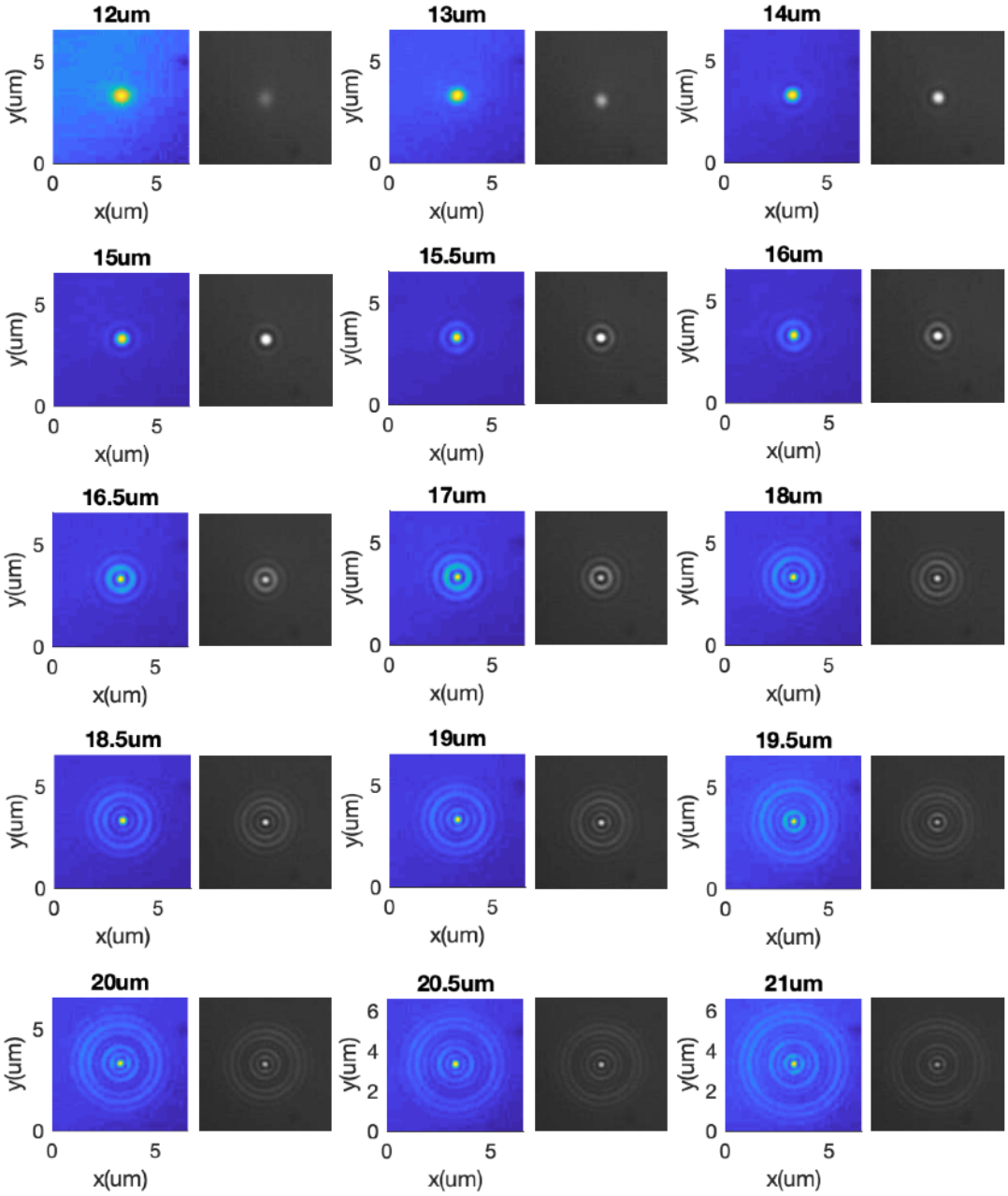



**Figure 5.16:** $z$-sweep intensity profiles of the laser spot. The blue plots show the intensity of the laser at various $z$ co-ordinates extracted from the corresponding ThorCam image shown in greyscale. The plot title denotes the $z$ co-ordinate of the piezo stage. From $z = 15.5\,\mu\text{m}$, interference rings can be seen around the Airy disks.

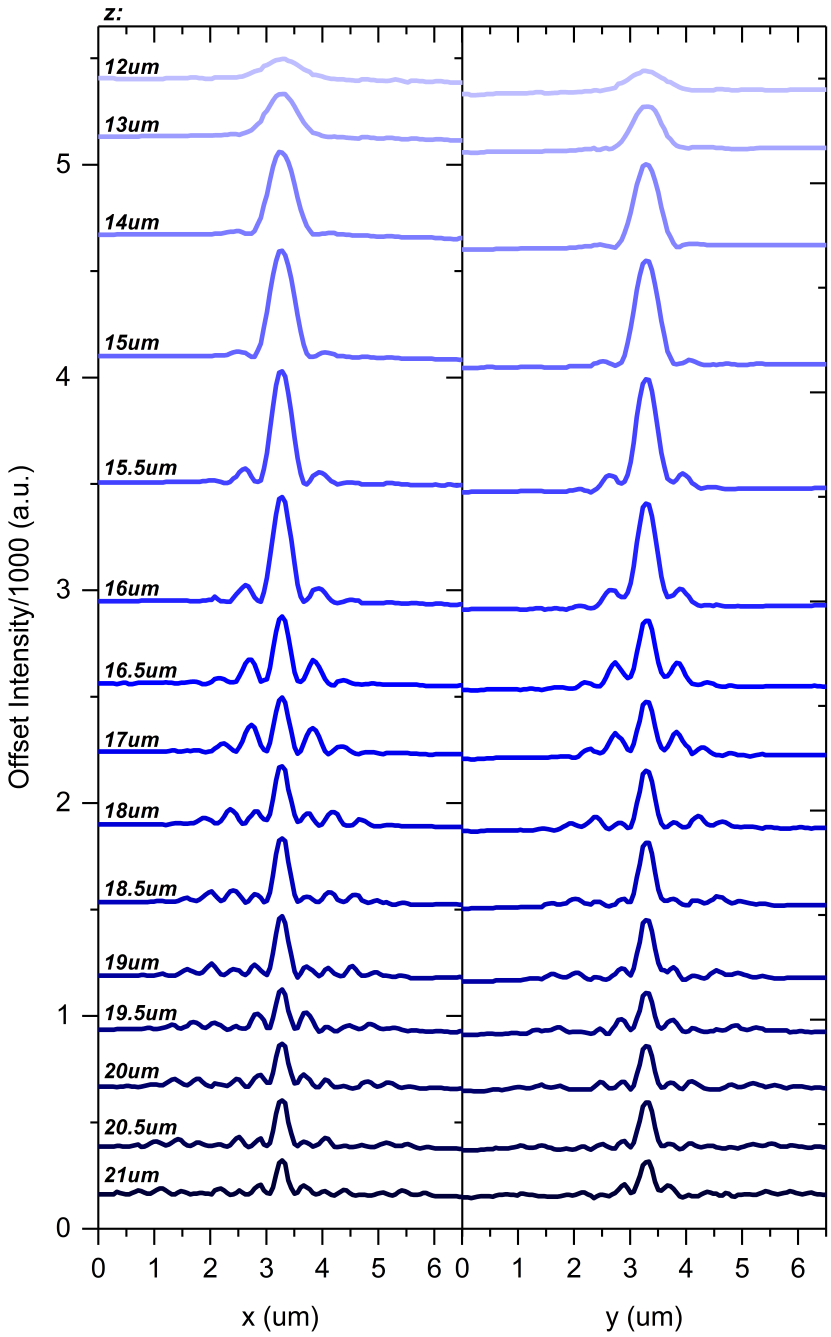



**Figure 5.17:** $x, y$ cross-sections of the $z$-sweep intensity plots showing the evolution of the laser spot as the piezo stage passes through the focal point of the objective.

| | Theoretical | x | y |
|---|---|---|---|
| NA | 1.4 | | |
| n | 1.518 | | |
| $\lambda$ (nm) | 400 | | |
| $\theta$ (rad) | 1.174 | | |
| $\omega_0$ (nm) | 108.5 | $388 \pm 4$ | $382 \pm 6$ |
| $\omega_R$ (nm) | 153.4 | $549 \pm 6$ | $540 \pm 8$ |
| $z_R$ (nm) | 92.4 | $1183 \pm 26$ | $1144 \pm 36$ |
| FWHM (nm) | 128 | $457 \pm 5$ | $449 \pm 7$ |

**Table 5.1:** Theoretical and calculated beam parameters for the $x, y$ cross-sections of $z = 15\,\mu m$.

The central peaks of the beam cross-sections were fitted to a Gaussian, (Equation 5.12), to extract their FWHM and area. It can be seen from Figure 5.17 that as the beam moves past the focus, the Gaussian nature of the central peak is retained but its area is reduced. Therefore to find the optimum focus the FWHM and areas were plotted in Figure 5.18.

Once the piezo stage passes through the focus, the relative width of the central peak decreases, as energy is distributed amongst the interference rings. Therefore it is not sufficient to take the narrowest Gaussian as the most focussed beam, as this transfer of energy to the rings was not taken into account when only the central peak was fitted. This results in the beam appearing to narrow artificially, with the lowest FWHM at $z = 21\,\mu m$, which is clearly an unfocussed beam. Therefore the area of the Gaussian was also used to highlight the $z$ position that had the greatest energy in the central peak, signalling the largest number of photons. The focussed beam then clearly stood out at $z = 15\,\mu m$. It can be seen that beyond the focal point, the area and FWHM are seemingly correlated, representing the oscillation of the interference patterns and further signalling that the point of focus has been passed.

Using $z = 15\,\mu m$, the beam parameters were calculated from Equations 5.7, 5.8, 5.10 and 5.14, as shown in Table 5.1. From this data it can be seen that at the minimum spot size the Airy disc is $\sim 770\,nm$ ($2\omega_0$), and from the FWHM, the resolution was estimated to be $\sim 453\,nm$. Therefore a step size of 500 nm was deemed suitable to simplify map parameterising.

The sensitivity of the set-up to small fluctuations in $z$ is also apparent. The Rayleigh range, $z_R \approx 1160\,\text{nm}$, shows that a movement in $z$ beyond a micron could disturb the focus. Therefore, it was imperative that the set-up included a mechanism for monitoring and tweaking the focus during data acquisition.

As $z = 15\,\mu\text{m}$ is an arbitrary value arising from the manual micrometer control of the piezo stage and control of the piezo via the GUI, a method was derived to reach this focus point again: a collimation test. To start with, a rough focus was found manually, then the beam was deflected from the collection path via a temporary mirror system that increased the path length by roughly 4 m. With an eye on this distant spot, the $z$ was tweaked using the GUI until the beam was collimated along this path. It was then checked with ThorCam to ensure it followed the same profile as that seen for the $z = 15\,\mu\text{m}$ position above.

## 5.4 PFO Tests

Once the beam profile had been characterised, it was necessary to test it on PFO. Although PFO absorption peaks at 378 nm, it was found that $\lambda_{ex} = 400\,\text{nm}$ provided a higher PL signal. This was probably due to the beam being better transmitted through the fibre and better reflected by the dichroic. For the same reason it was also easier to see on ThorCam, so would enable easier monitoring of the focus.

### 5.4.1 Power Tests

Another consideration for PFO was the strength of the laser on the sample. Previous micro-PL had caused degradation of the sample by photo-oxidation, evident by a rise in G-band emission and consequent decay in blue signal (see Section 1.4.2). As the requirement of the set-up was to retain signal intensity in the blue region to measure phase contrast, this degradation was obviously to be avoided. Additionally, ensuring the integrity of the sample would allow patterns to be mapped repeatedly if required.

To find what laser power reached the sample, the power was measured at various points in the excitation path to understand the transmission of each component. From this a transmission factor could be derived from a point that was easy to

| | Power | Transmission |
|---|---|---|
| Laser Output (µW) | $70 \pm 0.5$ | n/a |
| Post Fibre (nW) | $139.5 \pm 0.5$ | 0.2% |
| Post Objective (nW) | $13.2 \pm 0.1$ | 9.5% |

**Table 5.2:** Transmission of laser power through the excitation path.

measure before data acquisition. The power was measured at the laser output, after the first mirror following the 45 mm focal length lens (post fibre) and at the sample position (post objective). This was initially conducted at $P_{\text{laser}} = 100\%$ (it was only possible to select power as %). Table 5.2 shows the values at 400 nm.

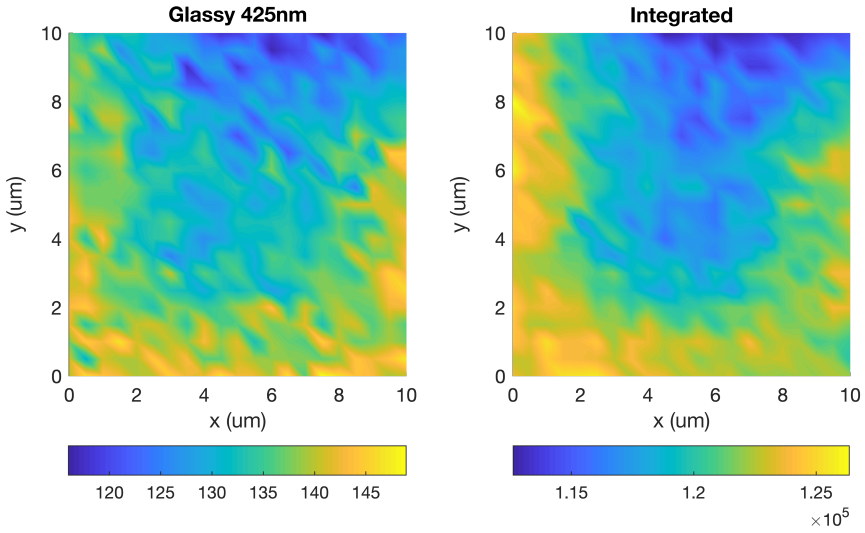



**Figure 5.19:** Power squares to identify photodegradation of PFO. The glassy wavelength selected map on the left shows a small drop in signal for the internal map of about 10 counts. The integrated map on the right amplifies this drop, clearly revealing the $5 \times 5$ µm map.

The power at the sample is very low at $(13.2 \pm 0.1)$ nW, with the optical fibre, 405 nm dichroic and objective all contributing significant losses. It was therefore not considered worthwhile to test powers $< 100\%$. However due to the risk of photo-oxidation, these low powers were considered promising for the measurement of PFO samples.

The set-up was therefore tested for degradation of PFO at $P_{\text{laser}} = 100\%$. A method was derived, wherein 2 concentric squares were mapped to enable the

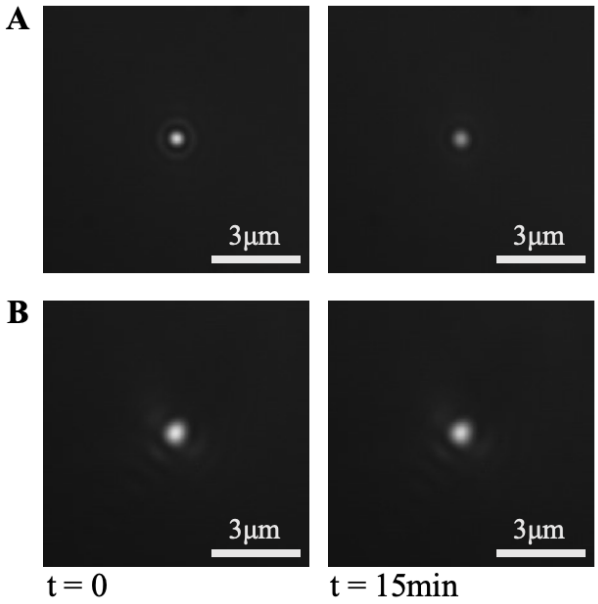



**Figure 5.20:** Stability of the piezo stage. **A** and **B** show before and after a solid micrometer stage was incorporated to support the piezo stage, respectively. Although not perfectly aligned, the solid stage of **B** is stable over the 15 min period.

imaging of a region that had already been subjected to the laser. The first square was mapped with an area of $5 \times 5\,\mu m$, then a larger $10 \times 10\,\mu m$ map was scanned about the same centre as the first map. Any degradation caused by the laser during the first map would therefore be visible as a drop in intensity within the central region of the second map. A region far from any patterns was chosen, and a small area mapped to ensure any variation in intensity observed was due to the laser, rather than local variances in the sample. A step size of 500 nm was used for reasons discussed above.

The results of these power tests can be seen in Figure 5.19. A small drop in intensity of about 10 counts can be seen in the glassy map. This is much clearer in the integrated map, in which the internal $5 \times 5\,\mu m$ is clearly visible. It was noted that the signal overall was very low, and would shrink further if $P_{\text{laser}}$ was reduced. Therefore the decision was taken to tolerate the small amount of degradation as a necessary sacrifice for signal preservation.

### 5.4.2 Stability

As shown above, small changes in $z$ can significantly affect the resolution. Therefore the laser was filmed with ThorCam over some time to study the stability of the piezo stage $z$ position. Initially the piezo stage was mounted on a scissor-lift style micrometer stage.

The laser was recorded over a period of 15 minutes and found to be unstable. Figure 5.20**A** shows the stage relaxing below the focal plane, broadening the Gaussian and reducing the signal strength. This triggered the scissor stage to be replaced with a solid, metallic micrometer, and a second film was recorded. Although the beam in Figure 5.20**B** was out of alignment, it appears to be more stable with no change in shape or intensity.

Although a clear improvement, 15 minutes was short compared to the many hours taken to plot a map, and so these images demonstrate the need for periodic refocussing of the laser throughout the mapping period.

## 5.5 Conclusion

To conclude, the aims of Section 5.1 are revisited:

1. **High Resolution:** From the beam profiling calculation of Section 5.3.5, the resolution was found to be $\sim 453\,\text{nm}$ when in focus, which was suitably within the order of the target feature size. Therefore the resolution was considered to be sufficient for at least the first set of patterns, which would likely result in feature sizes between 500 nm and 1000 nm (an optimistic starting point).

2. **Sensitivity:** The low power recordings and minimal damage seen in the power squares of Section 5.4.1 indicated that the beam was not adversely affecting the PFO film, however the signal strength was fairly low. With a material sensitive to photooxidation such as PFO there will always be a trade-off between the signal strength and film integrity, and in this case the signal strength was further reduced by the fraction of the beam being used to continually monitor the focus. Due to resolution requirements, the focus

was considered to be of higher priority than the signal strength, and so the monitoring mechanism was left intact despite the low signal. This issue of continual monitoring could be addressed in future by installing a stability enhancing environment to reduce the required frequency of focus monitoring, or by incorporating into the design a mirror to periodically deflect and check the beam which does not unsettle the set-up in its operation (as the insertion of the beam splitter did). Better still, programming an analysis of the beam profile using a periodically sampled ThorCam image would enable the piezo stage to optimize the focus automatically, circumventing the need for manual interaction. However, these enhancements were beyond the scope and means of the project, but could be trialled in a future iteration.

3. **Contrast:** As described in Section 5.2.3, the reflectivity of the beam splitter supports good spectral contrast between the glassy and $\beta$ emission peaks. Therefore the set-up should be sufficiently sensitive for picking up small changes between the phases.

Although the set-up meets the aims described above, there are a number of additional analyses which would be useful for assessing the $\beta$ phase patterns. As described in Section 1.4.4, the PL does not allow precise calculation of the $\beta$ fraction. Although a PL estimation was considered sufficient for this study, calculating the fraction would be advantageous as it would enable the mapping of the refractive index, which would facilitate photonic structure design.Therefore, a set-up which could provide microscale absorbance or ellipsometry mapping could be useful. The current set-up could be redesigned to utilise the large aperture of the piezo stage for transmission measurements to characterize the absorbance, from which the $\beta$ fraction could be determined.

As well as the $\beta$ fraction, quantifying the film swelling via Atomic Force Microscopy (AFM) would be advantageous for structural design as it could identify sources of scattering. The swelling could also provide a method for imaging pattern boundaries, as well as inform the gradient of $\beta$ phase fraction over the boundary.

As with the monitoring systems above, these analyses were beyond the scope of this study, but anyone continuing this work may wish to explore these options.

To summarise, the set-up described above provided a method for imaging the DPN patterns and for analysing the DPN technique's potential for patterning photonic structures into PFO. The set-up was put to the test in the following chapter, which describes the DPN patterning of the $\beta$ phase in PFO.

# 6 Dip-Pen Patterning of PFO

## Contents


**6.1 Introduction . . . . . 132**
6.1.1 Overview and Aims . . . . . 132
6.1.2 Order of Work . . . . . 134
**6.2 Experimental . . . . . 135**
6.2.1 Sample Preparation . . . . . 135
6.2.2 DPN Patterning . . . . . 138
**6.3 Results . . . . . 140**
6.3.1 DPN Patterning . . . . . 140
6.3.2 Micro-PL Maps . . . . . 142
6.3.3 Dot Analysis . . . . . 150
**6.4 Conclusion . . . . . 156**


## 6.1 Introduction

### 6.1.1 Overview and Aims

Following Chapters 3 and 4 wherein the control of molecular and oligomer conformation was studied in solution, we move now to controlling the conformation of polymers in thin films. As described in Chapter 1, the $\beta$ phase of PFO has been patterned at millimetre scales through the use of PDMS masks [114], and then at sub-micron scales using dip-pen nanolithography (DPN) [23].

Here we further investigate the process of DPN as a means to fabricate photonic structures within PFO, and aim to better understand the parameters of the printing process with a view to scaling it up in future. The previous work investigated individual dots and lines, and so the focus here is on patterning dot arrays with multiple DPN tips. If the patterns are to form effective photonic structures, they must demonstrate the properties detailed below:

1. **Consistency:** Consistently sized dots are required to provide the regular periodic structures. Additionally, a long range of consistency is desirable, as frequent ink reloading can increase the position error of the DPN due to large movements to and from the inkwells. Consistency across tips is also essential, as to scale up the process it would be essential to use multiple tips simultaneously. There must be confidence that patterns are consistent between the tips, as beyond lab trials it would not be possible to image every pattern.

2. **Feature Size:** For the desired photonic effects, the periodicity of the patterned structure must be of the order of the working wavelength of the material. For PFO, the PL emission range of the glassy phase is $425 - 500\,\text{nm}$ and the $\beta$ phase $440 - 500\,\text{nm}$. Therefore the target dot diameter is $< 500\,\text{nm}$.

3. **Phase Contrast:** As discussed in Chapter 1, a large change in $n$ is desirable, though a small change can still provide some confinement and wavelength selective propagation. Therefore, the patterning aims to achieve a significant rise in the $\beta$ phase fraction within the patterned features, to provide a clear contrast in $n$. As we are not recording the change in absorption across the patterns, we will not be able to measure the $\Delta n$ achieved. However, previous work tells us that $\Delta n$ ranged from 0.2% at 1.5% $\beta$ phase to 1.5% at 10% $\beta$ phase [114], and up to 10.9% [23] when $\beta$ phase dominated the emission (all evaluated at 450 nm), so it is possible to estimate the range of $n$ achieved from the spectra of the patterns.

4. **Feature Contrast:** Sharp features, rather than a gradual change between the glassy and $\beta$ phase regions is desirable, as this corresponds to a sharp $n$ boundary. As discussed in Chapter 1, this boundary is essential for providing reflection points, which are the foundation of the photonic effects attempted here.

5. **Thin Film Integrity:** The patterning process must not damage the PFO film to ensure minimal introduction of scattering and maintain the PL efficiency. As well as contributing to loss of signal, scattering at the scale of the working wavelength or smaller ($< 500\,\text{nm}$) could introduce disorder into the structure, causing defects such as speckle.

The DPN processing parameters tested are pattern pitch, $a$, and dwell time, $d$, defined as the contact time between the sample and the tip. The impacts of these parameters on the properties listed above, as well as printing considerations such as blotting and ink capacity, are studied below.

### 6.1.2 Order of Work

The work detailed below includes the fabrication of glassy PFO thin films via spin-coating, followed by dip-pen patterning of $\beta$ phase dot arrays onto the film surface. The patterns were then imaged with the micro-PL set-up described in Chapter 5.

Preliminary measurements to gain familiarity with the DPN tool and identify suitable initial values of $a$ and $d$ were carried out on a second set-up, before the set-up described in Chapter 5 was built. The results from these measurements are included but separated due to both the sample and set-up being different. Details of this set-up can be found in [169]. To clarify the discussion, details of these measurements are denoted Preliminary or 'Pre.', and the later maps measured using the set-up described in Chapter 5 are referred to as the 'new' maps.

## 6.2 Experimental

### 6.2.1 Sample Preparation

To produce a sample appropriate for patterning, a variety of films were fabricated from solutions of PFO in toluene and THF, detailed in Table 6.1. The toluene was anhydrous to 99.8% (Sigma-Aldrich 244511) and the THF anhydrous to 99.9% (Sigma-Aldrich 401757). Both were newly opened. The solutions were made 1 day prior to film deposition, and left for 24 hrs with a magnetic spinner at 50 ℃ to ensure good solvation. Details of the solution and film prepared for the preliminary patterns are denoted in the tables 6.1 and 6.2 as 'Pre.'.

| Solution | Solvent | $\delta$ ($cal^{1/2}cm^{-3/2}$) | b.p. (℃) | Vol. (ml) | PFO (mg) | Concentration (mg/ml) |
|---|---|---|---|---|---|---|
| 1 | Toluene | 8.9 | 110.6 | 2.92 | 37.9 | 13 |
| 2 | THF | 9.1 | 66 | 1.23 | 16.0 | 13 |
| Pre. | Toluene | 8.9 | 110.6 | 2.6 | 33.8 | 13 |

**Table 6.1:** Details of the solutions used to fabricate the PFO films used for patterning. $\delta$ is the Hildebrand parameter of solubility [157].

In order to record the positions of the patterns (which was essential for identifying the patterns during imaging), NanoInk Silicon Dioxide substrates from Advanced Creative Solutions Technology (acs-t) with 250 µm spaced grid markers were used. The substrates were sonicated in toluene, chloroform and THF each for 10mins before being dried in nitrogen. They were then treated in ozone for 5 mins prior to spin-coating to remove any remaining organic material and increase the surface energy for good adhesion of the film.

Each film was spun in ambient conditions from 120 µl of solution at 2000 rpm for 1 min with an acceleration of 500. The films were then left to dry in the fume hood for 30 mins, and stored in a nitrogen atmosphere prior to patterning, only removed to measure their PL, shown below in Figure 6.1. The $\beta$ fraction of each film was estimated from the relative intensity of peaks at 440 nm and 425 nm, as described in [89].

| Film | Concentration | Solvent | Solution | Substrate | Annealing |
|---|---|---|---|---|---|
| A | 13 mg/ml | Toluene | 5 mins, 100 ℃ | RT | - |
| A2 | 13 mg/ml | Toluene | 5 mins, 100 ℃ | 5 mins, 100 ℃ | - |
| B | 13 mg/ml | Toluene | 5 mins, 100 ℃ | RT | - |
| C | 13 mg/ml | THF | RT | RT | - |
| D | 13 mg/ml | THF | 5 mins, 50 ℃ | RT | 5 mins, 50 ℃ |
| Pre. | 13 mg/ml | Toluene | 5 mins, 100 ℃ | RT | - |

**Table 6.2:** Thermal spinning conditions for PFO films spun from toluene (**A**, **A2**, **B**) and THF (**C**, **D**). Various thermal conditions were trialled to minimise the presence of $\beta$ phase.

A variety of different thermal conditions were trialled to minimise the $\beta$ phase fraction of the films, detailed in Table 6.2. Previous work with toluene solutions had shown that heating the solution to 100 ℃ was imperative to fabricate glassy films. Therefore the first films fabricated, **A** and **B**, were spun from a hot solution onto a substrate at room temperature (RT). The PL of these films, shown in Figure 6.1 shows that a small fraction of $\beta$ phase was present in the films (<0.1%), and so a third film, **A2** was spun from a hot solution onto a hot substrate, in an attempt to fully eradicate the $\beta$ phase. However, as shown in Figure 6.1, the hot substrate had little effect.

Additionally, films **C** and **D** were spun from the THF solution. As the boiling point of THF is much lower than toluene, these solution were heated only at 50 ℃ for 5 mins, with **D** being annealed following deposition to aid the rapid removal of solvent which has been shown to improve glassy films [89]. The annealing was also done in place of heating the substrate, as the highly volatile THF solution would not have formed a good quality film if both the substrate and solution were heated. However it was clear from their PL that significant fractions of $\beta$ phase persisted despite the heating.

From the PL of the films shown in Figure 6.1 the fractions for the films fabricated here ranged from <0.1% (film **B**) to 26% (films **C** and **D**). Film **B** was therefore selected for patterning, due to its minimal $\beta$ phase, which would provide the largest range of contrast between the two phases. Despite a small shoulder in the absorption

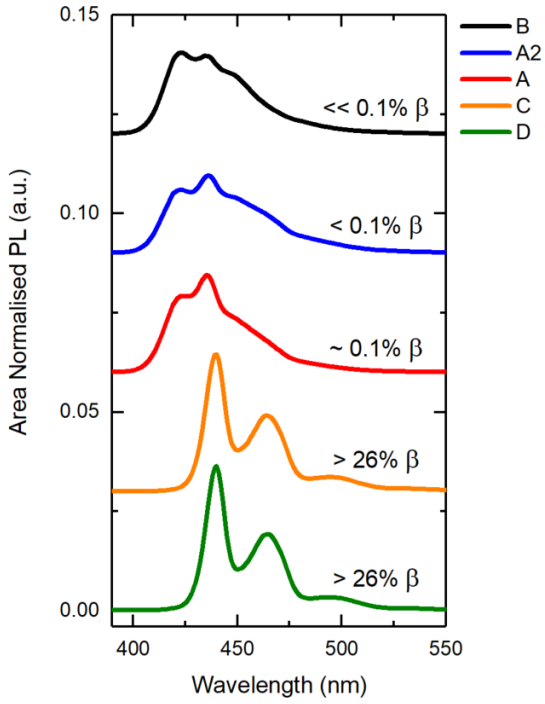



**Figure 6.1:** PL of films fabricated according to Table 6.2, displayed in order of increasing $\beta$ phase fraction. Offset for clarity.

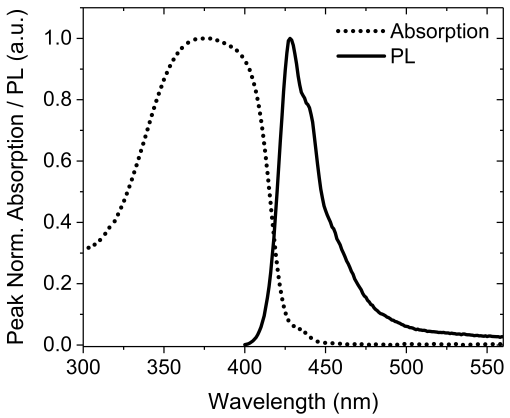



**Figure 6.2:** Absorption and PL of the film fabricated for the preliminary patterns. The absorption shows a hint of $\beta$ phase with a small shoulder at 435 nm, but the PL is predominantly glassy with no peak at 440 nm.

at 435 nm, the preliminary film PL seen in Figure 6.2 does not show any peak at 440 nm, and so was considered glassy.

### 6.2.2 DPN Patterning

The films were patterned in ambient conditions using the desktop NLP 2000 DPN system described in Section 1.5.2. Each inkwell was filled manually with 0.3 µl of solvent. Type M-2 tips were recommended, comprising 12 triangular tips, due to their design enabling high volumes of solvent loading [136].

To induce the $\beta$ phase, the solvent decalin ($\delta = 8.7\,\mathrm{cal}^{1/2}\mathrm{cm}^{-3/2}$) was used via the contact swelling method described in Section 1.4.6. Decalin was chosen to directly continue the work described in [23], in which the $\beta$ phase was first patterned using dip-pen nanolithography.

The patterning parameters investigated were $d$ ($d$ = 1 s, 3 s and 5 s) and $a$ ($a$ = 1 µm, 3 µm, and 5 µm). These values were selected based on the values used in the preliminary patterning, where $a$ = 10 µm and $d$ = 5 s, 10 s and 20 s, in an attempt to further reduce the size of the dots.

A strip of film between 2 rows of markers was given to each $d$, as shown in Figure 6.3, in which the space between row markers H and I contains an array of patterns all with $d$ = 3 s. Within the strip, 3 rows of patterns with varying $a$ were deposited, with a separation of 80 µm. Each row contained 12 patterns, from the 12 tips.

Before each pattern, the tips were loaded with decalin by resting them in the inkwell for 5 s. The tips were not blotted for the initial 3 rows of patterns shown in Figure 6.3, and so the initial large deposition of ink is clearly visible on the film.

A fourth, blotted row was made for the smallest pitch pattern, $a$ = 1 µm to prevent the inevitable overspill between dots in such close proximity. Due to their larger $a$, the other patterns were not repeated with blotting, as the blot effect should be clearly visible after the first few dots of the unblotted patterns, with the assumption that their $a$ would be large enough for overspill not to affect dot visibility.

$12 \times 12$ grids were patterned by each tip to maximise the space between adjacent tips, and in doing so maximise the chances of finding a pattern during micro-PL

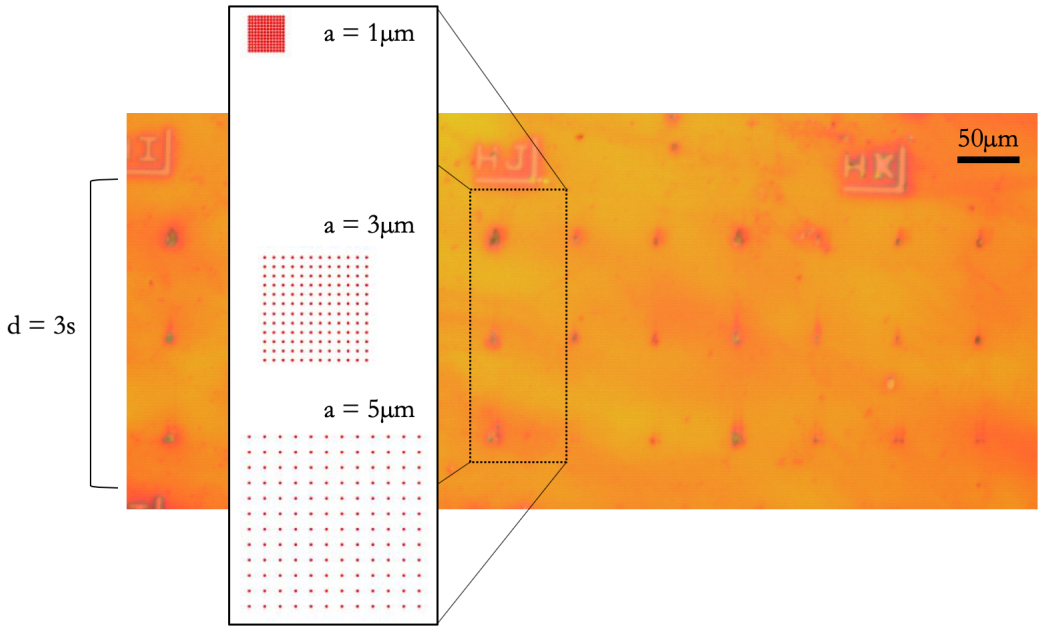



**Figure 6.3:** Layout of the new patterns, taken with the NLP 2000 microscope camera. The area beneath row 'H' corresponds to a $d = 3\,\mathrm{s}$, with 3 grids $a = 1\,\mu\mathrm{m}$, $3\,\mu\mathrm{m}$ and $5\,\mu\mathrm{m}$ offset by $80\,\mu\mathrm{m}$

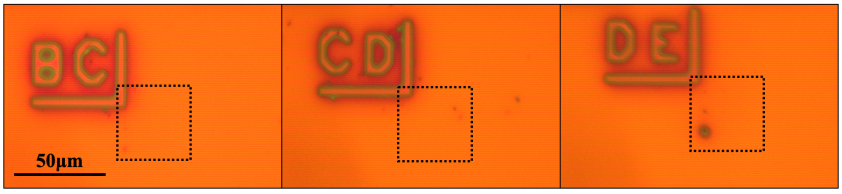



**Figure 6.4:** Layout of the preliminary patterns, taken with the NLP 2000 microscope camera. Position 'BC' refers to $d = 5\,\mathrm{s}$, position 'CD' to $d = 10\,\mathrm{s}$, and position 'DE' to $d = 20\,\mathrm{s}$. A $3 \times 3$ grid of $a = 10\,\mu\mathrm{m}$ was patterned at each position.

mapping. As shown in Figure 1.26**B**, the pitch of the tips is $66\,\mu\mathrm{m}$, and so at the largest pitch, $a = 5\,\mu\mathrm{m}$ a near continuous grid across the strip of film was patterned (with a pattern width of roughly $60\,\mu\mathrm{m}$). Each $12 \times 12$ grid was patterned on a single ink load, so the possible dot consistency within a single load could be measured.

For the preliminary measurements shown in Figure 6.4, $3 \times 3$ grids with $a = 10\,\mu\mathrm{m}$ were patterned on a single load of decalin at various points of the sample. Position 'BC' refers to $d = 5\,\mathrm{s}$, position 'CD' to $d = 10\,\mathrm{s}$, and position 'DE' to $d = 20\,\mathrm{s}$.

To dry, the sample was left in the NLP 2000 enclosure for 2 days, with the lights off and inkwell empty so only the deposited solvent remained.

## 6.3 Results

### 6.3.1 DPN Patterning

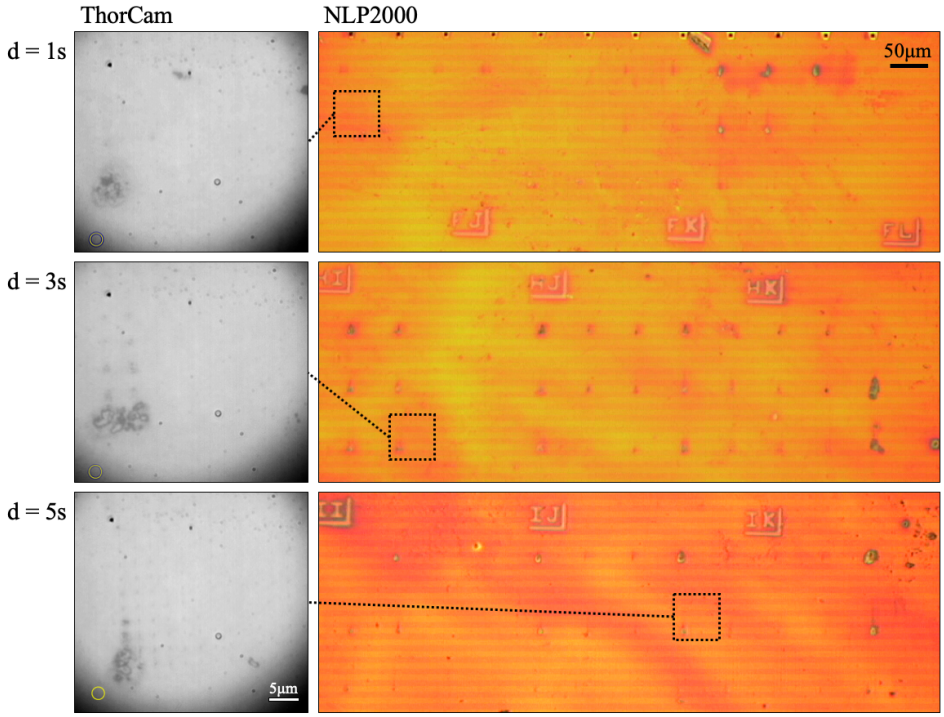



**Figure 6.5:** Array of new patterns achieved via DPN. The images on the right show the full array of patterns for each dwell time, taken using the NLP 2000 inbuilt camera. The ThorCam images on the left highlight the particular patterns analysed with the micro-PL set-up. The yellow ring shows the initial position of the laser prior to mapping.

Although the bottom left corner of the patterns are clearly visible in both the ThorCam & NLP 2000 images of Figure 6.5, on closer inspection it appears that the first few dots have damaged the film, and the following dots are very faint or not visible at all. It can also be seen from Figure 6.5 that the scale of deposition is not always even between adjacent tips. Large deposits of ink can be seen at the start of some patterns, but not others. The position of these patterns along the row appears to be random, suggesting that it was not due to the tip array being non-parallel to the film surface. Although the angle of the substrate relative to the tips can be adjusted with high precision to ensure they approach parallel to the surface, it is not possible to correct the tilt of individual tips. This could be be a limiting factor in the consistency of patterning large areas of surfaces which are not

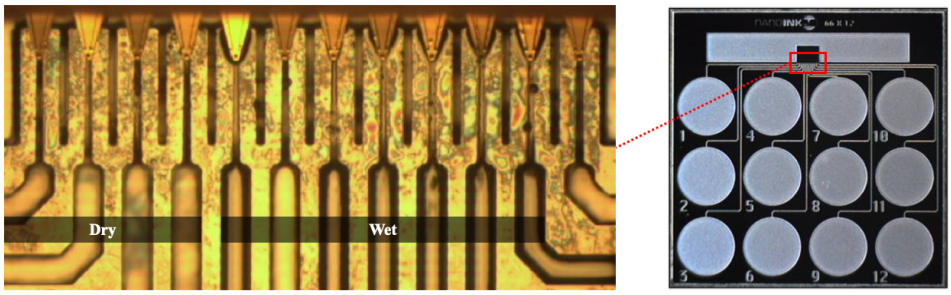



**Figure 6.6:** Solvent loading onto the tips from inkwells. The tips make contact with narrow channels supplied by circular inkwells, which are loaded manually with a pipette. Some inkwells dry up faster than others, leading to uneven loading. The bright tip is being pulled further into the solvent, indicating a larger volume of solvent. This is uneven even across the wet inkwells. Residue of dried solvent from earlier patterning can be seen on the surface.

perfectly smooth, such as PFO. A single tip would be easier to control, but has the disadvantage of not being suitable for high throughput, high volume fabrication.

This inconsistency could also be due to unevenness in ink loading, which has a large impact on the patterning. If tips are too heavily loaded they would require more blotting, however as the array is all blotted simultaneously this could lead to too much ink being lost in the less loaded tips. Inconsistency in deposition across the array mitigates any benefit of using an array as opposed to a single tip. The required frequency of reloading of the inkwell is also uneven, and would need to be closely monitored between patterns.

It is very difficult to control the interaction between the ink and the tip, seen in Figure 6.6, where even within the wet inkwells there is some discrepancy in loading. The bright tip, 5th from left, will be heavily loaded as there is a strong ink-tip interaction which draws it close to the ink. Similarly the inkwells, although each were filled with the same volume of solvent (0.3 µl), they appear to have different volumes in the collection channel. This is a clear contributor to the uneven loading across the tip array. In this case, it is clear that small particles are blocking some of the channel, highlighting the need for ultra clean inkwells and environment, as well as clean solvent itself. It can be seen in Figure 6.6 that some of the inkwells were empty, while others are full despite being loaded at the same time. Although decalin has a high boiling point of 190 ℃, solvent evaporation is likely accelerated

by the bright illumination and large surface area to volume ratio of the solvents in the micro channels of the inkwell chip. For other, more volatile solvent mixtures this could prove an even larger issue.

### 6.3.2 Micro-PL Maps

In order to achieve the required resolution on the micro-PL mapping, (500 µm), within a reasonable time frame, only the first 2 rows of each pattern were mapped. This totalled an area of 24 dots, (2 rows of 12), which should be a sufficient number to understand the basics of patterning periodic dots with a single load of ink, (as the tip are recommended to be re-inked every 10 dots [136]), and also surpassed the 9 dot grid of the preliminary maps. By patterning longer rows than the 3x3 preliminary grid, the micro-PL position error is reduced, as the majority of the movement is along a single axis, with infrequent snaking.

The patterns were analysed with the micro-PL set-up of Chapter 5. Although the full range of $a$ and $d$ was patterned and mapping attempted for all values, during patterning it became clear that it did not make sense to attempt to reduce $a$ until the impact of $d$ was better understood. The patterns with $a = 1\,\mu m$ were consistently swamped by solvent, causing the whole pattern to fail. Attempts to map the blotted patterns also failed, with no pattern being successfully imaged in the area. Therefore the results herein reflect the full range of $d$ at $a = 3\,\mu m$ or $5\,\mu m$, depending on which maps were successful. In general due to the dots not always being visible on the NLP 2000 camera, it is not easy to tell whether a pattern has failed until mapping is attempted. The micro-PL mapping parameters are shown in Table 6.3. The mapping parameters of the preliminary maps are shown in Table 6.4, of which only $d = 5\,s$ and $20\,s$ succeeded.

The positions of the patterns within the boundaries of the maps vary due to challenges with locating the patterns. As shown in Figure 6.5, often only the initial one or two dots were visible, and in some cases the positions could only be estimated relative to the nearest marker. Additionally the range on the piezo

| Dwell (s) | Pitch (µm) | x (µm) | y (µm) | z (µm) | Step (µm) | $\lambda_{ex}$ (nm) | Slit (µm) | Power (nW) | Acq. Time (s) |
|---|---|---|---|---|---|---|---|---|---|
| 1 | 3 | 90 | 10 | 13 | 0.5 | 400 | 1000 | 9.8 | 1 |
| 3 | 5 | 65 | 10 | 12 | 0.5 | 400 | 1000 | 9.8 | 1 |
| 5 | 3 | 65 | 10 | 11 | 0.5 | 400 | 1000 | 9.8 | 1 |

**Table 6.3:** Micro-PL mapping parameters of new dot patterns with tip dwell times of 1 s, 3 s and 5 s. Measured using the set-up described in Chapter 5.

| Dwell (s) | Pitch (µm) | x (µm) | y (µm) | Step (µm) | $\lambda_{ex}$ (nm) | Slit (µm) | Power (nW) | Acq. Time (s) |
|---|---|---|---|---|---|---|---|---|
| 5 | 10 | 40 | 40 | 0.5 | 399 | 20 | 15 | 0.5 |
| 20 | 10 | 40 | 40 | 0.5 | 399 | 20 | 15 | 0.5 |

**Table 6.4:** Micro-PL mapping parameters of preliminary dot patterns with tip dwell times of 5 s and 20 s, and a large pitch of 10µm. Maps taken with set-up described in Chapter 5.

stage was insufficient to avoid manual movement, especially as the majority of its range was required for the mapping.

Figures 6.7 to 6.9 show the new micro-PL maps for $d = 1$ s, 3 s and 5 s respectively. Figure 6.10 shows the preliminary maps measured on the set-up described in [169]. Both raw and area normalised (AN) maps are shown, with some intensity variation visible in the raw maps. This was likely caused by variation in the air temperature over the mapping period. Therefore the measurements of pattern features were conducted on the AN maps, ensuring any features were due to the phase change of PFO and not external factors. Area normalisation was used instead of peak normalisation as there was commonly a slight peak at the $\beta$ wavelength, 440 nm, and so it was not always effective in distinguishing the phases. AN better highlighted the shift in distribution between the phases.

Maps were phase-selected at 405 nm to study the impact of patterning on the film surface. In all the new maps, Figures 6.7 to 6.9, the raw 405 nm map shows some roughness where the first dots were patterned, suggesting the film was damaged by the dip-pen tips. The AN 405 nm maps show a lower signal within the patterned region specifically, which confirms that the tips and solvent roughened the surface

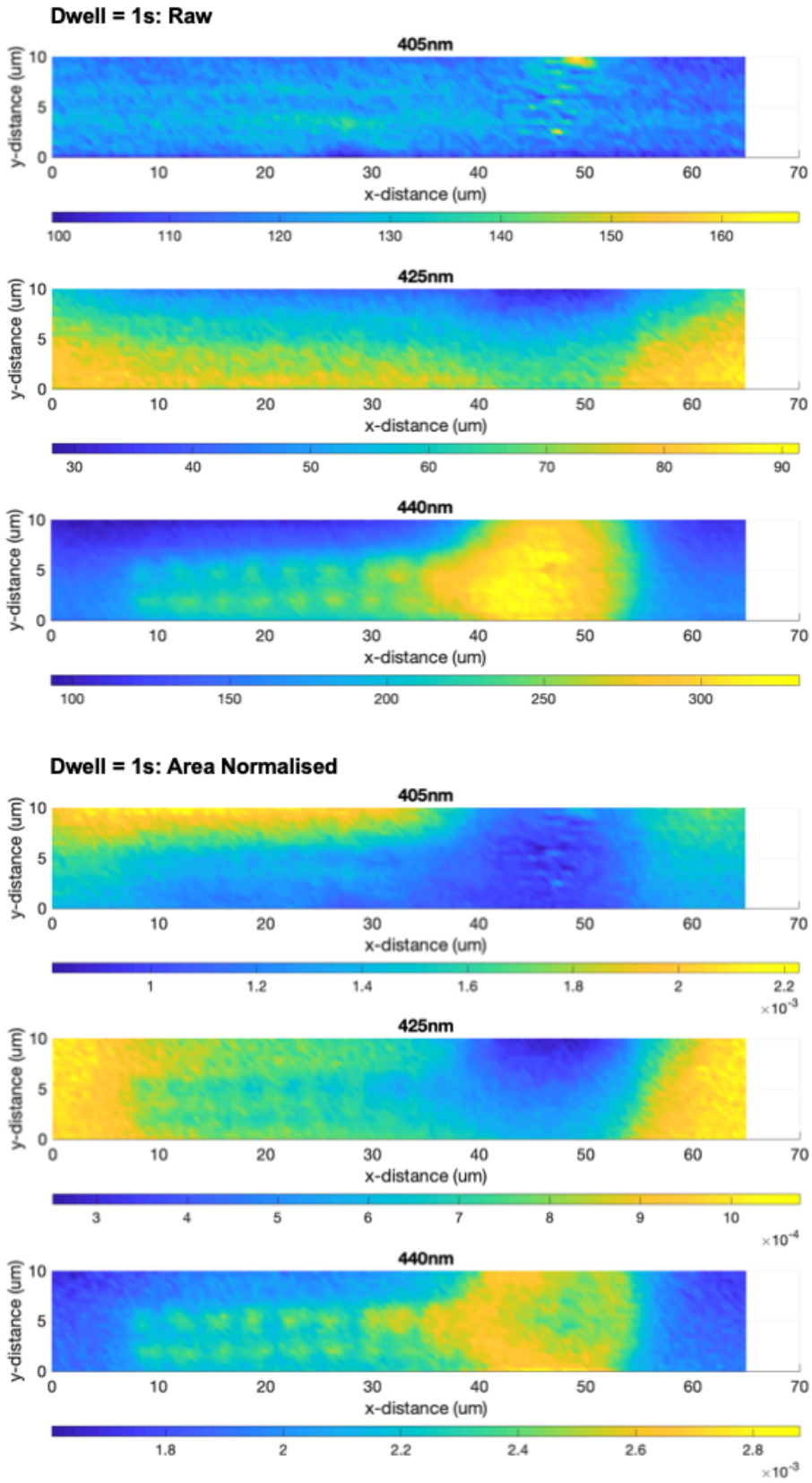



**Figure 6.7:** Raw and area normalised micro-PL maps with $d = 1\,\mathrm{s}$, $a = 3\,\mu\mathrm{m}$. Maps were phase-selected for the laser reflection, glassy phase, and $\beta$ phase at 405 nm, 425 nm, and 440 nm respectively.

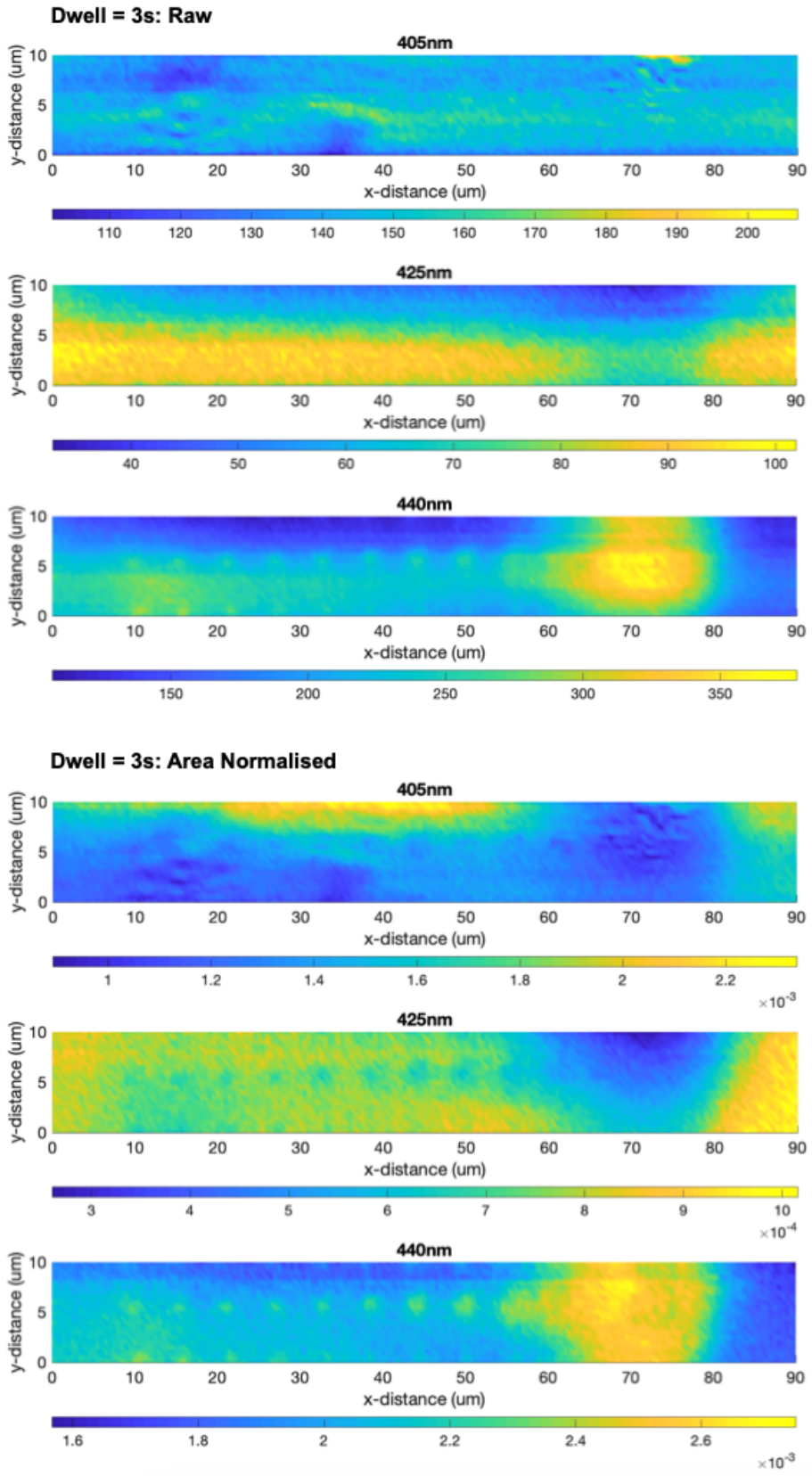



**Figure 6.8:** Raw and area normalised micro-PL maps with $d = 3\,\mathrm{s}$, $a = 5\,\mu\mathrm{m}$. Maps were phase-selected for the laser reflection, glassy phase, and $\beta$ phase at 405 nm, 425 nm, and 440 nm respectively.

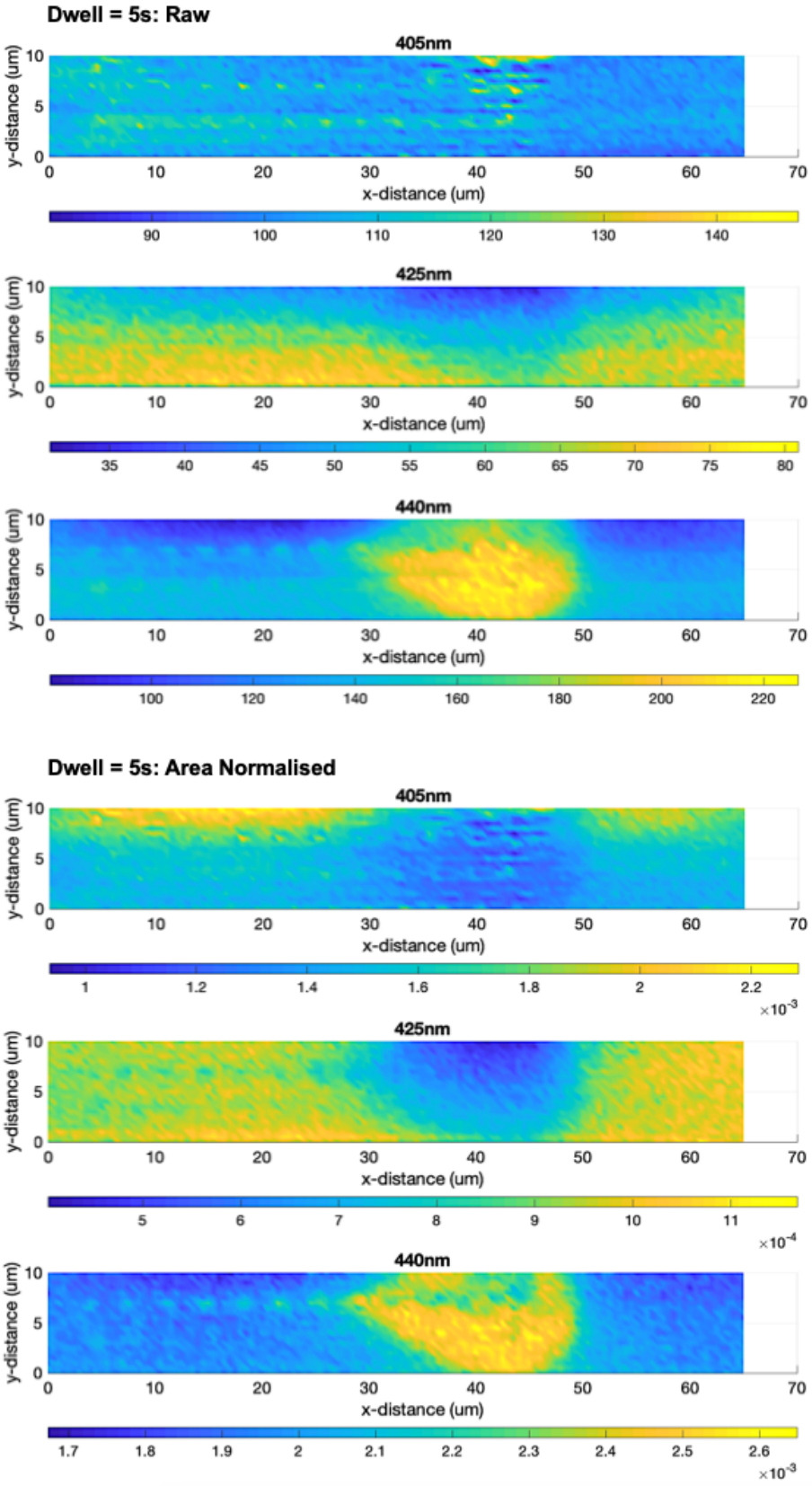



**Figure 6.9:** Raw and area normalised micro-PL maps with $d = 5\,\mathrm{s}$, $a = 3\,\mu\mathrm{m}$. Maps were phase-selected for the laser reflection, glassy phase, and $\beta$ phase at 405 nm, 425 nm, and 440 nm respectively.

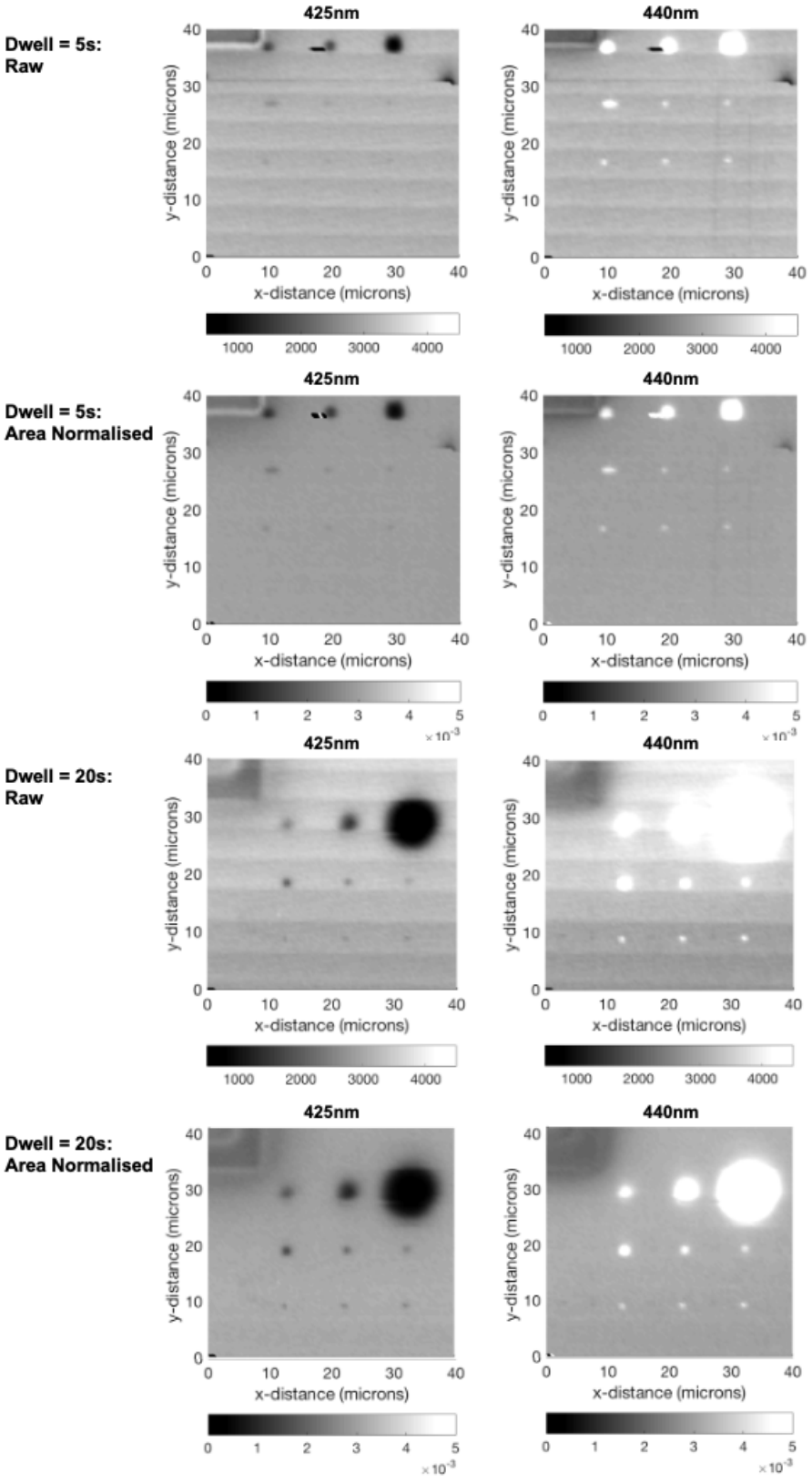



**Figure 6.10:** Raw and area normalised preliminary maps with $d = 5\,\mathrm{s}$ and $20\,\mathrm{s}$.

within this area. This effect was worse for the first dots, suggesting the larger volume of solvent, rather than the force of the tips was the main contributing factor to the roughness, indicating that the downward flow of the solvent from tip to film was too large and caused the film around the area to dissolve. This flow may have pushed the PFO outward from the tip, producing a large region of $\beta$ phase surrounding a low signal dot, shown in the AN 440 nm maps of Figures 6.7 and 6.9. The worst example of this effect was seen for $d = 5$ s in Figure 6.9, which also had the shortest trail of dots, perhaps due to the majority of the ink being used in the first dots. Film pitting was also evident in Figure 6.9 with bright dots seen at 405 nm, suggesting the tips had penetrated the film to reveal the smoother silicon dioxide substrate beneath, which reflects the laser better than the film. Therefore both the volume of solvent present and the proximity of the tips to the surface must be carefully monitored to prevent damage to the film.

When phase-selected for the peak glassy wavelength, 425 nm, the patterned dots would ideally be represented as dim regions within an intense map, with the inverse being true for the $\beta$ wavelength 440 nm. The AN maps for each $d$ show clearly the array of dots indicating that the patterning was successful in inducing the $\beta$ phase. However, in the raw 425 nm maps there was very little contrast visible between the phases, and the dots were only visible upon area normalisation at this wavelength. As the dots are visible in the raw maps at 440 nm, this suggests that only a small percentage of $\beta$ was patterned, due to the persistence of the 425 nm glassy in the PL of small percentages of $\beta$ phase, as shown in Figure 6.1.

It is clear from all raw maps that the PL signal is very low from the new micro-PL set-up. Though as this sample was not tested on the old set-up it is difficult to say for sure whether the sample was poor or the filter system described in Chapter 5 was too harsh for this particular sample. Although testing was done on PFO during the set-up, perhaps the alignment was not sustained throughout the mapping process, leading to loss in the signal. This is in sharp contrast to the preliminary maps, which demonstrate the large PL signal possible at this scale of collection. Their raw map signal is an order of magnitude higher than the new

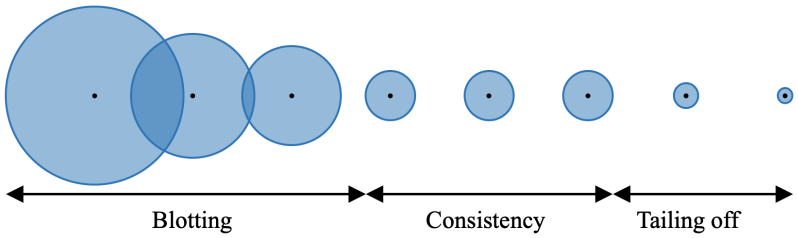



**Figure 6.11:** The various stages of dot patterning. After ink loading the tip releases large volumes of solvent for the first dots, the blotting stage. Then roughly consistent dots are patterned, the consistency stage, before the ink begins to run out - the tailing off stage. The number of dots in the blotting and consistency stage were measured for each pattern.

maps, suggesting that either the film or the set-up - or both - performed much better than the new sample and set-up of Chapter 5.

From the maps there are distinct stages in the dot patterning, shown in Figure 6.11. In some cases however the dots appear to be getting more intense as the ink runs out, such as the bright dot at (10, 0) in the AN 440 nm map of Figure 6.8. As the $z$-clearance of the dip-pen tips was equal for all maps, this was likely due to unevenness of the film surface reducing the distance between the film and tips. As described above in Section 6.3.1, this can be corrected at the macro scale by adjusting the tilt of the dip-pen, but cannot be anticipated at the scale of the film roughness.

The large initial deposits of solvent are evident in the broad expanse of $\beta$ phase at the start of each pattern, the blotting stage. The vapour from this volume of solvent could have affected the film surrounding the dots, and potentially contributed to the poor contrast of the maps by inducing small quantities of $\beta$ in the sounding film. This would in effect be increasing the noise of the spectral background by increasing the lower bound of the $z$ value of the map scale. To investigate this further, spectra from each dot and the unpatterned region was analysed below in Figure 6.12.

The preliminary maps shown in Figure 6.10 also demonstrate the need for blotting, with the first dots being significantly larger. The pitch of 10 µm has prevented them from overlapping, and no dissolution of the film is seen. This suggests that the patterning was more gentle on this sample, leading the tips to deposit a smaller volume of solvent. The largest dot is approximately 9 µm in

diameter at $d = 20\,\mathrm{s}$, much smaller than the large deposits in Figures 6.7 to 6.9, which span up to 20 µm despite the shorter $d$. This demonstrates the important of a light touch when patterning to control the flow of solvent to the surface and protect the integrity of the film.

It is clear from all maps that blotting is imperative to achieve consistently sized dots as early as possible, as well as to protect the film from thinning in the presence of too much solvent, as seen in the AN 405 nm and 440 nm maps of Figure 6.7. Of the new patterns, the most consistent dots appear to be in the $d = 1\,\mathrm{s}$ or $d = 3\,\mathrm{s}$ maps. Despite a higher signal, the preliminary patterns appear to be less consistent in dot size. The consistency, as well as dot size and approximate $\beta$ phase percentage is analysed in more detail below.

### 6.3.3 Dot Analysis

#### Dot Spectra

Figure 6.12 shows the PL from the centre of each dot of the new patterns, and the $\beta$ phase fraction estimated from the spectral profile (as described in [89]). The dots within each pattern each displayed a similar $\beta$ phase fraction. In contrast, the dot spectra of the preliminary maps in Figure 6.13 show much more $\beta$ phase in the first dots which decreases with each new dot, regardless of $d$. From the spectra of a nearby unpatterned region (dot 0) shown in grey for all dwell times, it is clear that a strong vapour effect has occurred as a result of large volumes of solvent being deposited on the film. The grey spectra consistently show a phase change relative to the raw film (dotted line).

For $d = 1\,\mathrm{s}$, there is less of a vapour effect than longer dwells. Highlighted by the vertical line at 450 nm, there is a contrast between the dot and nearby (dot 0) spectra, indicating the increased presence of $\beta$ phase within the dots (1%) relative to nearby (0.2%). Patterns $d = 3\,\mathrm{s}$ and 5 s do not exhibit this contrast and show a roughly equal fraction of $\beta$ phase across the area, suggesting that the longer $d$ affects the isolation of the solvent. This demonstrates that more work is needed to understand the relationship between solvent volume, pattern contrast,

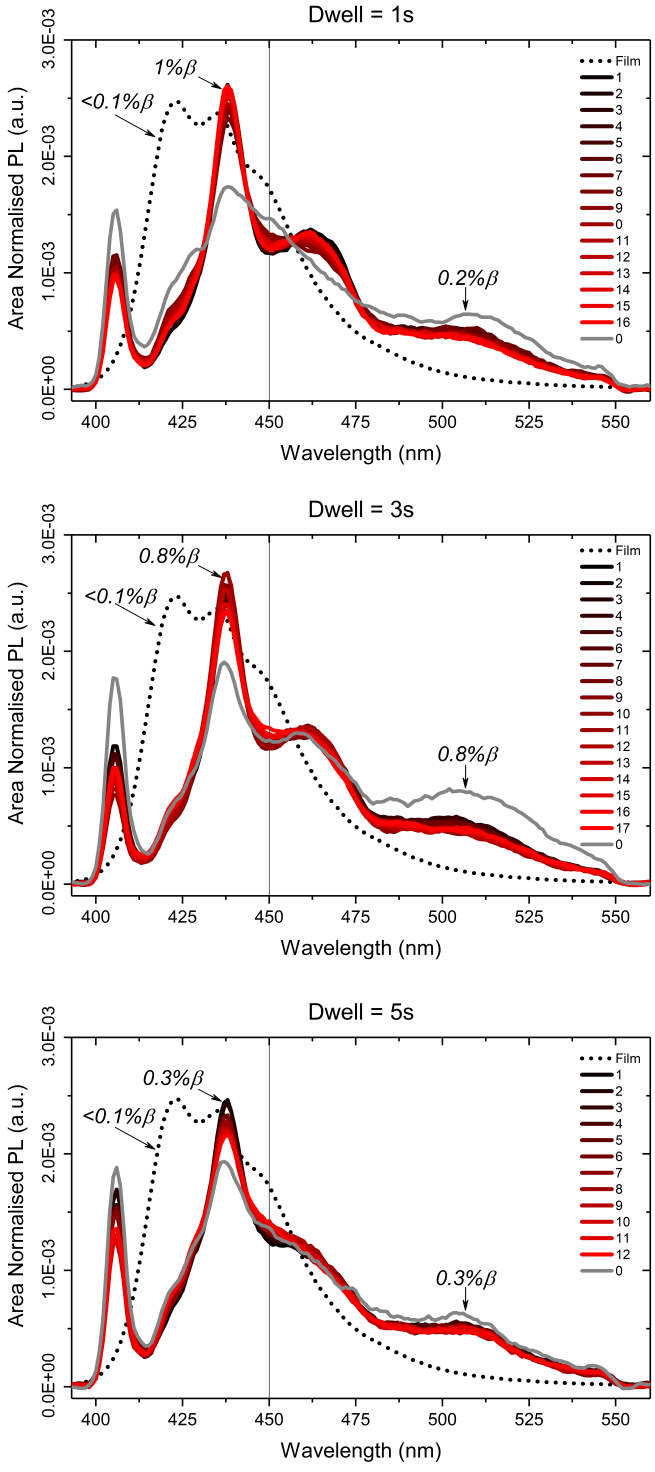



**Figure 6.12:** Area Normalised PL spectra of the dots imaged with the micro-PL set-up of Chapter 5, extracted from the coordinates of dot centres. The number denotes the order of patterning following blotting. The PL of the film prior to patterning is shown in the dotted line, and PL of an unpatterned point close to the patterns is shown in grey (dot 0). The dot spectra are overlaid as they were largely similar to each other, with an approximate $\beta$ fraction of 1%, 0.8% and 0.3% for $d = 1\,\mathrm{s}$, $3\,\mathrm{s}$ and $5\,\mathrm{s}$ respectively.

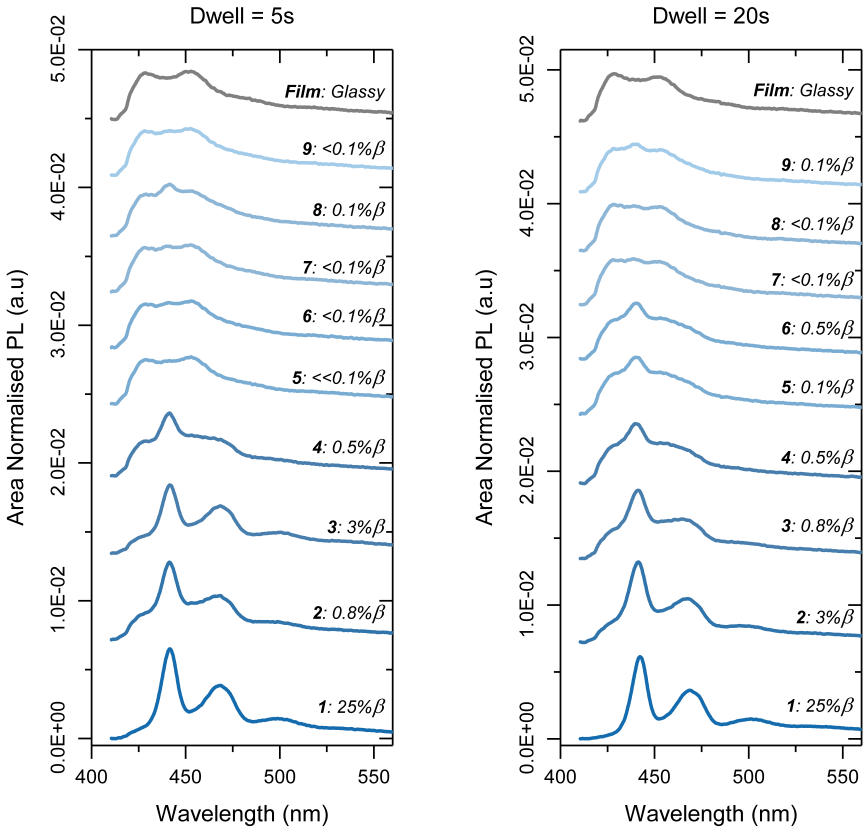



**Figure 6.13:** Area Normalised PL spectra of the preliminary pattern dots, extracted from the coordinates of dot centres. The number denotes the order of patterning. The PL of the raw film is shown in grey (dot 0). The dot spectra of the initial dots show a large $\beta$ fraction, approximately 25%, which drops with each successive dot to less than 0.1%. In this case there is little difference between $d = 5\,\mathrm{s}$ and 20 s, with considerably more $\beta$ phase present than the dwell of 5 s shown in Figure 6.12.

and the impact of different solvents, specifically to identify the maximum dot size achievable without inducing a detectable vapour effect.

The dot diameters, $\beta$ phase fractions, and number of dots in the blotting and consistency phases, as shown in Figure 6.11, are analysed in more detail below.

### Dot Measurements

To measure the size of the dots, the plots of Figure 6.7-6.10 were expanded and the $z$ scale adjusted to provide the highest contrast in the dot regions post blotting. Figure 6.14 shows the large degree of noise in the dot size, with little indication of a trend as each new dot is patterned. This could be due to the irregularity of the sample surface, or the fact that the PL does not measure the profile of the film. In

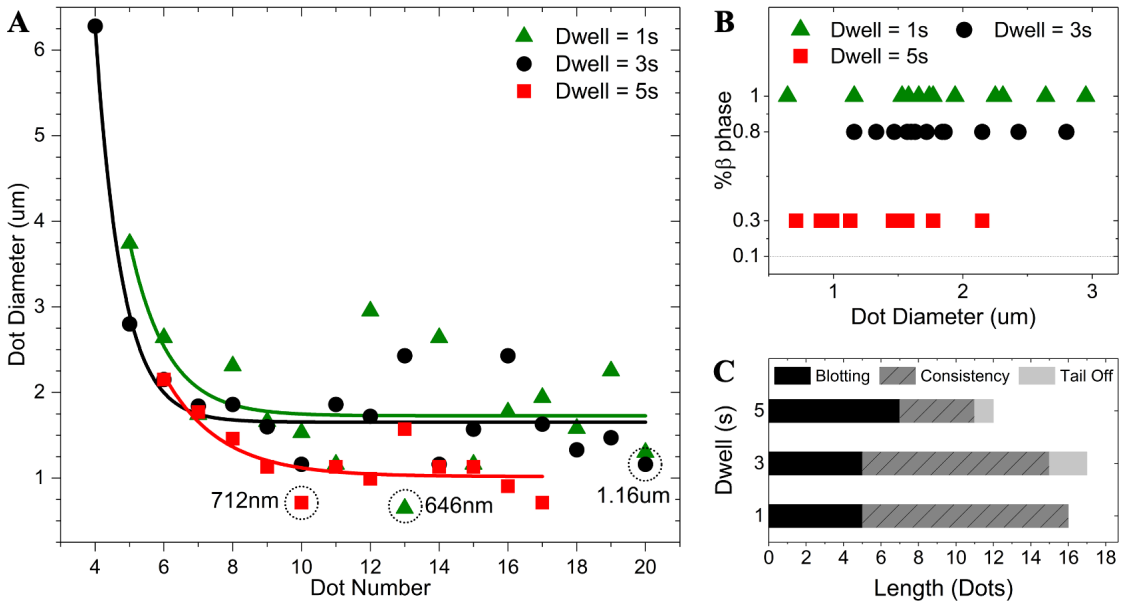



**Figure 6.14:** Measurement of the new pattern features. **A** shows the diameter of each dot in the order they were patterned (only dots that could be measured are included), **B** shows the relationship between the estimated $\beta$ phase fraction and diameter for each dot, and **C** shows the number of dots in the blotting and consistency stages for each $d$.

future, AFM should be utilised to measure the swell of the film and true dot size. In the absence of AFM, the values here can only be considered estimates.

Figures 6.14 and 6.15 show the measurements of various dot parameters for the new and preliminary patterns respectively. Although an area containing the first 24 dots of the new maps was mapped, it was not possible to measure all of them. All of the dots in the preliminary patterns were mapped and measured. Figures 6.14**A** and 6.15**A** show the diameter of each dot in sequence, and it can be seen in Figures 6.14 that the earliest dot number is 4. This is due to the initial dots for all $d$ of the new maps being swamped by the large solvent deposits described above, rendering them immeasurable. Similarly, none of the new maps showed dots beyond dot 20, either due to the ink running out before then ($d = 5\,\mathrm{s}$) or because the swamping had spread into the second row. The first non-measurable dots were included in the count of the blotting stage, as well as the dots that followed with large diameters. Once the diameter stabilised the dots were considered part of the consistency stage, and any further size reduction the tail-off stage. Of all maps, only 1 or 2 dots in $d = 3\,\mathrm{s}$ and $5\,\mathrm{s}$ in Figure 6.14**A** seem to tail off, which

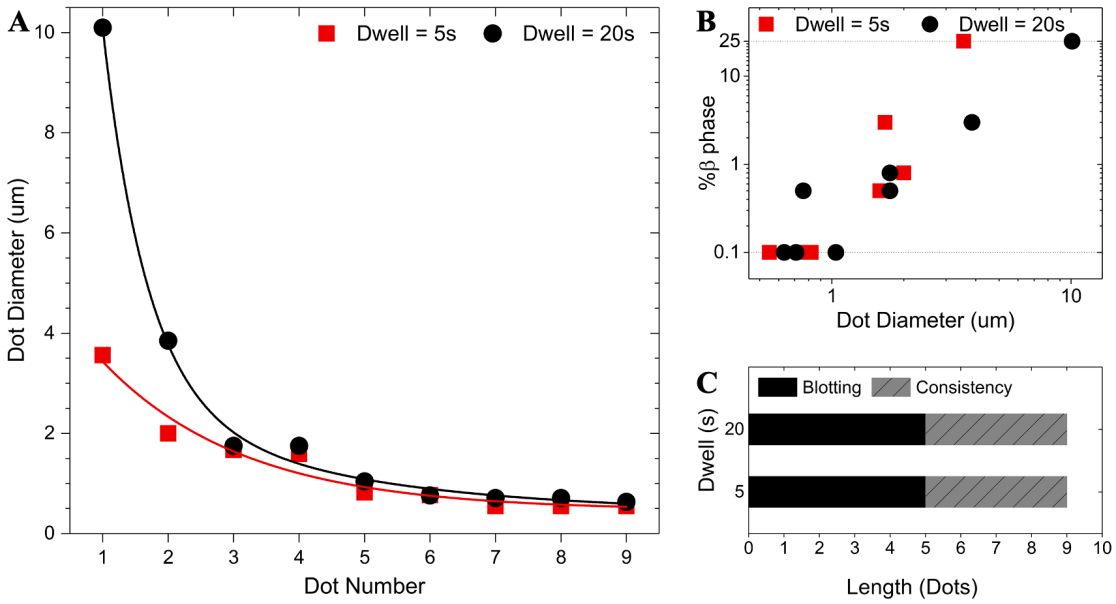



**Figure 6.15:** Measurement of the preliminary pattern features. **A** shows the diameter of each dot in the order they were patterned, **B** shows the relationship between the estimated $\beta$ phase fraction and diameter for each dot, and **C** shows the number of dots in the blotting and consistency stages for each $d$.

is promising as it suggests the ink lasted at least into the 3rd row of the pattern array despite heavy blotting. The number of dots in the blotting, consistency and tail off stages are shown in Figures 6.14**C** and 6.15**C**.

The **A** plots show that the decay of the dot diameter is roughly exponential, which could be expected due to the volume of remaining ink reducing. There does not appear to be a strong relationship between the sharpness of decay and the $d$, with the largest drops in diameter seen for $d = 20\,\text{s}$ and $3\,\text{s}$, with $d = 5\,\text{s}$ showing a modest decay in both sets of maps. The shortest $d = 1\,\text{s}$ showed very little change in diameter and was the noisiest data set of all patterns. For the new maps of Figure 6.14, the longest $d = 5\,\text{s}$ settles at a lower consistent dot size. However this is not a trend, with $d = 1\,\text{s}$ settling lower than $d = 3\,\text{s}$. The consistency length for $d = 1\,\text{s}$, is slightly higher than $d = 3\,\text{s}$, but as the consistency length starts when dots come into the same size region as the following dots, the noisiness of $d = 1\,\text{s}$ contributed to this stage starting a bit earlier than $d = 3\,\text{s}$, and in effect they have similar consistency lengths. Overall the new maps show an increase in consistency length as the $d$ is reduced, with the blotting length remaining roughly equal. For $d$

= 5 s where the blotting is slightly higher, there is a consequent drop in consistency length, suggesting most of the ink was deposited during blotting.

In the preliminary maps of Figure 6.15, no tail off is observed and the dots were fewer in number, so their consistency lengths could be higher than shown. Notably the blotting length is equal to the most consistent new maps, suggesting this value is independent on contact force. There is also significantly less noise in the diameter decay, which indicates that a lower contact force offers more control. The minimum dot size of the preliminary maps is for $d = 5$ s at 548 nm, slightly less than the 633 nm of the $d = 20$ s pattern, suggesting that reducing the $d$ could further reduce the diameter. Further work to pattern with a low contact force and a $d = 1$ s, as well as increasing the number of dots patterned to test the consistency lengths would hopefully improve these numbers and move closer to achieving the aims described in Section 6.1.

The **B** plots of Figures 6.14 and 6.15 investigate the relationship between dot diameter and $\beta$ phase fraction. The $\beta$ phase fractions are bound at 0.1% and 25%, as it is not possible to estimate the value spectrally outwith these bounds. The preliminary maps in Figure 6.15**B** show a clear correlation, with the smallest dots of each pattern showing the minimum estimated fraction of 0.1% and the largest dots reaching the maximum of 25%. In contrast, the new patterns in Figure 6.14**B** show a constant $\beta$ phase fraction for all diameters. While the highest fraction of $\beta$ phase of the new maps was seen for $d = 1$ s, as described above in Figure 6.12, the low values seen for $d = 3$ s and 5 s, further suggest that the patterning force damaged the film, limiting its ability to conform to the $\beta$ phase. Despite this, it is clear from the preliminary maps that there exists a trade-off between dot size and $\beta$ phase fraction. At the desired sub-micron diameters it may not be possible to achieve a significant phase change to enable sufficient contrast in refractive index. Although dots of the order of 500 nm in diameter were achieved, these showed only 0.1% $\beta$ phase. Significantly however, reducing the $d$ does not appear to reduce the $\beta$ fraction, with $d = 5$ s in Figure 6.15**B** achieving roughly same fractions as $d = 20$ s but at smaller diameters. Additionally the lowest dwell

time tested, $d = 1\,\mathrm{s}$ in Figure 6.14**B**, achieved a minimum diameter of 646 nm with a $\beta$ phase fraction of 1%, showing that it is possible to get 1% $\beta$ phase at sub-micron diameters. Therefore while the maximum fractions may be limited to large dots, reducing $d$ does not appear to hinder the resultant $\beta$ fraction. Therefore low dwells and low contact forces are desirable for both the long consistency lengths, and to maximise the $\beta$ phase fraction.

To achieve small features it is clear from the above results that blotting is essential. However it is also clear from Figure 6.14**B** $d = 5\,\mathrm{s}$ that blotting too much can reduce the volume of solvent such that long trails of dots become impossible. The solution to this could be to have a longer $d$ during the blotting and then a short $d$ and light touch for the consistency, allowing the dot diameter to decrease quicker, and remain constant for longer. This would also provide a more consistent $\beta$ fraction along the dots. Alternatively a short blotting $d$ could ensure sufficient solvent remains on the tips for the patterns, as demonstrated in Figure 6.14**A** $d = 1\,\mathrm{s}$. Regardless, the blotting should take place far away from the pattern area to maximise phase contrast by avoiding the vapour effect described above.

The remaining issue is the very small $\beta$ fraction achieved in sub-micron dots. Other solvent mixes used [23], tend to be more volatile than decalin, and so would likely induce even smaller fractions. Therefore any further work should initially focus on improving the issues identified above: improving sample quality and trialling various dwell time and blotting combinations before testing different solvent combinations.

## 6.4 Conclusion

The aim of patterning dot arrays with multiple tips simultaneously was achieved. However, while consistent rows of $\beta$ phase dots within certain arrays were studied above, large inconsistencies in patterns between tips were also observed, highlighting various pitfalls of the process.

From studying the parameters of a range of patterns the view of the parameter space has been broadened, but there are a number of things that should be taken

into consideration for future work. Although film **B** had only traces of the $\beta$ phase, patterning a fully glassy film would instead allow better quantification of the patterning parameters. Efforts to produce a pristine glassy film should therefore be the bedrock of any future work. As the thermal spin-coating methods described above were not sufficient, different PFO may be tested, or the PFO used here from oneMaterial may be analysed to ascertain its quality. Additionally, solutions of PFO in other solvents such as chloroform could be trialled.

In terms of the scalability of the patterning process, it was clear that both the loading of ink onto the tips, and the tip-film contact was not consistent across the tip array. Improving film quality to ensure a smooth surface, and more thorough cleaning of the inkwells could help reduce this imbalance, but does not address irregularity of tip alignment within the array. The inherent delicacy of the tips increases their chances of misalignment, so large scale monitoring of tip array condition would be required in a scaled up process. The process however would remain highly delicate and prone to tip defects, highlighting the need for only slight tip-film contact for the tip's sake as well as the film. The effects of a strong tip-film interaction on the film were evident with visible damage in the new patterns, paired with increased scattering indicated by a reduction in PL signal. Future work should make a small tip-film interaction imperative for all patterns. It is clear from these patterns that more lab work is required before larger scale trials can be conducted.

For the patterning parameters, it was seen that $a$ was secondary in importance to $d$ for the initial understanding of the process. Further work should focus on $d$ and only reduce $a$ once $d$ can be confidently patterned at the $< 500\,\text{nm}$ scale. This should avoid the instances of pattern failure seen above, where patterns with $a = 1\,\mu\text{m}$ were consistently swamped with solvent. Reducing the tip-film interaction should limit the volume of solvent deposited as well as prevent the damage to the film described above. Additionally for future patterns the $d$ should be reduced to 1 s as this provided the longest consistent range of dots. The micro-PL mapping of these patterns should then go further to properly identify the tail-off stage of the dots and determine an appropriate re-inking strategy to achieve a full 2D array of consistent dots.

Future work should also always include blotting prior to patterning at some distance from the patterns, with a study to confirm whether the number of blotting dots required is independent of $d$, as suggested in the data above. Although decalin did not bleed uncontrollably after the blotting stage, it also did not provide a significant $\beta$ fraction in the sub-micron dots. Further work is therefore required to test a range of solvent inks to determine their capability for inducing the $\beta$ phase at small volumes, and quantify any remaining vapour effect once the blotting stage has been removed from the patterns. Previous work has shown more volatile solvents are effective in patterning small features [23], however there is likely a trade-off with $\beta$ phase fraction and consistency length due to faster evaporation on the film and in the inkwells.

The lack of feature clarity in the new micro-PL maps suggests that they do not have the desired sharp change in $n$. Work to improve the sharpness of the phase change is therefore required in addition to reducing the vapour effect, and should be considered during future solvent studies. This work should include investigating ways to increase the surface tension of the solvent such that it is more confined to the deposition area - solvent blends that exhibit the Marangoni effect [170] could be utilised in this endeavour. Additionally, AFM would provide an improved view of the dot profiles, which would enable the spectral boundary to be accurately determined and consequentially the gradient of $n$ to be quantified.

In this work the drying of the patterns was not taken into account, and so different drying scenarios could be tested in future work. The samples were left to dry in the NLP 2000 enclosure, but they could instead be taken directly into ambient conditions or a nitrogen atmosphere. (The potential pitfall of the latter is that the sudden pressure change could draw the solvent across the film, leading to a loss of feature definition.) Alternatively heat could be used, but only at low levels to prevent the $\beta$ phase regions reverting to glassy, or the crystallisation of the film. The impact of different drying processes should therefore be included in future trials as they may have a large effect on feature and phase contrast.

Turning to the $\beta$ fraction, the ranges achieved were 0.1% to 25% which indicates a $\Delta n$ between 0% and 10.9% at 450 nm, based on the values referenced in Section 6.1. As described above the the fraction patterned was independent of $d$, but (at least in the preliminary patterns) correlated with the dot size, with the $\Delta n$ of 10.9% found in a dots with diameters $> 3.75$ µm. This presents a problem as in future work the feature size would need to be further reduced from the minimum achieved here (548 nm), while the $\beta$ phase fraction must be increased or at least maintained. The solvent work described above must therefore focus on the achievable $\beta$ phase fraction when identifying solvents and blends for consideration. The good news however is that reducing $d$ should not negatively impact the phase contrast.

From the PL emission we can only estimate the $\beta$ phase fraction and subsequent $n$, and so to fully analyse the patterns the micro-PL set-up could be adapted to instead measure absorption, as mentioned in Chapter 5. This would allow the calculation of $\beta$ phase fraction via deconvolution of the absorption spectra and the calculation of $n$ via Kramers-Kronig analysis as detailed in [107], providing a more exact method for analysing pattern success and identifying suitable photonic applications.

To summarise, DPN presents a complex parameter space to investigate, demonstrated by the level of noise and lack of trends in the data. Without the highly controlled conditions of a clean room, reproducibility is a challenge. Starting with a cleanly glassy film would help in accurately quantifying things such as the vapour effect, feature contrast and phase contrast. While the $\Delta n$ values achieved here are indeed sufficient for use in photonic devices, their application potential is currently limited by issues with contrast and size. Further work to explore solvents that will help solve these problems and enable fine tuning of the parameters is required before such devices can be fabricated and the process scaled.

# 7 Concluding Remarks

Following the detailed conclusions of each chapter, some ideas for future work are discussed below.

## 7.1 AIE

In Chapter 3 it was found that AIE monomers are able to emit without aggregation, disputing the theory that RIR is required to induce emission in AIE materials. As the degree of aggregation was correlated with the strength of the excimer emission, and RIR results from this aggregation, it makes sense to instead cite RIR as the reason for the higher PLQE of the excimer than the monomer.

Therefore, future work could study methods to achieve RIR without excimer formation, and investigate its effect on the monomer PLQE. This would enable further assessment of the RIR hypothesis, as any increase in the PLQE in the absence of excimers could be attributed to the reduction in non-radiative pathways of the monomer. To induce RIR, the AIE molecules could be dispersed in polymer films, as discussed in Section 3.4, furthering the work of the blend films which triggered this study.

Achieving RIR in monomers would enable tuning across a broad spectrum of efficient emission, similar to that seen in the F/O oligomer solutions. By locally

controlling aggregation, regions of monomer and excimer emission could be patterned within the polymer blend film. For example the DPN could be utilised to deposit additional AIE material which could induce excimer formation at the nanoscale by increasing the local concentration.

## 7.2 Fluorene/Fluorenone Oligomers

Patterning of excimer regions could also be trialled with the F/O oligomers. To produce good quality films, the oligomers could be blended into PF or PFO. Contact and vapour treatment with various polar solvents could be trialled to understand whether it is possible to affect the aggregation state of the fluorenone in the solid state. The dipole may cause the fluorenone moiety to reorient to screen the solvent dipole during exposure, and it may remain in this orientation following solvent evaporation.

If successful the solvent could be deposited via DPN, allowing local screening. Alternatively, additional oligomer solution could be deposited onto the film surface, forming patterns of enhanced excimer emission.

Through the slight thermal oxidation of FFF, the technique also revealed that the excimer formation is sufficiently sensitive to identify oxidation in very lightly oxidised samples, for which the oxidation was too subtle to show in the absorption or PL. This approach could therefore be further developed to work for larger molecules such as polymers, as discussed in Section 4.4.3.

Work to further oxidise the fluorene units could also be developed, by trialling exposure to UV radiation instead of thermal oxidation. This would provide more data at varying degrees of oxidation between FFO/FOO and FFF-ox2, facilitating the work to detect low levels of oxidation in polymers. Controlled UV degradation could also be employed as a patterning technique, wherein a UV laser could pattern regions of the G-band into glassy PFO.

## 7.3 Dip-Pen Patterning of PFO and Micro-scale Photoluminescence

As described in Section 6.4, much further work is required to produce consistently sized, reproducible $\beta$ phase patterns. To begin with, the focus should be on producing smooth, glassy films that provide a clear baseline for patterning. From the results above, it was clear that the film used to pattern the preliminary maps was superior to the new maps, resulting in a sharper PL contrast. Fabrication of future films could be done in a clean room to improve film quality and consistency.

Regarding the DPN patterning, the tip-film contact should be minimised going forward. This would prevent the film pitting seen above, as well as reduce the volume of solvent deposited, which would consequently reduce the feature size. Although the work here achieved a dot diameter of 548 nm, most of the dots were much larger due to the close tip contact enabling a high solvent deposition volume. Once the DPN operation can be improved to ensure the tips deposit only small solvent volumes without pitting the film, studies into different solvents and chamber humidities could be carried out. Increasing the humidity for example could help reduce solvent spreading, resulting in smaller features with greater definition.

Reproducibility was also an issue for the pattern imaging, with most micro-PL maps showing only a weak PL signal. To be able to progress the DPN patterning, effort should be made to improve the laser and emission signal of the micro-PL set-up, through better alignment and/or an alternative design with fewer opportunities for signal loss.

Beyond PL, different types of analysis could also be undertaken to further characterise the patterns. AFM should be measured prior to patterning to assess film quality, and again post patterning to quantify the degree of swelling and ensure film integrity is maintained. Mapping of the absorption would also be desirable to quantify the $\beta$ phase fraction and $\Delta n$ across the pattern. If achieved, photonic structures based on the measured $\Delta n$ could be modelled, and the DPN's bitmap import tool could be utilised to automate the patterning of modelled structures.

In conclusion, a number of examples of conformational control and its significant impact on the absorption and emission of a material have been studied. The significance of the material state and local environment has also been explored, with solution samples exhibiting large emission shifts in response to incremental changes to the molecular environment.

The studies of Chapters 4 and 6 demonstrate the versatility and breadth of potential applications offered by fluorene based molecules, while the findings of Chapter 3 provide a new foundation to our understanding of the AIE mechanism. It is clear that achieving control of the conformation at the molecular scale offers a multitude of new possibilities to the field of photonics, as well as new methods for the fabrication of photonic devices.

# Appendices

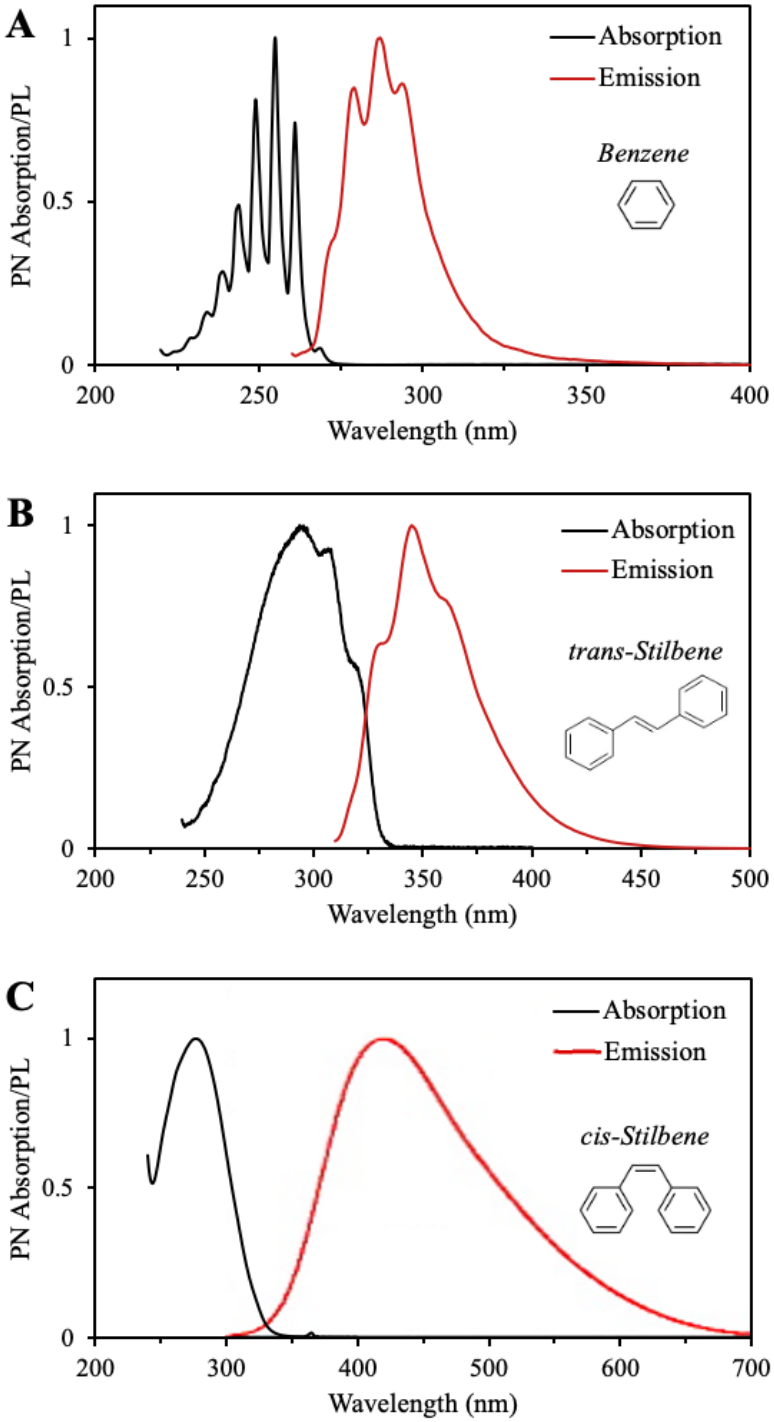



**Figure 1:** Absorption and emission of **A** Benzene, **B** trans-Stilbene and **C** cis-Stilbene. **A** and **B** plotted with data from [171][172]. **C** adapted from [173].

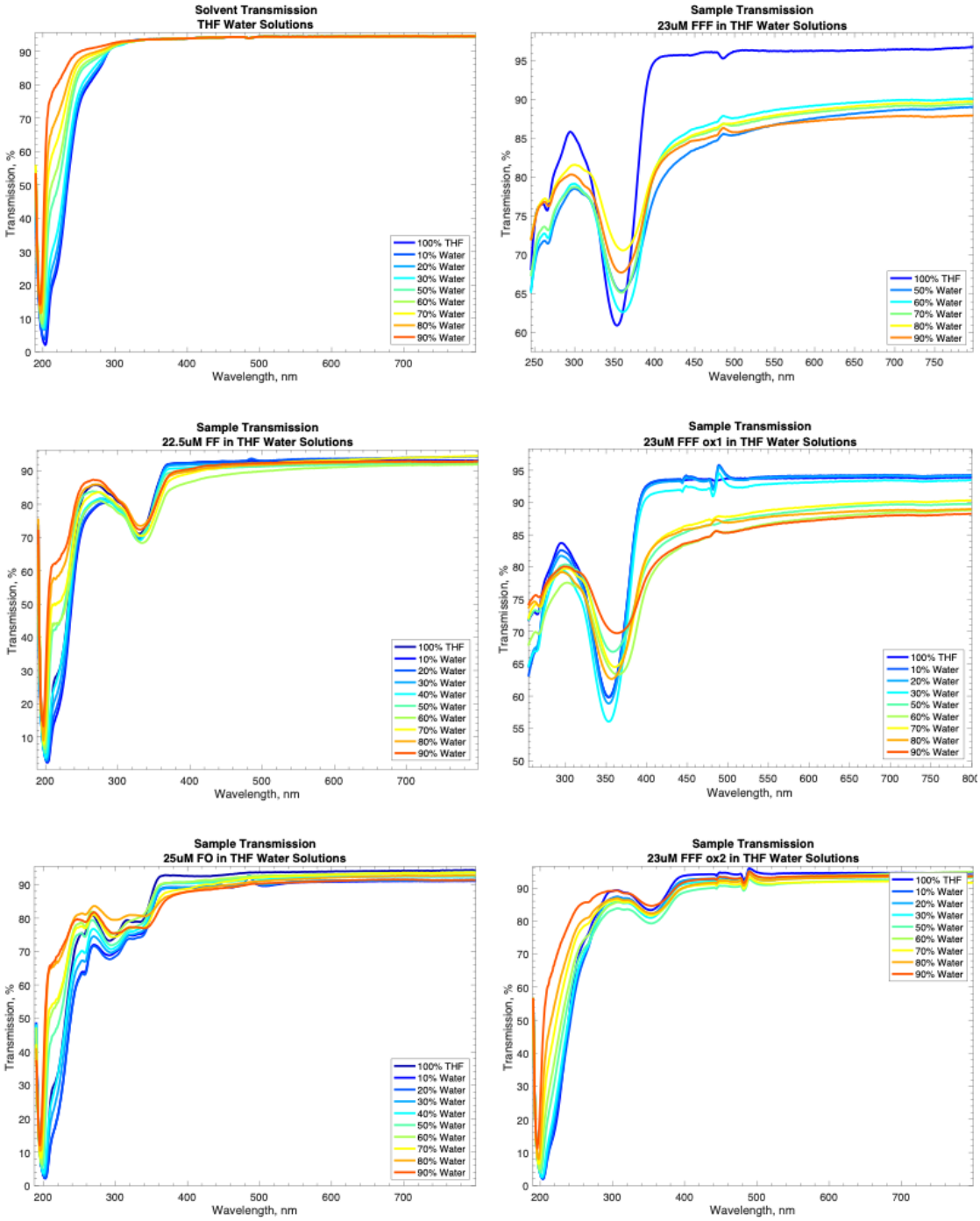



**Figure 2:** Transmission of solvents and FF, FO, FFF, FFF-ox1, FFF-ox2 solutions.

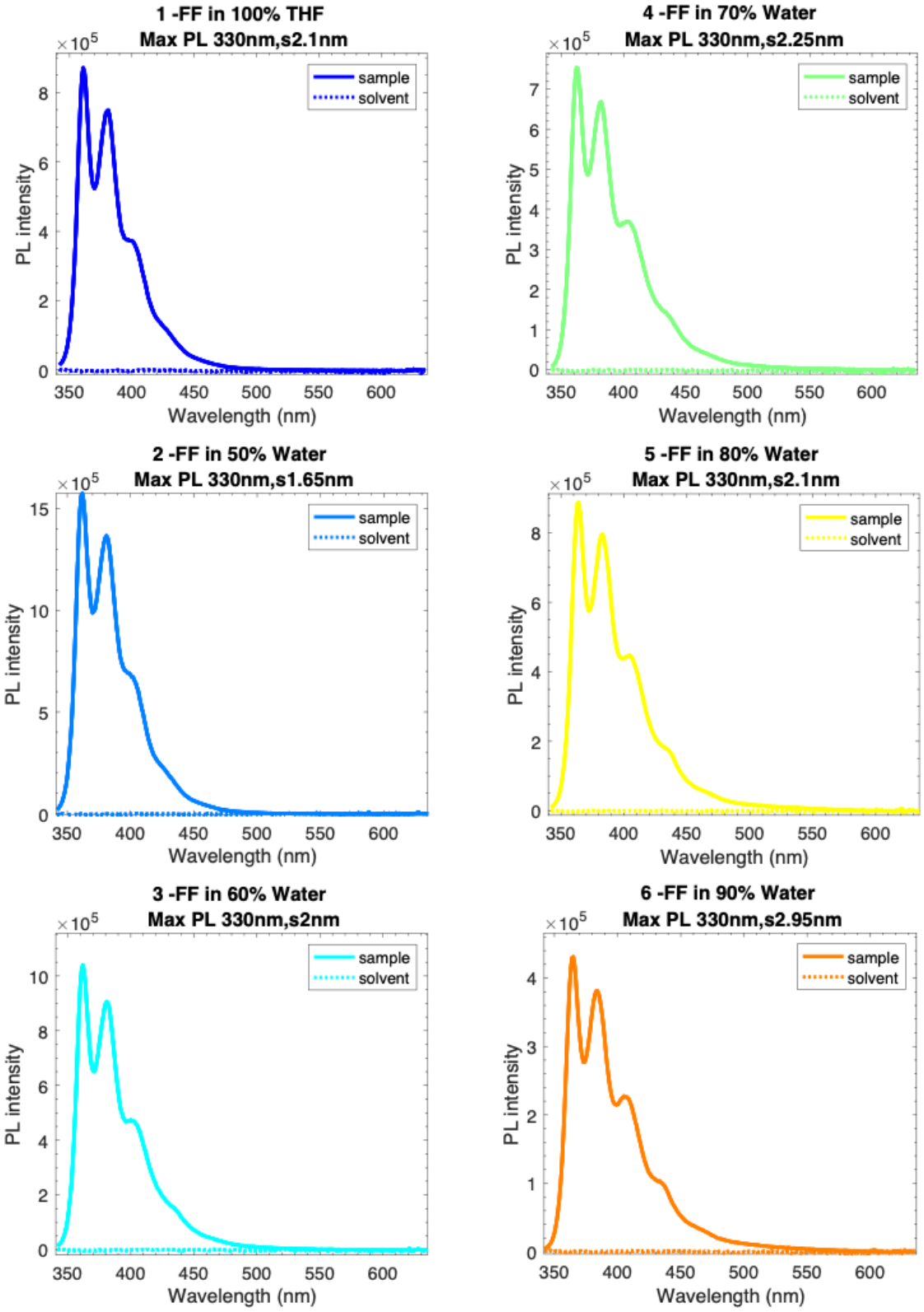



**Figure 3:** PL of solvents and corresponding FF solutions.

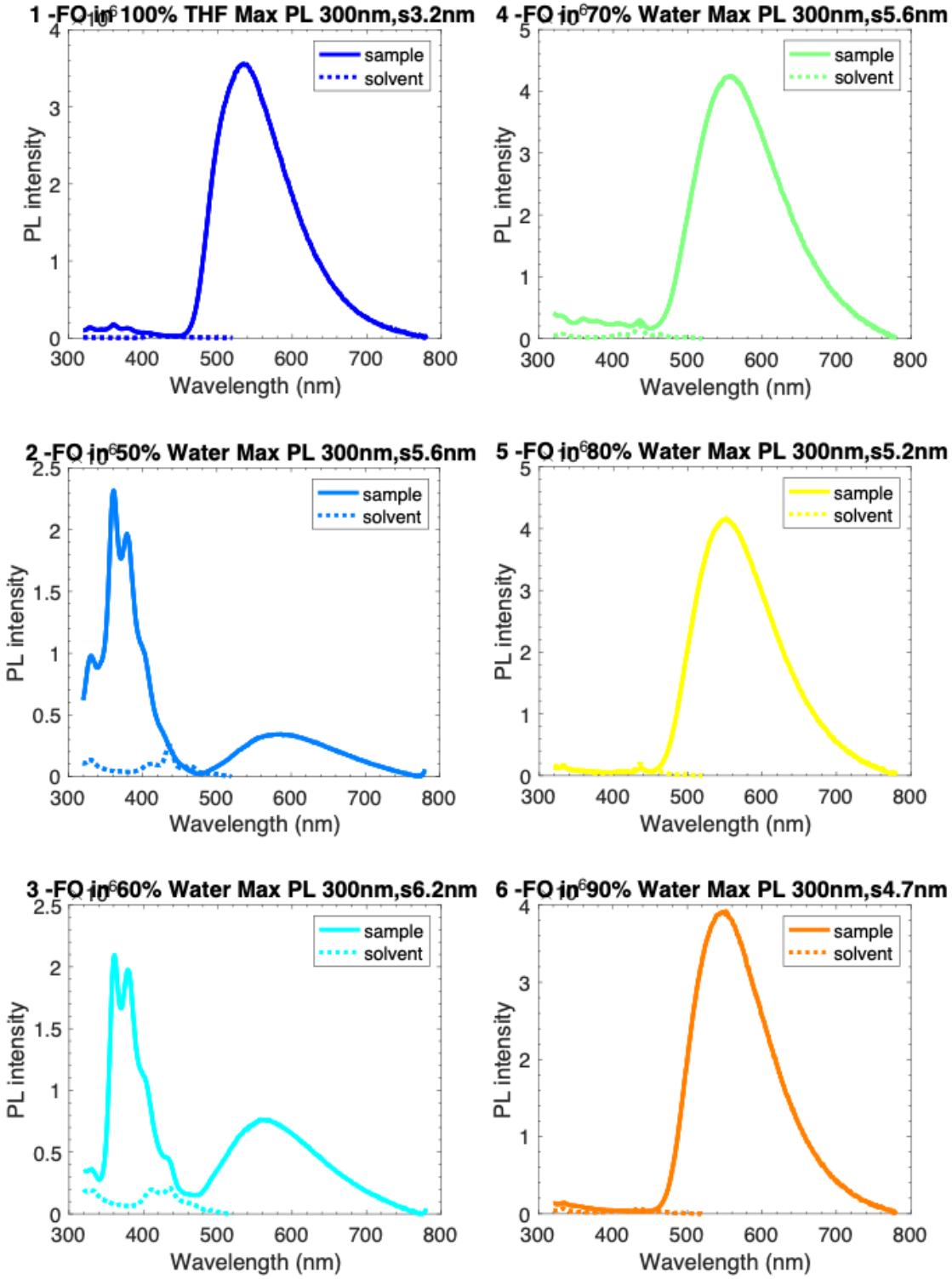
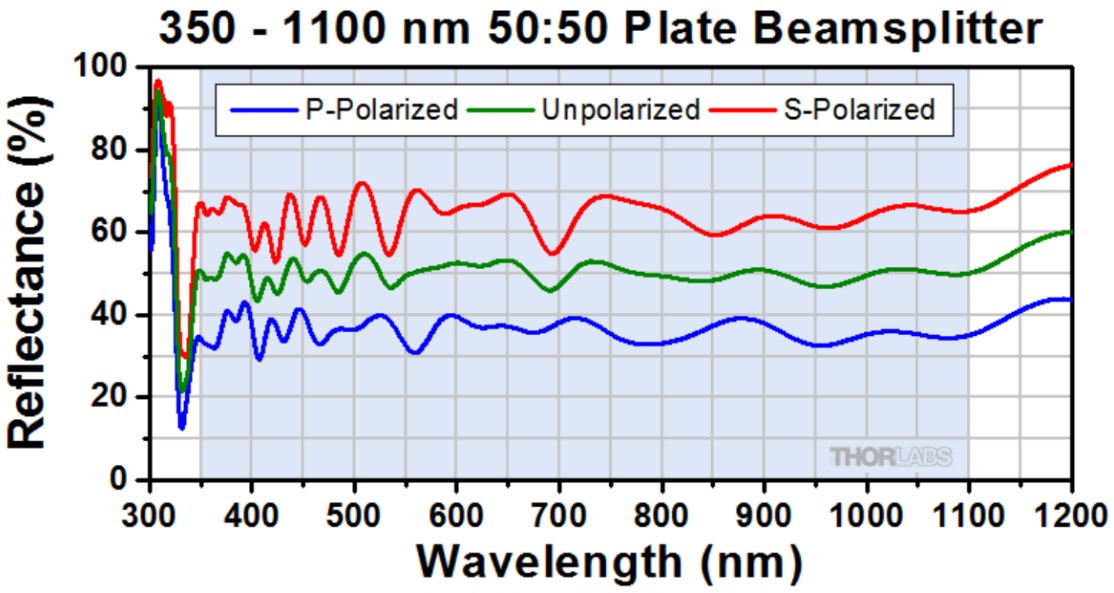



**Figure 4:** PL of solvents and corresponding FO solutions.




Reflectance curve at 45° angle of incidence for a 50:50 plate beamsplitter coated for 350 - 1100 nm (shaded region). Reflectance and transmission were measured separately using a Perkin Elmer Lambda 950 UV/VIS/NIR spectrophotometer with a calcite polarizer attachment.

**Figure 5:** Beam splitter reflection of polarised light [174].

# List of Components

**405 Dichroic** . . . . . Edmund Optics 25.2 × 35.6 mm, Dichroic Filter 86-330

**5050 Beamsplitter** . . . . . 350 − 1100 nm Plate Beamsplitter, Thorlabs (BSW26R)

**550 Filter** . . . . . Thorlabs (FES0550)

**Camera** . . . . . USB 2.0 CMOS Camera, 1280×1024, Monochrome Sensor, Thorlabs (DCC1545M)

**Camera Tube Lens** . . . . . Mitutoyo to C-mount Camera 152.5 mm Extension Tube, Edmund Optics (56-992)

**CCD** . . . . . Princeton Instruments PyLoN system 2048× 512, 13.5 µm x 13.5 µm pixels

**Circular Mirrors** . . . . . UV enhanced Aluminium, Thorlabs (PF10-03-F01) (between fibre & objective)

**Fibre** . . . . . Single Mode Patch Cable 320 - 430 nm, Thorlabs (P1-305A-FC-1)

**Fibre Coupling Objective** . . . . Olympus Plan N 20×, NA 0.4, Working Distance 1.2 mm, Cover Glass Thickness 0.17 mm

**Fibre Output Lens** . . . . . 45 mm, Ø" Achromatic Doublet, Thorlabs (AC254-045-A-ML)

**Imaging Objective** . . . . . Nikon CFI Plan Apo VC 100× Oil, NA 1.40, Working Distance 0.13 mm, Cover Glass Thickness 0.17 mm

| | |
|---|---|
| **Imaging Objective (Knife Edge)** | Mitutoyo M Plan Apo 100× NA 0.70 f=200 |
| **Laser** | SuperK Extreme High Power Supercontinuum White Light Laser, NKT Photonics with SuperK Extend-UV Deep UV supercontinuum extension unit for wl $250 - 500$ nm |
| **LED** | 625 nm Mounted LED Thorlabs (M625L4) |
| **Objective Oil** | Nikon Immersion Oil Type F, Index ne = 1.518 |
| **Optical Table** | Newport RS 4000, Sealed Hole Table Top with Tuned Damping |
| **Oval Mirrors** | 1" Broadband Dielectric Elliptical Mirror, $400 - 750$ nm, Thorlabs (BBE1-E02) (between laser & fibre, objective & spectrometer) |
| **Piezo Stage and Controller** | PiezoConcept LF3 |
| **Powermeter** | Newport Optical Power Meter, 1830-R, controlled with Newport Computer Interface Software v3.0.4 |
| **Spectrometer** | SpectraPro HRS-500, Princeton Instruments with ResXtreme Spectral Deconvolution |
| **Spectrometer Input Lens** | f40mm visible achromat, dia25.4 mm, Thorlabs (AC254-040-A) |

# References


[1] M. M Attala, E Tannenbaum, and E. J Scheibner. “Stabilization of silicon surfaces by thermally grown oxide”. In: *Bell Syst. Tech. J* 38 (1959), pp. 749–783.

[2] G Goos, J Hartmanis, and J van Leeuwen. “Optical supercomputing”. In: *Springer*. 2008.

[3] Andrew Steane. “Quantum computing”. In: *Reports on Progress in Physics* 61.2 (1998), pp. 117–173. arXiv: `9708022 [quant-ph]`.

[4] Iraj Sadegh Amiri et al. “Introduction to photonics: Principles and the most recent applications of microstructures”. In: *Micromachines* 9.9 (2018).

[5] Theodore Maiman. “Stimulated Optical Radiation in Ruby”. In: *Nature* 187.4736 (1960), pp. 493–494.

[6] R.C. Alferness et al. *Guided-Wave Optoelectronics*. Ed. by Theodor Tamir. 1995.

[7] Tim Berners-Lee. “The original proposal of the WWW”. In: *March 1989* (1989).

[8] Jd John D Joannopoulos et al. *Photonic crystals: molding the flow of light*. 2008, p. 286. arXiv: `arXiv:1011.1669v3`.

[9] James Clerk Maxwell. *On Faraday’s Lines of Force*. Transactions of the Cambridge Philosophical Society, 1856.

[10] J. C. Maxwell. *On physical lines of force*. Vol. 90. SUPPL.1. 1861, pp. 11–23.

[11] Thomas F Krauss, Richard M De La Rue, and Stuart Brandt. “Two-dimensional photonicbandgap structures operating at near-infrared wavelengths”. In: 383.October (1996), pp. 399–402.

[12] Jenny Clark and Guglielmo Lanzani. “Organic photonics for communications”. In: *Nature Publishing Group* 4.7 (2010), pp. 438–446. URL: `http://dx.doi.org/10.1038/nphoton.2010.160`.

[13] Jianli Miao and Fujun Zhang. “Recent Progress on Photomultiplication Type Organic Photodetectors”. In: *Laser and Photonics Reviews* 13.2 (2019), pp. 1–38.

[14] Ifor D.W. Samuel and Graham A. Turnbull. “Organic semiconductor lasers”. In: *Chemical Reviews* 107.4 (2007), pp. 1272–1295.

[15] A. Szent-Gyorgyi. “Internal Photo-electric Effect and Band Spectra in Proteins”. In: *Nature* 4000 (1946).

[16] D.D. Eley. “Phthalocyanines as Semiconductors”. In: *Nature* 4125 (1948).

[17] C. W. Tang and S. a. Vanslyke. “Organic electroluminescent diodes”. In: *Applied Physics Letters* 51.1987 (1987), pp. 913–915.

[18] J. H. Burroughes et al. “Light-emitting diodes based on conjugated polymers”. In: *Nature* 347.6293 (1990), pp. 539–541.

[19] Leslie Howard Sperling. *Introduction to Physical Polymer Science*. Vol. 78. 2006, p. 866. URL: http://pubs.acs.org/doi/abs/10.1021/ed078p1469.1.

[20] A. Nathan et al. "Flexible Electronics: The Next Ubiquitous Platform". In: *Proceedings of the IEEE*. Vol. 100. Special Centennial Issue. 2012, pp. 1486–1517.

[21] Ruediger Sprengard et al. "OLED devices for signage applications: a review of recent advances and remaining challenges". In: vol. 5519. 2004, pp. 173–183.

[22] H. Ma, A. K Y Jen, and L. R. Dalton. "Polymer-based optical waveguides: Materials, processing, and devices". In: *Advanced Materials* 14.19 (2002), pp. 1339–1365.

[23] Aleksandr Perevedentsev et al. "Dip-pen patterning of poly(9,9-dioctylfluorene) chain-conformation-based nano-photonic elements". In: *Nature Communications* 6 (2015), pp. 1–9.

[24] Ji-Seon (Imperial College) Kim. "Lecture 1 : Plastic electronics". In: *Molecular Physics & Optoelectronic Processes Lecture Course*. 2015.

[25] S.K Bhasin, Rajshree Khare, and Reena Gupta. *Pharmaceutical Organic Chemistry*. 1st ed. Elsevier, 2012, p. 338.

[26] Amitabh Banerji, Michael W. Tausch, and Ullrich Scherf. "Classroom Experiments and Teaching Materials on OLEDs with Semiconducting Polymers". In: *Educacion Quimica* 24.1 (2013), pp. 17–22. URL: http://dx.doi.org/10.1016/S0187-893X(13)73190-2.

[27] Ji-Seon (Imperial College) Kim. "Lecture 2 : Fundamental Excitations in Organic Semiconductors Excitations in organic semiconductors". In: *Molecular Physics & Optoelectronic Processes Lecture Course*. 2015.

[28] Ji-Seon (Imperial College) Kim. "Lecture 3 : Singlet and Triplet Excitons in Organic Semiconductors". In: *Molecular Physics & Optoelectronic Processes Lecture Course*. 2015.

[29] Joseph R. Lakowicz. *Principles of Fluorescence Spectroscopy*. 3rd. Springer US, 2006, p. 362. arXiv: arXiv:1011.1669v3.

[30] Ji-Seon (Imperial College) Kim. "Lecture 4 : Optoelectronic Processes in Organic Semiconductors Total wavefunction of a molecule". In: *Molecular Physics & Optoelectronic Processes Lecture Course*. 2015.

[31] Aadne Ore. "Intermolecular energy transfer and concentration depolarization of fluorescent light". In: *The Journal of Chemical Physics* 31.2 (1959), pp. 442–443.

[32] J. B. Birks. "Excimers and Exciplexes". In: *Nature* 214 (1967), pp. 1187–1190.

[33] Marras. *Marras Laboratory: Modes of energy transfer between fluorophores and quenchers*. URL: http://www.molecular-beacons.org/toto/Marras%7B%5C_%7Denergy%7B%5C_%7Dtransfer.html (visited on 01/07/2016).

[34] Thiago Messias Cardozo et al. "Dynamics of benzene excimer formation from the parallel-displaced dimer". In: *Physical Chemistry Chemical Physics* 21.26 (2019), pp. 13916–13924.

[35] Frans C. De Schryver et al. “Intrarnolecular Excimer Formation in Bichromophoric Molecules Linked by a Short Flexible Chain”. In: *Accounts of Chemical Research* 20.5 (1987), pp. 159–166.

[36] Misa Sugino et al. “Elucidation of anthracene arrangement for excimer emission at ambient conditions”. In: *Crystal Growth and Design* 13.11 (2013), pp. 4986–4992.

[37] Gursharan K. Bains et al. “The extent of pyrene excimer fluorescence emission is a reflector of distance and flexibility: Analysis of the segment linking the LDL receptor-binding and tetramerization domains of apolipoprotein E3”. In: *Biochemistry* 51.31 (2012), pp. 6207–6219.

[38] Joachim Vollbrecht. “Excimers in organic electronics”. In: *New Journal of Chemistry* 42.14 (2018), pp. 11249–11254.

[39] Jingdong Luo et al. “Aggregation-induced emission of 1-methyl-1,2,3,4,5-pentaphenylsilole”. In: *Chemical Communications* 381.18 (2001), pp. 1740–1741.

[40] Yi Ting Lee et al. “The first aggregation-induced emission fluorophore as a solution processed host material in hybrid white organic light-emitting diodes”. In: *Journal of Materials Chemistry C* 4.29 (2016), pp. 7020–7025.

[41] Yinghao Li et al. “Creation of Efficient Blue Aggregation-Induced Emission Luminogens for High-Performance Nondoped Blue OLEDs and Hybrid White OLEDs”. In: *ACS Applied Materials and Interfaces* 11.19 (2019), pp. 17592–17601.

[42] Yang Liu et al. “Fluorescent chemosensor for detection and quantitation of carbon dioxide gas”. In: *Journal of the American Chemical Society* 132.40 (2010), pp. 13951–13953.

[43] Lok Nath Neupane et al. “Selective and Sensitive Detection of Heavy Metal Ions in 100% Aqueous Solution and Cells with a Fluorescence Chemosensor Based on Peptide Using Aggregation-Induced Emission”. In: *Analytical Chemistry* 88.6 (2016), pp. 3333–3340.

[44] Linru Xu et al. “Enhancing the visualization of latent fingerprints by aggregation induced emission of siloles”. In: *Analyst* 139.10 (2014), pp. 2332–2335.

[45] Raghupathy Suresh, Senthil Kumar Thiyagarajan, and Perumal Ramamurthy. “An AIE based fluorescent probe for digital lifting of latent fingerprint marks down to minutiae level”. In: *Sensors and Actuators, B: Chemical* 258 (2018), pp. 184–192. URL: `http://dx.doi.org/10.1016/j.snb.2017.11.051`.

[46] Jesse Roose et al. “A colour-tunable chiral AIEgen: Reversible coordination, enantiomer discrimination and morphology visualization”. In: *Chemical Science* 7.9 (2016), pp. 6106–6114.

[47] Kai Li et al. “Photostable fluorescent organic dots with aggregation-induced emission (AIE dots) for noninvasive long-term cell tracing”. In: *Scientific Reports* 3 (2013), pp. 1–10.

[48] Wei Qin et al. “Biocompatible nanoparticles with aggregation-induced emission characteristics as far-red/near-infrared fluorescent bioprobes for in vitro and in vivo imaging applications”. In: *Advanced Functional Materials* 22.4 (2012), pp. 771–779.

[49] Sijie Chen et al. “An AIE-active hemicyanine fluorogen with stimuli-responsive red/blue emission: Extending the pH sensing range by "switch + knob" effect”. In: *Chemical Science* 3.6 (2012), pp. 1804–1809.

[50] Sijie Chen et al. “Full-range intracellular pH sensing by an aggregation-induced emission-active two-channel ratiometric fluorogen”. In: *Journal of the American Chemical Society* 135.13 (2013), pp. 4926–4929.

[51] Zikai He et al. “Aggregation-Induced Emission and Aggregation-Promoted Photochromism of Bis(diphenylmethylene)dihydroacenes”. In: *Chem. Sci.* 6 (2015), pp. 3538–3543.

[52] Youhong Tang and Ben Zhong Tang. *Principles and applications of aggregation-induced emission*. 2018.

[53] EE Jelley. “Molecular, Nematic and Crystal States of I: I-Diethyl–Cyanine Chloride”. In: *Nature* 139 (1937), pp. 631–631.

[54] Frank Würthner, Theo E. Kaiser, and Chantu R. Saha-Möller. “J-Aggregates: From Serendipitous Discovery to Supramolecular Engineering of Functional Dye Materials”. In: *Angewandte Chemie International Edition* 50.15 (2011), pp. 3376–3410.

[55] Xue Qing Li et al. “Highly fluorescent lyotropic mesophases and organogels based on J-aggregates of core-twisted perylene bisimide dyes”. In: *Chemistry - A European Journal* 14.27 (2008), pp. 8074–8078.

[56] Yalong Wang et al. “Aqueous Nanoaggregation-Enhanced One- and Two-Photon Fluorescence, Crystalline J-Aggregation-Induced Red Shift, and Amplified Spontaneous Emission of 9,10-Bis(p- dimethylaminostyryl)anthracene”. In: *Journal of Physical Chemistry C* 116.29 (2012).

[57] Ju Mei et al. “Aggregation-Induced Emission: The Whole Is More Brilliant than the Parts”. In: *Advanced Materials* 26.31 (2014), pp. 5429–5479.

[58] Chunhui Dai et al. “Boron ketoiminate-based conjugated polymers with tunable AIE behaviours and their applications for cell imaging”. In: *Journal of Materials Chemistry B* 3.35 (2015), pp. 7030–7036.

[59] Hui Li et al. “Aggregation-Induced Fluorescence Emission Properties of Dicyanomethylene-1,4-dihydropyridine Derivatives”. In: *The Journal of Physical Chemistry C* 119.12 (2015), pp. 6737–6748.

[60] Rongrong Hu et al. “Twisted intramolecular charge transfer and aggregation-induced emission of BODIPY derivatives”. In: *Journal of Physical Chemistry C* 113.36 (2009), pp. 15845–15853.

[61] Yuning Hong, Jacky W. Y. Lam, and Ben Zhong Tang. “Aggregation-induced emission”. In: *Chemical Society Reviews* 40.11 (2011), p. 5361.

[62] Dongwook Lee et al. “Room temperature phosphorescence of metal-free organic materials in amorphous polymer matrices”. In: *Journal of the American Chemical Society* 135.16 (2013), pp. 6325–6329.

[63] Francesco Ciardelli, Giacomo Ruggeri, and Andrea Pucci. “Dye-containing polymers: methods for preparation of mechanochromic materials”. In: *Chem. Soc. Rev.* 42.3 (2013), pp. 857–870.

[64] Brent R. Crenshaw and Christoph Weder. "Deformation-Induced Color Changes in Melt-Processed Photoluminescent Polymer Blends". In: *Chemistry of Materials* 15.25 (2003), pp. 4717–4724.

[65] Zhenguo Chi et al. "Recent advances in organic mechanofluorochromic materials". In: *Chemical Society Reviews* 41.10 (2012), p. 3878.

[66] Andrea Pucci and Giacomo Ruggeri. "Mechanochromic polymer blends". In: *Journal of Materials Chemistry* 21.23 (2011), p. 8282.

[67] Andrea Pucci, Ranieri Bizzarri, and Giacomo Ruggeri. "Polymer composites with smart optical properties". In: *Soft Matter* 7.8 (2011), p. 3689.

[68] Christiane Löwe and Christoph Weder. "Oligo(p-phenylene vinylene) excimers as molecular probes: Deformation-induced color changes in photoluminescent polymer blends". In: *Advanced Materials* 14.22 (2002), pp. 1625–1629.

[69] Qing Dai et al. "Aggregation-induced emission enhancement materials with large red shifts and their self-assembled crystal microstructures". In: *CrystEngComm* 13.14 (2011), p. 4617. URL: http://xlink.rsc.org/?DOI=c1ce05035d.

[70] Kazuya Nakagawa et al. "Excimer luminescence from nonresonantly excited pyrene and perylene molecules in solution". In: *Journal of Physical Chemistry A* 117.45 (2013), pp. 11449–11455.

[71] Guo-feng Zhang et al. "Direct validation of the restriction of intramolecular rotation hypothesis via the synthesis of novel ortho-methyl substituted tetraphenylethenes and their application in cell imaging". In: *Chemical Communications* 50.81 (2014), pp. 12058–12060. URL: http://xlink.rsc.org/?DOI=C4CC04241G%7B%5C%%7D5Cnhttp://dx.doi.org/10.1039/C4CC04241G.

[72] Zujin Zhao, Jacky W. Y. Lam, and Ben Zhong Tang. "Tetraphenylethene: a versatile AIE building block for the construction of efficient luminescent materials for organic light-emitting diodes". In: *Journal of Materials Chemistry* 22.45 (2012), p. 23726. URL: http://xlink.rsc.org/?DOI=c2jm31949g.

[73] Junwu Chen et al. "Synthesis, Light Emission, Nanoaggregation, and Restricted Intramolecular Rotation of 1,1-Substituted 2,3,4,5-Tetraphenylsiloles". In: *Chemistry of Materials* 15.7 (2003), pp. 1535–1546.

[74] Zujin Zhao, Bairong He, and Ben Zhong Tang. "Aggregation-induced emission of siloles". In: *Chem. Sci.* 6 (2015), pp. 5347–5365. URL: http://pubs.rsc.org/en/Content/ArticleLanding/2015/SC/C5SC01946J.

[75] Kohei Tamao et al. "Silole derivatives as efficient electron transporting materials". In: *Journal of the American Chemical Society* 118.47 (1996), pp. 11974–11975.

[76] H. Y. Chen et al. "Highly efficient organic light-emitting diodes with a silole-based compound". In: *Applied Physics Letters* 81.4 (2002), pp. 574–576.

[77] Yuqi Zhang et al. "Silole-infiltrated photonic crystal films as effective fluorescence sensor for Fe3+ and Hg2+". In: *ChemPhysChem* 15.3 (2014), pp. 507–513.

[78] Dong Hui Wang et al. "Tuning the fluorescence of tetraphenylethylene in dilute solutions: Via modulating multiple-hydrogen-bonding interactions between a Hamilton receptor and cyanuric acid". In: *Organic and Biomolecular Chemistry* 16.24 (2018), pp. 4429–4432.

[79] A. Hoekstra and Aafje Vos. "The Crystal and Molecular Structures of Tetraphenylhydrazine and Related Compounds at 160°C. II. The Crystal Structures of Tetraphenylethylene (TPE) and Diphenylaminotriphenylmethane (DTM)". In: *Acta Crystallographica Section B* B31 (1975), pp. 1716–1721.

[80] Colin R. Groom et al. "The Cambridge structural database". In: *Acta Crystallographica Section B: Structural Science, Crystal Engineering and Materials* 72.2 (2016), pp. 171–179.

[81] Dongwook Kim. "A theoretical study of the formation of benzene excimer: Effects of geometry relaxation and spin-state dependence". In: *Bulletin of the Korean Chemical Society* 35.9 (2014), pp. 2738–2742.

[82] Alice M Smith. *A study into the optical properties of polymer: AIE blend thin films and their applications in nano-lithography.* Tech. rep. Imperial College London, 2016.

[83] By Martin Grell et al. "Blue Polarized Electroluminescence from a Liquid Crystalline Polyfluorene". In: *Communications* (1999), pp. 671–675.

[84] M Ariu et al. "The effect of morphology on the temperature-dependent photoluminescence". In: *Journal of Physics: Condensed Matter* 14.42 (2002), p. 9975.

[85] Martin Grell et al. "A glass-forming conjugated main-chain liquid crystal polymer for polarized electroluminescence applications". In: *Advanced Materials* 9.10 (1997), pp. 798–802.

[86] M. Redecker et al. "Nondispersive hole transport in an electroluminescent polyfluorene". In: *Applied Physics Letters* 73.11 (1998), p. 1565.

[87] D. Braun and A. J. Heeger. "Visible light emission from semiconducting polymer diodes". In: *Applied Physics Letters* 58.18 (1991), p. 1982.

[88] W C Tsoi and D G Lidzey. "Raman spectroscopy of fluorene oligomers in the $\alpha$-, $\beta$- and $\gamma$-phases". In: *Journal of Physics: Condensed Matter* 20.12 (2008), p. 125213.

[89] Aleksandr Perevedentsev. "Chain Conformation and the Photophysics of Polyfluorenes". PhD thesis. Imperial College, 2015.

[90] Aleksandr Perevedentsev et al. "Solution-Crystallization and Related Phenomena in 9,9-Dialkyl-Fluorene Polymers. I. Crystalline Polymer-Solvent Compound Formation for Poly(9,9-dioctylfluorene)". In: *Journal of Polymer Science Part B: Polymer Physics* 53.21 (2015), pp. 1481–1491.

[91] T a M Ferenczi, M Sims, and D D C Bradley. "On the nature of the fluorenone-based emission in oxidized poly(dialkyl-fluorene)s". In: *Journal of Physics: Condensed Matter* 20.4 (2008), p. 045220.

[92] Marc Sims et al. "Understanding the origin of the 535 nm emission band in oxidized poly(9,9-dioctylfluorene): The essential role of inter-chain/inter-segment interactions". In: *Advanced Functional Materials* 14.8 (2004), pp. 765–781.

[93] Noboru Mataga, Yozo Kaifu, and Masao Koizumi. "Solvent Effects upon Fluorescence Spectra and the Dipole moments of Excited Molecules". In: *Bulletin of the Chemical Society of Japan* 29.4 (1956), pp. 465–470.

[94] Noboru Mataga, Yozo Kaifu, and Masao Koizumi. "The Solvent Effect on Fluorescence Spectrum. Change of Solute-Solvent Interaction during the Lifetime of Excited Solute Molecule". In: *Communication* 28.8 (1955).

[95] Francisco Montilla and Ricardo Mallavia. "On the origin of green emission bands in fluorene-based conjugated polymers". In: *Advanced Functional Materials* 17.1 (2007), pp. 71–78.

[96] Soundaram Jeevarathinam Ananthakrishnan et al. "Offsetting the problem of charge trapping in white polymer light-emitting diodes using a fluorenone-based luminogen". In: *Journal of Materials Chemistry C* 2.42 (2014), pp. 9035–9044.

[97] Nadzeya A. Kukhta et al. "Can Fluorenone-Based Compounds Emit in the Blue Region? Impact of the Conjugation Length and the Ground-State Aggregation". In: *Chemistry of Materials* 29.4 (2017), pp. 1695–1707.

[98] Soundaram Jeevarathinam Ananthakrishnan et al. "A solution processable fluorene-fluorenone oligomer with aggregation induced emission enhancement". In: *Chemical Communications* 49.91 (2013), pp. 10742–10744.

[99] Stéphane Dufresne et al. "Insights into the effect of the ketylimine group on the fluorescence deactivation of oligofluorenes". In: *Journal of Physical Chemistry C* 114.30 (2010), pp. 13106–13112.

[100] Patricia Robert, Andréanne Bolduc, and W. G. Skene. "Oligofluorenes as polymeric model compounds for providing insight into the triplets of ketone and ketylimine derivatives". In: *Journal of Physical Chemistry A* 116.37 (2012), pp. 9305–9314.

[101] M Sims et al. "Effect of varying ground state interaction on the intermolecular emission in fluorenone-centred oligofluorenes: Evidence of a well-defined excited state geometry underlying the green emission band".

[102] L. S. Liao et al. "Electronic structure and energy band gap of poly(9,9-dioctylfluorene) investigated by photoelectron spectroscopy". In: *Applied Physics Letters* 76.2000 (2000), p. 3582.

[103] Nathan Cheetham. "Energy and charge transfer studies of a polyfluorene : triarylamine conjugated copolymer series". PhD thesis. Imperial College, 2014, pp. 1–76.

[104] P Prins et al. "Enhanced charge-carrier mobility in b-phase polyfluorene". In: *Physical Review B* 74 (2006), p. 113203.

[105] M. Grell et al. "Interplay of physical structure and photophysics for a liquid crystalline polyfluorene". In: *Macromolecules* 32.18 (1999), pp. 5810–5817.

[106] W. Chunwaschirasiri et al. "Chain Conformations and Photoluminescence of Poly(di-n-octylfluorene)". In: *Physical Review Letters* 94.10 (2005), p. 107402.

[107] P N Stavrinou et al. "The change in refractive index of poly(9,9-dioctylfluorene) due to the adoption of the $\beta$-phase chain conformation". In: *Journal of Physics: Condensed Matter* 19.46 (2007), p. 466107.

[108] a. J. Cadby et al. "Film morphology and photophysics of polyfluorene". In: *Physical Review B - Condensed Matter and Materials Physics* 62.23 (2000), pp. 15604–15609.

[109] H.-H. Lu et al. "Self-Dopant Formation in Poly(9,9-di-n-octylfluorene) Via a Dipping Method for Efficient and Stable Pure-Blue Electroluminescence". In: *Advanced Materials* 19.18 (2007), pp. 2574–2579.

[110] M C Chen et al. "Nanoscale Ordered Structure Distribution in Thin Solid Film of Conjugated Polymers: Its Significance in Charge Transport Across the Film and in Performance of Electroluminescent Device". In: *Journal of Physical Chemistry B* 113.32 (2009), pp. 11124–11133.

[111] Jeffrey Peet et al. "Controlled beta-phase formation in poly(9,9-di-n-octylfluorene) by processing with alkyl additives". In: *Advanced Materials* 20.10 (2008), pp. 1882–1885.

[112] Valerio Lucarini et al. *Kramers-Kronig Relations in Optical Materials Research*. Springer Berlin Heidelberg, 2005.

[113] Donal D C Bradley et al. "Influence of Aggregation on the Optical Properties of a Polyfluorene". In: *Optical Probes of Conjugated Polymers*. Vol. 3145. 1997, pp. 254–259.

[114] Gihan Ryu, Paul N Stavrinou, and Donal D C Bradley. "Spatial Patterning of the beta-Phase in Poly (9,9-dioctylfluorene): A Metamaterials-Inspired Molecular Conformation Approach to the Fabrication of Polymer Semiconductor Optical Structures". In: *Advanced Functional Materials* 19.20 (2009), pp. 3237–3242.

[115] Alexander J. C. Kuehne et al. "Sub-Micrometer Patterning of Amorphous- and $\beta$-Phase in a Crosslinkable Poly(9,9-dioctylfluorene): Dual-Wavelength Lasing from a Mixed-Morphology Device". In: *Advanced Functional Materials* 21.13 (2011), pp. 2564–2570. URL: http://doi.wiley.com/10.1002/adfm.201002553.

[116] Alexander J C Kuehne and Malte C. Gather. "Organic Lasers: Recent Developments on Materials, Device Geometries, and Fabrication Techniques". In: *Chemical Reviews* 116.21 (2016), pp. 12823–12864.

[117] W Fahrner. *Nanotechnology and Nanoelectronics: Materials, Devices, Measurement Techniques*. EngineeringPro collection. Springer Berlin Heidelberg, 2005, p. 173. URL: https://books.google.co.uk/books?id=Y-g2FL8Qv2kC.

[118] Yong Kwan Kim et al. "Focused ion beam nanopatterning for optoelectronic device fabrication". In: *IEEE Journal on Selected Topics in Quantum Electronics* 11.6 (2005), pp. 1292–1297.

[119] S. Cabrini et al. "Focused ion beam lithography for two dimensional array structures for photonic applications". In: *Microelectronic Engineering* 78-79.1-4 (2005), pp. 11–15.

[120] O. Wilhelmi et al. "Focussed ion beam fabrication of large and complex nanopatterns". In: *Journal of Experimental Nanoscience* 5.3 (2010), pp. 244–250.

[121] John Melngailis. "Focused Ion Beam Lithography and Implantation". In: *IEEE*. 1989. URL: http://stacks.iop.org/0957-0233/26/i=9/a=095601?key=crossref.a70b9aa7dbb3b35fa05f6f656066aff5.

[122] Ronghua Zhu et al. “Fabrication of speckle patterns by focused ion beam deposition and its application to micro-scale residual stress measurement”. In: *Measurement Science and Technology* 26.9 (2015), p. 095601. URL: http://stacks.iop.org/0957-0233/26/i=9/a=095601?key=crossref.a70b9aa7dbb3b35fa05f6f656066aff5.

[123] Fengwei Huo et al. “Beam pen lithography”. In: *Nature Nanotechnology* 5.9 (2010), pp. 637–640.

[124] R M Parker et al. “An Integrated Reconfigurable Bragg Grating utilising a Photoresponsive Co-polymer”. In: *European Conference on Integrated Optics* (2010), pp. 1–2.

[125] Takashi Fukuda et al. “Photofabrication of surface relief grating on films of azobenzene polymer with different dye functionalization”. In: *Macromolecules* 33.11 (2000), pp. 4220–4225.

[126] Richard D Piner et al. ““Dip-Pen” Nanolithography”. In: *Science* 283.5402 (1999), pp. 661–664.

[127] Guoqiang Liu et al. “Development of Dip-Pen Nanolithography (DPN) and Its Derivatives”. In: *Small* 15.21 (2019).

[128] C. Maedler et al. “Creation of nanopatterns by local protonation of P4VP via dip pen nanolithography”. In: *Journal of Applied Physics* 104.1 (2008), p. 014311. URL: http://link.aip.org/link/JAPIAU/v104/i1/p014311/s1%7B%5C&%7DAgg=doi.

[129] Khalid Salaita, Yuhuang Wang, and Chad a Mirkin. “Applications of dip-pen nanolithography.” In: *Nature nanotechnology* 2.3 (2007), pp. 145–155.

[130] Hiroshi Nakashima et al. “Liquid deposition patterning of conducting polymer ink onto hard and soft flexible substrates via dip-pen nanolithography”. In: *Langmuir* 28.1 (2012), pp. 804–811.

[131] Zeev Fradkin et al. “Fabrication of polymeric photonic structures using dip-pen nanolithography”. In: *Journal of Micro/Nanolithography, MEMS, and MOEMS* (2020).

[132] Seunghun Hong and Chad A. Mirkin. “A nanoplotter with both parallel and serial writing capabilities”. In: *Science* 288.5472 (2000), pp. 1808–1811.

[133] J R Haaheim et al. “Dip-Pen Nanolithography: A Maturing Technology for High-Throughput Flexible Nanopatterning”. In: *SPIE Proceedings* 6556 (2007), p. 8.

[134] Robert J Stokes, Robert M Marchmont, and Alexander Smetana. *Science at the Sharp End: Recent Advances in Tip-based Nanolithography for the Fabrication and Modification of Plasmonic Structures and Sensors*. Tech. rep. 1999. 2008.

[135] NanoInk. *NLP 2000 System Data Sheet*. Tech. rep. 2000, pp. 1–5.

[136] Acs-t. *Desktop Nano Lithography Platform System (NLP 2000)*. 2015.

[137] Leilei Huang et al. “Waveguide fabrication in KDP crystals with femtosecond laser pulses”. In: *Applied Physics A: Materials Science and Processing* 118.3 (2014), pp. 831–836.

[138] Jun Guan et al. “Hybrid laser written waveguides in fused silica for low loss and polarization independence”. In: 25.5 (2017), pp. 4845–4859. arXiv: arXiv:1602.02840v1.

[139] Robert Taylor. *Optoelectronics Minor Option Lecture 8 - Integrated Optics in Comms . Systems 1 Fibre Connectors , Couplers , Mixers and Splitters*. Tech. rep.

[140] Bernard C. Kress. *Field Guide to Digital Micro Optics*. SPIE Press, 2014, p. 8.

[141] Julian Hauss et al. “On the interplay of waveguide modes and leaky modes in corrugated OLEDs.” In: *Optics express* 19.7 (2011), A851–A858.

[142] P.N. Stavrinou. *Photonics Course: Microcavities*. Tech. rep. 2016.

[143] Jeroen Missinne et al. “Planar polymer waveguides with a graded-index profile resulting from intermixing of methacrylates in closed microchannels”. In: *Optical Materials* 76 (2018), pp. 210–215. URL: https://doi.org/10.1016/j.optmat.2017.12.039.

[144] Kohei Abe, Yutaro Oizumi, and Takaaki Ishigure. “Low-loss graded-index polymer crossed optical waveguide with high thermal resistance”. In: 26.4 (2018), pp. 4512–4521.

[145] Beer. “Bestimmung der Absorption des rothen Lichts in farbigen Flussigkeiten”. In: *Annalen der physik* 162.5 (1852), pp. 78–88.

[146] Johann Heinrich Lambert. *Lambert’s Photometrie: (Photometria, Sive De Mensura et Gradibus Luminis, Colorum et Umbrae) (1760): Deutsch hrsg. von E. Anding*. Leipzig: W. Engelmann, 1892, p. 432. URL: http://books.google.com/books?id=Fq4RAAAAYAAJ.

[147] Pierre Bouguer. *Bouguer, P. Essai d’optique sur la gradation de la lumière.* Paris: Claude Jombert, 1729.

[148] Nathan James Cheetham. “The Effect of Highly-Ordered Molecular Conformations on the Optoelectronic Properties of Conjugated Polymers”. PhD thesis. 2018.

[149] Frank L. Pedrotti and Leno S. Pedrotti. *Introduction to Optics*. 2nd ed. Prentice-Hall International, Inc., 1993, p. 11.

[150] John C. de Mello, H. Felix Wittmannn, and R.H. Friend. “An Improved Experimental Determination of External Photoluminescence Quantum Efficiency”. In: *Advanced materials (Deerfield Beach, Fla.)* 9.3 (1997), p. 230. arXiv: 97/0302-023 [0935-9648]. URL: http://www.ncbi.nlm.nih.gov/pubmed/20217798.

[151] Christian Würth et al. “Comparison of methods and achievable uncertainties for the relative and absolute measurement of photoluminescence quantum yields”. In: *Analytical Chemistry* 83.9 (2011), pp. 3431–3439.

[152] Laurent Porrès et al. “Absolute measurements of photoluminescence quantum yields of solutions using an integrating sphere”. In: *Journal of Fluorescence* 16.2 (2006), pp. 267–272.

[153] Jonathan Mooney and Patanjali Kambhampati. “Get the Basics Right: Jacobian Conversion of Wavelength and Energy Scales for Quantitative Analysis of Emission Spectra”. In: *The Journal of Physical Chemistry Letters* 3318.2 (2013), pp. 3316–3318.

[154] M. Sajadi et al. "Time-resolved fluorescence spectra of cis-stilbene in hexane and acetonitrile". In: *Chemical Physics Letters* 489.1-3 (2010), pp. 44–47. URL: http://dx.doi.org/10.1016/j.cplett.2010.02.034.

[155] Ruoyu Zhan et al. "AIE Polymers: Synthesis, Properties, and Biological Applications". In: *Macromolecular Bioscience* 17.5 (2017), pp. 1–19.

[156] Xiaofeng Ma et al. "Fluorescence Aggregation-Caused Quenching versus Aggregation-Induced Emission: A Visual Teaching Technology for Undergraduate Chemistry Students". In: *Journal of Chemical Education* 93.2 (2016), pp. 345–350.

[157] Charles M. Hansen. *Hansen Solubility Parameters: A User's Handbook*. URL: http://www.ebookstore.tandf.co.uk/..

[158] Franklin Jaramillo-Isaza and Michael L. Turner. "Synthesis and properties of conjugated oligomers containing fluorene, fluorenone, thiophene and cyclopentadithiophenone units". In: *Journal of Materials Chemistry* 16.1 (2006), pp. 83–89.

[159] Xiuwen Zhou et al. "First-principles simulation of the absorption bands of fluorenone in zeolite L". In: *Physical Chemistry Chemical Physics* 15.1 (2013), pp. 159–167.

[160] Shin-ichi Yusa et al. *Polymer Micelles*. MDPI, 2018.

[161] Lukas Novotny and Bert Hecht. *Principles of Nano-Optics*. Cambridge University Press, 2006.

[162] E. Abbe. "Beiträge zur Theorie des Mikroskops und der mikroskopischen Wahrnehmung". In: *Archiv für Mikroskopische Anatomie* (1873).

[163] University of Utah. *Super-Resolution Tutorial - Education - Advanced Microscopy*. URL: https://advanced-microscopy.utah.edu/education/super-res/ (visited on 09/04/2020).

[164] Sandeep Gorantla. *Lecture 11: Contrast Transfer Function in HRTEM*. Tech. rep. University of Oslo.

[165] Reinhart (Aachen University) Poprawe. *Gaussian beam - YouTube*. 2016. URL: https://www.youtube.com/watch?v=MU4eOJw2sBQ (visited on 09/04/2020).

[166] Anthony E. Siegman. *Lasers*. University Science Books, 1986.

[167] Eric Weisstein. *Gaussian Function - from Wolfram MathWorld*. URL: https://mathworld.wolfram.com/GaussianFunction.html (visited on 09/04/2020).

[168] John M. Khosrofian and Bruce A. Garetz. "Measurement of a Gaussian laser beam diameter through the direct inversion of knife-edge data". In: *Applied Optics* 22.21 (1983), pp. 3406–3410.

[169] Mark J. Holmes. "Optical spectroscopy of wide bandgap semiconductor nanoscale structures". PhD thesis. 2011. URL: http://ora.ox.ac.uk/objects/uuid%7B%5C%%7D3Ab8318654-dd3a-4875-8a8e-1e57d877b0f2.

[170] Carlo Marangoni. "On the expansion of a drop of liquid floating on the surface of another liquid". In: *Tipographia dei fratelli Fusi, Pavia* (1865).

[171] Masahiko Taniguchi and Jonathan S. Lindsey. "Database of Absorption and Fluorescence Spectra of >300 Common Compounds for use in PhotochemCAD". In: *Photochemistry and Photobiology* 94.2 (2018), pp. 290–327.

[172] Masahiko Taniguchi, Hai Du, and Jonathan S. Lindsey. "PhotochemCAD 3: Diverse Modules for Photophysical Calculations with Multiple Spectral Databases". In: *Photochemistry and Photobiology* 94.2 (2018), pp. 277–289.

[173] Takumi Nakamura et al. "Revised steady-state fluorescence spectrum and nature of the reactive S1 state of cis-stilbene in solution". In: *Chemical Physics Letters* 465.4-6 (2008), pp. 212–215. URL: http://dx.doi.org/10.1016/j.cplett.2008.09.076.

[174] ThorLabs. *25 mm x 36 mm Plate Beamsplitters*. URL: https://www.thorlabs.com/newgrouppage9.cfm?objectgroup%7B%5C_%7Did=6265%7B%5C&%7Dpn=BSW26R (visited on 09/22/2020).